UNIVERSITY OF GHANA

COLLEGE OF BASIC AND APPLIED SCIENCES

# MONITORING AND HIGH RESOLUTION STUDIES OF SOME HYDROXYL AND METHANOL MASERS IN THE HIGH MASS STAR FORMING REGION G9.62 + 0.20 E

BENEDICTA WOODE

DEPARTMENT OF PHYSICS

JULY 2020

UNIVERSITY OF GHANA COLLEGE OF BASIC AND APPLIED SCIENCES

# MONITORING AND HIGH RESOLUTION STUDIES OF SOME HYDROXYL AND METHANOL MASERS IN THE HIGH MASS STAR FORMING REGION G9.62 + 0.20 E

BY

BENEDICTA WOODE

(10220100)

A THESIS SUBMITTED TO THE UNIVERSITY OF GHANA, LEGON, IN PARTIAL FULFILLMENT OF THE REQUIREMENTS FOR THE AWARD OF THE DEGREE OF DOCTOR OF PHILOSOPHY IN PHYSICS

DEPARTMENT OF PHYSICS

JULY 2020

# ABSTRACT

This thesis presents the observational data reduction and results of an investigation into the 1.6 GHz OH and 6.7 GHz methanol masers in the G9.62 + 0.20E massive star forming region. Monitoring observations from the Hartebeesthoek Radio Astronomy Observatory (HartRAO) radio telescope were employed to establish correlated variabilities between the 6.7 GHz methanol masers and the left and right circular polarizations (LCP and RCP) of the mainline 1.6 GHz OH masers. This is the first reported incidence of periodic variations of the LCP and RCP components of the 1.6 GHz OH mainline masers associated with the 6.7 GHz methanol masers in this high mass star forming region. Correlated variability between the varying features in the LCP components of both hydroxyl masers and methanol masers was observed but the variability profiles were different for both species. Time lags were recorded between the methanol and the OH maser variabilties. Within the OH masers the variability profiles were preceded by a dip in flux density. The first high resolution observation of the L-band and C-band continuum of G9.62 + 0.20E were conducted with the e-MERLIN interferometric array. A flux density of $2.25 \pm 0.20$ mJy and an angular size of 130 mas were measured for the C-band continuum. At L-band, an upper limit of 162 $\mu$Jy on the integrated flux density was calculated at the position of the continuum. These results unlike previous observations reveal that the spectrum turns over steeply at low frequencies which could be explained with a truncated inverse square law density distribution model. The peak brightness temperature indicates that the continuum is optically thin at C-band and optically thick at L-band. In the context of the colliding wind binary model for periodic maser sources it is the variation of the seed photons from the background HII region that explains the variability. The continuum results in this thesis place firm constraints on models of the HII region that can be used to test the predictions of the colliding wind binary model in terms of the variability profiles of the OH and methanol masers.

# DECLARATION

I, Benedicta Woode, hereby declare that except where specific reference is made to the work of others, the contents of this dissertation are original and have not been submitted in whole or in part for consideration for any other degree or qualification in this or any other university and that this submission undertaken in the University of Ghana is my own work under the supervision of the undersigned.

............................................

Candidate: Benedicta Woode

Supervisors:

...........................................

Dr. Amos Kuditcher

..............................................

Prof. Melvin G. Hoare

.............................................

Dr. Sharmila Goedhart

# DEDICATION

To the memory of my maternal grandmother, Madam Georgina Adjoa Besema Enchill, and to astronomy in Ghana.

# ACKNOWLEDGEMENTS

This work is the output of four years of research which several persons have through technical support, advice, financial support and in diverse ways helped to produce. I wish to express my sincere gratitude to all of them.

I wish to thank Dr. Amos Kuditcher for guiding and nurturing me from my undergraduate days till now, Prof. Melvin Hoare, the man who makes everything happen, and Dr. Sharmila Goedhart for giving me the data on her baby, G9.62 + 0.20 E. I am also grateful to Dr. Gordon Macleod for scheduling my HartRAO observations.

I wish to acknowledge support from Dr. Javier Molden for painstakingly taking me through the rudiments of interferometric data reduction, Dr. James Chibueze, Dr. Jabulani Maswangegy, Mavis Seidu, Dr. Benito Marcote and Ziad Modak who were very instrumental in my study of Python. I also thank Dr. Rosalind Skelton who introduced me to the rudiments of the field and Dr. Robert Beswick who has been as he himself will put it ’lovingly excellent.’ I am also grateful to Prof Alberto Sanna for providing the Q-band size of G9.62 + 0.20 E.

It has been a pleasure working with members of the Department of Physics in the University of Ghana, School of Physics and Astronomy in the University of Leeds, Jodrell Bank Center for Astronomy in the University of Manchester and the Ghana Space Science and Technology Institute; I am grateful for their support.

Research reported in this thesis was supported by a Newton Fund project, DARA (Development in Africa with Radio Astronomy), and awarded by the UK’s Science and Technology Facilities Council (STFC) - grant reference ST/R001103/1. I am grateful to Prof. Yaa Ntiamoah Baidoo and the Carnegie Corporation, New York, for funding this work under the Next Generation of Academics in Africa grants. I am also indebted to the European Union Horizon 2020 Research and Innovation programme via Jumping Jive for funding my stay in Manchester.

I thank my family and friends for the love and encouragement throughout my long years of study. And to my husband, Akwasi Boakye and my son Nana Kwabena Baffour Boakye, what exactly could I have done without you?

# TABLE OF CONTENTS

# LIST OF FIGURES

# LIST OF TABLES

# LIST OF SYMBOLS

| | |
|---|---|
| $L_\odot$ | Solar luminosity |
| $M_\odot$ | Solar mass |
| $M_{\mathrm{crit}}$ | Critical mass for gravitational collapse |
| $M_J$ | Jeans mass |

# LIST OF ABBREVIATIONS

| | |
|---|---|
| ATCA | Australian Telescope Compact Array. |
| CMC | Cold Molecular Cloud. |
| CWB | Colliding Wind Binary. |
| Dec | Declination. |
| e-MERLIN | Enhanced-Multi Element Radio Linked Interferometer Network. |
| FIR | Far Infrared. |
| GMC | Giant Molecular Cloud. |
| HartRAO | Hartebeesthoek Radio Astronomy Observatory. |
| HMC | Hot Molecular Cloud. |
| HR | Hertzsprung-Russell. |
| IR | Infrared. |
| ISM | Interstellar Medium. |
| JVLA | Jansky Very Large Array. |

| | |
|---|---|
| KH | Kelvin-Helmholtz. |
| LBA | Long Baseline Array. |
| LCP | Left Circular Polarisation. |
| MC | Molecular Cloud. |
| MIR | Mid Infrared. |
| MS | Main Sequence. |
| MYSO | Massive Young Stellar Object. |
| PAH | Polycyclic Aromatic Hydrocarbon. |
| PDR | Photo-Dissociation Regions. |
| PMS | Pre Main Sequence. |
| RA | Right Ascension. |
| RCP | Right Circular Polarisation. |
| RFI | Radio Frequency Interference. |
| submm | Submillimeter. |
| UCHII | Ultracompact. |
| VLBA | Very Long Baseline Array. |
| VLBI | Very Long Baseline Interferometry. |
| ZAMS | Zero Age Main Sequence. |

# CHAPTER 1

# INTRODUCTION

High mass star formation involves the processes by which gases in the interstellar medium (ISM) are transformed into stars of various masses greater than 8 $M_\odot$ and luminosities greater than $10^3$ $L_\odot$ (Urquhart et al., 2015; Guzman et al., 2016) either in isolation or in clusters. During these processes matter and energy are continuously exchanged within the ISM, forming a recycle hub of energy and matter. Hence, the formation of high mass stars is of great importance for understanding the evolution of galaxies, and the quest to understand the physics governing these processes has inspired a lot of research in the field of astrophysics.

The theory on how low mass stars (mass less than 8 $M_\odot$) form has greatly been shaped by their theoretical and observational studies in our Galaxy (Shu et al., 1987). This has been possible because of the proximity of some low mass stars to Earth and their abundance in our Galaxy. The closest low mass star forming region, Ophiuchus is located at about 120 pc (Loinard et al., 2008). Our observation of how high mass stars form, however, is greatly hindered by various factors, which are also part of the environmental conditions necessary for their formation. First, high mass stars are rare, and availability of exemplars on which to base theoretical and observational studies are severely limited. They are formed at large distances away from the Earth, with the closest high mass star forming region being Orion KL at 437 pc (Genzel et al., 1981; Hirota et al., 2007) and the next in proximity being Cepheus A at $\sim$ 700 pc (Moscadelli and Reid, 2009; Dzib et al., 2011). The whole process of the formation of high mass stars is shrouded in dense cocoons of gas and dust resulting in high extinction which makes the region opaque to optical probes (Zinnecker and Yorke, 2007). Hence, their study relies heavily on observations of thermal dust emission at infra-red (IR) and submillimeter (submm) wavelengths, ionized hydrogen emission at radio wavelengths and spectral line emissions from the surrounding molecular gas clouds. Figure 1.1 is a three-colour composite image of the G9.62 + 0.20 high mass star forming region showing emissions at 8 $\mu$m in red, at 4.5 $\mu$m in green and at 3.6 $\mu$m in blue (Liu et al., 2017). Labelled A, B, C, D and E on the figure are the radio sources as named by Garay et al. (1993), with the white contours being 450 $\mu$m emissions which trace dust emissions from the region and the red contours being 8 $\mu$m emissions showing polycyclic aromatic hydrocarbon (PAH) emissions tracing photo-dissociation regions (PDR's) which hitherto have not been revealed with optical probes. In addition to all the factors given so far, the relatively short time scales of important stages of high mass star formation present a problem when tracking their evolutionary phases. For example, the Kelvin-Helmholtz (KH) timescale (time it takes for a young stellar object or stellar core to radiate its thermal energy content) is typically $10^7$ yr for low mass stars but less than $10^4$ yr for high-mass stars. To compound the problem high mass stars are mostly found in clusters with their low mass counterparts, making it difficult to observe them individually (Andrews et al., 2014).

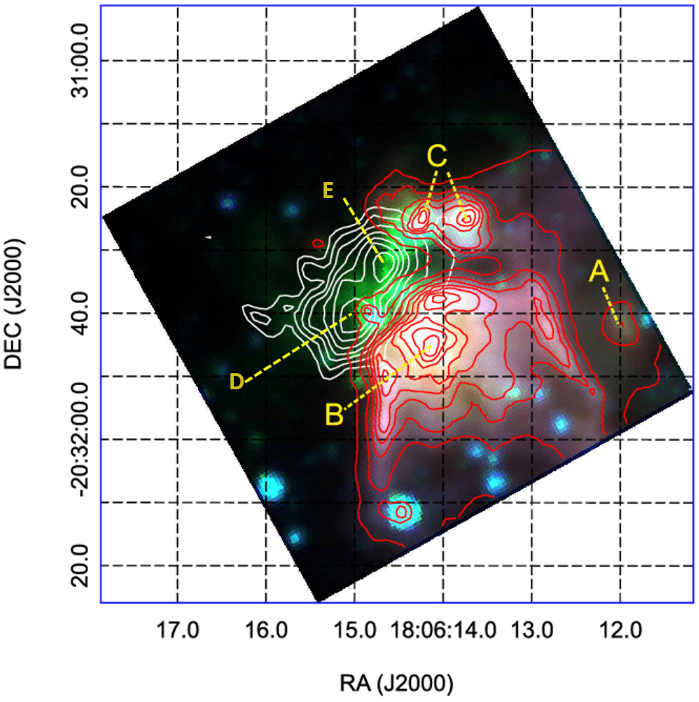

Figure 1.1: A three-colour composite Spitzer image of the G9.62 + 0.20 complex showing emissions at 8 $\mu$m in red, 4.5 $\mu$m in green, and 3.6 $\mu$m in blue. The contours are constant intensity lines for which the white contours trace dust emissions at 450 $\mu$m and the red contours trace photo-dissociation regions at 8 $\mu$m (Liu et al., 2017).

In spite of the challenges in their observation, the critical role played by high mass stars in the evolution of galaxies and the universe cannot be over emphasised (Hoyle, 1954). High mass stars disperse large amounts of radiative energy across galaxies. They also serve as the origin of elements, that is, they are the chemical factories of the ISM, producing atoms, molecules and ionised gases, and thus are the principal source of heavy elements in the universe (Hoyle, 1954). Despite decades of work a general theory of star formation that explains the birth of stars of all masses emanating from different environmental conditions is still sketchy. Depending on their masses, luminosities, and how they die, star formation is grouped into low mass star formation for stars with $M < 8\ M_{\odot}$ that end their lives as white dwarves and high mass star formation for stars with $M > 8\ M_{\odot}$ that end their lives in a Type II supernova.

Generally, star formation occurs in warm dense cores of giant molecular clouds (GMC) which consist of cold dense molecular gas and dust concentrated in the spiral arms of a galaxy. Molecular clouds (MC's) are observed to be highly turbulent (McKee and Tan, 2003) with properties as given in Table 1.1.

Table 1.1: Properties of molecular clouds (Shu et al., 1987).

| Property | Value |
|---|---|
| Mass range ($M_{\odot}$) | $10$ - $10^{6}$ |
| Size range (pc) | 1 - 100 |
| Density range (cm$^{-3}$) | $10^{3}$ - $10^{4}$ |
| Temperature (K) | 10 - 20 |
| Age (yr) | $10^{5}$ - $10^{9}$ |

Within the molecular clouds there are filamentary and hierarchical structures such as clumps, cold molecular cores (CMC) and hot molecular cores (HMC) (Arzoumanian et al., 2011; Hacar et al., 2013; Smith et al., 2014; Wang et al., 2019). These structures are made up of different density regions with typical densities, sizes (McGuire et al., 2016) and other important properties as given in Table 1.2 (Zinnecker and Yorke, 2007; Stahler and Palla, 2004). These regions of high density gradients of compressed gas and dust occur as a result of a complex interplay between gravity and several opposing forces such as turbulence, gas pressure, magnetic fields and radiative pressure (Traficante et al., 2020).

To form a star of average density $10^{3}$ kg m$^{-3}$ from a GMC density of order $10^{-18}$ kg m$^{-3}$, the GMC must be sufficiently compressed which can only be possible by self gravity; thus,

Table 1.2: Properties of giant molecular clouds and the structures found within them (Zinnecker and Yorke, 2007; Stahler and Palla, 2004).

| Property | GMC | Clumps | CMC | HMC |
|---|---|---|---|---|
| Mass ($M_\odot$) | $10^4$ - $10^{6.5}$ | $10^2$ - $10^3$ | 100 - 500 | $<100$ |
| Size (pc) | 10 - 100 | 1 - 1.5 | 0.2 - 0.3 | 0.1 |
| Mean density (cm$^{-3}$) | 50 - 500 | $10^3$ - $10^4$ | $10^4$ - $10^5$ | $\approx 10^7$ |
| Temperature (K) | $\approx$ 10 - 20 | 10 - 30 | 8 - 12 | $\geqslant 100$ |

gravity must overcome the turbulence, gas pressure, magnetic fields and radiative pressure. Consider a spherical shell of radius $r$ and mass $dM(r)$ in a single isolated spherically symmetric cloud. At equilibrium the outward pressure on the shell will be equal to the force of gravity acting on the shell, giving

$$4\pi r^2 dP(r) = -\frac{GM(r)}{r^2} dM(r) \tag{1.1}$$

where $G$ is the gravitation constant (Stahler and Palla, 2004). Integrating from centre to surface over a sphere of volume $V(R_c) = \frac{4}{3}\pi R_c^3$ gives

$$3\int_{P_0}^{P_s} V(r)\, dP(r) = \int_{M_c}^{0} \frac{GM(r)}{r} dM(r) \tag{1.2}$$

where $P_s$ and $P_0$ are the pressures at the surface and center, $M_c$ is the cloud mass and $R_c$ is the cloud radius. The total gravitational energy content of the cloud therefore is

$$\Omega = -\int_{0}^{M_c} \frac{GM(r)}{r} dM(r) \tag{1.3}$$

and for an ideal mono-atomic gas the mean kinetic energy is

$$U = \frac{3}{2} N k_B T \tag{1.4}$$

where $k_B$ is the Boltzmann constant, $T$ is the uniform temperature of the cloud and $N$ is the total number of molecules in the cloud. For a cloud with constant density $\rho$, constant pressure $P_c$ and zero external pressure, $P_s = 0$ and $U$ is the total thermal energy content of the cloud, yielding the virial equation

$$2U + \Omega = 0 \tag{1.5}$$

If $2U = -\Omega$, the cloud is stable and in equilibrium. When $2U > \Omega$, pressure overcomes gravity and the cloud is dispersed. When $2U < -\Omega$, gravity overcomes pressure and the cloud contracts. Thus, for contraction

$$\frac{3}{5}\frac{GM^2}{R_c} > 3V_cP_c \tag{1.6}$$

where $P_c = Nk_BT/V_c$ and $R_c = (3M_c/4\pi\rho_c)^{1/3}$ have been used. Substituting $N = M_c/\mu M_H$, where $\mu M_H$ is the mean molecular mass of the gas in the cloud in Equation 1.6 leads to a critical mass

$$M_{\text{crit}} = \left(\frac{5k_BT}{G\mu M_H}\right)^{3/2}\left(\frac{3}{4\pi\rho_c}\right)^{1/2} \tag{1.7}$$

above which the cloud collapses; that is, the cloud collapses if $M_c > M_{\text{crit}}$. The critical mass for collapse is proportional to $v_T^3$, where $v_T = \sqrt{k_BT/\mu M_H}$ is the isothermal speed of sound in the cloud.

For a cloud undergoing collapse (ignoring pressure and assuming gravity dominates) the equation of motion for a thin shell with an initial radius $R_c$ is

$$\frac{d^2r}{dt^2} = -\frac{GM(r)}{r^2} = -\frac{4\pi G{R_c}^3\rho_c}{3r^2} \tag{1.8}$$

Assuming the mass and acceleration remain constant, a free-fall time of

$$t_{ff} = \left(\frac{3\pi}{32G\rho_c}\right)^{1/2} \tag{1.9}$$

is obtained. The free-fall time is long for low-density regions and short for high-density regions. Thus the virial equation, Equation 1.5, sets the stability criterion of a molecular cloud supported by thermal pressure alone. A cloud supported only by thermal pressure will collapse if its mass exceeds the Jeans mass

$$M_J \propto (T)^{3/2}(\rho)^{-1/2} \tag{1.10}$$

(See Equation 1.7.) Further contraction of a collapsing star results in approximately half of the gravitational energy gained being used to increase the internal temperature of the cloud and the residual energy being radiated into space. The duration for this further contraction is the Kelvin-Helmholtz (KH) time given by

$$t_{KH} = \frac{GM^2}{L_* R_*} \tag{1.11}$$

where $L_*$ is luminosity of the the star and $R_*$ is its radius. This duration determines how quickly a proto-star contracts during its pre-main sequence (PMS) phase before it enters the zero age main sequence (ZAMS) stage and hydrogen burning in its core through fusion reactions subsequently begins. It then joins the main sequence (MS) stars on the Hertzsprung-Russell (HR) diagram.

The paradigm of low mass star formation as given by Shu et al. (1987) describes the sequence of events for isolated cases of low mass star formation by linking the theories of low mass star evolution to the observed situation reported by Adams et al. (1987). The scheme of events was extended by Lada (1985) and Andre et al. (1993) to include much earlier states of young stellar objects when they are still hidden in their natal clouds and can only be seen at FIR and submm wavelengths as in Figure 1 of Feigelson and Montmerle (1999) and Figure 1.1 of Isella (2006). In this model, the formation of a low mass star is divided into four distinct stages. The first stage involves slowly rotating cloud cores being formed from a molecular cloud as shown in Figure 1.2(a). This occurs by ambipolar diffusion resulting from the slow drift of ions and neutral atoms which causes the clouds to lose magnetic and turbulent support. In addition, clumps of mass greater than the critical mass for collapse may also fragment as they contract and flatten (Shu et al., 1987; Zhang et al., 2015).

The second stage sets off when the cloud core becomes unstable in a dynamic inside out collapse as in Figure 1.2(b). The slowly rotating cloud of gas then contracts to form a central proto-star. The proto-star then enters the third stage of evolution which is the bipolar outflow

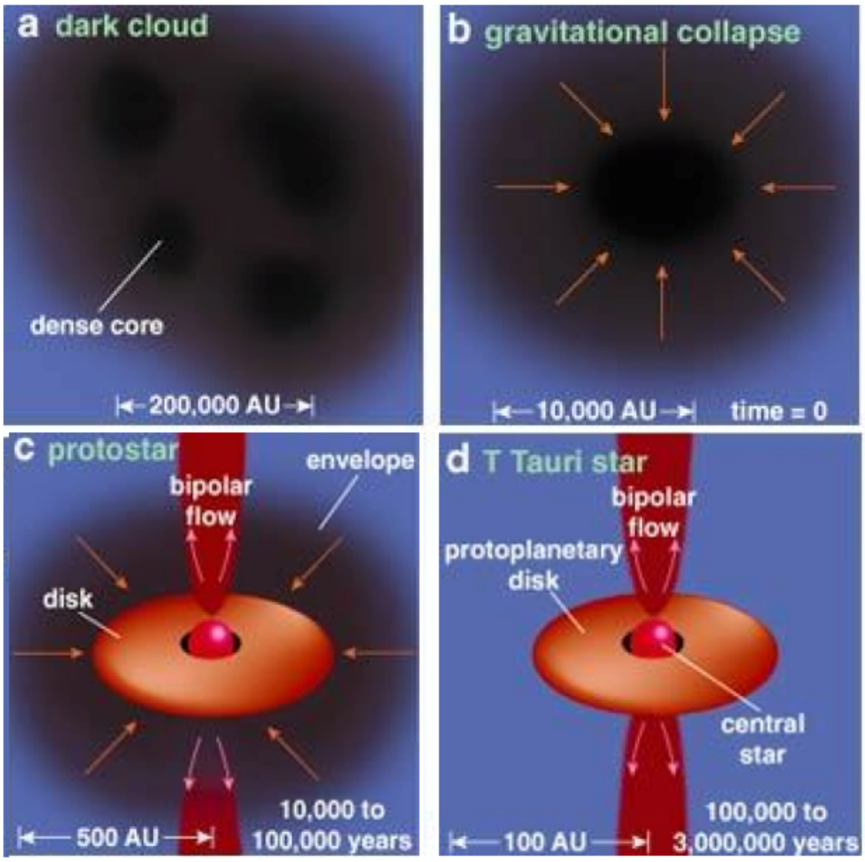

Figure 1.2: The four stages of the low mass star formation process as illustrated by Shu et al. (1987); van Dishoeck and Blake (1998); Greene (2001). Plate (a) depicts the fragmentation of a molecular cloud into pre-stellar cores as the cloud collapses under its gravity. In plate (b) the proto-star builds up mass from in-falling gas as it continues to collapse. Plate (c) shows the formation of a disc in the nebula as the proto-star conserves angular momentum and the breakout out of bipolar outflows along the the axis of rotation of the T-Tauri star. Finally the nebula is swept away in Plate (d) revealing the newly formed pre-main sequence star and the remains of the accretion disk.

phase in Figure 1.2(c) (Swift and Welch, 2008; Wang et al., 2014). The cloud of gas contracts further, forming a rotating sphere, and to conserve angular momentum, flattens into an accretion disk surrounded by an in-falling envelope of dust and gas (Luhman et al., 1998). The proto-star accretes incoming material which falls onto the disk rather than onto the center (Dunham and Vorobyov, 2012). Fast moving gas molecules are driven along the rotational axis in the form of collimated jets and bipolar outflows. As time progresses, the opening of the stellar outflows sweeps across all directions revealing the fourth stage of a young stellar object (YSO) surrounded by a remnant nebular disk as can be seen in Figure 1.2(d) (Chen et al., 2016). As accretion stops the PMS star begins its journey of evolution on the HR diagram.

High mass stars on the other hand do not follow the process described above in their formation. Since both low and high mass stars are formed in regions of similar densities they should have the same free fall time (the timescale it takes for a pressure-free cloud to collapse dynamically to a very small size under its own gravity) and acrshortKH time. For the relatively short life span of high mass stars the theoretical considerations of their formation run into problems when the free fall time is comparable to the KH time. The KH time is short for high mass stars implying they arrive on the main sequence while still embedded in their molecular clouds and still accreting matter and radiating before collapse is complete, in spite of their high luminosity which creates an outward radiation pressure that should stop matter from being accreted on to the new star (Beuther et al., 2007).

Theoretically three models have been advanced to explain the formation mechanisms of massive stars. These are monolithic collapse and turbulent core accretion models, competitive accretion and runaway growth models, and stellar collision and binary merger models. In the monolithic collapse and core accretion models, the high turbulence of the cores enable them drive a high accretion rate in order to build a massive star. This massive star formation model remains a generalization of the low mass case, but with the mass of the collapsing core related to the mass of the final star (Yorke and Sonnhalter, 2002; McKee and Tan, 2003; Krumholz et al., 2010). This model does not address why the core of the massive proto-stellar object does not further fragment into small stars but remains massive (Dobbs et al., 2005).

The competitive accretion and run away growth model invokes the cluster nature of high mass star forming regions to form massive stars via accretion onto a central proto-star in the proto-cluster by gravitational collapse in which the central proto-star has access to more matter falling into the center (Zinnecker, 1982; Bonnell et al., 1997, 2004; Bonnell and Bate, 2006). Here the central argument is that accretion is dependent on the large scale flows within the gravitational potential of the molecular clumps. Stars located at the centre of the gravitational potential are thus able to acrete more materials. This theory does not explain why accretion is not halted in the face of such high radiative pressure.

In an attempt to overcome the problem of radiation pressure the stellar collision and binary merger model suggests that massive stars form by direct collisions of lower mass stars. However, the process requires high initial stellar densities (Bonnell and Davies, 1998; Bonnell et al., 2003). This model has been discredited largely due to the extremely high cluster densities required and moreover this mechanism is not required to get over the issue of accretion given the work that is later described on Rayleigh- Taylor instabilities (Kuiper et al., 2013).

These formation mechanisms largely depend on stellar formative environment, that is, whether the stars form in isolation or in clusters. These mechanisms also seek to answer the questions of how proto-stellar cores avoid further fragmentation, how massive proto-stars gain their final mass in the face of great radiative pressure and subsequently how binary stars form (Krumholz, 2014, 2015*a*). Simulations in 2D and 3D have been used to explore the effect of radiative transfer and magnetic fields on star formation (Commerçon et al., 2011; Meyers and Mckee, 2013). The results confirm the suppression of cores from further fragmentation. On the issue of radiative pressure halting accretion, molecular gas outflows at high velocities in opposite directions present mechanisms through which radiation can escape whilst the star still accretes material via the disk.

The effects of disks (compact flattened structures around the luminous object) (Kuiper et al., 2016; Maud et al., 2018), outflows (Kolligan and Kuiper, 2017) and jets on radiative pressure (Kuiper et al., 2013) have been simulated. Observationally the existence of disks around massive stars have been revealed with radio investigations (Sanchez-Monge et al., 2014; Johnston et al., 2015; Beuther et al., 2017), and the search for jets have also proved successful (Guzman et al., 2016; Purser et al., 2016). Outflows have also been observed in some massive stellar objects (Beuther et al., 2007,b). The effect of radiation pressure is accounted for in the simulation when in-falling materials strike the disk at great distances and are not heated at sublimation temperatures but are shielded from the pressure so the radiation can escape along the perpendicular outflow channels (Krumholz, 2015*b*). The disk efficiently dissipates the radiation by absorbing the photons and re-radiating them from its surface (Tan et al., 2014; Stahler and Palla, 2004).

Observationally, before the main sequence stage, the processes of massive star formation are embedded in obscuring clouds (Traficante et al., 2015; Eden et al., 2019; Svoboda et al., 2019). The stages of events, shown in Figure 1.3 (Purcell et al., 2006; Breen et al., 2010), involve

IR dark molecular clouds (Figure 1.3(i)) of temperature of about 15 K and mass about 100 $M_{\odot}$ emitting strongly in the submm spectral range due to cold dust. These IR dark molecular clouds may or may not posses starless cold cores (Sridharan et al., 2005; Urquhart et al., 2008; Peretto and Fuller, 2009).

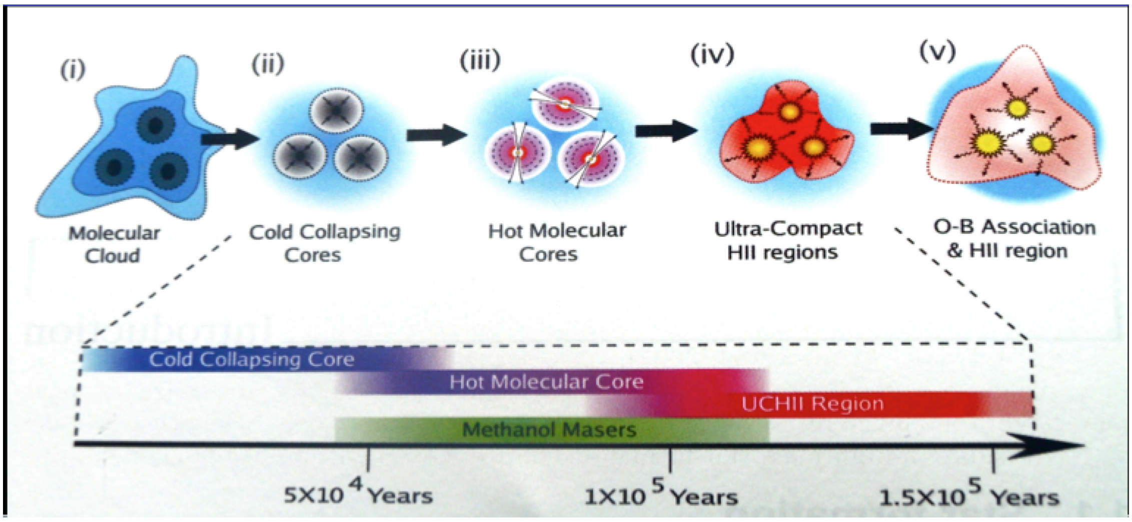

Figure 1.3: The observed evolutionary stages of high mass stars after the fragmentation and collapse of molecular clouds (i). The prestellar cold collapsing cores (ii) develop into hot molecular cores (iii), which are heated by the embedded massive star. An ultracompact HII region (region of ionised gas) is formed around the young star (iv) which evolves into a diffuse HII region in OB associations (v) (Purcell et al., 2006; Breen et al., 2010).

It is hypothesised that isothermal collapse of the cold cores as in Figure 1.3(ii) under their own gravity increases the core density, releases gravitational potential energy as heat and thereby increases the kinetic energy of the molecules which results in the formation of hot molecular cores (see Figure 1.3(iii)). With a growing proto-star at the center and outflows from its poles (Cesaroni et al., 2006; Pestalozzi et al., 2004) the hot molecular core begins to warm up its surrounding dust and gas, resulting in the evaporation of molecules formed from the warmed dust grains (Menten, 1991; Walsh et al., 1998; Viti and Williams, 1999; De Buizer and Minier, 2005; Hill et al., 2005; Linz et al., 2005). The proto-star, now a massive young stellar object (MYSO) still embedded in the cloud becomes bloated (swollen star model) as its radius increases by rapid accretion at high rates and pulsates (Hosokawa and Omukai, 2009; Hosokawa et al., 2010; Davies et al., 2011; Liu et al., 2011). The MYSO then disperses its envelope along with the outflows and emits in the mid infra-red (MIR) and FIR. As accretion ends whilst the MYSO contracts to the main sequence phase, hydrogen burning begins and the Lyman continuum produced (Hoare, 2002; Hoare et al., 2007, 2005) starts to ionise the surrounding atomic and neutral hydrogen as seen in Figure 1.3(iv) leading to the formation of ultra compact HII (UCHII) and classical HII regions (Kurtz, 2005; Hoare and Franco, 2007). Usually, massive stars are formed in OB association as in Figure 1.3v (Billington et al., 2018). The RMS survey (Urquhart et al., 2008, 2013) also points to a high mass classification scheme as outlined by a review of the observed stages which follows the sequence of events in the evolution of high mass stars (Zinnecker and Yorke, 2007).

## 1.1 HII regions in massive star formation

As massive stars evolve and start burning hydrogen in their core they produce copious amounts of far ultraviolet (FUV) radiation (Morton, 1967; Keto, 2007) which is absorbed by gas and dust. The ionised Ultracompact (UCHII) regions produced by the interactions of the UV radiation with their surroundings uniquely trace massive star formation (Wood and Churchwell, 1989; Walsh et al., 1997, 1999). The HII regions emit strongly at radio wavelengths via free-free emission.

## 1.2 HII regions

An HII region is a localised volume of gas surrounding a massive star in which all the hydrogen has been ionised. As the star contracts and heats up its UV output increases. The UV photons with energies above the Lyman limit are absorbed by the atomic hydrogen surrounding the star in a process called photo-ionisation. Photo-ionisation is balanced by recombination which occurs when ions capture free electrons. Thermal pressure causes the ionised region to expand. If the density of the region is constant, the HII region forms a sphere (Strömgen sphere) of ionised gas with radius $r_s$ (Strömgen radius) having a well defined boundary called an ionisation front (Strömgren, 1939). At equilibrium, the Strömgen radius is given by

$$r_s = \left( \frac{3Q_*}{4\pi\alpha n_H^2} \right)^{1/3} \tag{1.12}$$

where $Q_*$ is the number of ionising photons emitted per second, $n_H$ is the gas density and $\alpha$ is the recombination rate coefficient which is weakly dependent on temperature (Strömgren, 1939).

### 1.2.1 Free-free emission

Thermal bremsstrahlung from ionized hydrogen, also called free–free emission, results from interactions between charged particles in thermal equilibrium; in this case a free electron is accelerated by a proton. The electrons are free before and after the interaction. The strength and spectrum of radio emission from an HII region depends on the distributions of the velocities of the electrons, their temperature and other collision impact parameters. The resulting emission from free-free interactions has a broad spectrum across a range of frequencies.

In Figure 1.4, the shape of the spectrum for free-free emissions from a spherical, uniform and isothermal HII region is shown. This follows a black body spectrum at low frequencies when it is optically thick and opaque with optical depth $\tau \gg 1$. The spectral intensity at low frequencies correspond to the optically thick region which varies with frequency quadratically up to a turn over frequency $\nu_{\text{turnover}}$ where the optical depth is $\tau = 1$ depicted by a spectral break (Wilson et al., 2009; Condon and Ransom, 2016). At high frequencies, where the region is optically thin and transparent, the emission varies approximately as $\nu^{-0.1}$ and the optical depth $\tau \ll 1$ (Burke and Graham-Smith, 2002). The flux density at high frequencies is proportional to the emission measure along the line of sight of the HII region and is given by

$$\mathrm{EM} = \int_0^L (n_e)^2 \, ds \tag{1.13}$$

where $n_e$ is the electron density for the region. EM is a factor contained in the specific intensity $S_\nu$. The optical depth is given by

$$\tau_\nu = 3.28 \times 10^{-7} \left( \frac{T_e}{10^4 \text{ K}} \right)^{-1.35} \left( \frac{\nu}{\text{GHz}} \right)^{-2.1} \left( \frac{\text{EM}}{\text{pc cm}^{-6}} \right) \tag{1.14}$$

where $T_e$ is the electron temperature (Mezger and Henderson, 1967; Condon and Ransom, 2016). The electron temperature $T_e$ in addition to the optical depth $\tau$ gives the brightness

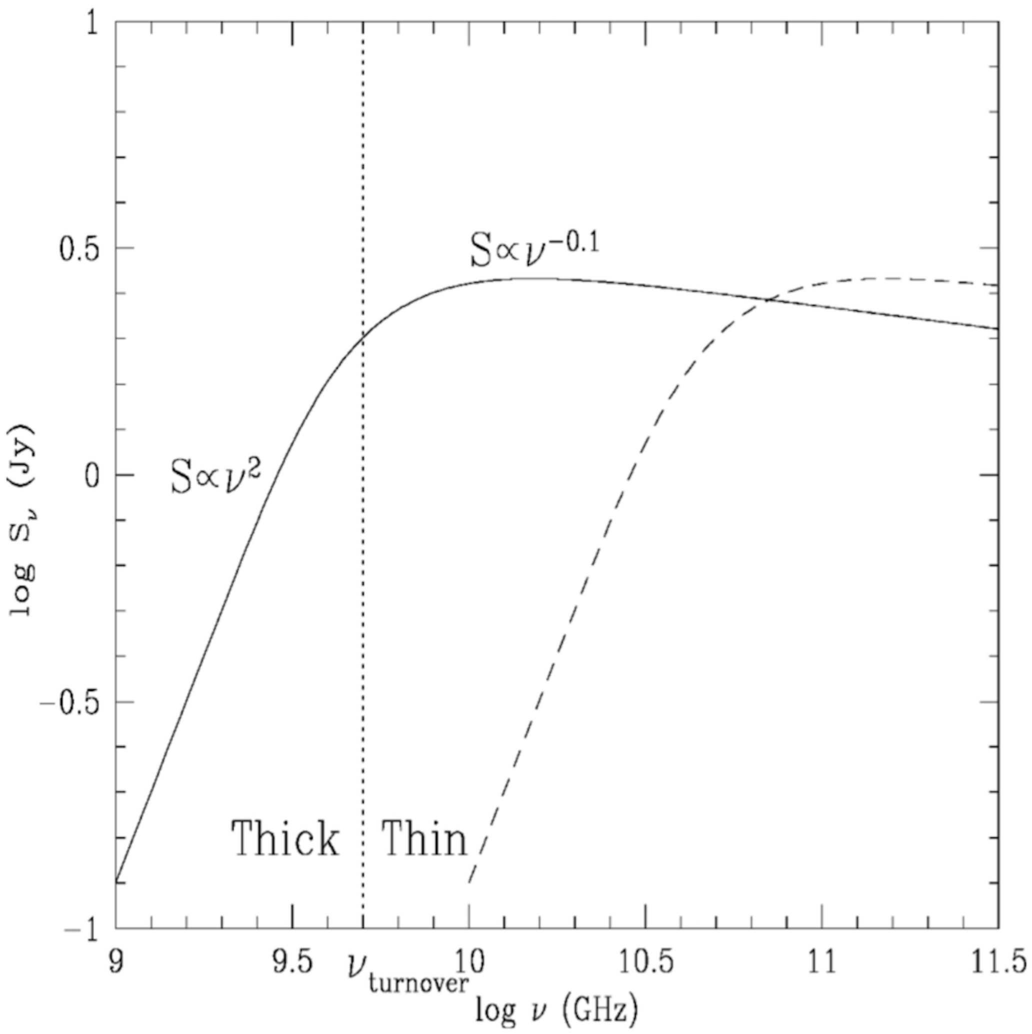

Figure 1.4: The ideal radio spectrum of an HII region. The solid line shows the free-free emission from the UCHII region and the dashed line depicts free-free emission from the HCHII region. The vertical dotted line separates the optically thick part from the optically thin part of the UCHII region (Kurtz, 2005).

temperature

$$T_b = T_e\left(1 - e^{\tau}\right) \tag{1.15}$$

Hence, at low frequencies the brightness depends on the electron temperature whilst the brightness depends on the EM at high frequencies (Wilson et al., 2009).

### 1.2.2 Classification of HII regions

The expansion of the HII region caused by the thermal pressure depends on the density distribution of the region (Franco et al., 2000). HII regions have been classified into classical, compact, ultracompact, hypercompact and extended based on their angular size and the position of the ionisation front. The hypercompact HII regions are the extremely young objects confined to very small sizes of about 0.003 pc. The ultracompact HII regions are the immediate high pressure environment of the star within its parental molecular cloud and are about 0.1 pc in size (Kurtz et al., 1994, 2000). Compact HII regions are those carving their way out of the clouds with low densities and are located in more evolved zones of the clouds with sizes 0.1 pc-0.3 pc. When they mature they have sizes of up to several parsecs and these are the extended HII regions. The expansion of these objects is important for our understanding of the structure and fate of clouds with active star formation and the objects themselves. HII regions are often associated with maser emission and are surrounded by dense molecular gas.

### 1.2.3 Molecule formation in the interstellar medium

In the ISM a large number of chemical reactions are responsible for the formation of molecules. Chemical bonds are formed by radiative association, grain surface formation and associative detachment. Bonds are also broken by photo-dissociation, dissociative recombination and collision dissociation. There are also rearrangement reactions consisting of ion molecule exchange, charge transfer and neutral collisions (Tennyson, 2003; Caselli and Ceccarelli, 2012). The dense molecular clouds have temperatures as low as 10 K-100 K. They also contain matter in the form of grains of dust made up of carbon rich grains or silicates. At low temperatures the cores also grow mantles of other molecules forming ice mantles. The grain surfaces provide the path by which atomic hydrogen combines to form other chemicals on grain surfaces (Hatchell et al., 1998; Tielens, 2013). During the hot molecular core phase of massive star formation the dust temperature becomes high enough to sublimate molecules from the ices, injecting them into the gas phase. The molecules considered in this thesis are OH and methanol.

#### 1.2.3.1 Hydroxyl molecule formation pathways

The hydroxyl molecule (OH), shown in Figure 1.5, is formed by oxygen hydrogenation on grain surfaces via the reaction (Willacy and Williams, 1993; Das et al., 2008)

Figure 1.5: Model of the hydroxyl molecule.

$$H + O \rightarrow OH \tag{1.16}$$

Alternatively UV photons from massive stars are absorbed by the $H_2O$ molecules in the ice. On absorption of a Lyman photon the $H_2O$ molecule dissociates into H and the OH radical which is retained on the mantle:

$$H_2O \rightarrow H^+ + OH^- \tag{1.17}$$

The H atom carries most of the excess energy in the dissociation reaction in Equation 1.17. The $OH^-$ radical releases an electron to form an OH molecule (Yamamoto, 2017; Viti et al., 2000):

$$OH^- \rightarrow OH + e^- \tag{1.18}$$

#### 1.2.3.2 Methanol molecule pathways

In the ISM methanol molecules form by grain surface reactions (Das et al., 2008). One such reaction is the evaporation of molecular ices on dust grains (Viti and Williams, 1999). CO molecules adsorbed onto dust grains are subjected to grain-surface reactions which result in the formation of $CH_3OH$ molecules in the grain mantles (Sakai et al., 2010):

$$H + CO \rightarrow HCO \tag{1.19}$$

$$H + HCO \rightarrow H_2CO \tag{1.20}$$

$$H + H_2CO \rightarrow H_3CO \tag{1.21}$$

$$H + H_3CO \rightarrow CH_3OH \tag{1.22}$$

Figure 1.6 shows the molecular structure of the methanol molecule. The thermal emission lines of methanol are a good probe of the physical and chemical conditions in the star forming regions (Cragg et al., 2005).

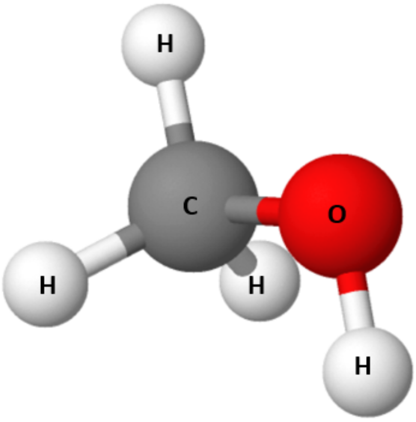

Figure 1.6: Model of the methanol molecule.

## 1.3 Astrophysical masers

Astrophysical masers are a coherent source of amplified microwave radiation from certain molecules in the ISM. Masers are produced terrestrially by the amplification of microwave radiation in cavities whereas they are produced naturally under the necessary conditions of seed radiation, population inversion, sufficient amplification path length, and a low velocity gradient along the amplification path (velocity coherence) in space. Masers are compact, have high brightness temperature, are variable (Caswell, Vaile and Ellingsen, 1995), and can be polarised (Elitzur, 1998; Trung, 2009). Their polarisation can help measure the magnetic field strengths of their environment.

Maser emissions arising from molecular clouds have become important tools for the study of the chemical components and physical processes of their environment (Minier et al., 2003; Edris et al., 2007). Maser species such as water, hydroxyl, and methanol trace a number of stellar phenomena such as shocks, outflows, infall and circumstellar disks as high-mass stars advance in the early stages of their evolution. It has been suggested that masers are not associated with different evolutionary stages of massive stars (De Buizer, 2003; De Buizer et al., 2005). However, the role of masers in tracing different evolutionary stages is still debated (Ellingen et al., 2011). Hydroxyl masers in massive star forming regions (SFRs) usually have associated UCHII regions and often occur in close association with class II methanol and water masers (Edris et al., 2007). They trace shocked neutral gas ahead of expanding UCHII regions (Fish and Reid, 2006) and jets (Argon and Reid, 2003) and serve as indicators of the velocity and magnetic fields on a very small scale (Fish and Reid, 2006).

Methanol masers are divided into two classes (class I and class II) depending on the strongest maser transition (Batrla et al., 1987; Menten, 1991). Class I methanol masers are usually found between molecular outflows (Menten, 1991) and the parent cloud apart from compact continuum sources and trace an earlier stage than class II methanol masers (Ellingsen, 2006). They are pumped by collisions between the outflowing materials and the ambient interstellar material occurring at the interfaces of shock fronts. Class II methanol masers, which are associated with the proto-star phase, trace hot molecular cores and are also found close to UCHII regions (Batrla et al., 1987) though they sometimes occur earlier than the UCHII phase (Minier et al., 2005; Ellingsen, 2006). Class II masers are pumped by the intense radiation of the warm dust heated by the proto-star and manifest at frequencies of 6.7 GHz, 12.2 GHz, 19.9 GHz, 23.1 GHz, 28.9 GHz, 37.7 GHz, 38.2 GHz, 38.4 GHz, 107.0 GHz, 108.8 GHz, 156.6 GHz and 157 GHz whereas class I methanol masers emit at 9.9 GHz, 25.0 GHz, 36.2 GHz, 44.1 GHz, 84.5 GHz, 95.2 GHz and 146.6 GHz.

### 1.3.1 Maser theory

The principles governing maser emission include radiative transfer, population inversion, optical depth, saturation and pumping which are explained below.

#### 1.3.1.1 Radiative transfer

A travelling radio wave of intensity $I_\nu$ encounters a cloud of matter (neutral gas) and interacts with it. The cloud of matter may absorb some of the radiation, scatter some, and further emit some of the radiation. These processes change the intensity of the transmitted radiation (Elitzur, 1992). In the case of pure absorption, a beam of area $dA$ propagating a distance $ds$ into matter of absorption cross-section $\sigma_\nu$ and number density $n$ suffers a change in intensity

$$dI_\nu = -\alpha_\nu I_\nu \, ds \tag{1.23}$$

where $\alpha_\nu = n\sigma_\nu$ is opacity. The transmitted intensity after propagating a finite distance in the cloud is then

$$I_\nu \propto e^{-\tau_\nu} \tag{1.24}$$

where $\tau_\nu$ is the optical depth for a perfectly absorbing medium. The attenuation suffered by the beam is termed optical depth $\tau_\nu$ and is defined by

$$\tau_\nu = \int \alpha_\nu \, ds \tag{1.25}$$

$\tau_\nu$ is a measure of the absorption as the intensity of the beam decreases through the cloud. The medium is optically thin when chances of interaction of the photons in the beam with particles of the medium are small. For this the value of $\tau_\nu$ is less than unity. The medium however is optically thick if the photons in the beam have a high chance of interacting with the particles of the medium. Here $\tau_\nu$ is greater than unity and no radiation passing through that region reaches the observer.

On the other hand an atom after absorbing a photon and going into a higher energy level

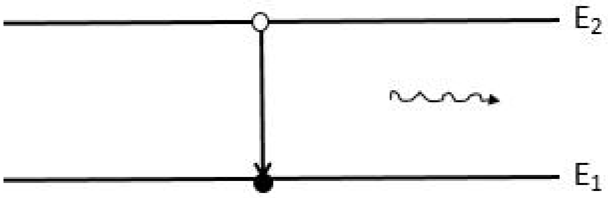

Figure 1.7: An excited atom de-exciting from a high energy level to a low energy level via the spontaneous emission of a photon.

(excited state) may de-excite to a lower energy level by spontaneously emitting a photon with energy equal to the difference in energy of the levels as shown in Figure 1.7. In another mode of de-excitation as shown in Figure 1.8, a photon of the same wavelength called the seed photon interacts with an atom already in its excited state. The photon stimulates the atom into emitting a photon to return to its lower energy state. The new photon's phase, frequency, polarization, as well as direction of travel are identical to those of the photon that stimulated the emission. The photon emitted by the stimulated emission process can further stimulate other atoms in a progressive cascade of emission, thereby amplifying the intensity of the incident radiation.

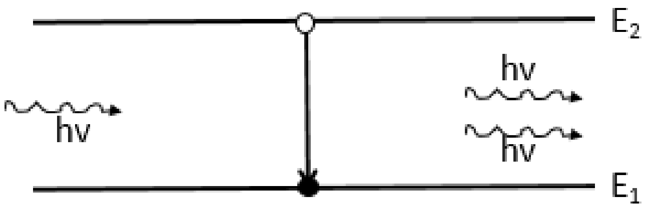

Figure 1.8: An incoming photon of a specific frequency interacts with an excited atom, causing it to de-excite to a lower energy level. The emitted photon is identical to the incident photon.

The process of stimulated emission is akin to negative absorption and leads to growth of beam intensity when the net gain it provides exceeds absorption. Thus, stimulated emission accounts for amplification of radiation as it propagates through the cloud. The emission coefficient, $\varepsilon_{\nu}$, or emissivity, is defined as the energy emitted per unit time per unit volume per unit solid angle per unit frequency; hence, on crossing the path length $ds$, the intensity of the beam is increased by

$$dI_\nu = \varepsilon_\nu \, ds \tag{1.26}$$

Combining the processes of emission and absorption defines the radiative transfer equation

$$\frac{dI_\nu}{ds} = -\alpha_\nu I + \varepsilon_\nu \tag{1.27}$$

which describes how the intensity of radiation varies as it propagates in a medium.

### 1.3.1.2 Population inversion

Figure 1.9 shows a two-level system under normal conditions of thermal equilibrium. The number of particles in an energy level $E$ is proportional to the Boltzmann factor $e^{-E/k_BT}$ for that level where $T$ is the equilibrium temperature.

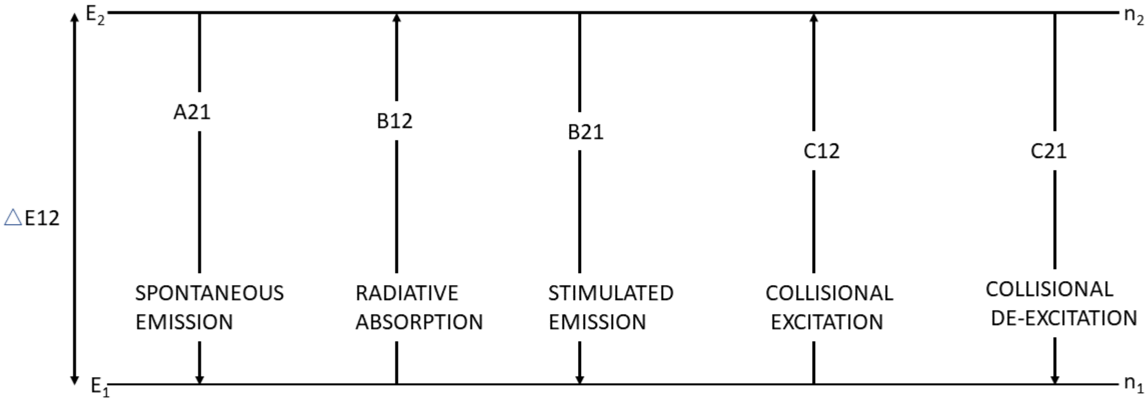

Figure 1.9: The different processes that populate or depopulate the levels in a collection of two level systems in thermodynamic equilibrium. The radiative processes are absorption characterized by coefficient $B_{12}$, spontaneous emission characterized by coefficient $A_{21}$ and stimulated emission characterized by coefficient $B_{21}$. Collisional processes are characterized by coefficients $C_{12}$ for excitation and $C_{21}$ for de-excitation.

In thermal equilibrium, the number, $n_2$, of particles in the higher level $E_2$ is always less than the number, $n_1$, of particles in the lower level $E_1$. Hence, the population ratio, given by

$$\frac{n_2}{n_1} = \frac{g_2}{g_1} e^{\frac{-h\nu}{kT}} < 1 \tag{1.28}$$

satisfies

$$\frac{n_1}{g_1} > \frac{n_2}{g_2} \tag{1.29}$$

where the $g_i$'s are the statistical weights of the upper and lower states. The emissivity for spontaneous emission assumes the same line profile function $\phi(\nu)$ which governs the absorption of a photon and is given by

$$\varepsilon_\nu = n_2 A_{21} \frac{h\nu}{4\pi} \phi(\nu) \tag{1.30}$$

where $A_{21}$ is the Einstein coefficient for spontaneous emission. The absorption coefficient is given by

$$\alpha_\nu = (n_1 B_{12} - n_2 B_{21}) \frac{h\nu}{4\pi} \phi(\nu) \tag{1.31}$$

where $B_{12}$ is the Einstein coefficient for absorption and $B_{21}$ is the Einstein coefficient for stimulated emission. The Einstein coefficients are related by the equations

$$\frac{A_{21}}{B_{21}} = \frac{2h\nu^3}{c^2} \tag{1.32}$$

and

$$B_{12} = \frac{g_2 B_{21}}{g_1} \tag{1.33}$$

where $h$ is the Planck constant and $c$ is the speed of light in vacuum. In order for the net emission to be stimulated the rate of stimulated emission must be greater than the rate of absorption which is not achievable in thermal equilibrium. Population inversion only occurs if the rate at which particles move from the $n_2$ population is less than the rate at which particles move to $n_1$ implying that $n_2$ should always be greater than $n_1$. A mechanism that removes a sufficient number of particles from the lower to the higher energy level thereby inverting the normal population is needed which will lead to

$$\frac{n_1}{g_1} < \frac{n_2}{g_2} \tag{1.34}$$

resulting in a net gain. Thus the absorption coefficient becomes negative and the gas cloud adds to the radiation field and hence amplification of the radiation occurs.

#### 1.3.1.3 Pumping

Population inversion in the energy levels of molecules is a necessary condition for maser action. The population inversion from radiative, collisional or chemical pumping may result from small departures of the normal population from the Boltzmann distribution. This occurs naturally in the ISM due to low gas densities, thus, a combination of dense molecular gas and dust in addition to either strong IR radiation fields (source of excitation) or long collisional times in outflows or both leads to pumping of molecules to the desired higher levels in certain molecules such as OH, $H_2O$, and $CH_3OH$ (Elitzur, 1976, 1992). At low densities purely radiative pumping occurs whereas collisional excitation results in purely collisional pumping. A combination of both radiative and collisional pumping occurs in some molecules.

For any molecule, the total angular momentum $J$ without the nuclear spin arises from coupling of the electronic orbital angular momentum $L$, end-over-end rotation $K$ and the electronic spin $S$ quantum numbers. The OH molecule in Figure 1.5 with an unpaired electron occupying the $2p\pi$ orbital for instance has a total angular momentum quantum number (exclusive of nuclear spin) given by $J = 1 \pm 1/2$ in the rotational ground state ($K = 0$) which leads to the two $^2\pi$ states designated by $^2\pi_{3/2}$ and $^2\pi_{1/2}$.

Figure 1.10 shows the two allowed rotation ladders associated with the $^2\pi_{3/2}$ and the $^2\pi_{1/2}$ rotational ground states of OH. Each level in the ladder, designated by its $J$ value, is split by interaction of the electronic motion and the molecular rotation into doublets (lambda doubling) labelled '$+$' or '$-$' on the Figure. The lambda doublets are further split by the nuclear hyperfine interaction to give the energy levels shown in Figure 1.10 between which the OH microwave

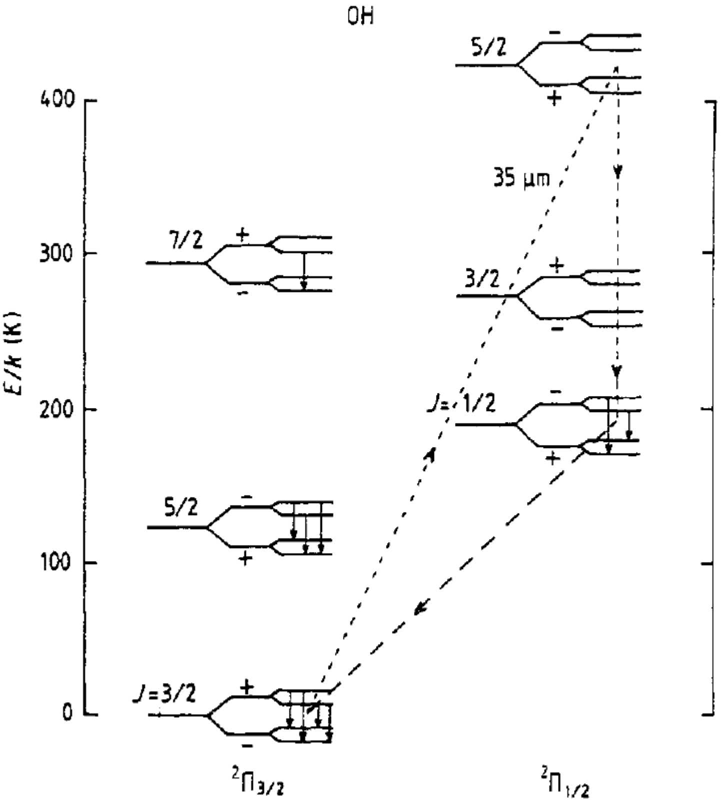

Figure 1.10: Energy levels of the two ladders of the rotational states of OH. The splitting of the ground state of OH occurs via lambda doubling and hyperfine interactions. The broken lines show the pumping scheme for the 1612 MHz maser transition in OH (Elitzur, 1976).

transitions of interest occur (Elitzur, 1976). Figure 1.11 shows the hyperfine levels of the $^2\pi_{3/2}, J = 3/2$ state. Each level is labelled with its total angular momentum quantum number $F$ which includes the nuclear contribution. Allowed transitions between these hyperfine levels are governed by the selection rules $\triangle J = 0$ and $\triangle F = 0, \pm 1$ which give rise to the four components of the hydroxyl emission at 18 cm as shown in Figure 1.11

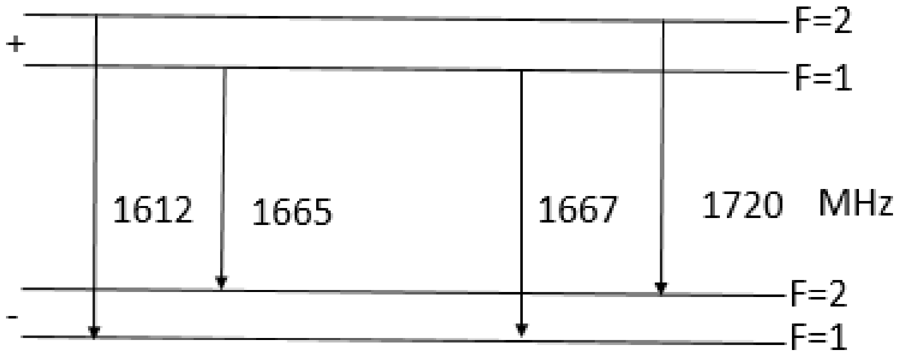

Figure 1.11: Part of the rotational energy level diagram of the hydroxyl ground state showing the hyperfine splitting of the rotational states that give rise to the 18 cm hydroxyl emission. Shown are the four hyperfine masing transitions of the OH ground state.

The transitions for which $\triangle F = 0$ give rise to the 1665 MHz and 1665 MHz maser lines collectively called the mainlines. The 1612 MHz and 1720 MHz transitions occur when $\triangle F = \pm 1$ and are called the satellite lines.

For the 1612 MHz OH line, warm dust radiating at a wavelength of 35 $\mu$m excites the OH molecule from its ground state $^2\pi_{3/2}, J = 3/2$ manifold to the excited state $^2\pi_{1/2}, J = 5/2$ manifold as shown in Figure 1.10. A metastable state is populated via the $^2\pi_{1/2}$ ladder. The final $^2\pi_{1/2}, J = 1/2 \rightarrow {}^2\pi_{3/2} J = 3/2$ transition causes the inversion of the ground state population.

The methanol model in Figure 1.6 shows that the bond between the methyl and the hydroxyl groups of the methanol molecule constitutes an axis about which the methyl group rotates relative to the OH group. This rotation is constrained by interaction between the H atoms of the two groups, with the result that the rotation is reduced to torsional oscillations about the O–H bond. The coupling of the angular momentum associated with the torsional motion to the total angular momentum results in two torsional symmetry states which lead to the A-type and E-type methanol maser transitions as shown in Figure 1.12.

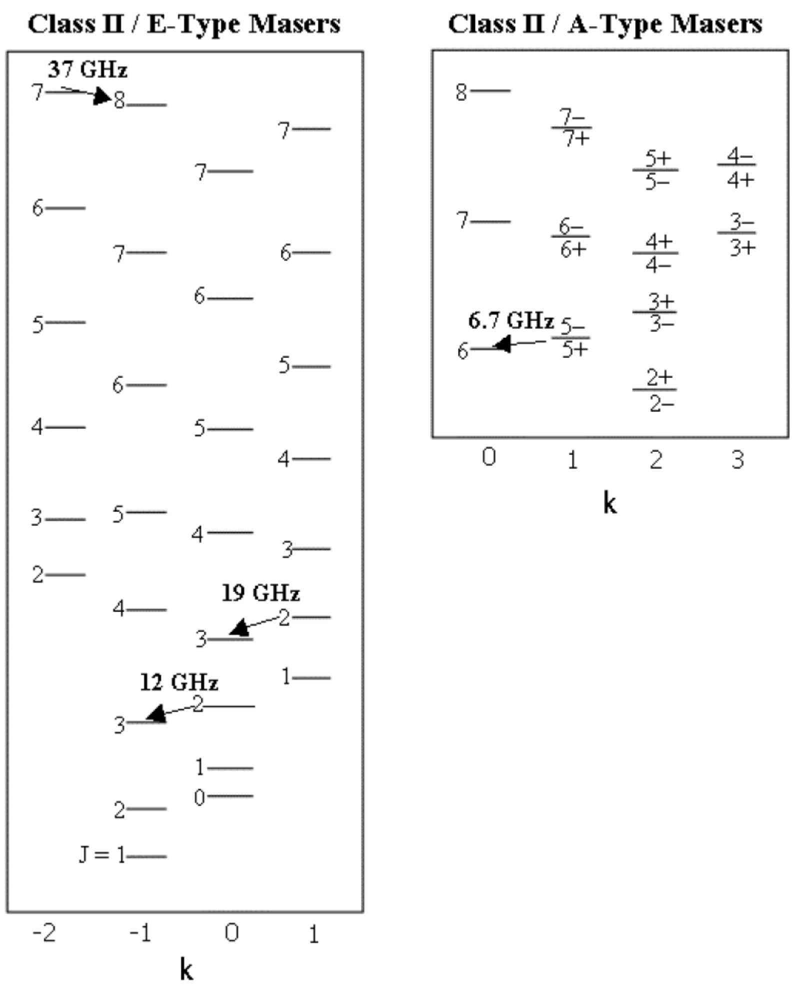

Figure 1.12: Energy level diagram for E-type (left) and A-type (right) symmetry states of the ground state methanol transitions. The E-type symmetry for which $k < 0$ indicates transitions for $CH_3OH$ $E^-$ levels whereas the E-type symmetry for which $k > 0$ indicates transitions for $CH_3OH$ $E^+$ levels. The A-type symmetry for which $k > 0$ indicate both $CH_3OH$ $A^-$ and $CH_3OH$ $A^+$ levels. The A- type levels are further split into doublets indicated by $+$ and symbols. The arrows in both A-type and E-type diagrams show observed methanol maser transitions. The arrow in the A-type diagram shows the 6.7 GHz maser transition (De Buizer, 2000).

The methanol molecule's rotational, vibrational and electronic eigenstates are characterised by quantum numbers with selection rules that only allow transitions from A-type to A-type and E-type to E-type. Maser action only occurs on these allowed transitions as guided by quantum mechanical selection rules for transitions between two energy states. A-type to E-type transitions and vice versa are forbidden. Rotation states for both A-type and E-type are characterised by $J_k$ where $J$ is total angular momentum and $k$ is the projection of the angular momentum on the molecular symmetry axis. A-type energy levels are characterized by quantum numbers

$k > 0$ with an example being the 6668 MHz emission line which occurs between the $5_1$ and $6_0$ levels. The E-type energy levels are characterized by quantum numbers $\pm k$ with an example being the 12178 MHz emission line for $k$ being negative and the transition occurring between the $2_0$ and $3_1$ levels. In the $5_1 - 6_0$ $\mathrm{A}^+$ transition of the 6668 MHz and the $2_0 - 3_1$ E transition of the 12178 MHz methanol lines shown in Figure 1.12 radiative pumping occurs. The methanol molecule in its ground state $(J,\ k = 0)$ on absorption of an infra-red photon is excited to the $(J = 1,\ k = 0)$ or $(J = 1,\ k = 1)$ states. Then the molecule decays to the metastable $(J = 1,\ k = 0)$, $(J = 2,\ k = 2)$ and $(J = 2,\ k = 0)$ levels before cascading back down. If the infra-red pumping rate is faster than the spontaneous decays population levels in low energy states are efficiently transferred to more excited states.

#### 1.3.1.4 Saturation

For a maser medium which has been pumped to inversion, some of the atoms excited to the upper level fall back to the lower level through stimulated emission and spontaneous decay. The rate equation for the population of the upper state of the two level system contains a contribution from absorption given by

$$\left.\frac{dn_2}{dt}\right|_{\mathrm{abs}} = B_{12} n_1 K \tag{1.35}$$

a contribution from stimulated emission given by

$$\left.\frac{dn_2}{dt}\right|_{\mathrm{stim}} = -B_{21} n_2 K \tag{1.36}$$

and a contribution from spontaneous emission given by

$$\left.\frac{dn_2}{dt}\right|_{\mathrm{spon}} = -A_{21} n_2 \tag{1.37}$$

with similar considerations for the lower level. The populations of the levels $n_1$ and $n_2$ in this system are thus governed by the rate equations

$$\frac{dn_1}{dt} = n_2 A_{21} + (n_2 - n_1) B_{21} K + P_1 (n - n_1 - n_2) - \Gamma_1 n_1 \tag{1.38}$$

and

$$\frac{dn_2}{dt} = -n_2A_{21} - (n_2 - n_1)B_{21}K + P_2(n - n_1 - n_2) - \Gamma_2 n_2 \tag{1.39}$$

where $n$ is the total number density of the molecular species involved in the maser, $P_1$ and $P_2$ are the pump rates per molecule into level 1 and 2, $\Gamma_1$ and $\Gamma_2$ are the loss or damp rate for level 1 and 2 and the saturation intensity

$$K = \frac{1}{4\pi}\int I_\nu d\Omega \tag{1.40}$$

is the number of photons crossing a unit volume per unit time from all directions. For a photon emitted spontaneously, the inverted medium serves as the gain medium as it travels through it (Cohen, 1989). The negative optical depth of a maser amplifies it exponentially according to

$$I_\nu \propto e^{\tau_\nu} \tag{1.41}$$

Initially the exponential growth dominates as the pumping mechanism maintains the inverted population by stimulated emission against the increasing losses. The fluence increases exponentially with distance as well. The maser is said to be unsaturated and is characterised by a narrow linewidth, rapid variability and a compact size. As population inversion is dependent on the differences between the pump and the loss rates and the losses by the stimulated emission, a change in the population levels that brings $n_2$ close to $n_1$ means absorption and emission go to zero. Thus the maser itself affects the population inversion and is then said to be saturated when

$$K = \frac{\Gamma_2}{2B_{21}} \tag{1.42}$$

Figure 1.13 is an illustration of the behaviour of the maser when it is unsaturated for the exponential growth, and saturated where the maser growth becomes linear.

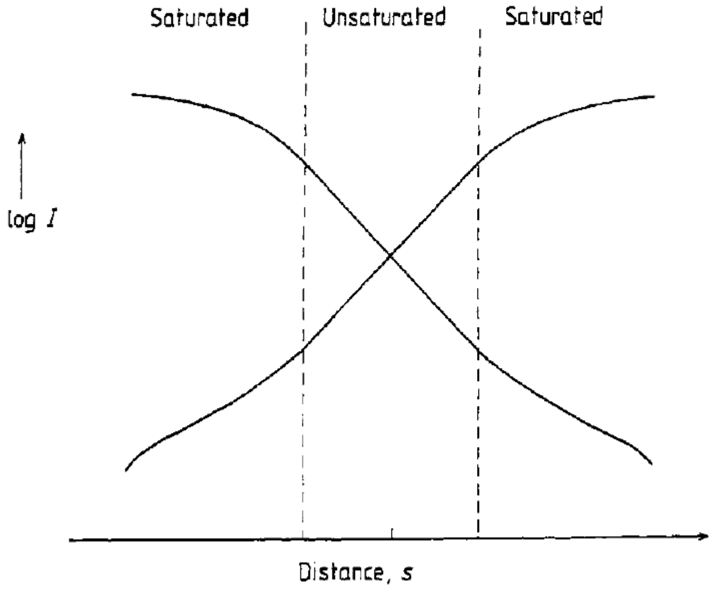

Figure 1.13: Maser saturation plot adopted from Cohen (1989) in which for an unsaturated system the maser growth is exponential until such a distance demarcated with the broken line when it becomes saturated and the growth becomes linear.

#### 1.3.1.5 Polarization

In the presence of magnetic fields some hyperfine levels of paramagnetic molecules further split into sublevels which give rise to additional line components. The extent of this splitting (Zeeman effect) gives an indication of the magnetic field strength and the direction of the field towards or away from the observer. The lines corresponding to the splitting exhibit polarization effects, resulting in some maser polarization being as high as 100% (Cohen, 1989).

Figure 1.14 shows Zeeman splitting of the hydroxyl $^2\pi_{3/2}$ hyperfine levels that gives rise to polarization of the 1665 MHz transition (Garcia-Barreto et al., 1988). The $\pi$ transitions occur when $\triangle m_l = 0$ giving rise to linear polarisation. Transitions in which $\triangle m_l = \pm 1$ result in the $\sigma$ components and give rise to circular polarisation. Here the electric field vector at a fixed location is constant in magnitude but describes a circle in the plane perpendicular to the wave vector (Jackson, 1999). The $+\sigma$ component gives the left circular polarisation and the $-\sigma$ the right circular polarisation.

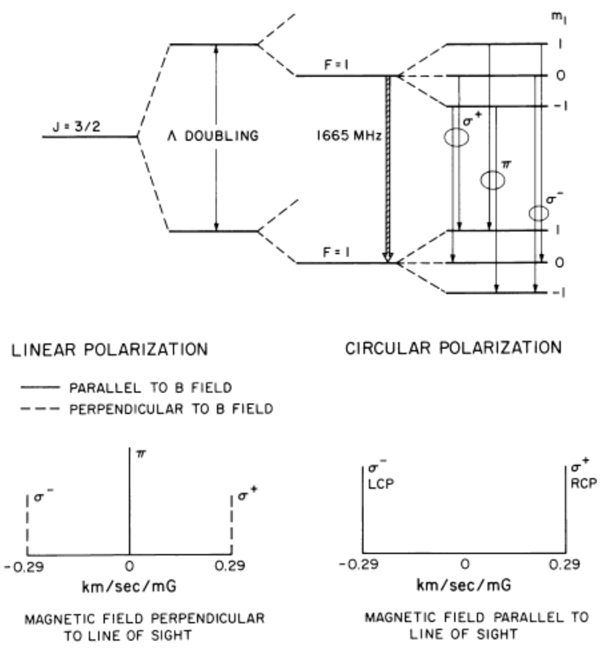

Figure 1.14: The Zeeman splitting of the hydroxyl $^2\pi_{3/2}$ hyperfine levels that gives rise to the 1665 MHz transition polarizations. Adapted from Garcia-Barreto et al. (1988).

## 1.4 Variability of masers

It has been shown (Sullivan and Kerstholts, 1976; Caswell, Vaile and Ellingsen, 1995; Macleod and Gaylard, 1996; Goedhart et al., 2003, 2004; Green et al., 2012) that some masers in massive star forming regions show variations in their flux density. These flux variations can be a flare or a fluctuation in amplitude over a period ranging from days to several years (Sullivan and Kerstholts, 1976; Macleod and Gaylard, 1996). The behaviour of the fluctuations may be characterised as unchanging, monotonic increase or decrease in flux density, sporadic, aperiodic, quasi-periodic and periodic with the change in amplitude either decreasing or increasing. Some sources show a slow change in flux density (Szymczak et al., 2001) over the period of observation whereas others show rapid change over short durations (Goedhart et al., 2004). Some sources are even reported to exhibit coherent variations in all their maser features whereas others only vary in a particular maser feature (Sullivan and Kerstholts, 1976).

In establishing how common the 6.7 GHz methanol variabilities are in massive star forming regions, Goedhart et al. (2004) monitored a sample of 54 sources and reported 55% of the 372 maser features to show significant variations, confirming the results of Caswell, Vaile and Ellingsen (1995) but with a higher percentage. Caswell, Vaile and Ellingsen (1995) studied variations in the intensity of methanol masers at 6.7 GHz and 12.2 GHz and found independent correlated variation in some features.

Closely associated with methanol masers in massive star forming regions are the OH mainline masers (1665 MHz and 1667 MHz). The spatial relationships between OH masers and class II methanol masers have been mapped (Caswell, Vaile and Forster, 1995; Walsh et al., 1998; Minier et al., 2001). These close associations and expectations from numerical modelling (Cragg et al., 2002) suggest that both maser species are pumped by infra-red radiation from the surrounding dust warmed by the central proto-star, so a level of similarity in behaviour could be expected. Various changes in the degree of circular polarisation of several masers have been reported (Szymczak et al., 2001). Investigations of the variability of the left circular polarisation (LCP) and right circular polarisation (RCP) of the 1665 MHz OH masers in some complexes found 8 of the 10 exhibiting variabilities on the time scale of weeks, months and even years (Clegg and Cordes, 1991). Monitoring of the 1.6 GHz hydroxyl and the 6.7 GHz methanol masers in the massive star forming region $G351.78-0.54$ from 1993 to mid 1995 showed monthly variation superimposed on long term changes varying for years in the LCP (Macleod and Gaylard, 1996) and studies of 13 sources over the period from 1970 to 1971 found the mainline OH masers to vary in all four Stokes parameters on short time scales compared to the satellite lines (Sullivan and Kerstholts, 1976). In contrast, a monitoring campaign (Green et al., 2012) on the 1.6 GHz masers in $G12.889+0.489$ showed no significant variation in the polarisation properties.

## 1.5 $G9.62+0.20E$

The massive star forming complex $G9.62+0.20$ has been found to be located at 5.2 kpc from the Sun (Sanna et al., 2009, 2015). Within this complex shown in Figure 1.1 are a number of HII regions at various stages of development (Hofner et al., 1996, 2001; Testi et al., 2000; De Buizer, 2003; Liu et al., 2011) named A to I in increasing order of compactness (Garay et al., 1993; Testi et al., 2000). The component E has been been detected at cm wavelengths from 3 cm to 7 mm (Linz et al., 2005). This has been interpreted (Hofner et al., 1996) to be a young star surrounded by a very small UCHII region which on the Kurtz-Franco classification (Kurtz and Franco, 2002) is dense and compact. Component E also harbours sources that emit some hydroxyl maser lines (Caswell, 1998; Fish et al., 2005; Hofner et al., 1996), water maser lines (Hofner et al., 1996; Testi et al., 1998; Forster and Caswell, 2000; Farmer, 2014) and methanol maser lines (Menten, 1991; Goedhart et al., 2003) of which the 6.7 GHz transition is the strongest in the Galaxy (Caswell, 1998; Sanna et al., 2015).

## 1.6 Periodicity of the 6.7 GHz methanol masers in G9.62 + 0.20E

The 6.7 GHz methanol transition in G9.62 + 0.20E was reported to show periodic changes in its flux density in the form of regular flares with a period of 244 days (Goedhart et al., 2003, 2004). Figure 1.15 is a plot showing the periodic flares of the 6.7 GHz masers in G9.62 + 0.20E (Goedhart et al., 2004).

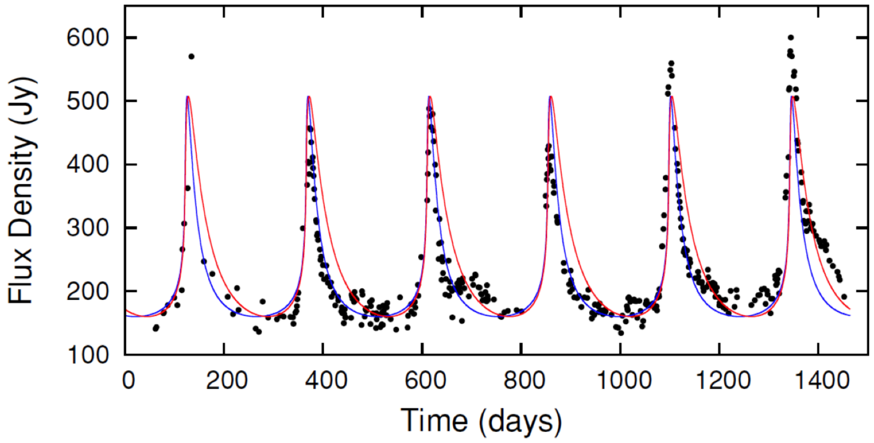

Figure 1.15: Time series of the peak velocity channel of the 6.7 GHz masers in G9.62 + 0.20E (Goedhart et al., 2004).

G9.62 + 0.20E is of interest because of the outstanding questions posed by the source of the variability of the flux density of its associated 6.7 GHz and 12.2 GHz masers. Ten years of monitoring of the regularly varying source using the Hartebeesthoek 26 m telescope produced more results to confirm the periodic variation (Goedhart et al., 2014). The source of the flares or variabilities of the maser's intensity has been interpreted in a number of ways with several models depending on the location the maser is speculated to be sited. Three of the models invoke the presence of a binary system whereas two invoke the presence of an independent pulsating star.

### 1.6.1 Pulsating star models

The pulsating star model is derived from the swollen star model, in which a growing proto-star under rapid mass accretion rate $\dot{M}_* \gtrsim 10^{-3} M_\odot$ yr$^{-1}$ may become unstable and pulsate before reaching the ZAMS (Hosokawa and Omukai, 2009; Hosokawa et al., 2010). In this model it is the IR pumping radiation that is modulated and results in the periodicity of the masers. Inayoshi et al. (2013) invoke the pulsational instability of bloated proto-stars in general with high accretion rates to explain the observed maser periodicity and predict that the period depends on the adopted accretion rates and gets longer with increasing accretion rates. Sanna et al. (2015) also invoke the presence of an independent pulsating massive young proto-star with high accretion rate of $4 \times 10^{-3} M_\odot$ yr$^{-1}$ (Liu et al., 2011) and the superposition of two independent IR sources (radiation field ) which provides the pumping mechanism for the maser to explain variable maser behaviour in G9.62 + 0.20E.

### 1.6.2 Accretion disk models

The binary system models invoke the presence of a circumbinary disk to explain the dust temperature variation which is assumed to cause the periodic variability. In one such model, the observed variabilities in formaldehyde and methanol masers are explained as due to periodic accretion of material from a circumbinary disk in a young eccentric binary system that heats the dust and changes the pumping radiation field (Araya et al., 2010). Here the material from the circumbinary disk is accreted onto the individual proto-star, heating the dust and increasing the infra-red radiation field resulting in the large maser gain which leads to the high amplification. This model follows predictions of the smoothed particle hydrodynamics simulations (Artymowicz and Stephen , 1996) to arrive at this result.

Parfenov and Sobolev (2014), however, propose periodic emission from rotating spiral shocks in the gaps of a circumbinary accretion disk around young binary stars to heat up the dust. The variation in dust temperature is caused by radiation from the bow shock illuminating the dust which may again change the infra-red pumping field.

### 1.6.3 Colliding wind binary model

Methanol masers associated with UCHII regions are excited by strong external radiation from hot dust (pumped by infra-red radiation) associated with the free-free emission from young HII regions. The colliding wind binary (CWB) model has been employed to explain the observed periodic variabilities of such masers (van der Walt et al., 2009; van der Walt, 2011*b*,*a*; van den Heever et al., 2019). Unlike the previous models, here the seed photons are provided by the HII region with high emission measure (Slysh et al., 2002; Sobolev et al., 2007).

In this model it is the seed photons that are periodically modulated causing the observed periodicity. The model involves two massive OB stars in an eccentric binary system as in Figure 1.16 of which one or both produces large amounts of ionising radiation surrounding both to power an HII region. The interaction of their stellar winds produces shocked gas which emits more ionizing photons. A pulse of ionising photons is produced as the binary system approaches periapsis. The pulse then propagates to the ionisation front of the HII region unattenuated. This causes an increase in the electron density at the ionisation front resulting in the subsequent increase in the free-free emission from that part of the HII region. The HII region undergoes recombination and returns to its initial stage after the transit of the pulse. The maser assumed to be projected against the edge of the HII region is expected to respond to the changes in the free-free seed photons.

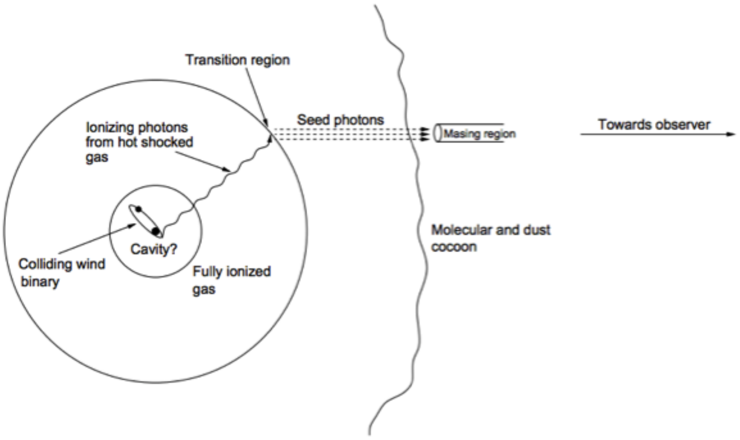

Figure 1.16: A toy model of the colliding wind binary model (van der Walt, 2011*a*).

The colliding wind binary model therefore suggests that such periodic sources could be important pointers for finding massive binary stars since massive stars have a high frequency of forming in binaries and multiples (Zinnecker and Yorke, 2007). Massive close binary objects going supernova may form binary black holes or neutron stars. When the binary objects merge they generate gravitational waves as recently detected by the Laser Interferometer Gravitational- Wave Observatory (LIGO) (Abbott et al., 2017, 2009*a*,*b*). Observational studies of the early stages of high mass stars provide insight into the problem of how they form.

## 1.7 Thesis goals and overview

Closely associated with methanol masers in newly formed massive star forming regions are hydroxyl masers, both of which are proposed to be excited by a common infra-red radiation mechanism (Cragg et al., 2002). The CWB model suggests that these radiatively pumped masers should vary together. However, the exact location of these masers in relation to the proto-star is unknown presently. Sanna et al. (2015) used high resolution separate VLA and VLBA astrometry to show the positions of masers relative to the 43 GHz UCHII region in G9.62 + 0.20E. The results of the VLA continuum (UCHII) at 43 GHz does not map the actual seed photons in the continuum at 1.6 GHz and 6.7 GHz.

This Ph.D. project seeks to find the correlation between the polarisations of the 1.6 GHz OH and 6.7 GHz methanol masers, and to improve the picture of the positional relationship between the maser emission and the HII regions of the high mass star by investigating the natal environment of G9.62 + 0.20E using hydroxyl and methanol maser emissions that uniquely trace the regions within which massive stars are born and reside. In particular, the project utilizes the 26 m HartRAO dish to monitor the highly polarised mainline 1.6 GHz hydroxyl transitions and the associated 6.7 GHz methanol maser emission in G9.62 + 0.20E to:

(a) investigate the variability of the left circular polarisation (LCP) and right circular polarisation (RCP) components of the 1665 MHz and 1667 MHz OH maser lines.

(b) compare the results in (a) with the 6.7 GHz methanol maser line variabilities to investigate the relationship between the flaring behaviour of the methanol maser and the OH masers.

To understand the mechanism causing the maser flaring or variability in (a) and (b) above the capability of e-MERLIN's 150 mas resolution at L-band and 40 mas resolution at C-band is employed to examine simultaneous high resolution images of the 1.6 GHz hydroxyl and 6.7 GHz methanol maser spots and their radio continuum emissions arising from G9.62 + 0.20E to:

(c) measure the L-band and C-band continuum to high accuracy.

(d) determine the relative positions of the variable and non-variable maser spots in (a) and (b).

This thesis thus investigates the relationship between the OH and $CH_3OH$ maser emissions and the relationship between the masers and the HII region associated with them. The rest of the thesis is organised as follows.

Chapter 2 introduces the techniques for reducing the single dish data of the 1.6 GHz main-line OH polarisations and the 6.7 MHz methanol line in G9.62 + 0.20E. The differences and similarities in the variabilities are discussed and an attempt is made to explain these variable behaviours within the colliding wind binary model. Chapter 3 gives a general overview of interferometry and the data reduction procedure for the high resolution interferometric data of G9.62 + 0.20E at L-band. The study is continued in Chapter 4 by finding the positions of the 6.7 GHz methanol maser spots in G9.62 + 0.20E relative to the 6.5 GHz radio continuum emission using the high resolution observations. The concluding chapter gives a summary of all inferences made from Chapter 2, Chapter 3 and Chapter 4 and how they all fit into the general massive star formation theory.

# CHAPTER 2

# MONITORING THE POLARISATIONS OF THE HYDROXYL MASERS IN THE PERIODIC METHANOL MASER SOURCE G9.62 + 0.20E

Modelling the conditions necessary for maser formation has revealed that OH and methanol masers are likely pumped by the same excitation mechanism. Hence, a spatial association between the two species is expected (Cragg et al., 2002). Monitoring of the total intensity of the OH mainline masers in G9.62 + 0.20E with KAT-7 found variations similar to those observed in the 6.7 GHz and 12.2 GHz methanol transitions (Goedhart et al., 2019). However, a drop in flux density of the OH masers which coincided with the rise of the 12.2 GHz methanol transition was found (Goedhart et al., 2019). Polarisation variations in G9.62 + 0.20E were not reported. However, the left and right circular polarisations of the OH mainline masers are thought to originate from different regions in a molecular cloud and differences in behaviour of the polarization components of the OH mainline masers are therefore expected.

Presented in this chapter are the results of the observation, reduction and analysis of data obtained from the monitoring of the polarisation of the 1665 MHz and 1667 MHz hydroxyl masers and the regularly varying 6.7 GHz methanol maser in G9.62 + 0.20E. The aim is to find correlated variation between the 6.7 GHz methanol masers and the left and right circular polarisations of the OH masers. Such information is valuable for identifying the source of the periodic variation observed in some maser species. The monitoring campaign was instituted with the 26 m HartRAO radio telescope in 2011.

Section 2.1 gives brief explanations of the observational data collection techniques employed. In section 2.2 detailed descriptions of radio astronomical spectroscopic data reduction are given, and section 2.3 presents the results of the reduction. The results are discussed in section 2.4.

## 2.1 Observational techniques

Data for both OH and methanol maser observations were obtained using the 26 m Hartebeesthoek Radio Astronomy Observatory (HartRAO) microwave telescope which is an equatorial mount with an 85 foot Cassegrain dish design, built by Blaw Knot in 1961. Table 2.1 gives the specifications for the telescope.

Table 2.1: Specification for the 26 m HartRAO telescope.

| Parameter | Specification |
|---|---|
| Diameter (m) | 25.9 |
| Focal ratio ($f/D$) | 0.424 |
| Surface tolerance (mm rms) | 0.5 |
| Wavelength limit (cm) | 1.3 |
| Feed system | Cassegrain |
| Pointing resolution (deg) | 0.001 |
| Repeatability (deg) | 0.004 |
| Slew rate on each axis (deg/s) | 0.5 |

Depending on the purpose of the observation different techniques were employed. The amount of power measured by a telescope consists of noise from the atmosphere and radiation from the radio source. To measure the power due to the radio source the noise is subtracted from the total measured power. This is achieved through switched observations of the source. The switching technique takes a number of forms: position, beam, load and frequency switching. For spectral line and some continuum observations, position, frequency and load switching are used whereas beam switching and drift scans are used for continuum observations of point sources.

Two monitoring windows, a regular and an intensive window, were employed for the collection of the data. The regular monitoring data had been taken by HartRAO staff and archived whereas the intensive window data were the product of a follow up proposal for monitoring of the source led by Benedicta Woode which was accepted by HartRAO. The regular monitoring window spanned the period 2011 day 294 to 2015 day 189 for the observation at 1665 MHz and 2014 day 066 to 2015 day 189 for the observation at 1667 MHz. For the 1665 MHz line, 144 observations were recorded whereas for the 1667 MHz line 66 observations were recorded. The 6668 MHz methanol maser data for the regular monitoring window were supplied by Dr. Sharmila Goedhart from her monitoring campaign data taken at HartRAO. The intensive monitoring data were taken during the 2017 January to April flare window which covered day 007 to day 130 for the observation of both OH and methanol emissions. A total of 48 observations were taken for the methanol maser line, 22 observations were taken for the 1665 MHz OH line and 30 observations were taken for the 1665 MHz OH line.

### 2.1.1 Frequency switching

Observations were carried out with the spectrometer configured to produce 1024 channels across a 0.25 MHz bandwidth in both LCP and RCP. The instrumental gain response as a function of frequency, which is the bandpass, changes slowly with time as the observation progresses, and correlator artefacts as well as standing waves add to this variation. Provision is made for this in HartRAO by observing either in position switching mode or frequency switching mode, both of which involve the subtraction of a reference spectrum (off-source) from the signal (on-source) observation in order to remove all common effects.

For position switching the reference spectrum is taken by pointing the telescope a few beamwidths away from the source. The disadvantage of this method is that half the observation time is spent off the target, and in crowded regions it may not be possible to get away from other emission sources. In frequency switching, the spectral line occupies a narrow band of the frequency range of the instrument. To generate the signal and the reference spectral pair, the central observing frequency is shifted by the local oscillator slightly on and off the spectral line such that the line emission falls on different sides of the band. This way the common contributions from both the receiver and the atmosphere are recorded in both frequency settings, which is a more efficient use of telescope time compared to position switching. This technique, however, is not always possible if the frequency range of the line emission is more than half the spectrometer bandwidth.

The frequency switching technique was employed in monitoring the source at intervals of

1–2 weeks during the regular monitoring window and the monitoring interval was decreased to 2–3 days during its projected flaring phase. Daily monitoring was done during the intensive monitoring window and as the source entered its quiescent phase the observations were reduced to 2–3 day intervals.

### 2.1.2 Drift scans

The contraction and expansion of a radio telescope which comes about as a result of changes in atmospheric temperature conditions as well as the earth's gravitational force as it points away from zenith causes the deformation of the telescope's structure. This deformation introduces errors in the measurements of flux densities. At the shorter wavelengths, that is, $\leq$ 6 cm for the HartRAO 26 m telescope, the main beam becomes small resulting in slight variations in its pointing, thus the full width at half maximum of the main beam decreases with increasing frequency. To accurately measure the peak flux of the source, drift scans at the expected north and south half-power points as well as the centre were taken. For the methanol observations short, one minute pointing checks to the half power cardinal points (north, south, east, and west) followed by two on-source centre position observations were carried out. These were followed by a pair of full length five minute scans on the central position. Pointing checks were not required for the OH observations as the beam is larger. For calibration purposes drift scans through the chosen calibrators were used. This is done by parking the telescope at a coordinate ahead of the calibrator's current location along its path. The moving source then drifts over the telescope beam.

Table 2.2 summarizes the observing parameters for 1665 MHz and 1667 MHz frequencies and Table 2.3 gives the observing parameters for the 6668 MHz frequency.

## 2.2 Data reduction

Reduction of the data was performed with a Python script optimized for the processing of the spectral line data. A plot of antenna temperature against radial velocity generated the raw spectra which show the details of the bandpass. For example, Figure 2.1 shows the spectrum

Table 2.2: Observing parameters for G9.62 + 0.20E at 1665 MHz and 1667 MHz.

| Parameter | Specification |
|---|---|
| Rest frequency at 1665 MHz (MHz) | 1665.401840 |
| Rest frequency at 1667 MHz (MHz) | 1667.359030 |
| Half power beamwidth (arcmin) | 28.5 |
| System temperature (K) | 39 |
| Number of spectral channels | 1024 |
| Polarizations | LCP + RCP |
| Correlator bandwidth (MHz) | 0.25 |
| Frequency switch offset (MHz) | 0.125 |
| Channel width (kHz) | 0.244 |
| $V_{lsr}$ (km/s) | 2.5 |

Table 2.3: Observing parameters for G9.62 + 0.20E at 6668 MHz.

| Parameter | Specification |
|---|---|
| Rest frequency (MHz) | 6668.518000 |
| Half power beamwidth (arcmin) | 7.1 |
| System temperature (K) | 57 |
| Number of spectral channels | 1024 |
| Polarizations | LCP + RCP |
| Correlator bandwidth (MHz) | 1.0 |
| Frequency switch offset (MHz) | 0.5 |
| Channel width (kHz) | 0.976 |
| $V_{lsr}$ (km/s) | 2.5 |

for an observation on day 066 of 2014 during the regular monitoring window. This observation is used to illustrate the single dish reduction procedure adopted for both monitoring windows.

The total power output in LCP shown in Figure 2.1 comprises the maser line visible at 2.5 km/s, the sky level at about 45 K, the bandpass profile which falls off drastically near the edges, and the correlator artefact in the form of a spike at about 13 km/s. The spectrum's velocity axis has been calibrated to radial velocity ($V_{\rm lsr}$) scale and Doppler tracking was also applied at HartRAO.

### 2.2.1 Bandpass correction

The bandpass effect of the spectrum, which is the most dominant component from the instrument, was corrected by subtracting the sky emission ($\sim$ 45 K) and the edge of the bandpass using the frequency switched spectra. The frequency switched spectra consist of a reference spectrum and signal observations. Figure 2.2 shows the spectrum of the output of the correlator

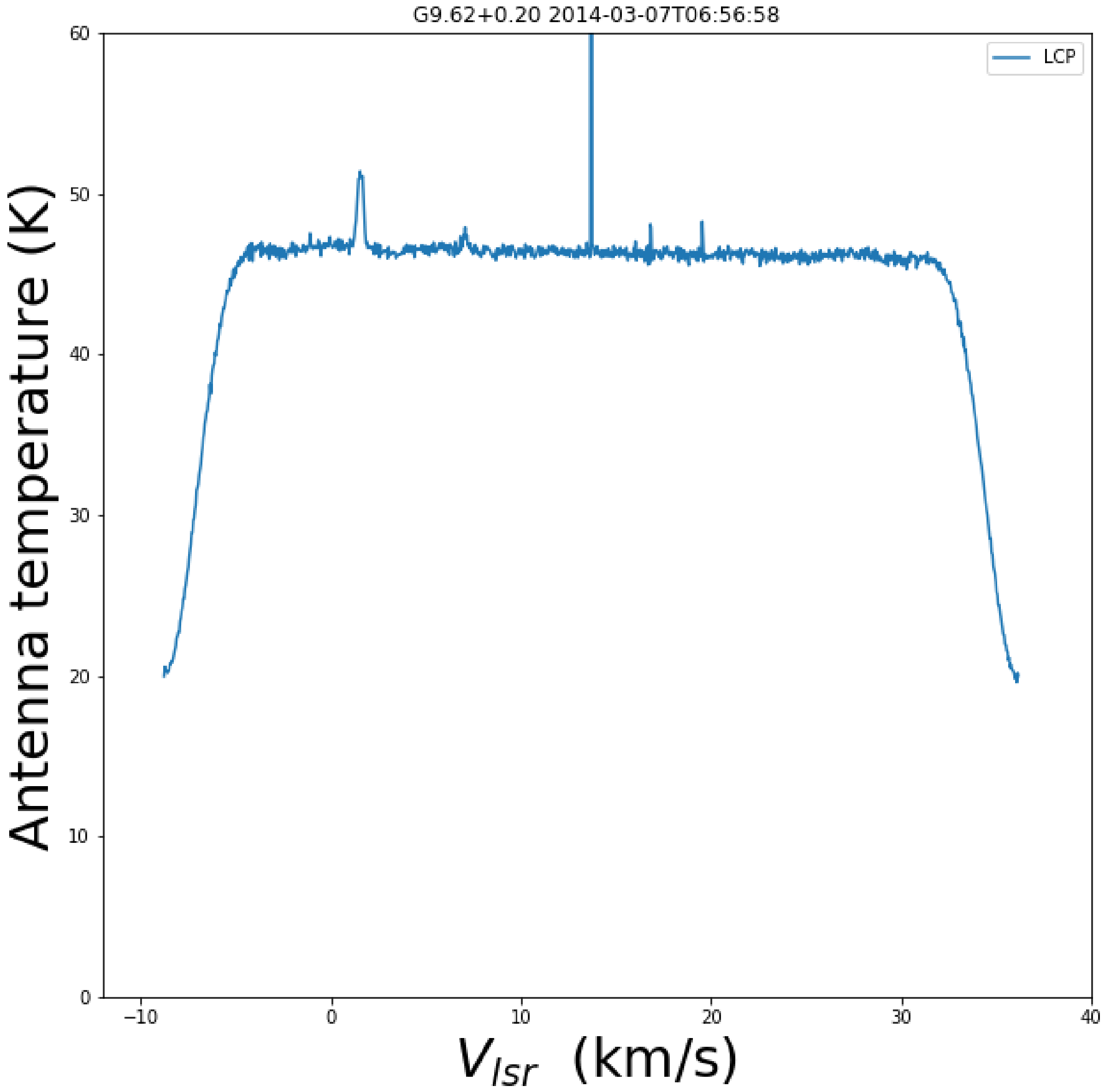

Figure 2.1: The raw total power spectrum from the 1024 channel spectrometer showing the bandpass and the maser signal in the left circular polarisation (LCP).

which constitutes with Figure 2.1 a frequency switched pair. The left half of the spectrum in Figure 2.1 and the right half of the spectrum in Figure 2.2 share common velocity channels. Similarly, the right half of the spectrum in Figure 2.1 and the left half of the spectrum in Figure 2.2 also share common velocity channels but Figure 2.2 has negative values. A channel by channel subtraction of the spectrum in Figure 2.2 from the spectrum in Figure 2.1, and vice versa, returns the two spectra shown in Figure 2.3.

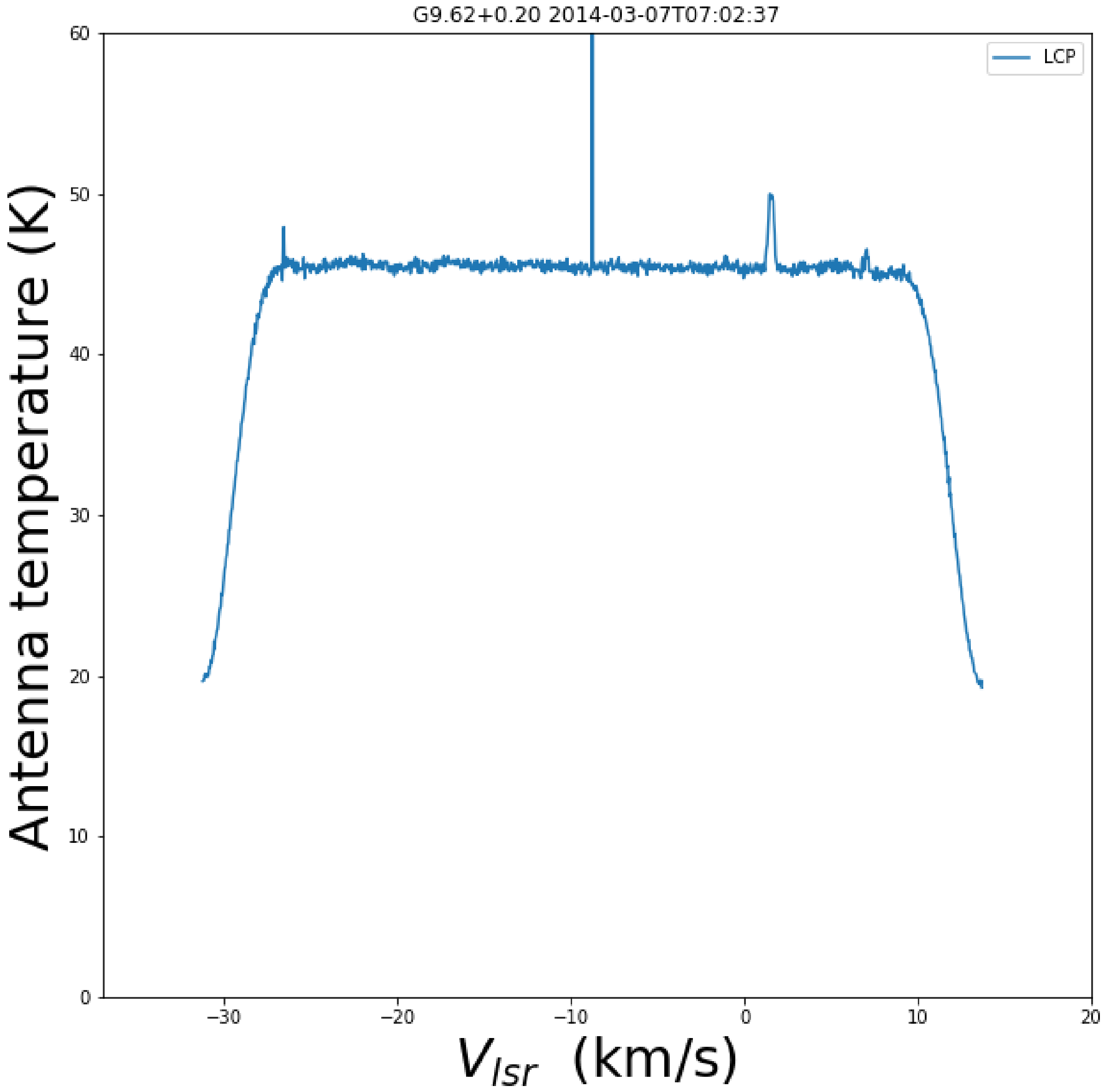

Figure 2.2: The second spectrum of the frequency switched pair in LCP showing the bandpass with the spectrometer artefact at about $-7$ km/s and maser line emission offset by half the bandwidth to the right of the spectrum.

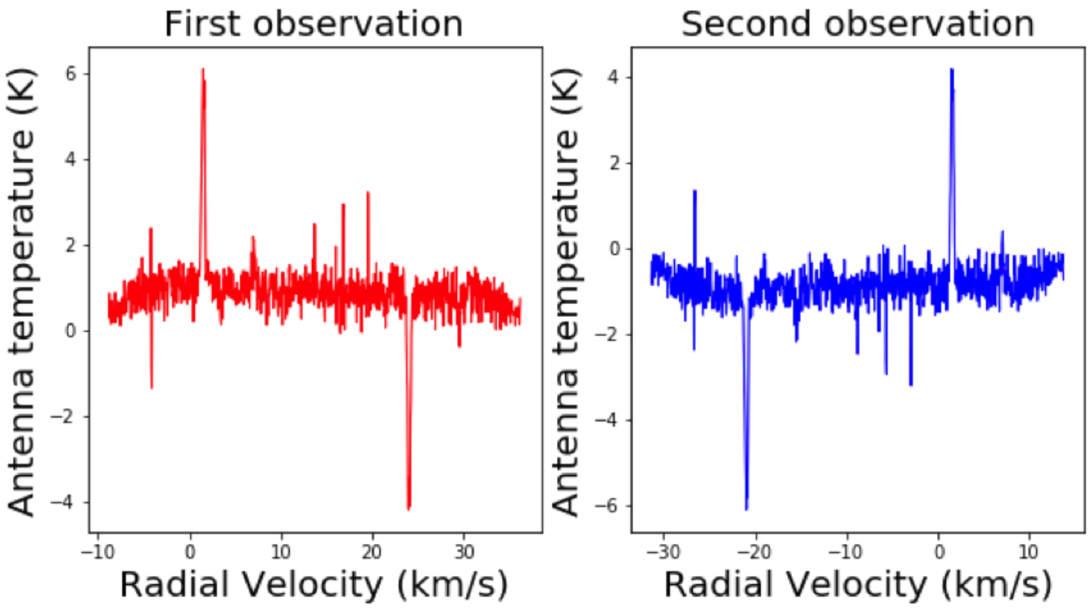

Figure 2.3: The first observation of the frequency switched pair and the second observation of the frequency switched pair both showing positive and negative velocity maser features offset by 22.5 km/s.

The first resulting spectrum has a maser feature at 2.5 km/s and a feature at a negative velocity offset by 22.5 km/s (0.125 MHz) from the positive velocity feature as shown in the first observation in Figure 2.2. Similarly, the second resulting spectrum has a positive velocity maser feature at 2.5 km/s and a negative velocity feature offset by 22.5 km/s ( 0.125 MHz) as in the second observation in Figure 2.3. The two spectra were combined as shown in Figure 2.4 and the average spectrum over the common velocity range −8.75 km/s to 13.75 km/s is shown in Figure 2.5. It can be seen that the continuum level is now close to zero. The procedure also removes the central spike from the spectrometer but leaves residual frequency dependent effects, which manifest as a slope in the baseline. In some cases ripples appeared in the baselines of the spectra but were also removed with this procedure. These ripples were caused by the blocked aperture of the HartRAO telescope which produces standing waves between the secondary and the main surface.

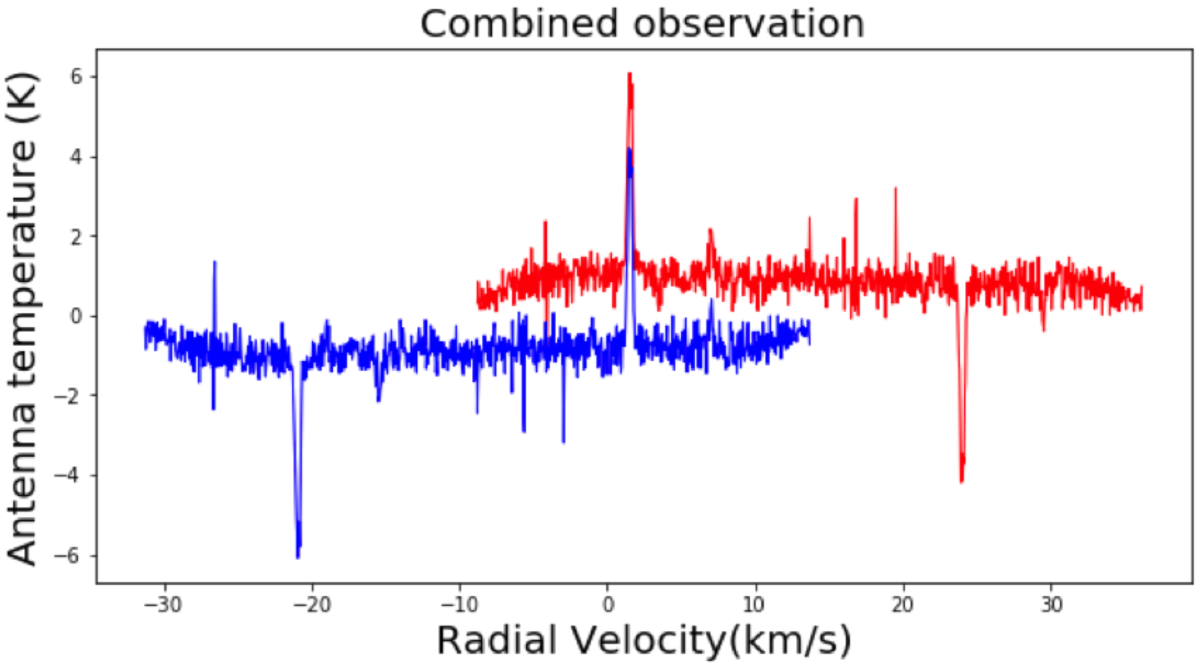

Figure 2.4: Combined observation of the frequency switched pair.

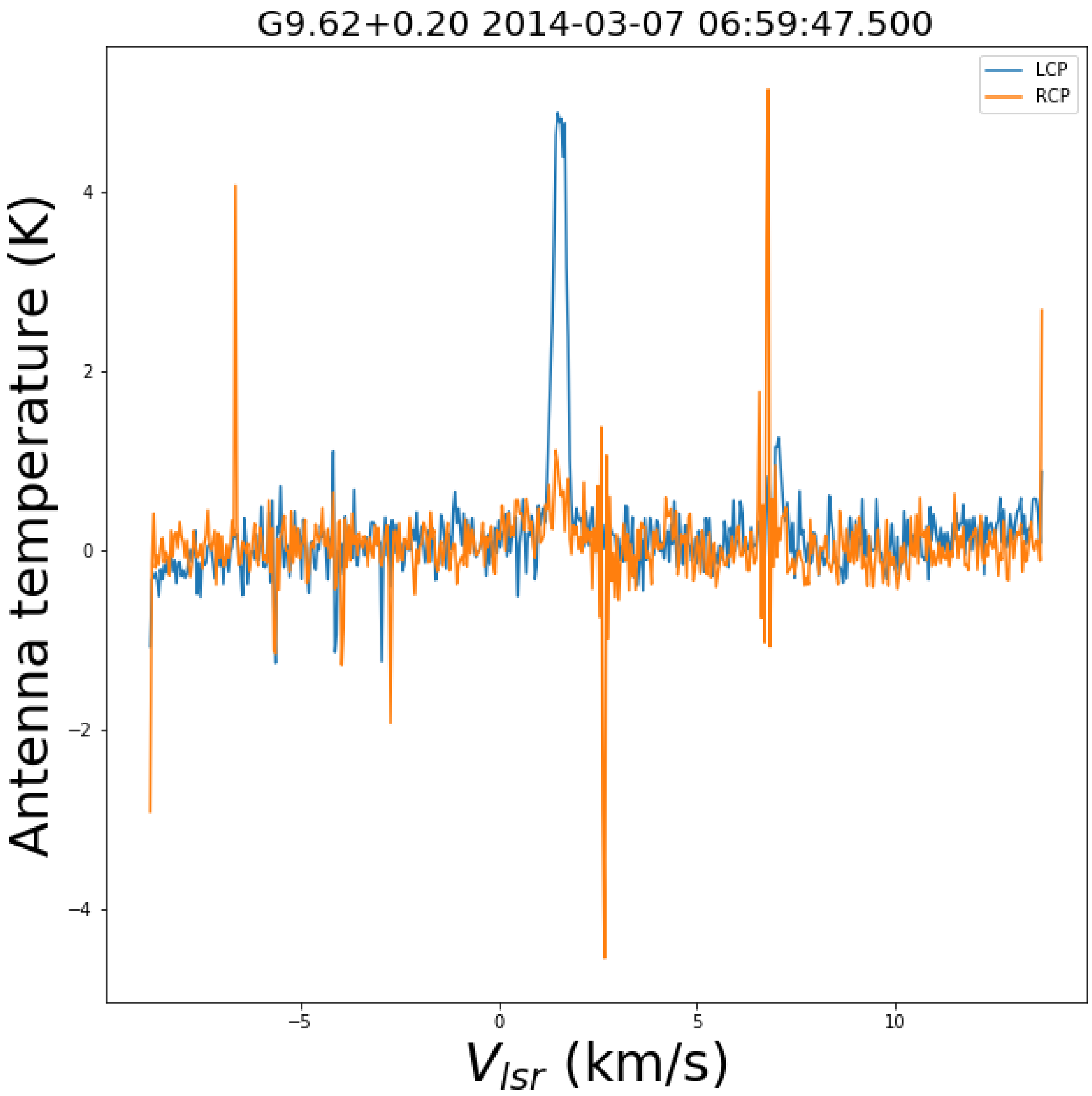

Figure 2.5: Averaged frequency switched spectra showing the baseline level removed.

### 2.2.2 Radio-frequency interference excision

The spectra from some of the L-band datasets were corrupted with strong radio-frequency interference (RFI), which manifested as spikes in the spectrum. Figure 2.6, a spectrum from the observation on day 092 of 2014 for the regular monitoring window shows an example of such data with spikes at $-7$ km/s and 14 km/s. The negative RFI at 2.5 km/s and $-5$ km/s result from the bandpass correction process using the frequency switched pairs. In most of the infested spectra from the dataset the radio-frequency interference spikes were randomly distributed. For these corrupted data a spike removal exercise was employed to remove the spikes from the spectra.

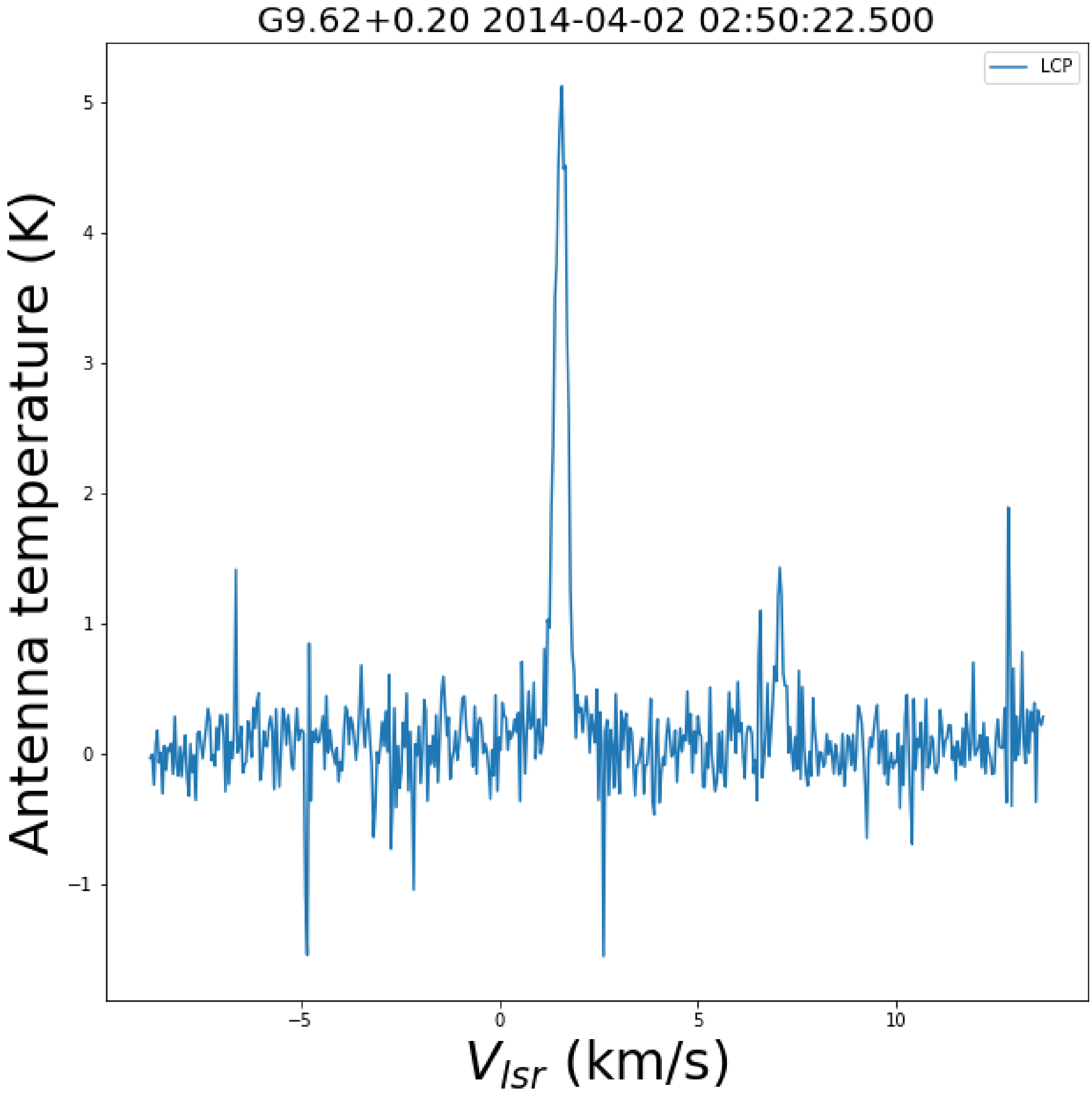

Figure 2.6: Spectrum showing persistent radio-frequency interference manifesting as spikes and dips.

The RFI spikes were removed by first masking the maser lines. A median absolute deviation (MAD) was then calculated on the rest of the emission-free spectrum. The MAD was multiplied by 1.48 to return an estimate of the standard deviation $\sigma$ assuming normally distributed data. Any deviation greater than the estimated threshold by $3\sigma$ was treated as an outlier and replaced with a local median calculated over 5 channels. Figure 2.7 shows the spectrum in Figure 2.6 with RFI adequately excised.

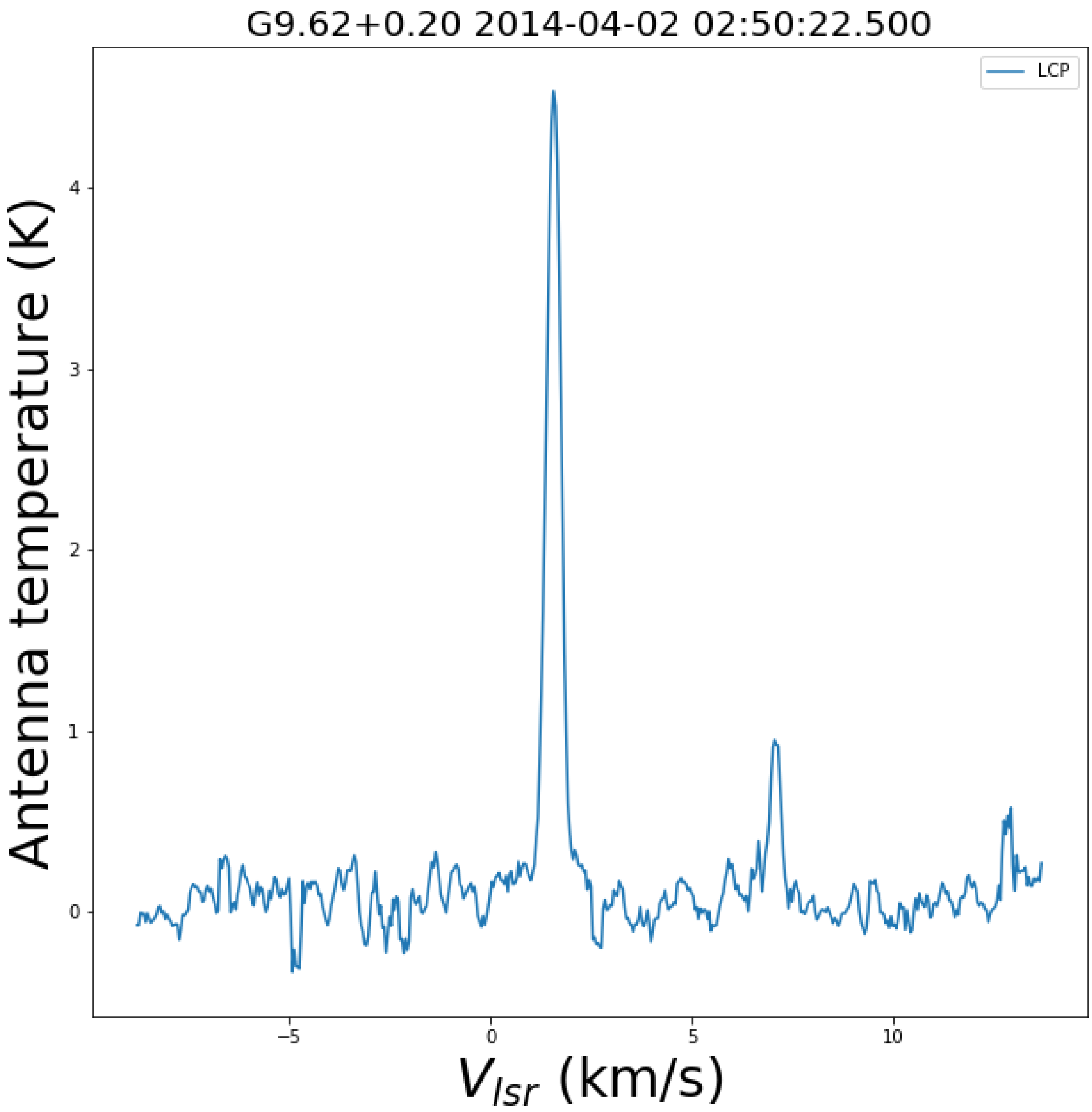

Figure 2.7: The spectrum in Figure 2.6 with RFI spikes and dips removed.

### 2.2.3 Smoothing of spectrum

In some instances the RFI was so strong that it resulted in ringing of the baseline. The spectrum was smoothed with a Hanning window with a width of 6 channels. This improves the SNR by a factor of $\sqrt{6}$. The Hanning window was used because it uses a smoothening kernel which does not reduce the number of channels. Figure 2.8 shows the result of performing the smoothing procedure on the spectrum shown in Figure 2.7. The ringing in the unsmoothed spectrum is substantially decreased by the procedure.

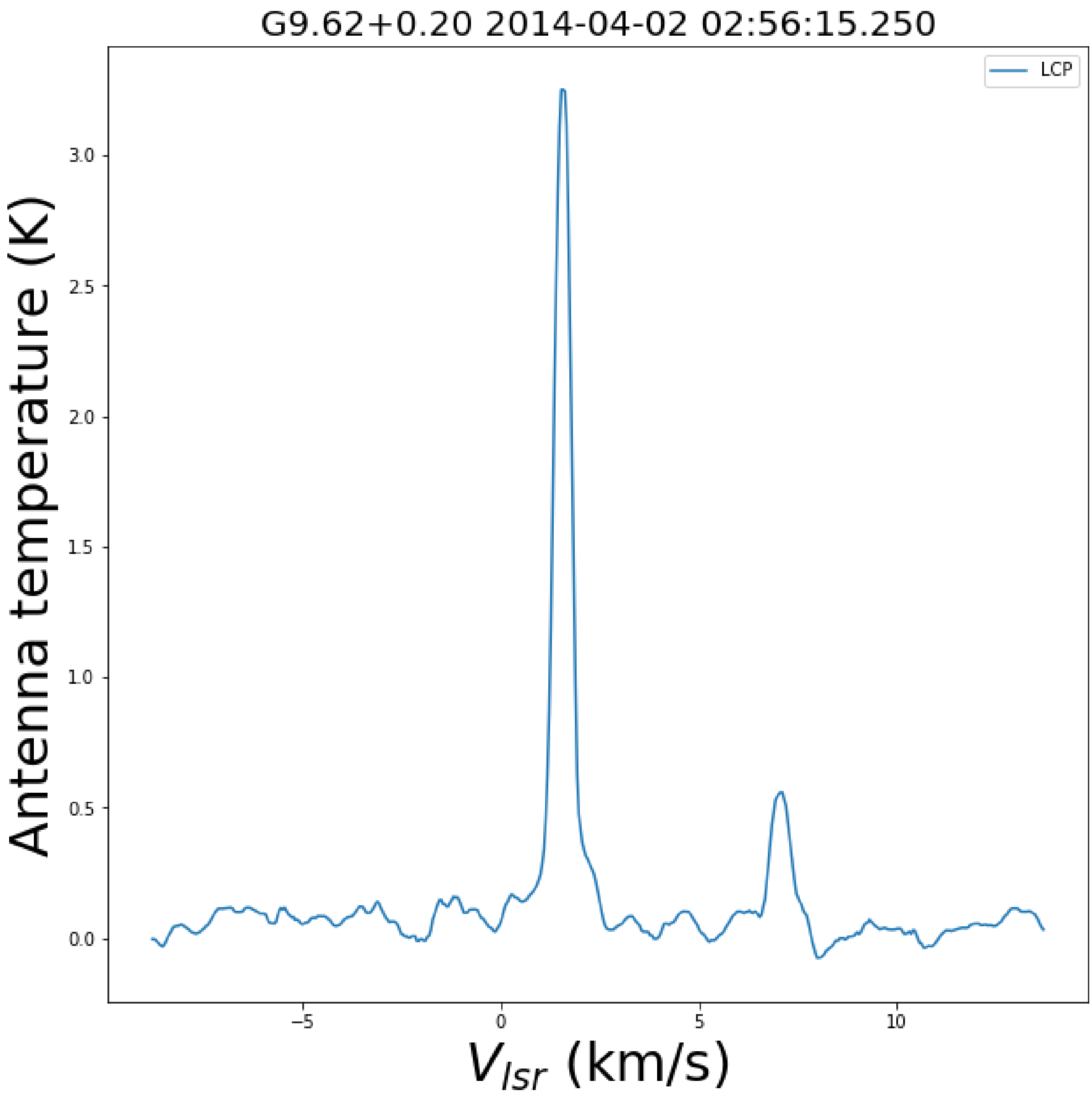

Figure 2.8: Ringing in the baseline smoothed out with a Hanning window algorithm.

### 2.2.4 Baseline flattening

The residual baseline variation was removed by fitting a polynomial to the baseline of the bandpass. First the two maser line ranges which occur at 0 km/s–3 km/s and 5 km/s–7 km/s for 1665 MHz and 0 km/s–3 km/s and 6 km/s–8 km/s for 1667 MHz were masked. A third order polynomial was fitted to the baseline as shown in Figure 2.10. This provided a better improvement of the systematics against the other baseline fits and was also of an order low enough as not to distort the emission features in the spectrum. A second order fit did not capture the trend in the data, nor correct adequately for the variation in the sky level. A higher order of four over-fitted the data, fitting most points in the data and introducing ripples under the source as evidenced in Figure 2.9.

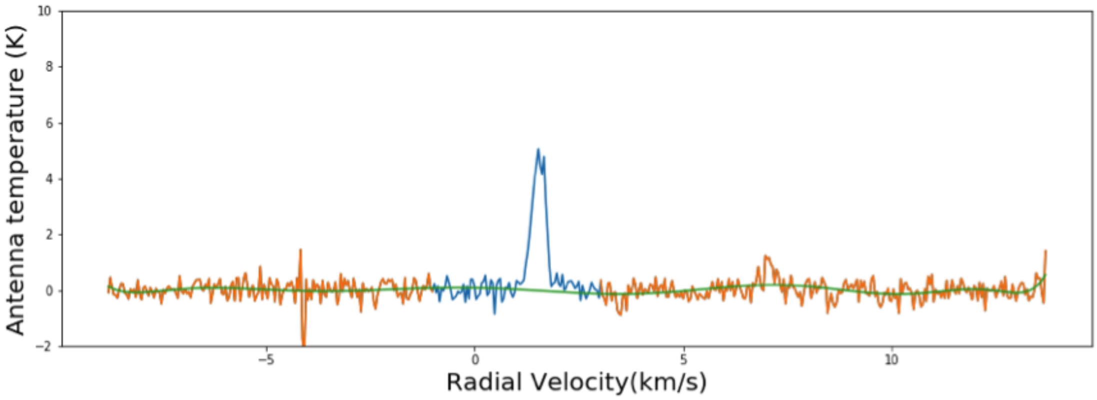

Figure 2.9: A fourth-order polynomial fit of a green curve to the spectral baseline showing an uneven fit to the bandpass. The blue coloured part of the spectrum shows the masked maser line and the orange part of the spectrum shows the baseline.

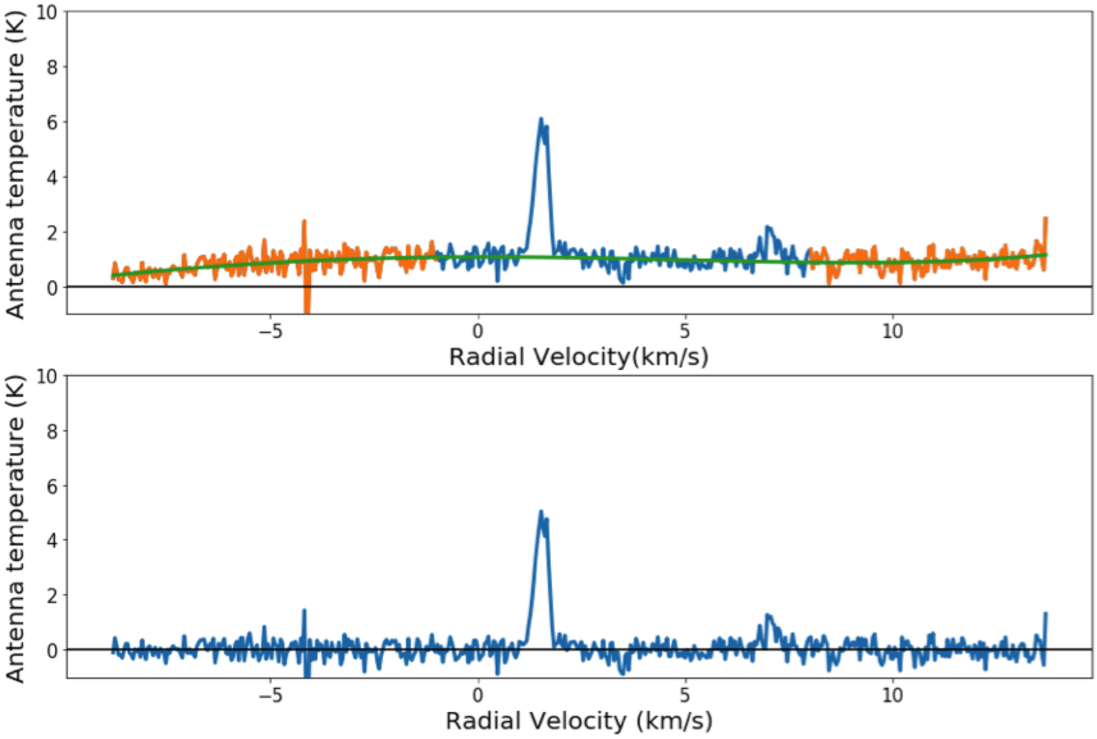

Figure 2.10: The top plot illustrates a third-order polynomial fit of a green curve to the spectral baseline with the masked range being the start and end velocity of line emissions shown in blue.The bottom plot shows the results of the subtraction of the baseline fit from which flattens the bandpass.

A plot of the resulting spectrum, presented in Figure 2.11, shows removal of the slope, sky (level) and other contributions with the best fit for the data and baseline, a third order polynomial.

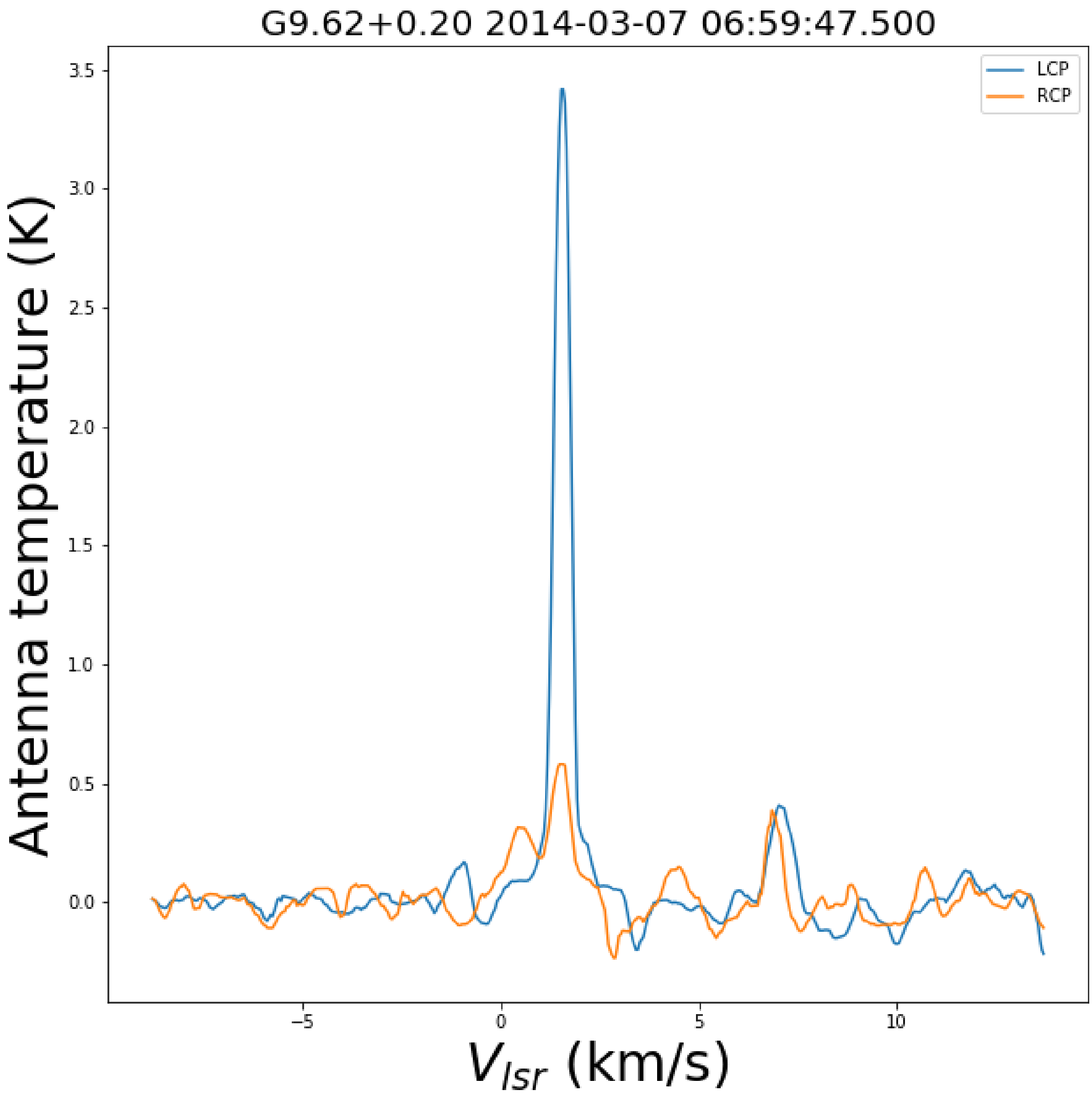

Figure 2.11: The spectrum showing the flattened baseline of both LCP and RCP with the mean signal at 0 K antenna temperature.

### 2.2.5 Pointing correction

To calculate the pointing correction factor, short five point scans on the source (in this case the methanol maser) were taken by offsetting half of the beam width to the cardinal points (north, south, east and west) from the requested source center. If the pointing is correct half the power at the center is recorded at the half power points but if the pointing is off, more power is recorded at some cardinal points than others. Thus for a perfect pointing model, the peak of the scan is recorded at zero right ascension (RA) offset. The cross-section $P$ of the main beam of the telescope can be approximated by a Gaussian profile given by

$$P = P_0 \exp\left(-\ln 2\left(\frac{\delta\theta}{b}\right)^2\right) \tag{2.1}$$

Here $P$ represents the main lobe of the antenna beam pattern, $\delta\theta$ is the offset between the source and the centre of the beam and $b$ is the half power beam width. Hence a Gaussian fitted to the main beam data (peak of each maser line) as in Figure 2.12 measures the amplitude (maximum power) of the peak for each cardinal point.

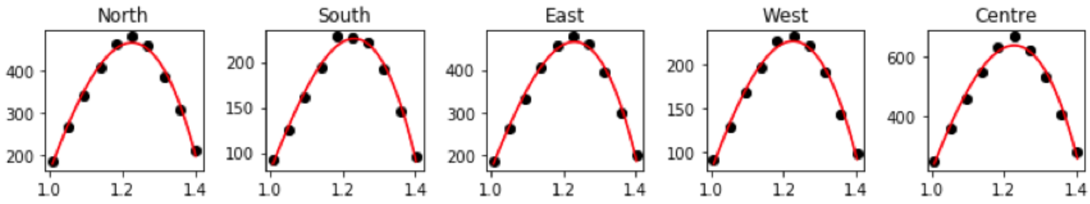

Figure 2.12: Peak power of the spectra taken at the half power point of cardinal points (north, south, east and west) and on the source center.

If the telescope has a good pointing model the peak of the Gaussian is expected close to the centre of the scan. Given the power measured at the half-power point north, south, east, west and on the center of the beam, the pointing offset for the north-south direction as well as that for the east-west direction which is the measured signal amplitude as a function of offset position (peak) was calculated. An example of a pointing offset calculation in degrees for north-south and east-west directions for an observation is shown in Figure 2.13. The pointing offset values are the pointing correction factors applied to the on-source amplitude. The average pointing correction factor for the 6668 MHz data was 1.067.

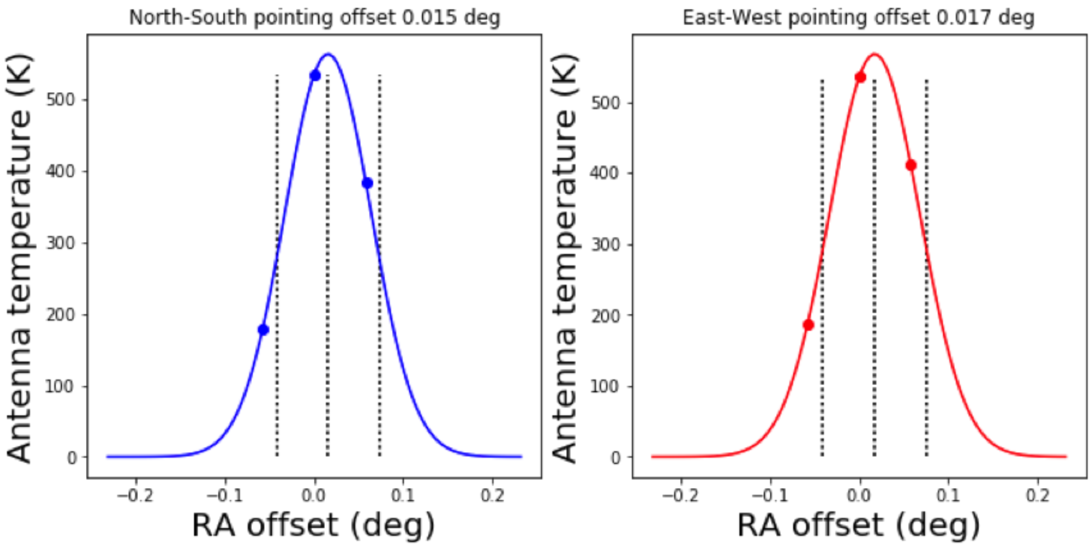

Figure 2.13: The left plot shows the north-south pointing offset with an offset of 0.015 deg from the center and the right plot displays the east-west pointing offset of 0.017 deg from the center.

### 2.2.6 Flux density calibration

To calibrate the flux density of the maser lines in the spectra, three drift scans on the flux calibrators were taken, one through the expected center of the beam and the others through the expected north and south half-power points respectively. The amplitudes were calculated by approximating each scan to a Gaussian and fitting a Gaussian plus a linear baseline to the main peak of each drift scan as shown in Figure 2.14. The Gaussians used for the fitting are:

$$T_{\text{center}} = T\ \exp\left(-\ln 2\left(\frac{\delta\theta}{b}\right)^2\right) \tag{2.2}$$

$$T_{\text{north}} = T\ \exp\left(-\ln 2\left(\frac{\delta\theta+b}{b}\right)^2\right) \tag{2.3}$$

$$T_{\text{south}} = T\ \exp\left(-\ln 2\left(\frac{\delta\theta-b}{b}\right)^2\right) \tag{2.4}$$

where $T_{\text{center}}$ is the peak amplitude at the center, $T_{\text{north}}$ is the peak amplitude at the north and $T_{\text{south}}$ is the peak amplitude at the south half-power points on the beam. $T$ evaluates to the antenna temperature which is used to obtain a conversion factor between the signal of the source in units of antenna temperature $T_A$ and flux density $S$ (in Jy ). The conversion factor, the point source sensitivity (PSS), which is the flux density in janskys that produces one kelvin of antenna temperature change and measured in Jy/K, is used to convert the spectrum intensity measured in antenna temperature to flux density. The inverse of this is the gain $G$ (Marr et al., 2016). For an unresolved point source the relationship between antenna temperature $T_A$ and flux density $S$ is given by

$$S = 2k_B T_A A_{\text{eff}} \tag{2.5}$$

where $k_B$ is Boltzmann's constant and $A_{\text{eff}}$ is the effective geometric area of the telescope. Thus the PSS for each polarization of a polarized radio point source is given by

$$\text{PSS} = S/2K_s T_A \tag{2.6}$$

where $K_s$ is the correction factor for the source ($K_s = 1$ for a point source). The flux density $S_{src}$ of some source now becomes

$$S_{src} = \text{PSS}_{\text{cal}} T_{Asrc} \tag{2.7}$$

where $\text{PSS}_{\text{cal}}$ is the PSS of the calibrator and $T_{Asrc}$ is the antenna temperature produced by the source.

Three sources, 3C123, Hydra A and Virgo A, were observed for calibration purposes. Virgo A is the brightest calibrator of the three and was used to calculate the PSS at 1665 MHz, 1667 MHz and 6668 MHz. The flux densities of the calibrators were found from published scales (Ott et al., 1994).

The antenna temperature in each polarization was converted to flux density by multiplying it with the PSS of the corresponding polarization for both 1665 MHz and 1667 MHz maser lines. For the flux density of the methanol 6668 MHz line, however, the antenna temperature of the two polarizations were added to get the total antenna temperature which was then multiplied by the PSS to obtain the flux density of the calibrated spectrum. Figure 2.15 shows the flux calibrated spectrum for a hydroxyl maser.

The calculated point source sensitivities are recorded in Table 2.4.

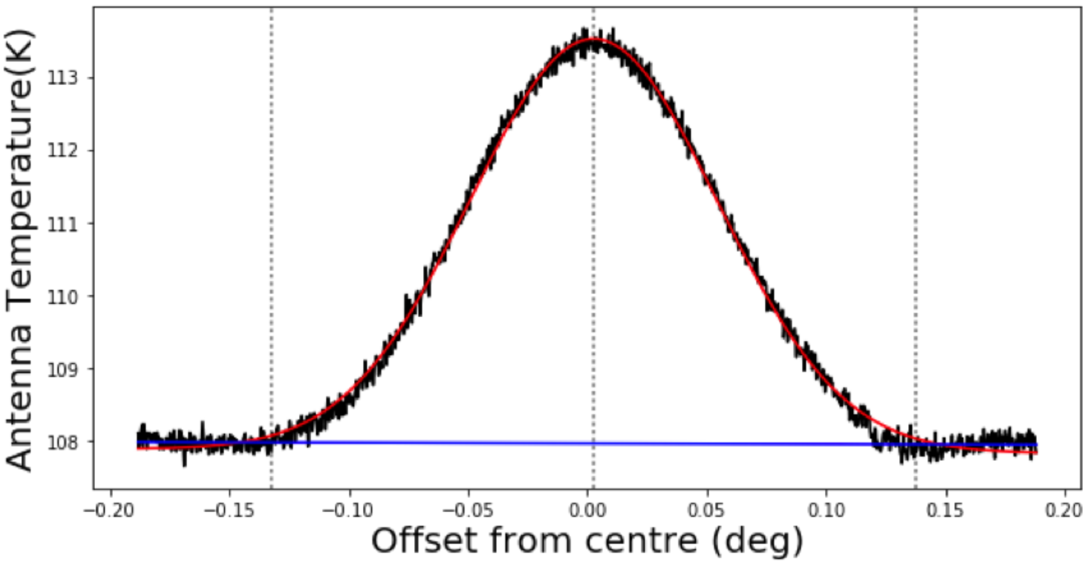

Figure 2.14: Fitting of a Gaussian beam plus linear baseline to the drift scan on Virgo A to calculate the amplitude of the peak.

Table 2.4: Point Source Sensitivity values calculated for LCP and RCP.

| Monitoring window | PSS LCP (Jy $K^{-1}$) | PSS RCP (Jy $K^{-1}$) |
|---|---|---|
| Regular window | 6.1 | 5.2 |
| Intensive window | 5.1 | 5.2 |

## 2.3 Results

The averaged spectra, plots of range of variation of the flux density and time series of the hydroxyl masers in LCP and RCP for both transitions as well as the methanol maser for both regular and intensive monitoring windows are presented in this section. The OH profiles recorded during the survey were bright in the LCP and faint in the RCP. Each profile was examined visually and bad data were removed from the data set. RFI which had not been removed satisfactorily and not located close to the maser line did not affect the maser line; hence, such spectra were included in the data. Ninety four spectra representing 27% of the data were removed from the analysis because some RFI persisted after the RFI excision procedure. The root mean square (rms) noise over the line-free emission region was measured by masking the line emission range and calculating the noise of the line-free channels. The average flux density and rms noise levels in the spectra for the hydroxyl and methanol lines are tabulated in Table 2.5 and Table 2.6 for the different monitoring windows.

Generally the spectra for LCP were found to contain more flux density than the RCP for

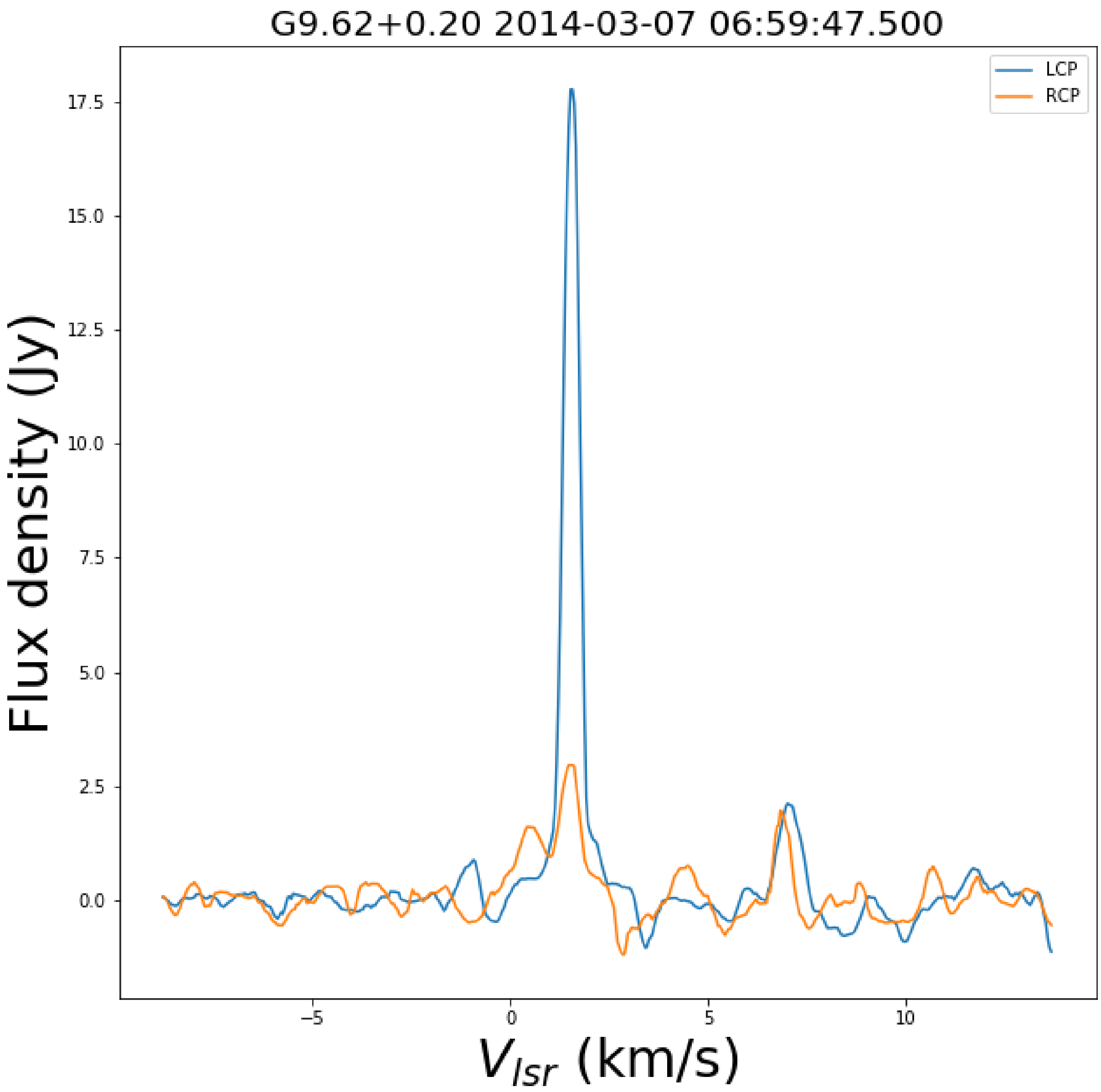

Figure 2.15: Calibrated spectrum after correction factor PSS has been applied to the on-source amplitude of the antenna temperature of the hydroxyl spectrum to covert it to flux density.

Table 2.5: Average flux density and rms noise for the regular monitoring window.

| Frequency (MHz) | Average flux density (Jy) | Average rms noise (Jy) |
|---|---|---|
| 1665 LCP | 10.34 | 0.50 |
| 1665 RCP | 8.48 | 0.41 |
| 1667 LCP | 23.66 | 0.54 |
| 1667 RCP | 3.24 | 0.44 |
| 6668 I | 5500.00 | 74.00 |

both monitoring windows as can be seen in Table 2.5 and Table 2.6. This, of course, is so because the OH maser is almost 100% polarised in the LCP (Reid and Moran, 1981). A com-

Table 2.6: Average flux density and rms noise for the intensive monitoring window.

| Frequency (MHz) | Average flux density (Jy) | Average rms noise (Jy) |
|---|---|---|
| 1665 LCP | 23.28 | 1.07 |
| 1665 RCP | 6.11 | 0.41 |
| 1667 LCP | 25.23 | 0.78 |
| 1667 RCP | 2.87 | 0.47 |
| 6668 I | 3500 | 82 |

parison of the average flux densities in both windows shows that for the 1665 MHz line, the flux density for LCP increased whereas the flux density in the RCP decreased. The same trend is seen for the 1667 MHz line though the increase in the 1665 MHz LCP flux density was about a factor of two greater than the increase in the 1667 MHz.

### 2.3.1 Averaged spectra for regular monitoring

The averaged spectra for each polarization of the OH mainlines and the total intensity for the methanol lines are displayed in Figure 2.16 through to Figure 2.20 for the regular monitoring window. The averaged spectra are the combination of the median values at each spectral channel taken from the values of the monitoring window. Each spectrum of the maser line is made up of a number of peaks which represent emissions from maser spots at different velocities. A velocity range of 25 km/s spread from $-10$ km/s to 15 km/s was used to display the detected features in each spectrum. Table 2.7 displays the velocity channels with OH maser emissions that were detected and their corresponding flux densities for the regular window.

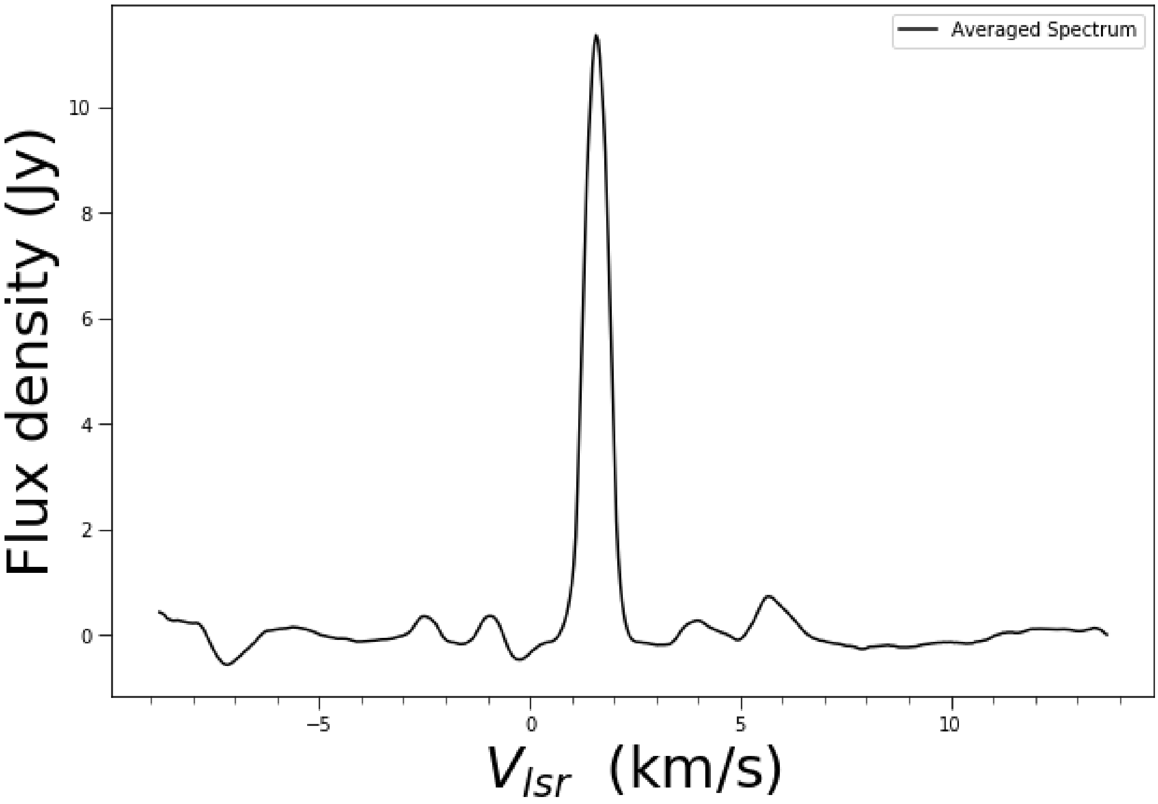

Figure 2.16: Averaged spectrum for the 1665 MHz maser line in LCP.

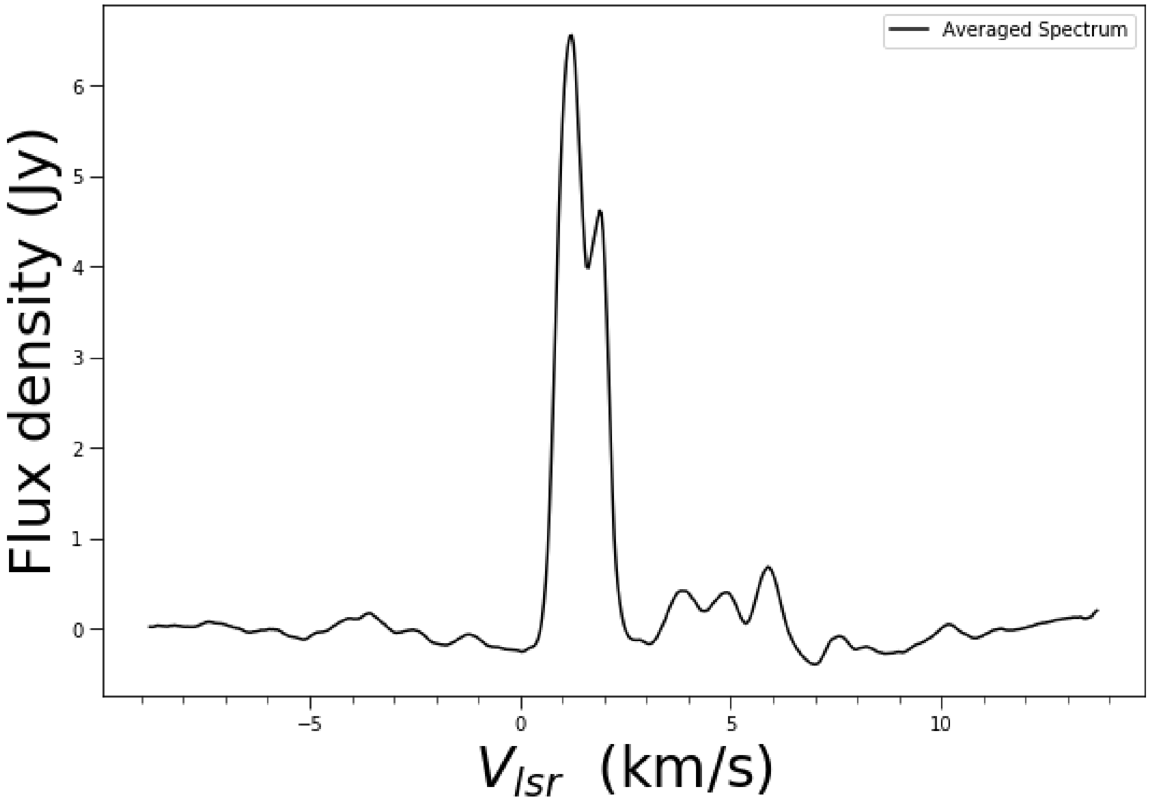

Figure 2.17: Averaged spectrum for the 1665 MHz maser line in RCP.

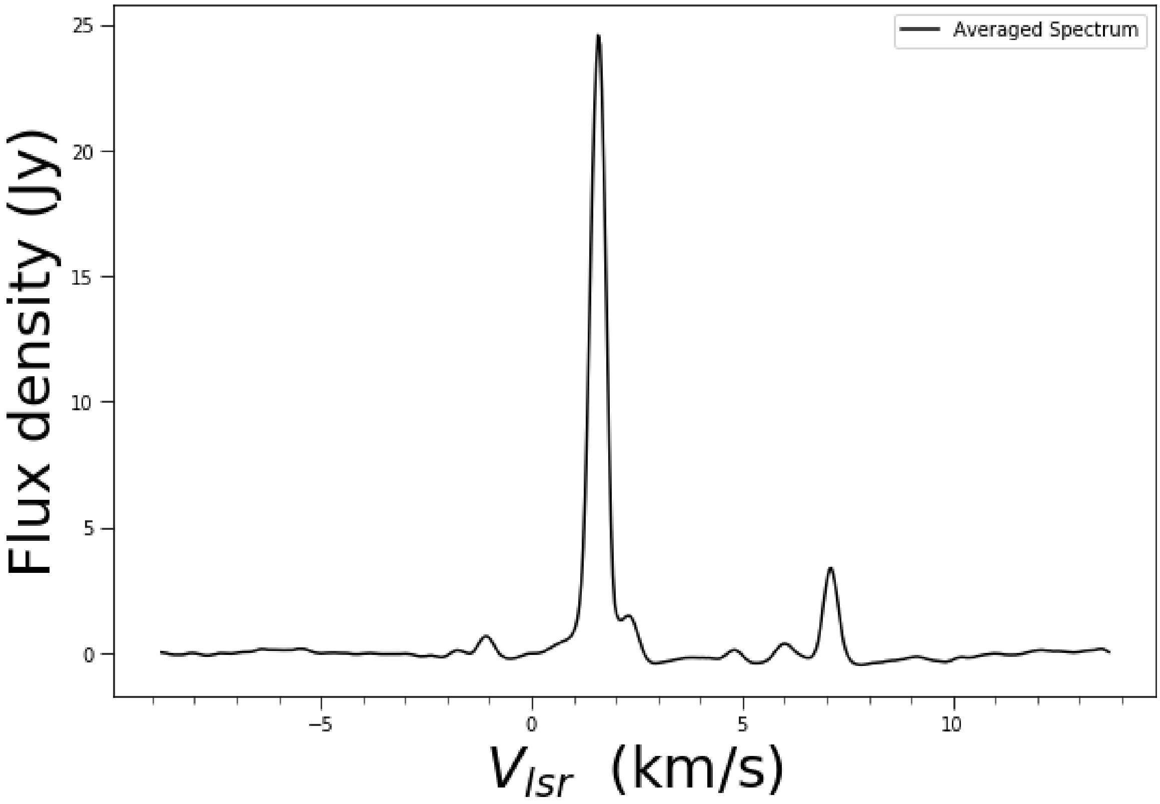

Figure 2.18: Averaged spectrum for the 1667 MHz maser line in LCP.

The prominent maser components in each spectrum lie in the range 0 km/s to 3 km/s for the hydroxyl maser and those of the methanol maser lie in the range 0.5 km/s to 3 km/s. The velocities that have no emissions correspond to the noise level in the maser spectra.

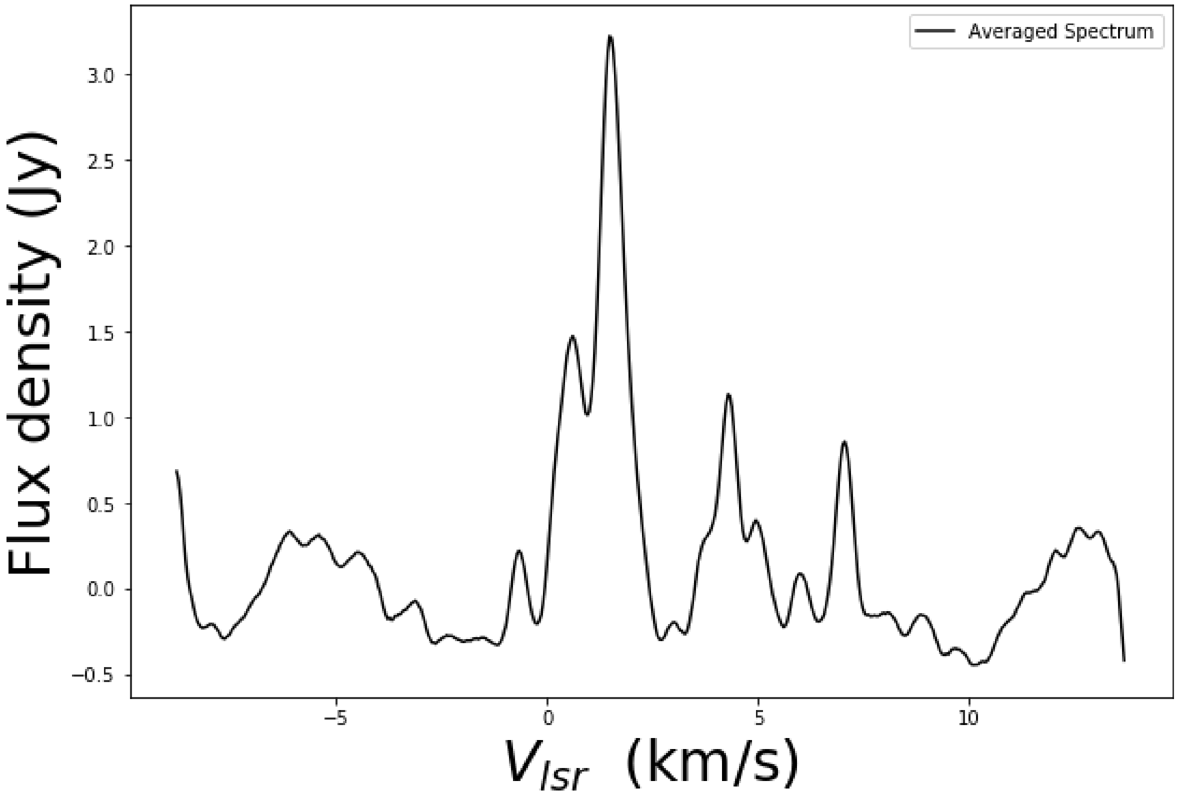

Figure 2.19: Averaged spectrum for the 1667 MHz maser line in RCP.

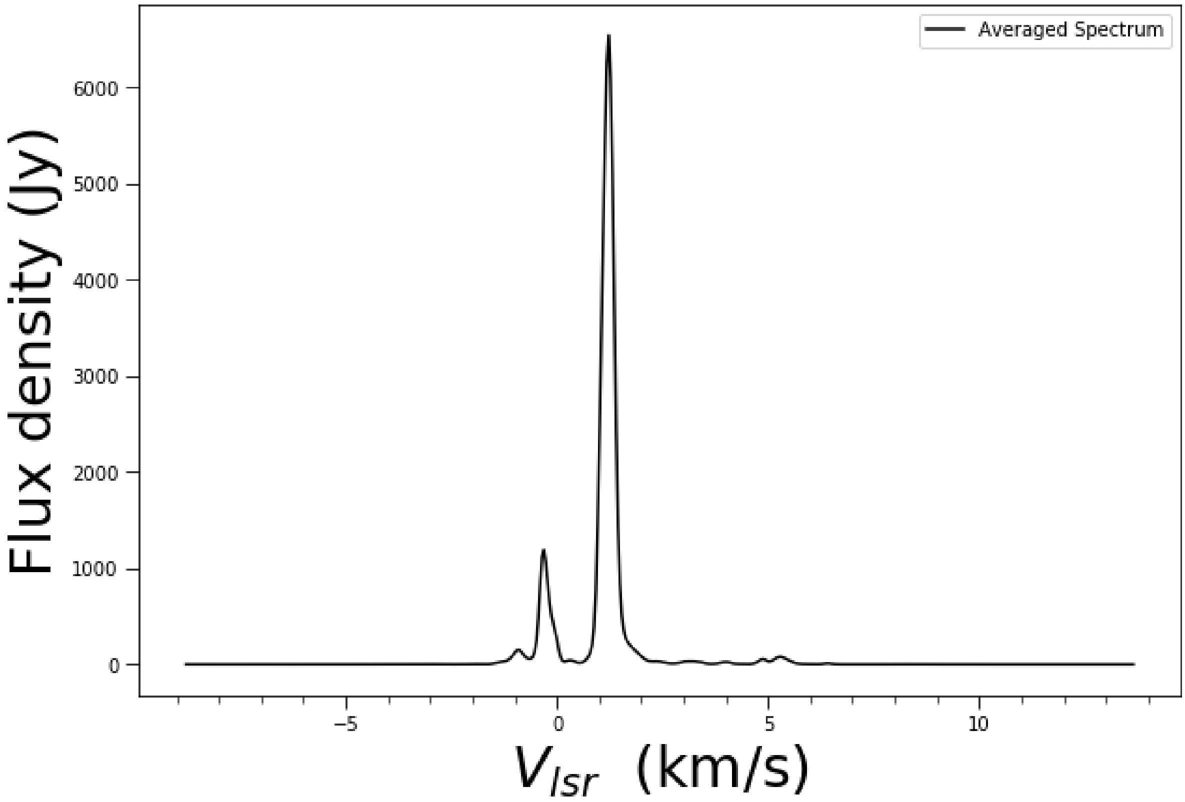

Figure 2.20: Averaged total intensity spectrum for the 6668 MHz maser line.

Table 2.7: Detected OH maser velocity channels and their flux densities for the regular monitoring window.

| | 1665 MHz Flux density (Jy) | | 1667 MHz Flux density (Jy) | |
|---|---|---|---|---|
| $V_{lsr}$ (km/s) | LCP | RCP | LCP | RCP |
| $-2.5$ | 0.7 | – | – | – |
| $-1.5$ | – | – | – | 0.3 |
| $-1.0$ | – | – | 1 | – |
| 0.5 | – | – | – | 1.5 |
| 1.0 | 0.7 | 7 | – | – |
| 1.5 | 12 | – | 25 | 3.8 |
| 2.0 | – | 4.9 | – | – |
| 4.0 | 0.6 | 0.3 | – | – |
| 4.2 | – | – | – | 1.2 |
| 5.0 | – | 0.3 | 0.5 | 0.4 |
| 6.0 | 1 | 0.6 | 0.7 | 0.1 |
| 7.0 | – | – | 4 | 1 |

### 2.3.2 Averaged spectra for intensive monitoring

Figure 2.21 through to Figure 2.25 show the averaged spectra for both transitions of OH and the methanol line for the intensive monitoring windows. In Table 2.8 the maser features of the OH transitions with their corresponding flux densities for the intensive monitoring window are presented.

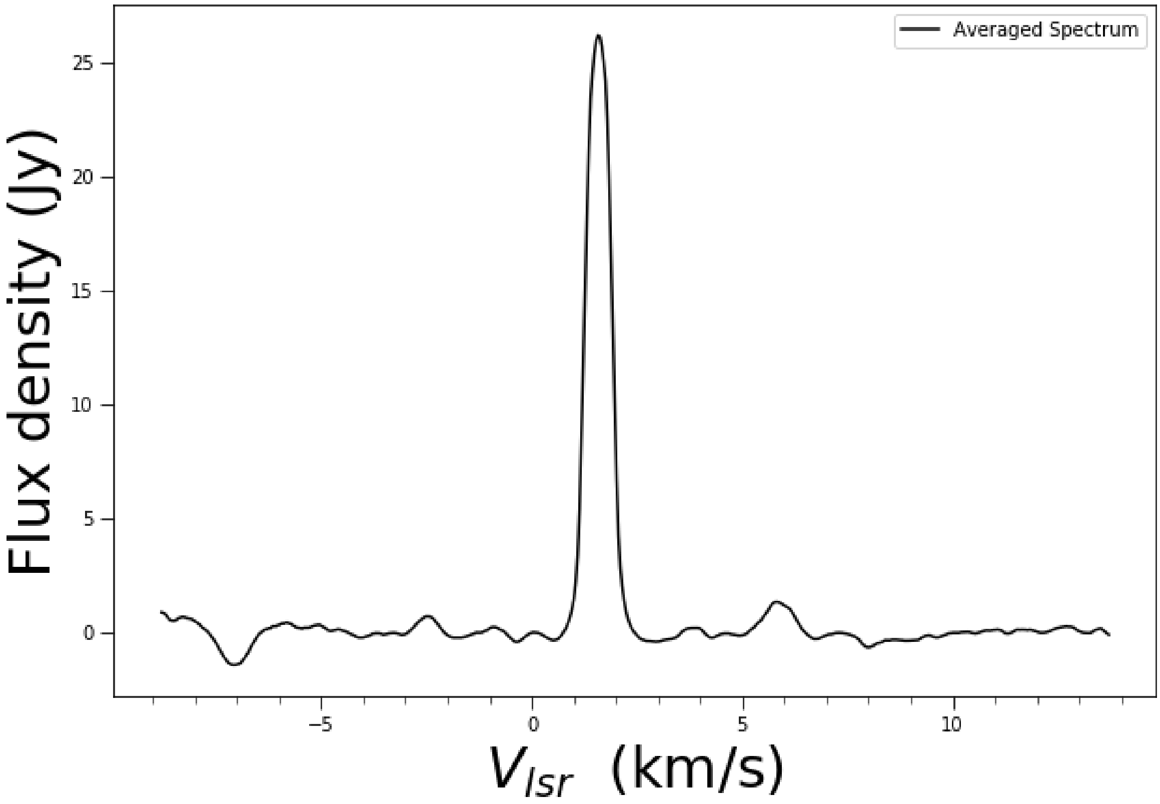

Figure 2.21: Averaged spectrum for the 1665 MHz maser line in LCP.

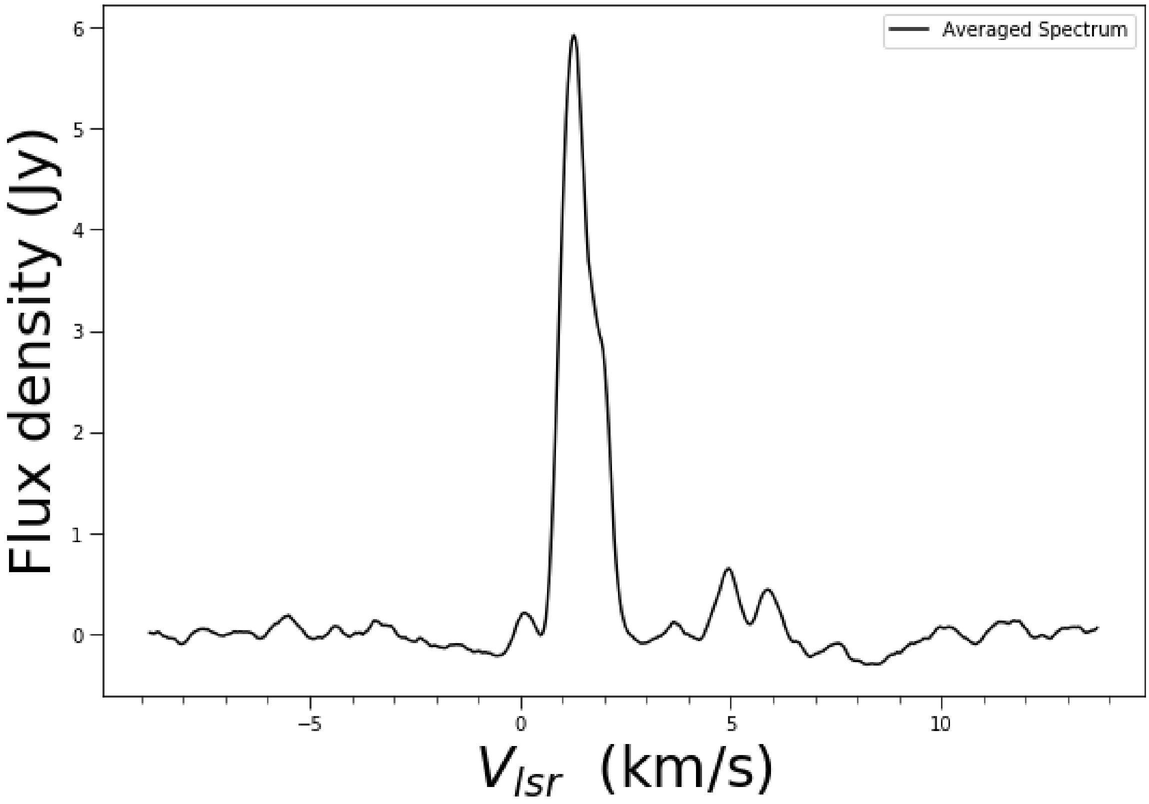

Figure 2.22: Averaged spectrum for the 1665 MHz maser line in RCP.

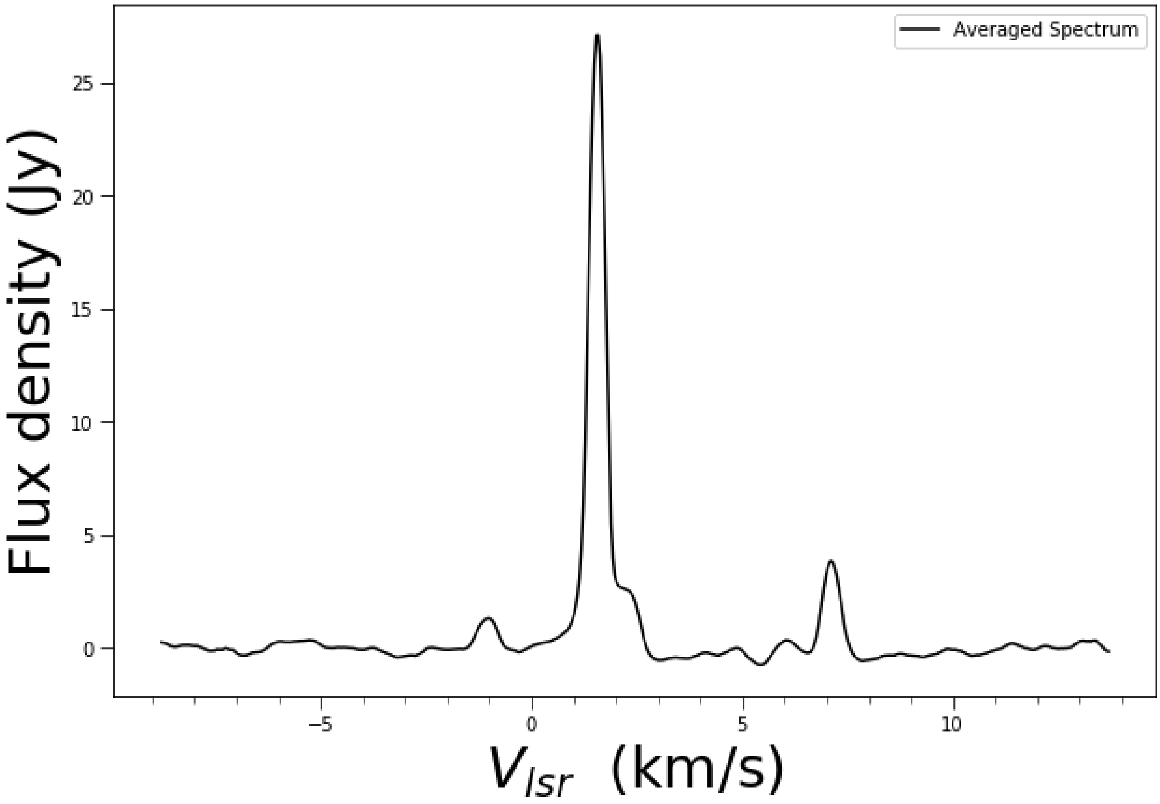

Figure 2.23: Averaged spectrum for the 1667 MHz maser line in LCP.

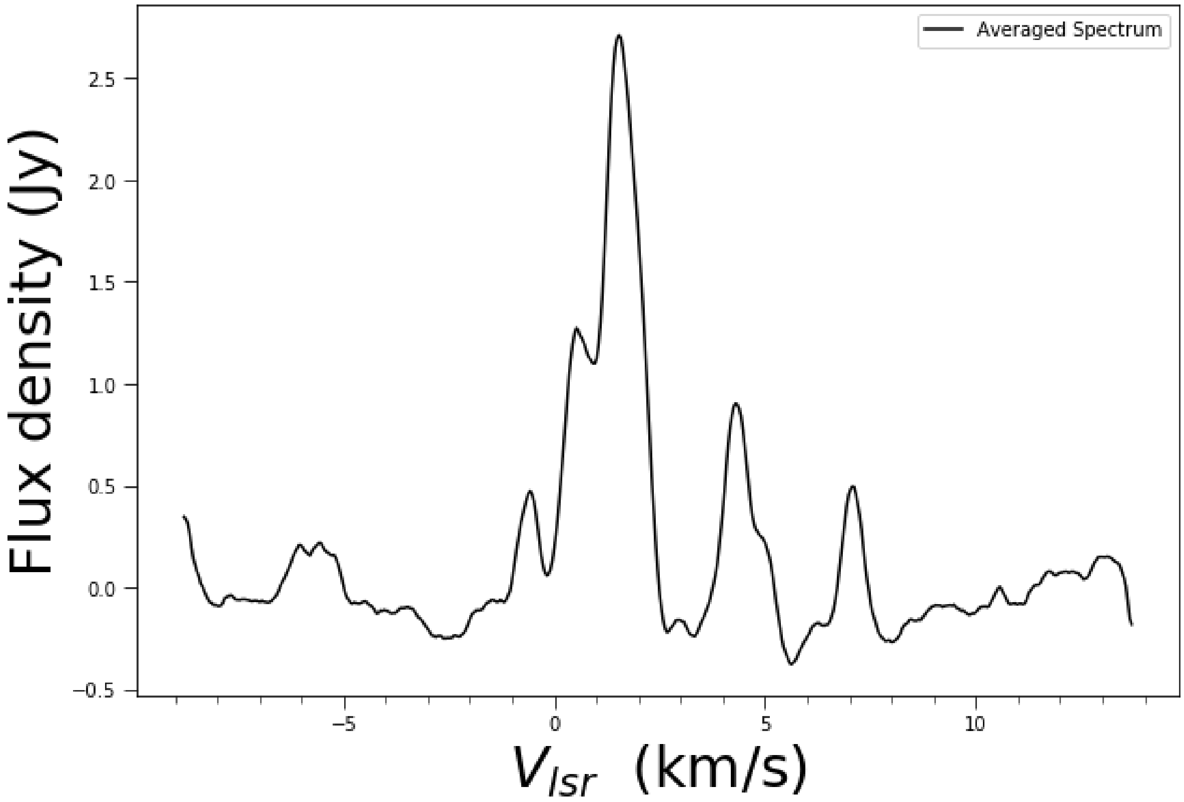

Figure 2.24: Averaged spectrum for the 1667 MHz maser line in RCP.

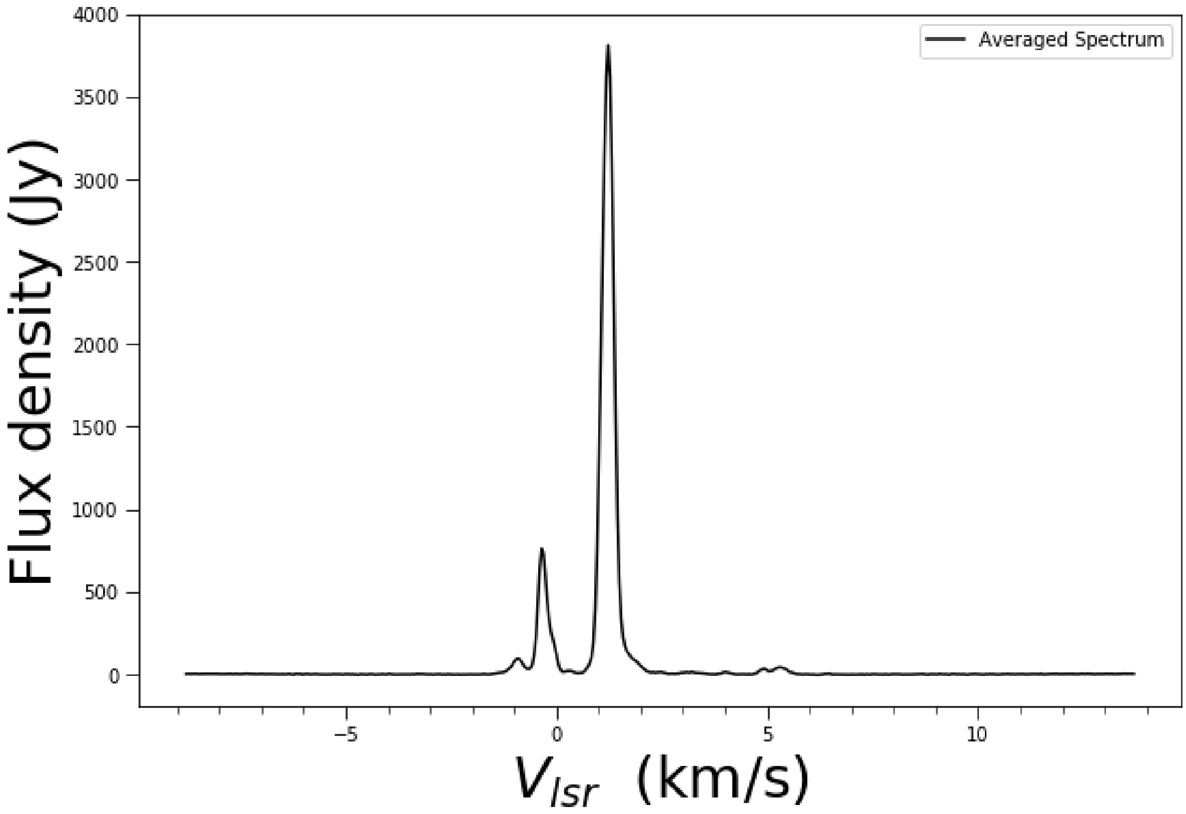

Figure 2.25: Averaged total intensity spectrum for the 6668 MHz maser line.

Table 2.8: Detected OH maser velocity channels and their flux densities for the intensive monitoring window.

| | 1665 MHz | Flux density (Jy) | 1667 MHz | Flux density (Jy) |
|---|---|---|---|---|
| $V_{lsr}$ (km/s) | LCP | RCP | LCP | RCP |
| −2.5 | 1 | – | – | – |
| −1.0 | 0.5 | – | 1 | – |
| −0.5 | – | – | – | 0.5 |
| 0 | – | 0.3 | – | – |
| 0.5 | – | – | – | 1.03 |
| 1.5 | 27 | 6 | 28 | 2.8 |
| 4.0 | 0.5 | – | – | 1 |
| 5.0 | – | 0.5 | – | – |
| 6.0 | 2 | 0.4 | 0.5 | – |
| 7.0 | – | – | 4 | 0.5 |

### 2.3.3 Spectra from Caswell et al. (2013)

Plots of the OH mainline polarization spectra adapted from Caswell et al. (2013) are presented in Figure 2.26 and Figure 2.27. This ATCA observation of the G9.62 + 0.20 region consisting of G9.619 + 0.193, G9.620 + 0.194 and G9.621 + 0.196 is covered by the beam for the HartRAO telescope. Also presented in Table 2.9 are the maser emissions which fall in the velocity range −10 km/s to 30 km/s. The flux densities recorded in the velocity channels are presented in Table 2.9 as well. In the absence of individual polarisation spectra from this region these plots will be compared to the results.

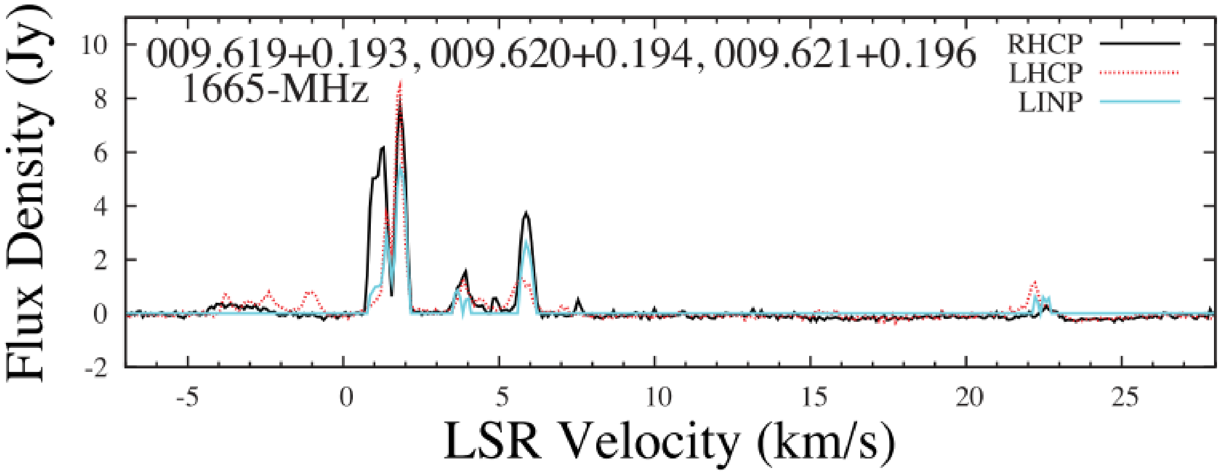

Figure 2.26: The 1665 MHz spectrum of the three regions G9.619 + 0.193, G9.620 + 0.194 and G9.621 + 0.196 in G9.62 + 0.20 from Caswell et al. (2013) showing the left circular polarisation, right circular polarisation and linear polarisation features.

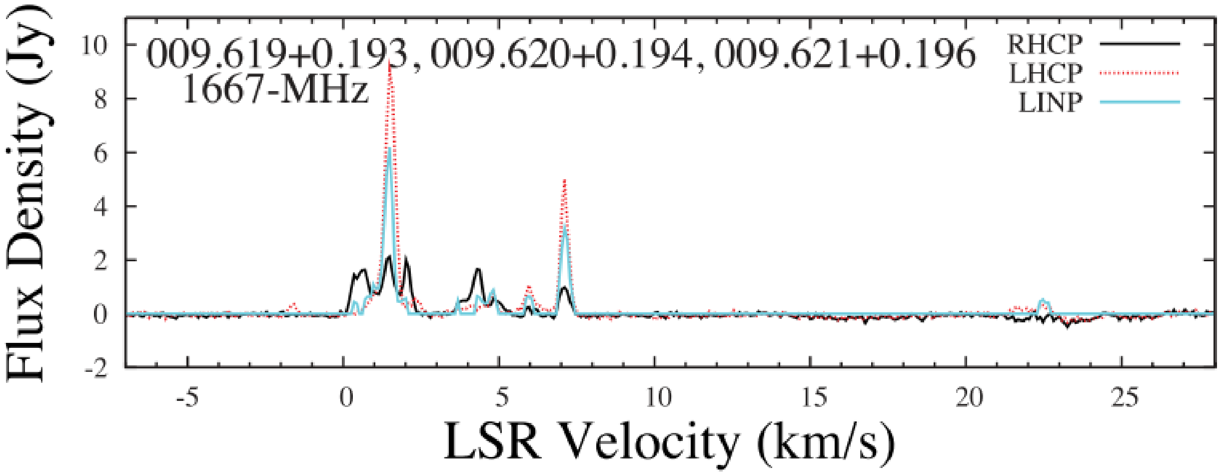

Figure 2.27: The 1667 MHz spectrum of the three regions G9.619 + 0.193, G9.620 + 0.194 and G9.621 + 0.196 in G9.62 + 0.20 from Caswell et al. (2013) showing the left circular polarisation, right circular polarisation and linear polarisation features.

Table 2.9: Detected OH maser velocity channels and their flux densities derived from Caswell et al. (2013).

| | 1665 MHz Flux density (Jy) | | 1667 MHz Flux density (Jy) | |
|---|---|---|---|---|
| $V_{lsr}$ (km/s) | LCP | RCP | LCP | RCP |
| −4.0 | 0.5 | – | – | – |
| −2.5 | 0.5 | – | – | – |
| −1.5 | – | – | 0.2 | – |
| −1.0 | 1 | – | – | – |
| 0.5 | – | – | – | 1.9 |
| 1.0 | – | 6 | – | – |
| 1.5 | – | – | 9 | 2.1 |
| 2.0 | 9 | 8 | – | 2.6 |
| 4.0 | 2 | 2 | – | – |
| 4.2 | – | – | – | 2.6 |
| 5.0 | – | 0.2 | – | 0.2 |
| 6.0 | 4 | 4 | 1 | 0.1 |
| 7.0 | – | – | 5 | 1 |

### 2.3.4 Comparison of the averaged spectra of OH for regular and intensive monitoring window with Caswell et al. (2013)

Here the results for both the regular and the intensive monitoring windows are compared with those reported by Caswell et al. (2013). For the regular monitoring window Table 2.7 derived from the regular monitoring plots shows five major emissions for both polarisations of the 1665 MHz line and the LCP of the 1667 MHz line whereas two more emissions are recorded in RCP for the 1667 MHz line. A comparison of these results with the data in Table 2.9 shows that all emissions reported in 2013 were again detected except the emission at channel 1 km/s. An additional emission at −1 km/s for the 1665 MHz line in LCP was detected whereas the 1665 MHz RCP shows no emission at 4 km/s, 2 km/s and 1 km/s but rather at 1.5 km/s. The 1665 MHz RCP also shows signals at −3.5 km/s and −1 km/s which are not spurious. For the 1667 MHz spectrum detections of all the emissions except that at 5 km/s were made for the LCP whereas for the RCP two additional emissions, at −0.5 km/s and 4 km/s, were made but no emissions were recorded at −1.5 km/s, 4.2 km/s and 5 km/s. The RCP of the 1667 MHz line also shows signals at −6 km/s, −4.5 km/s, −5 km/s, −1.5 km/s and some emissions occur at velocities greater than 10 km/s.

Turning to the intensive monitoring window a comparison of Table 2.8 for the intensive monitoring window with Table 2.9 shows that all emissions for the LCP of the 1665 MHz line except the features 1.5 km/s and 1 km/s were detected with additional emissions detected at −4 km/s and −1 km/s. All maser emissions in RCP were coincident with those of Caswell et al. (2013); however, an emission detected at −4 km/s is not real. The maser emissions in the 1667 MHz transitions were also coincident with those of Caswell et al. (2013) except the emission at 5 km/s and a new emission which was detected at −1.5 km/s in the LCP. Emissions coincident with those of Caswell et al. (2013) were recorded for the RCP at all channels except at −1.5 km/s. An additional emission at 2 km/s was also recorded. Emissions were also recorded at channels −6 km/s, −0.5 km/s and 10.5 km/s of the RCP component but these are not real.

### 2.3.5 Comparison of the averaged spectra of methanol for the regular and intensive monitoring window with Goedhart et al. (2004)

The flux density for the 6.7 GHz methanol line from G9.62 + 0.20E was first measured to be 4870 Jy (Menten, 1991). Almost two decades later the same telescope measured the flux to be 5240 Jy (Green et al., 2010). A flux density of 4375 Jy has also been recorded with HartRAO (Goedhart et al., 2004). Table 2.10 shows the results for the detected emissions during the regular and intensive monitoring of the 6.7 GHz methanol maser. A comparison of Table 2.10 with the detected emissions from Goedhart et al. (2004) presented in Table 2.11 shows that all emissions were detected. The flux density in the main velocity channel 1.23 km/s was 4504 Jy for the regular window and 4320 Jy for the intensive window whereas Goedhart et al. (2004) recorded 4375 Jy suggesting an increase in the flux density over time.

Table 2.10: Detected 6668 MHz maser velocity channels and their flux densities for both regular and intensive monitoring windows.

| Regular window | | Intensive window | |
|---|---|---|---|
| $V_{lsr}$ (km/s) | Flux (Jy) | $V_{lsr}$ (km/s) | Flux (Jy) |
| −1.89 | 21 | −1.89 | 25 |
| −1.27 | 38 | −1.27 | 44 |
| −0.84 | 113 | −0.84 | 94 |
| −0.22 | 677 | −0.22 | 521 |
| 1.18 | 3698 | 1.18 | 4300 |
| 1.23 | 4320 | 1.23 | 4504 |
| 3.03 | 46 | 3.03 | 44 |
| 3.73 | 30 | 3.73 | 26 |
| 5.26 | 76 | 5.36 | 79 |
| 6.36 | 26 | 6.36 | 27 |

Table 2.11: Detected 6668 MHz maser velocity channels and their flux densities derived from Goedhart et al. (2004).

| $V_{lsr}$ (km/s) | Flux (Jy) |
|---|---|
| −1.88 | 20 |
| −1.21 | 30 |
| −0.76 | 41 |
| −0.42 | 34 |
| −0.14 | 423 |
| 1.26 | 4375 |
| 1.94 | 121 |
| 3.12 | 68 |
| 5.31 | 62 |
| 6.43 | 13 |

### 2.3.6 Range of variation for regular monitoring

Table 2.5 and Table 2.6 give the average flux density in each polarization for the 1665 MHz and 1667 MHz maser lines. Within each velocity channel of each polarisation a minimum and a maximum flux density is recorded which gives an indication of the range of variability of the flux density. Figure 2.28 to Figure 2.32 display the range of flux density variation for the regular monitoring window.

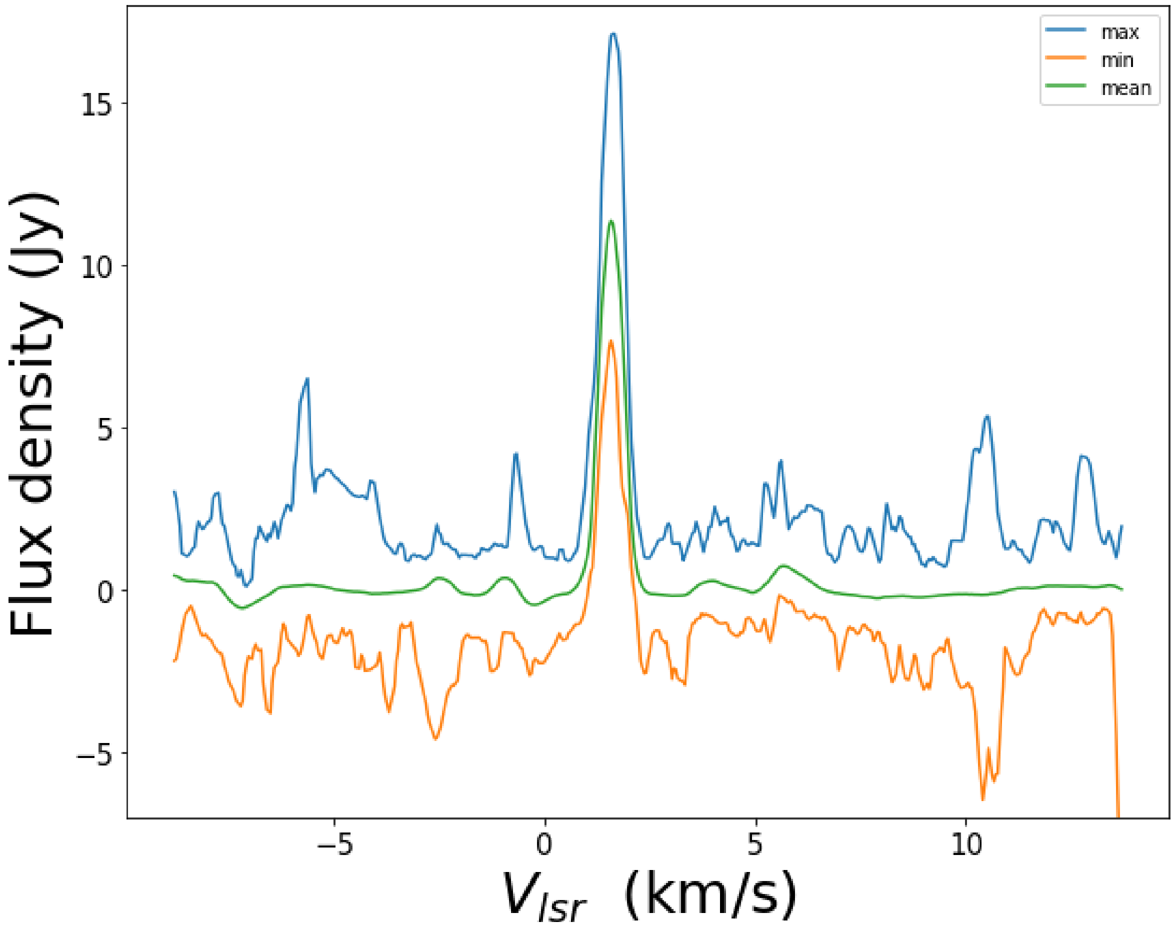

Figure 2.28: Range of variation of flux density in the spectrum of 1665 MHz LCP. The blue line represents the upper envelope, the green line shows the averaged spectrum, and the orange line shows the lower envelope.

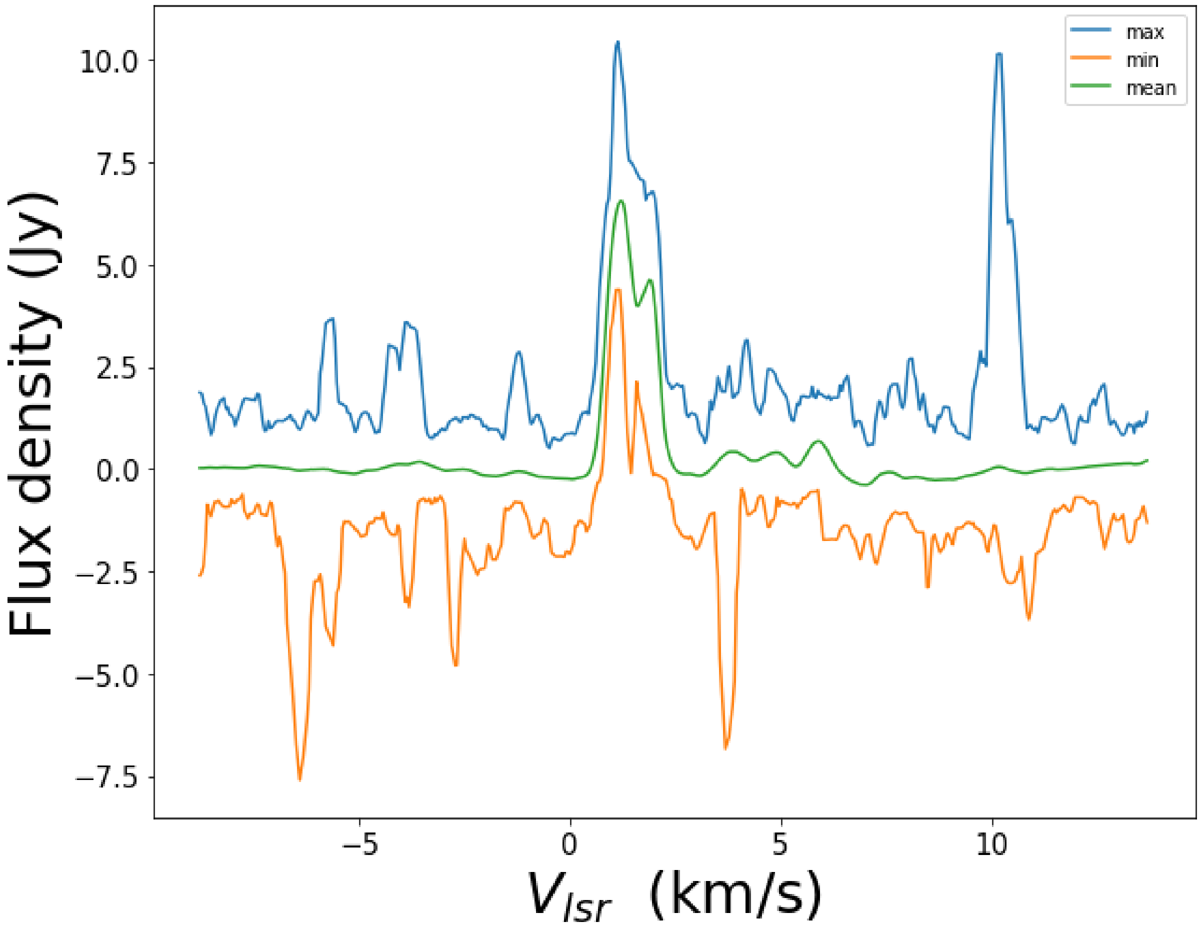

Figure 2.29: Range of variation of flux density in the spectrum of 1665 MHz RCP. The blue line represents the upper envelope, the green line shows the averaged spectrum, and the orange line shows the lower envelope.

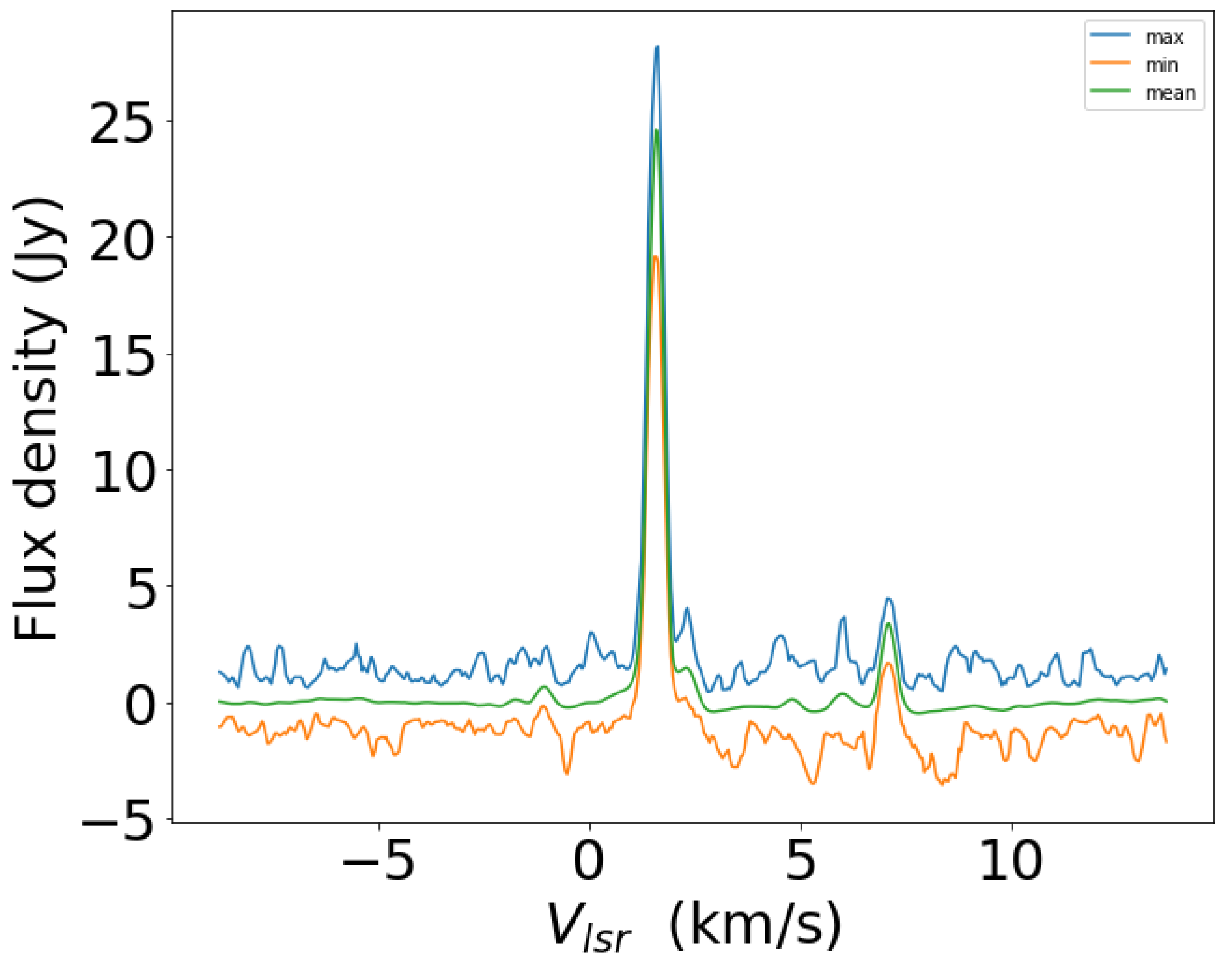

Figure 2.30: Range of variation of flux density in the spectrum of 1667 MHz LCP. The blue line represents the upper envelope, the green line shows the averaged spectrum, and the orange line depicts the lower envelope.

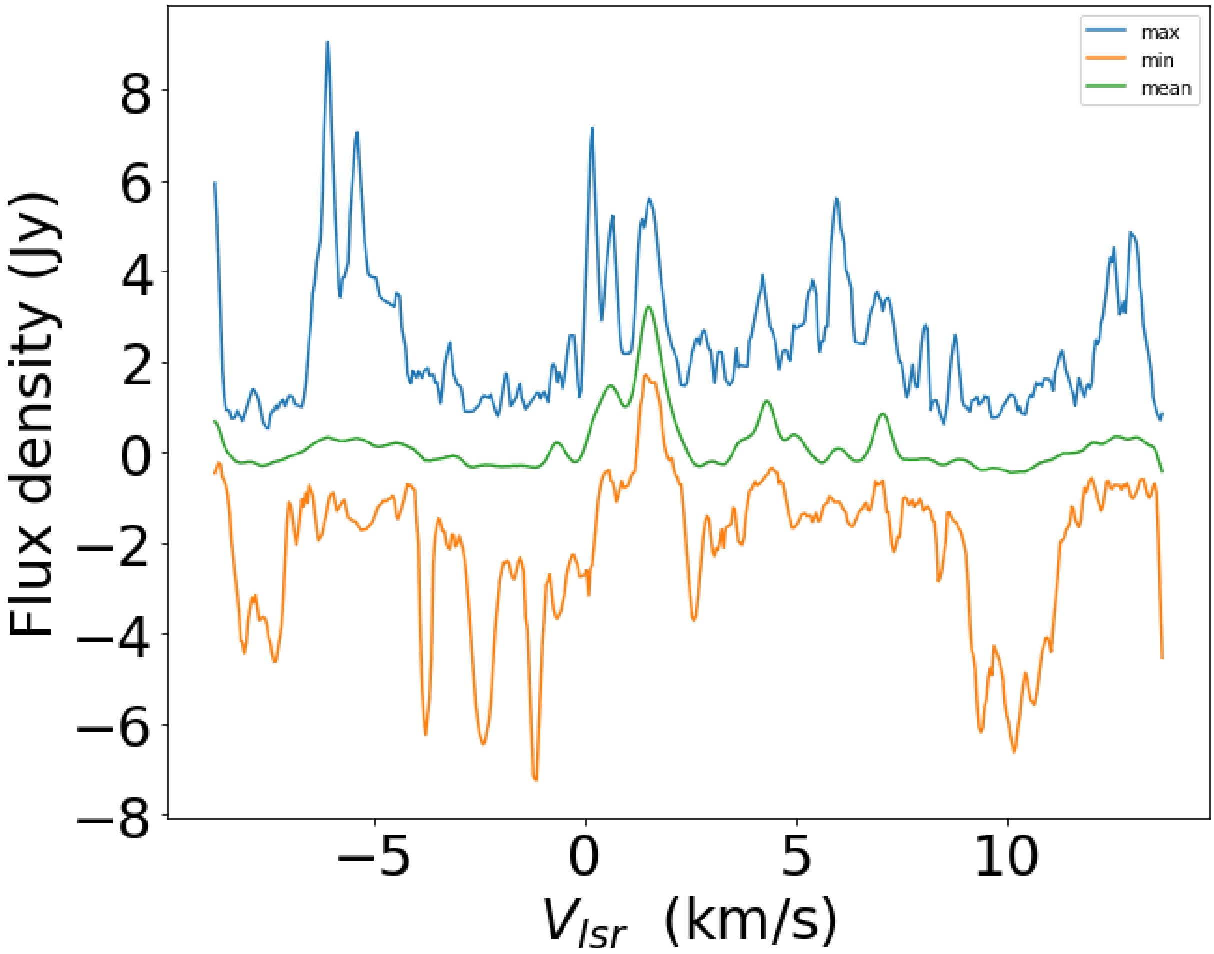

Figure 2.31: Range of variation of flux density in the spectrum of 1667 MHz RCP. The blue line represents the upper envelope, the green line shows the averaged spectrum, and the orange line depicts the lower envelope.

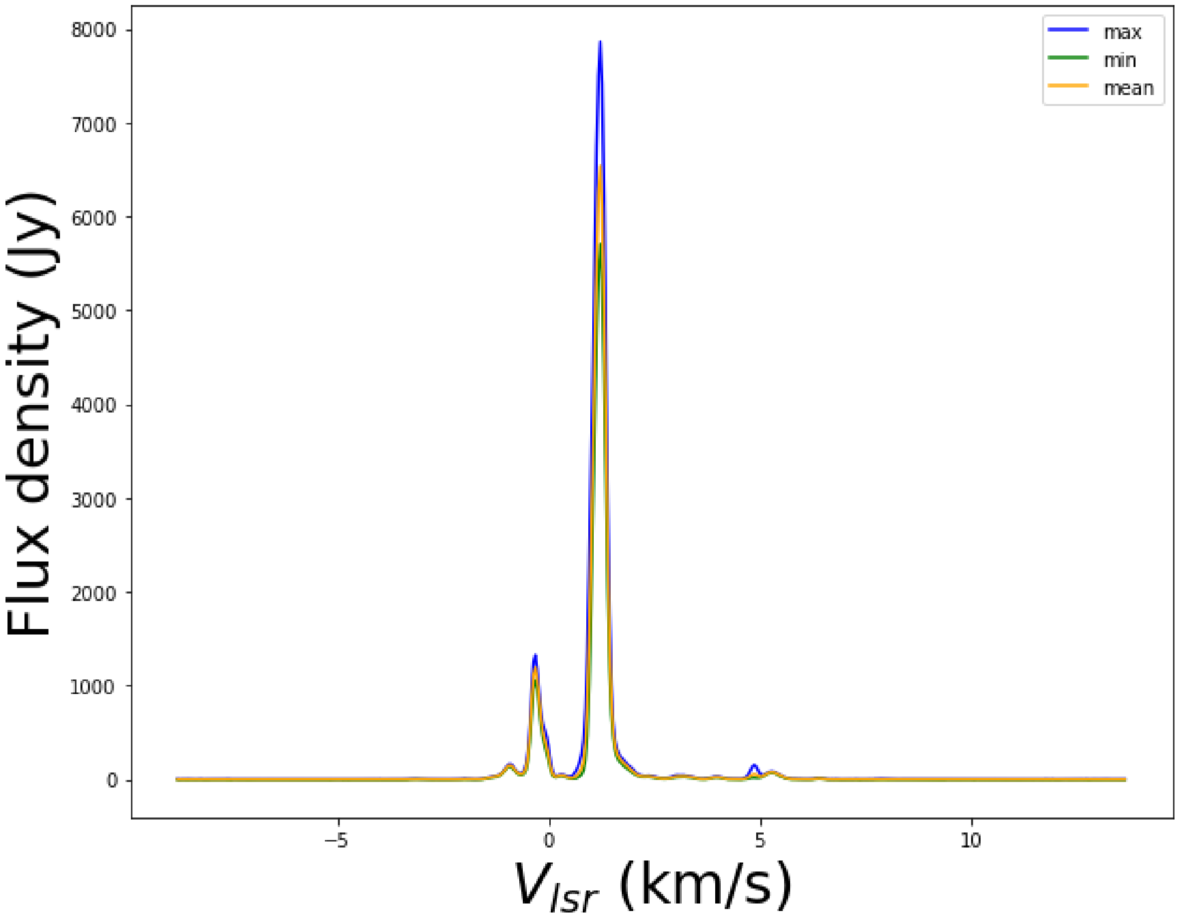

Figure 2.32: Range of variation of flux density in the spectrum of 6668 MHz. The blue line represents the upper envelope, the green line shows the averaged spectrum, and the orange line depicts the lower envelope.

### 2.3.7 Range of variation for intensive monitoring

Figure 2.33 to Figure 2.37 show the range of variation for the intensive monitoring window.

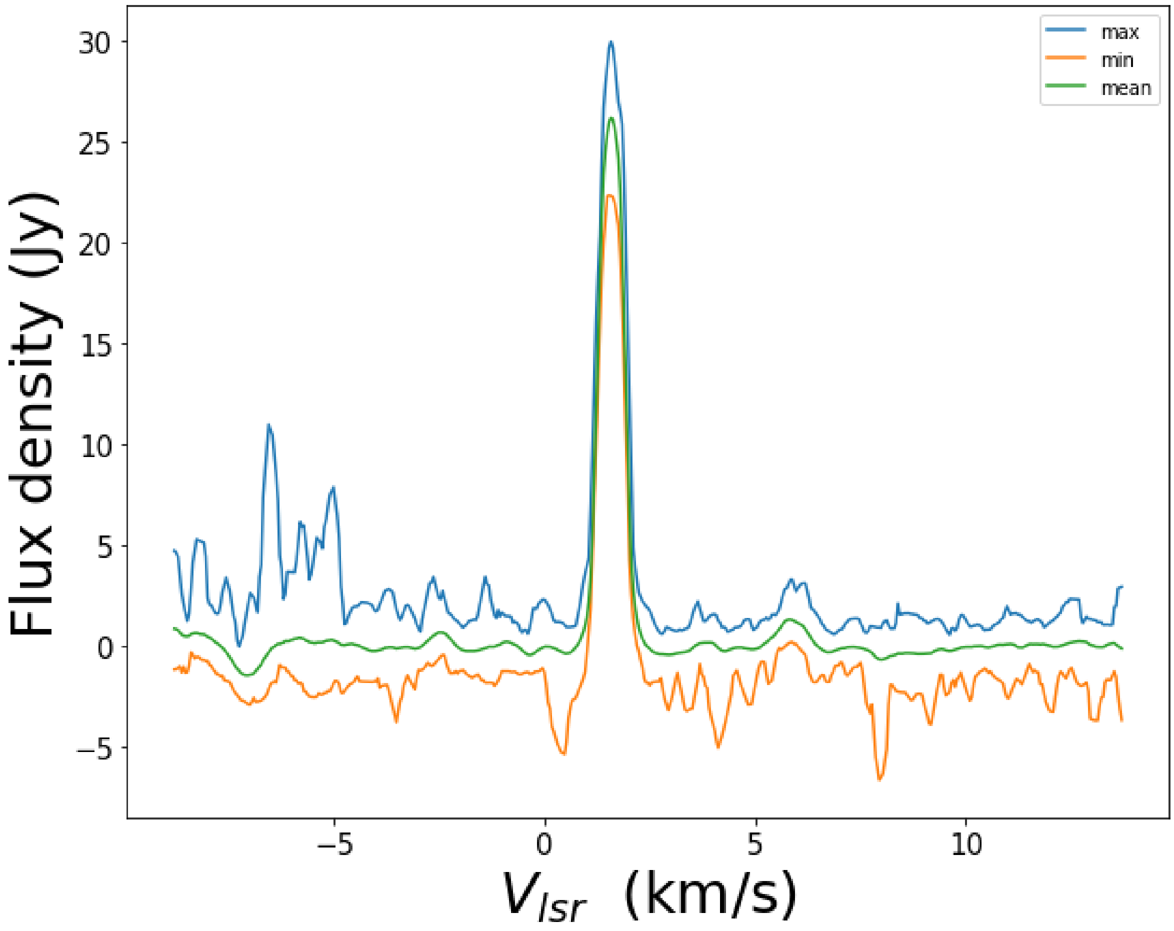

Figure 2.33: Range of variation of flux density in the spectrum of 1665 MHz LCP. The blue line represents the upper envelope, the green line shows the averaged spectrum, and the orange line depicts the lower envelope.

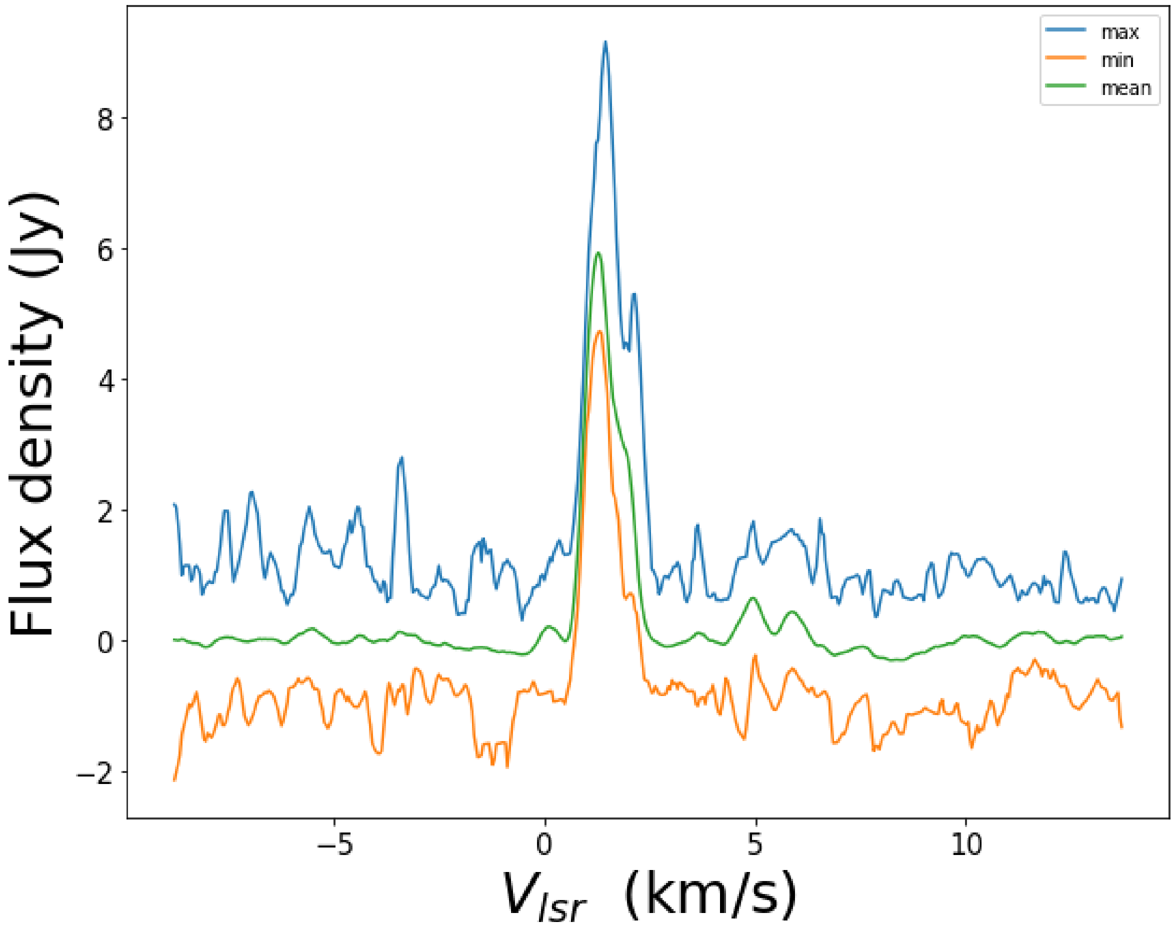

Figure 2.34: Range of variation of flux density in the spectrum of 1665 MHz RCP. The blue line represents the upper envelope, the green line shows the averaged spectrum, and the orange line depicts the lower envelope.

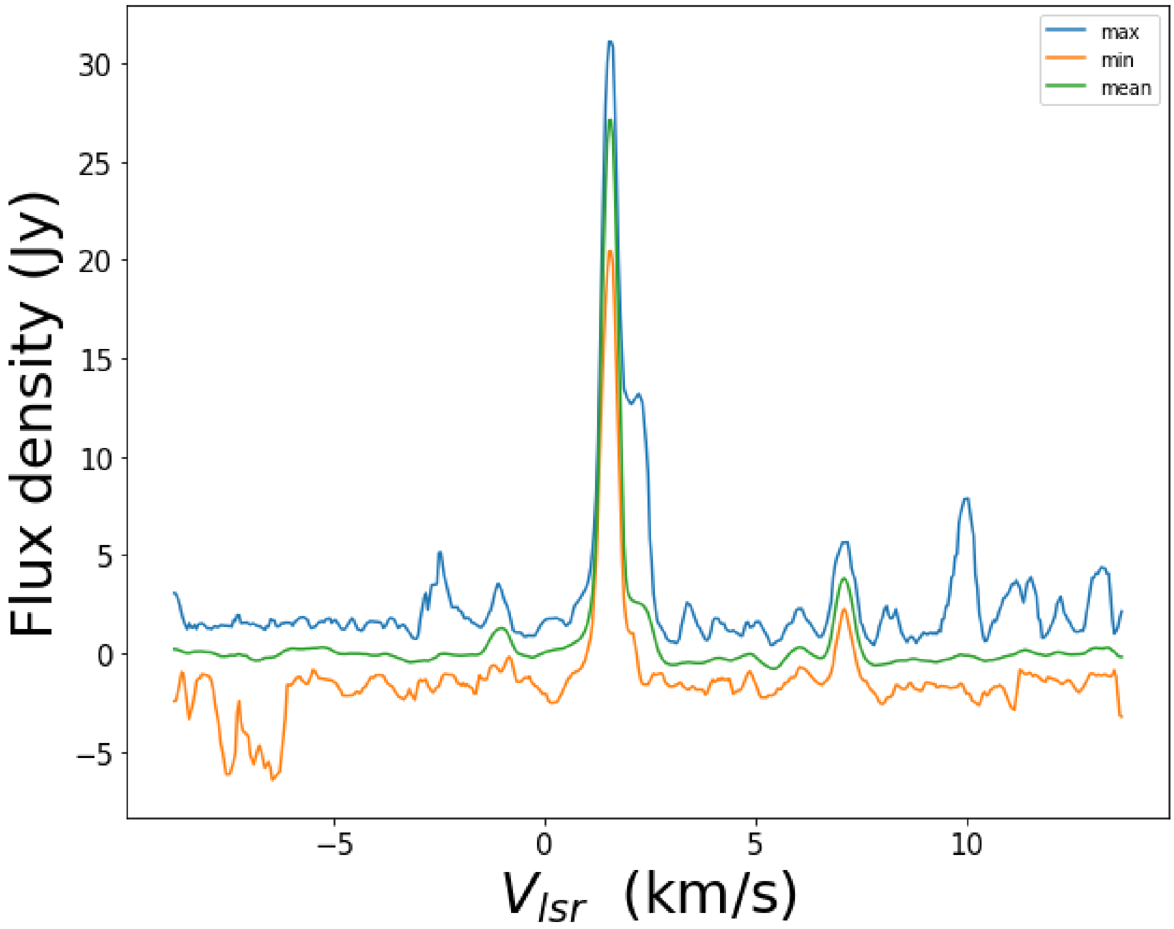

Figure 2.35: Range of variation of flux density in the spectrum of 1667 MHz LCP. The blue line represents the upper envelope, the green line shows the averaged spectrum, and the orange line depicts the lower envelope.

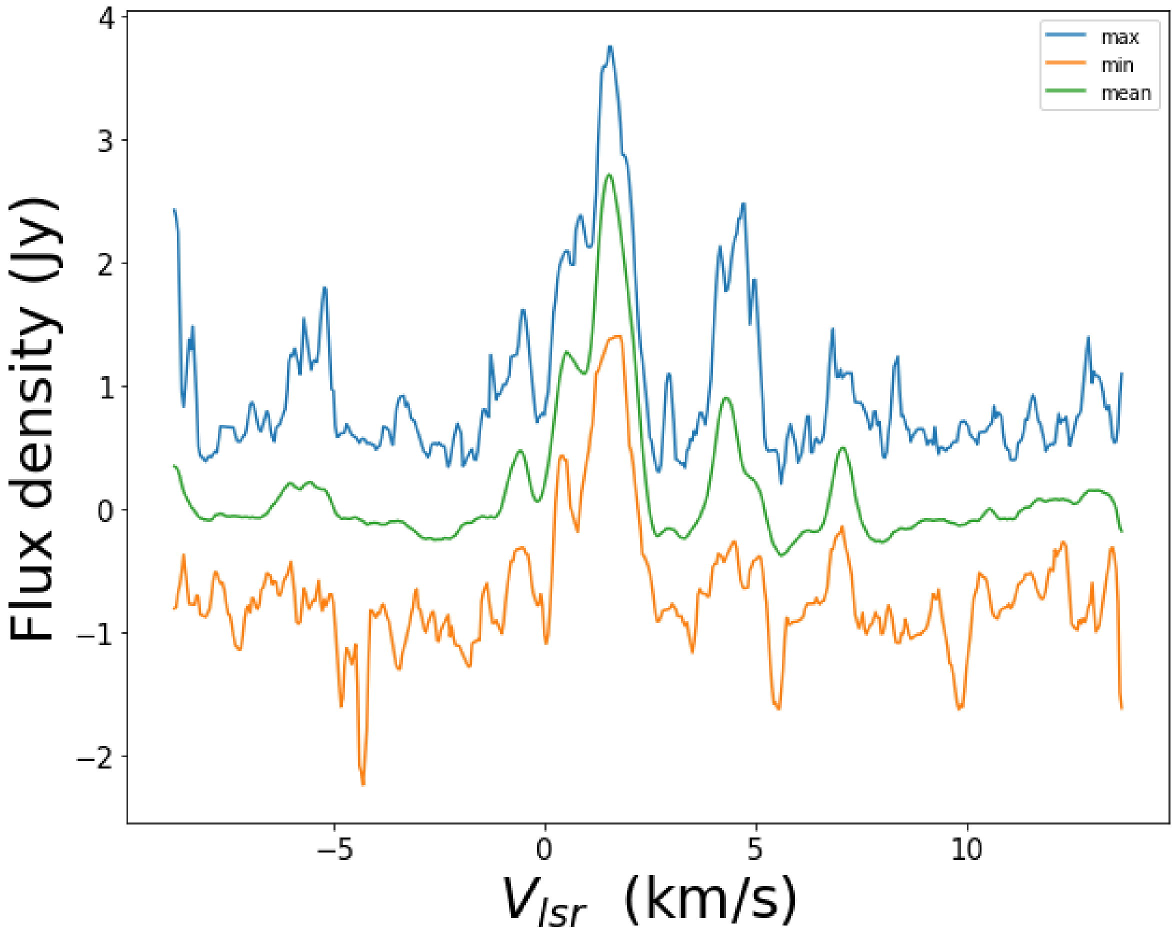

Figure 2.36: Range of variation of flux density in the spectrum of 1667 MHz RCP. The blue line represents the upper envelope, the green line shows the averaged spectrum, and the orange line depicts the lower envelope.

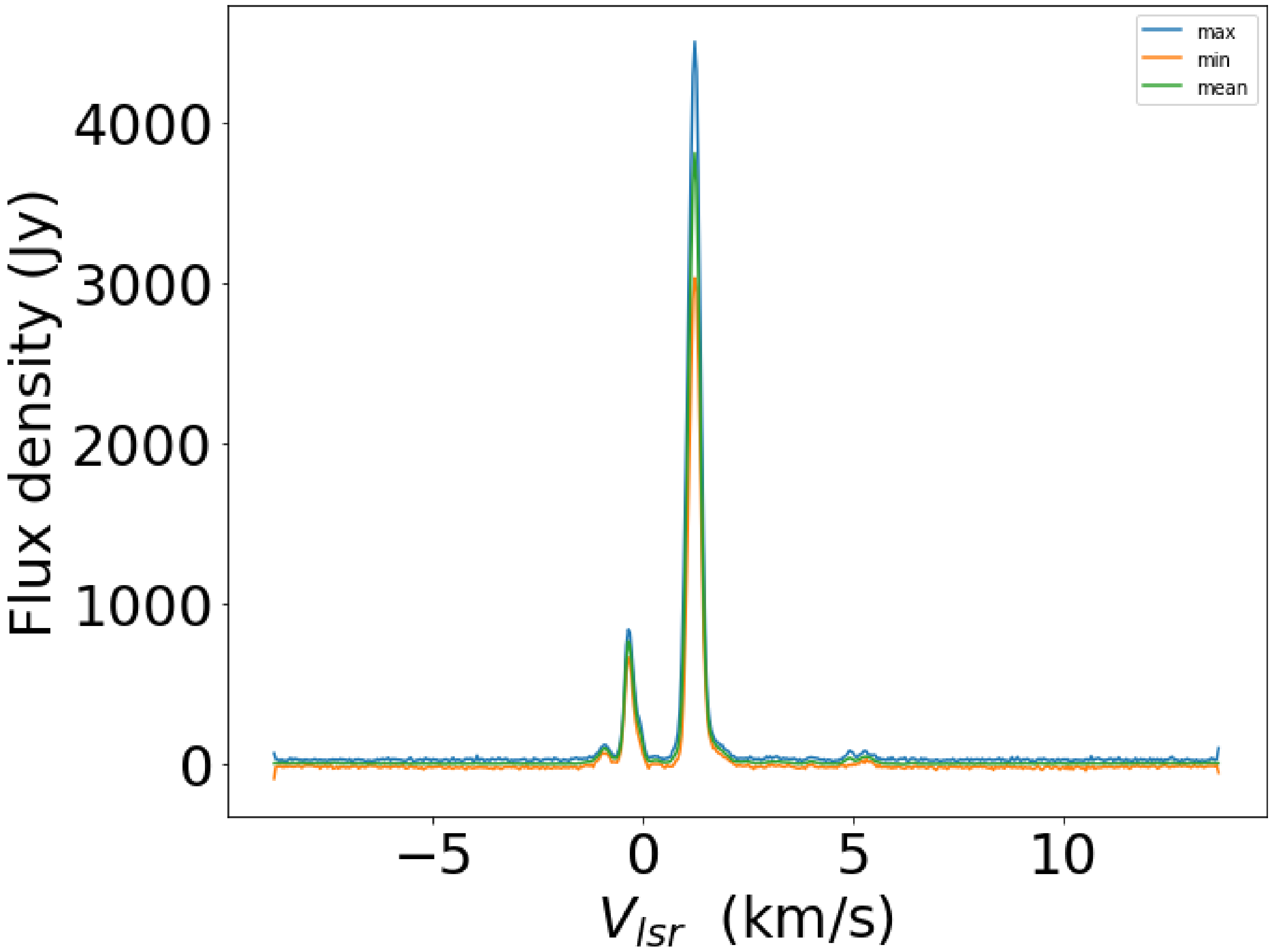

Figure 2.37: Range of variation of flux density in the spectrum of 6668 MHz. The blue line represents the upper envelope, the green line shows the averaged spectrum, and the orange line depicts the lower envelope.

### 2.3.8 Comparison of the range of variation for regular and intensive monitoring windows

During the regular monitoring campaign, the flux density of the 1665 MHz LCP component varied between 8 Jy and 18 Jy as shown in Figure 2.28 whereas the flux density of the 1665 MHz LCP component in the intensive monitoring window varied from 24 Jy to 30 Jy as seen in Figure 2.33. This shows an increase in flux density variation with the change in flux density being almost two fold. The flux densities of the RCP components in the 1665 MHz line in Figure 2.29 and Figure 2.34, however, varied between a maximum of 10 Jy and a minimum of 6 Jy.

For the 1667 MHz spectra similar variation behaviour was recorded as for the 1665 MHz as can be seen in Figure 2.30, Figure 2.35, Figure 2.31 and Figure 2.36. The methanol line from

Figure 2.32 and Figure 2.37 however shows the same flux density variation with a maximum of 8000 Jy but a minimum of 5500 Jy for the regular monitoring window and 3200 Jy for the intensive monitoring window.

### 2.3.9 Time series of some selected channels: regular monitoring

Figure 2.38 to Figure 2.42 present time series for the OH and methanol lines for the regular monitoring window. Five time series corresponding to five velocity channels are plotted for each transition. The first three time series are selected from the most varying velocity channels at peak of the main maser line. Since some OH lines presented double peaked spectra care was taken so as to include only velocity channels from the maximum of the main peak. The remaining two velocity channels were selected from line-free channels. This was done to demonstrate the extent of variation between the emission channels and line-free channels. Here also MJD represent the day of observation using the mean Julian calender. For simplicity the first two digits "24" are dropped.

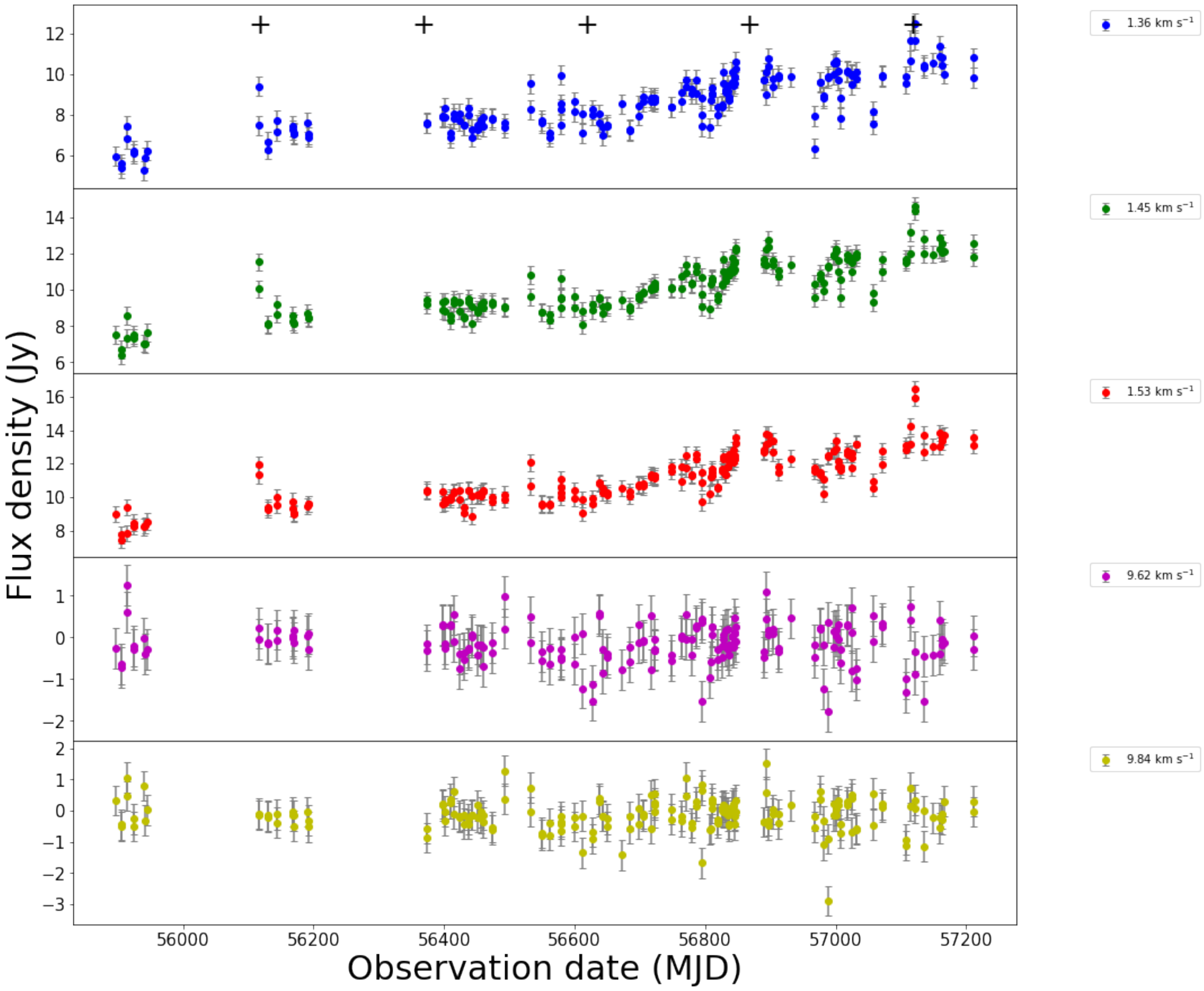

Figure 2.38: Time series for selected velocity channels of the 1665 MHz LCP component in the regular monitoring window. The features in the velocity channels 1.36 km/s, 1.45 km/s and 1.53 km/s follow a monotonic increase in flux density from 6 Jy to 18 Jy whilst the features in the velocity channels 9.62 km/s and 9.84 km/s show no variation. The black + signs plotted on the 1.36 km/s velocity channel show the times the flares are expected.

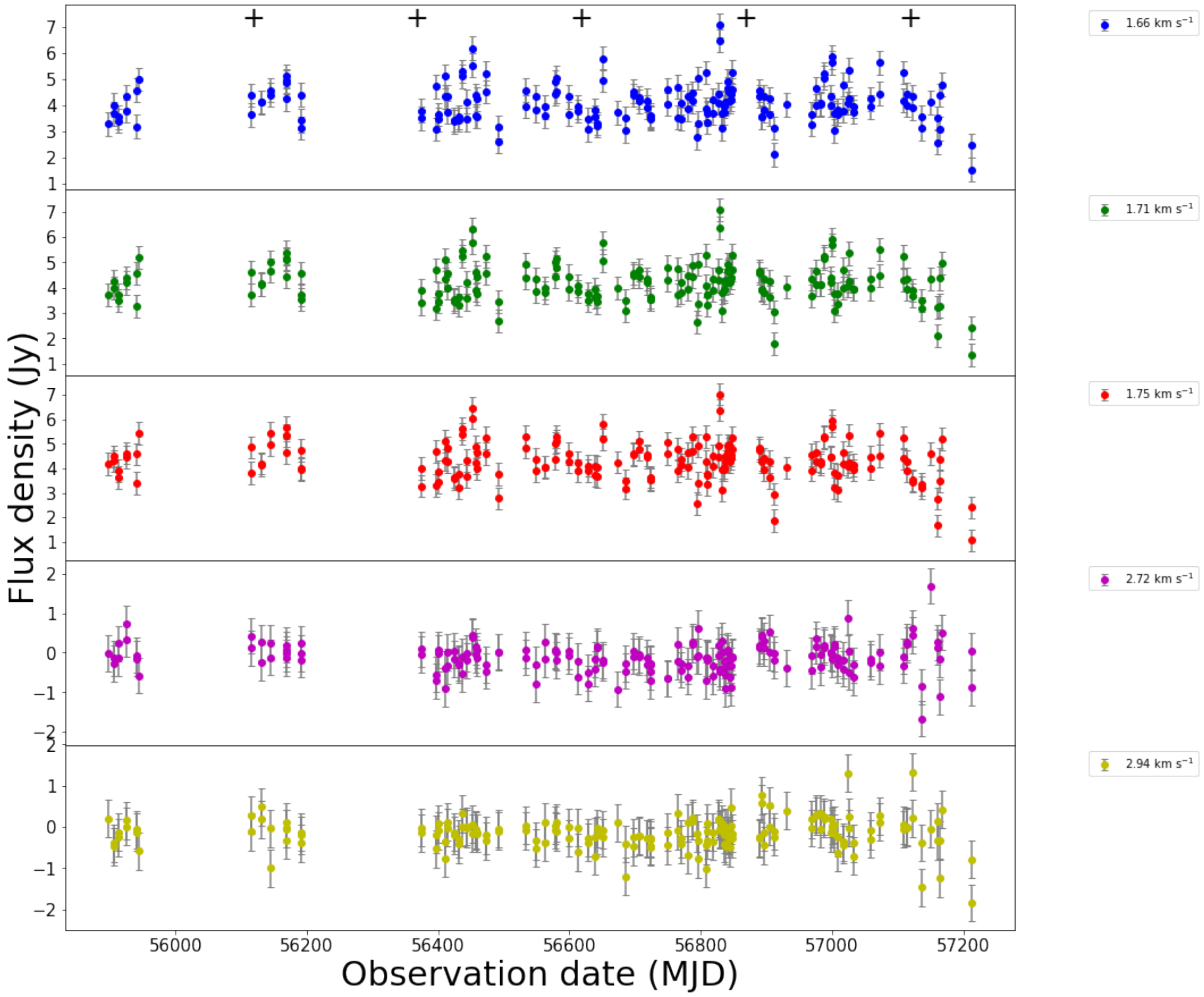

Figure 2.39: Time series for selected velocity channels of the 1665 MHz RCP component in the regular monitoring window. The features in the velocity channels 1.66 km/s, 1.71 km/s, 1.75 km/s, 2.72 km/s and 2.94 km/s only show sporadic variation in flux density from 4 Jy to 7 Jy. The black + signs plotted on the 1.66 km/s velocity channel show the times the flares are expected.

The time series show a variety of behaviour. A feature considered for the test of variation must have a flux density greater than 3 times the noise level. A feature is said to be varying if the change in amplitude above the $3\sigma$ level is recorded. Variations were not recorded in all features but were limited to a handful of features with the strongest variation usually occurring at peaks of the spectra. Variabilities above the noise level were not detected for weaker features with low signal-to-noise ratios. For both transitions of the OH species the behaviour of the time series in some selected channels of the LCP component exhibited both short term and long term variations for the regular monitoring period. In Figure 2.38 and Figure 2.39 which show the behaviour of the time series in some selected channels for the 1665 MHz LCP and

RCP components the LCP component exhibited significant variation in flux density whilst the RCP component exhibited a form of sporadic variation in flux density. The 1665 MHz LCP component showed three flares at 56325 MJD, 56900 MJD and 57100 MJD. The peak of the flare at 57100 MJD in Figure 2.38 is not visible because of flagged data.

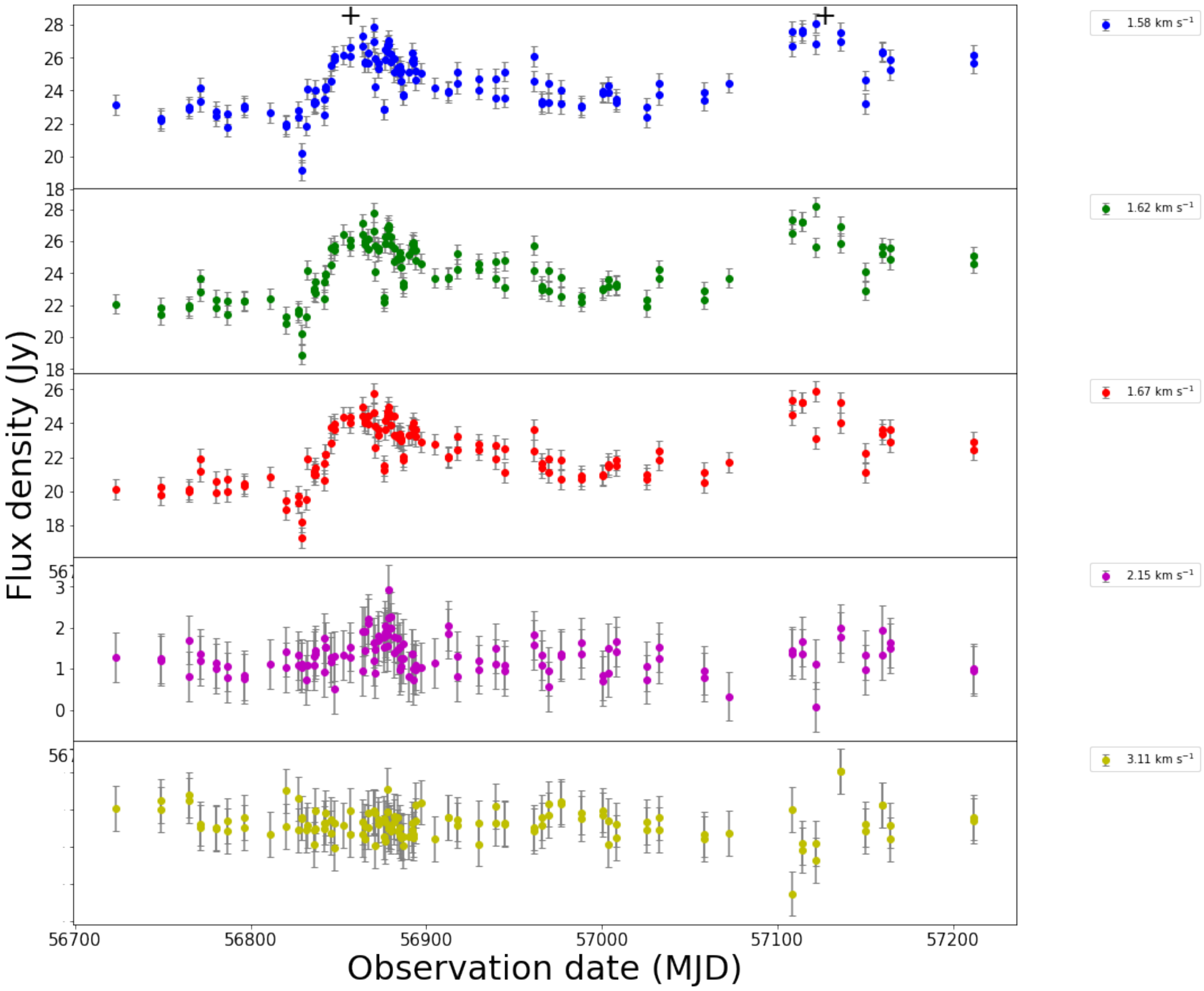

Figure 2.40: Time series for selected velocity channels of the 1667 MHz LCP component in the regular monitoring window. Features in the velocity channels 1.58 km/s, 1.62 km/s and 1.67 km/s vary in flux density from 6 Jy to 24 Jy with two significant flares at 56900 MJD and 57100 MJD marked with + signs on channel 1.58 km/s. The features in the velocity channels 2.15 km/s and 3.11 km/s show no change in flux density except a minor flare at 56900 MJD.

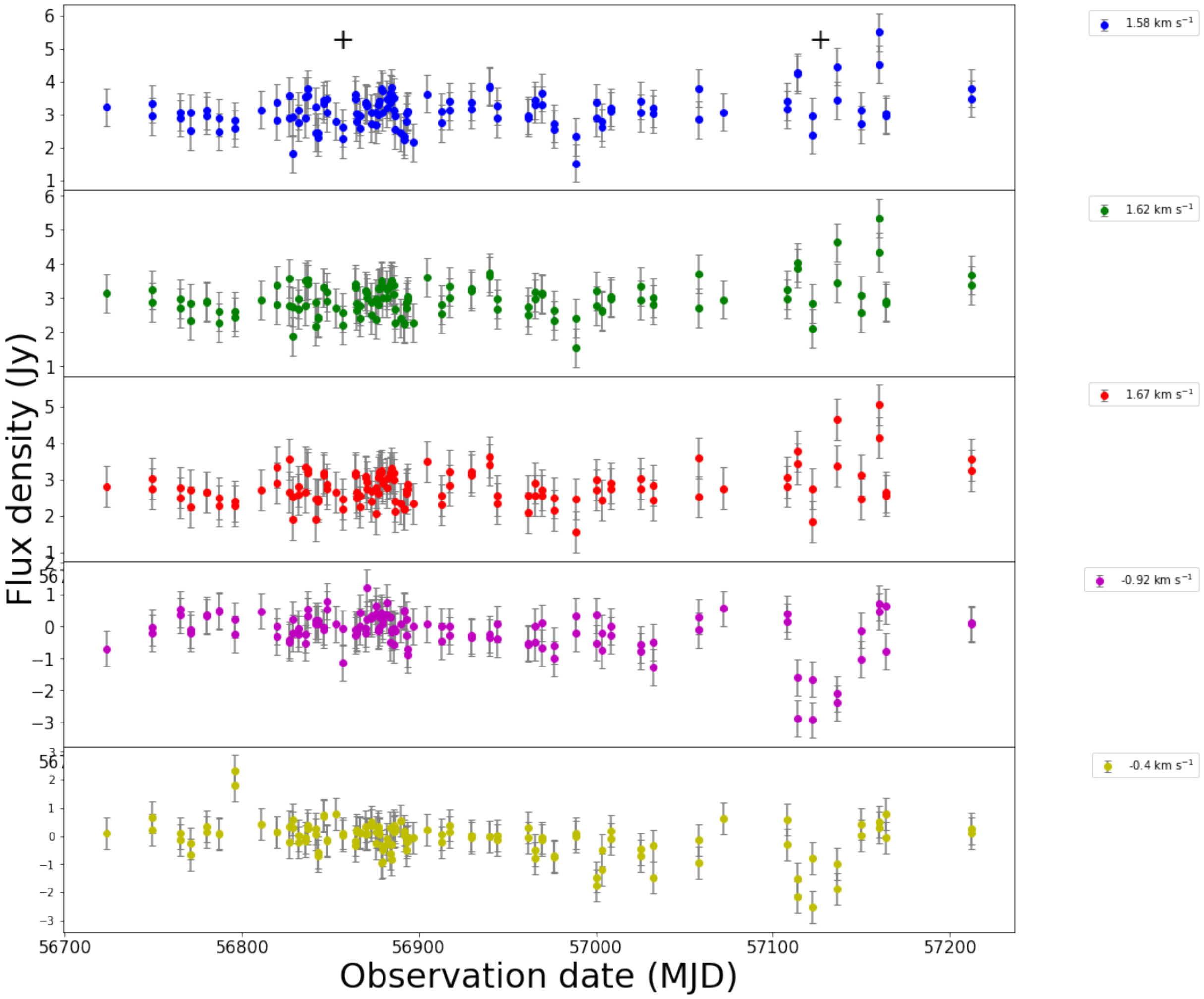

Figure 2.41: Time series for selected velocity channels of the 1667 MHz RCP component in the regular monitoring window. The features in the velocity channels 1.58 km/s, 1.62 km/s, 1.67 km/s, −0.92 km/s and −0.42 km/s show no variation. The two black + signs plotted on the 1.58 km/s velocity channel show the times the flares are expected.

The 1667 MHz transition also showed variation in the behaviour of the time series in both LCP and RCP as shown in Figure 2.40 and Figure 2.41 but the variation in the RCP component was not significant until the end of the monitoring window. There was a general increase in flux density over the monitoring window with flux density increasing from 16 Jy to 28 Jy in the LCP component. Flares were also recorded at 56900 MJD and 57150 MJD. The LCP component shows a dip in flux density just before each flare. Linear variation in flux density barely above the noise over the period was recorded in the RCP component. For the methanol line Figure 2.42 shows fifteen recurring flares with a periodicity of 246 days (Goedhart et al., 2004) in the selected varying channels. The longer time range for the methanol data is because the data dates back from an earlier ongoing campaign. There was also a general increase in the flux density. The variability in the velocity channel 1.2 km/s has been reported to be as intense as 10% but stable for all other features (Caswell, Vaile and Ellingsen, 1995).

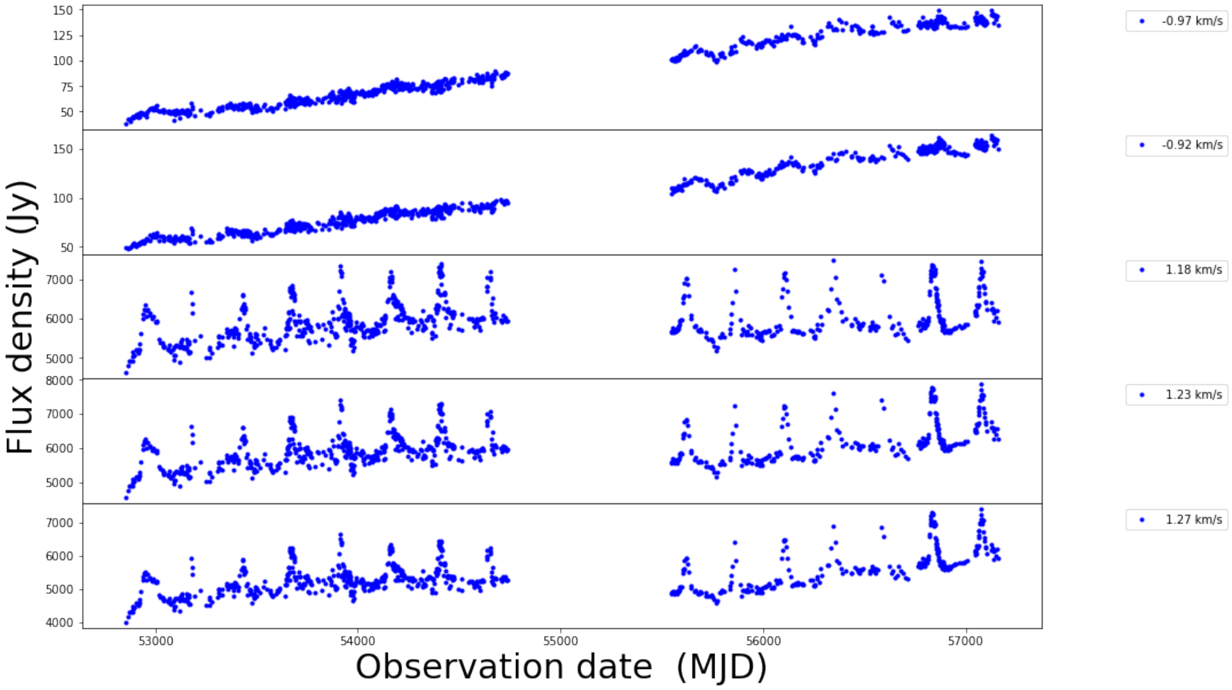

Figure 2.42: Time series for selected velocity channels of the 6668 MHz methanol maser transition in the regular monitoring window. The features at 1.18 km/s, 1.23 km/s and 1.27 km/s show 15 periodic flares. Part of the data from 54900 MJD to 55600 MJD has been flagged because of bad data. However the features in channel −0.97 km/s and channel −0.92 km/s show a monotonic increase in flux from 50 Jy to 150 Jy.

### 2.3.10 Times series of some selected channels: intensive monitoring

The time series for the intensive monitoring window are presented in Figure 2.43 through Figure 2.47. The intensive monitoring window showed similar behaviour in variability for both transitions of OH.

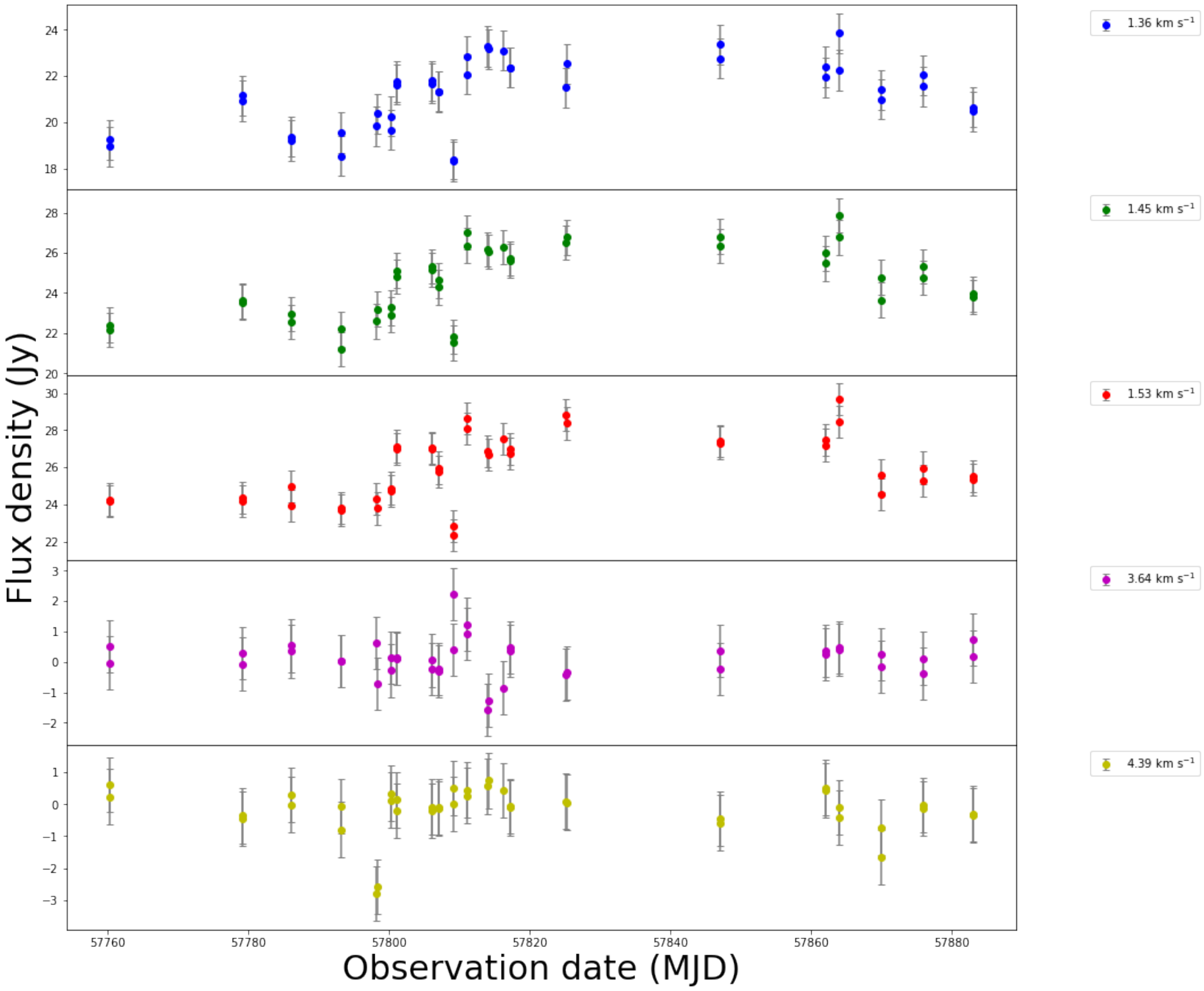

Figure 2.43: Time series for selected velocity channels of the 1665 MHz LCP component in the intensive monitoring window. Features at 1.36 km/s, 1.45 km/s and 1.53 km/s show a significant flare with a peak moderately variable in flux density from 18 Jy to 28 Jy. The features in channels 3.64 km/s and 4.39 km/s show no variation. Some data from 57820 MJD to 57890 MJD have been flagged because of RFI.

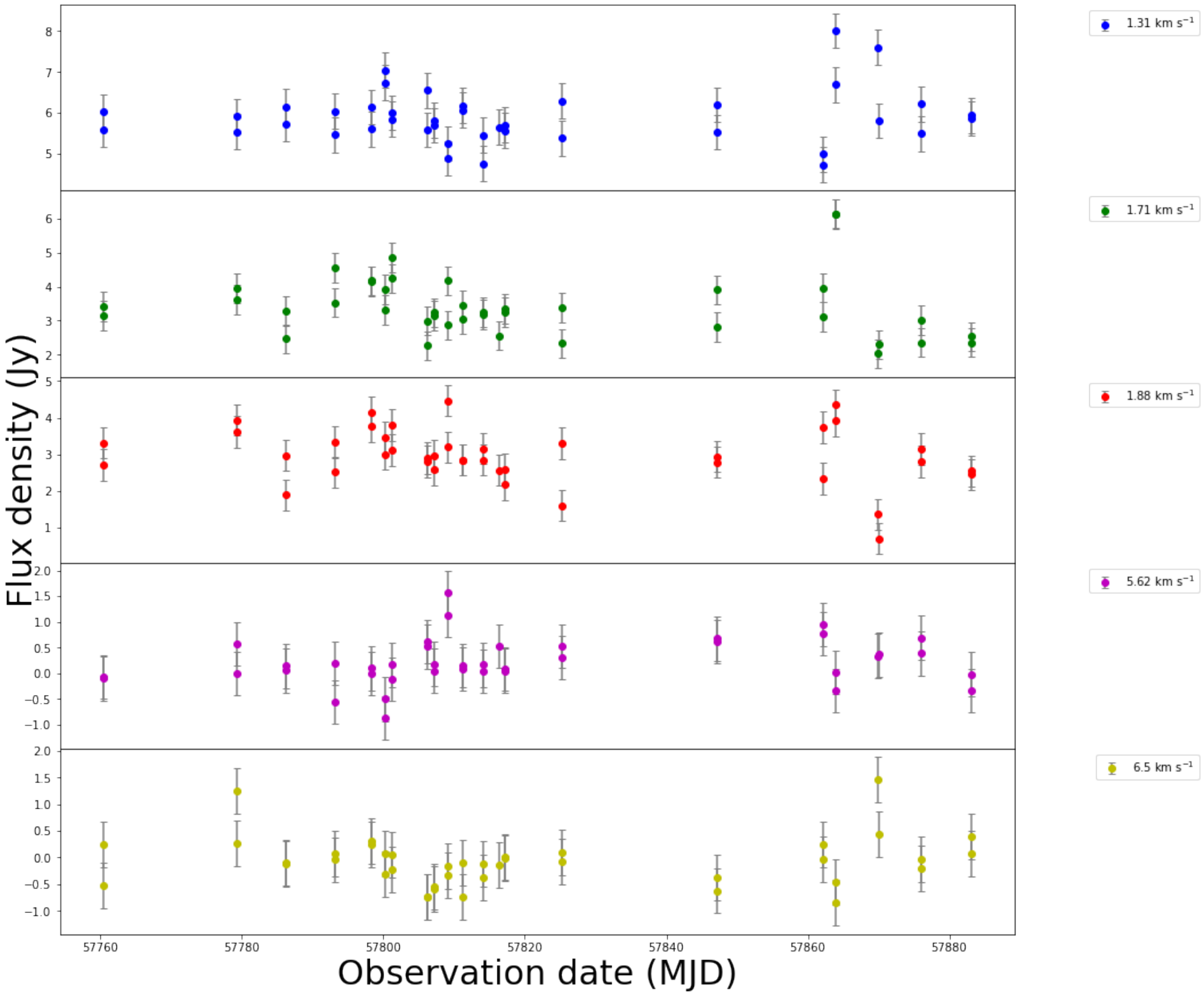

Figure 2.44: Time series for selected velocity channels of the 1665 MHz RCP component in the intensive monitoring window. The features in channels 1.31 km/s, 1.71 km/s, 1.88 km/s and 1.93 km/s show no variation in flux density. The data from 57820 MJD to 57890 MJD have been flagged because of RFI.

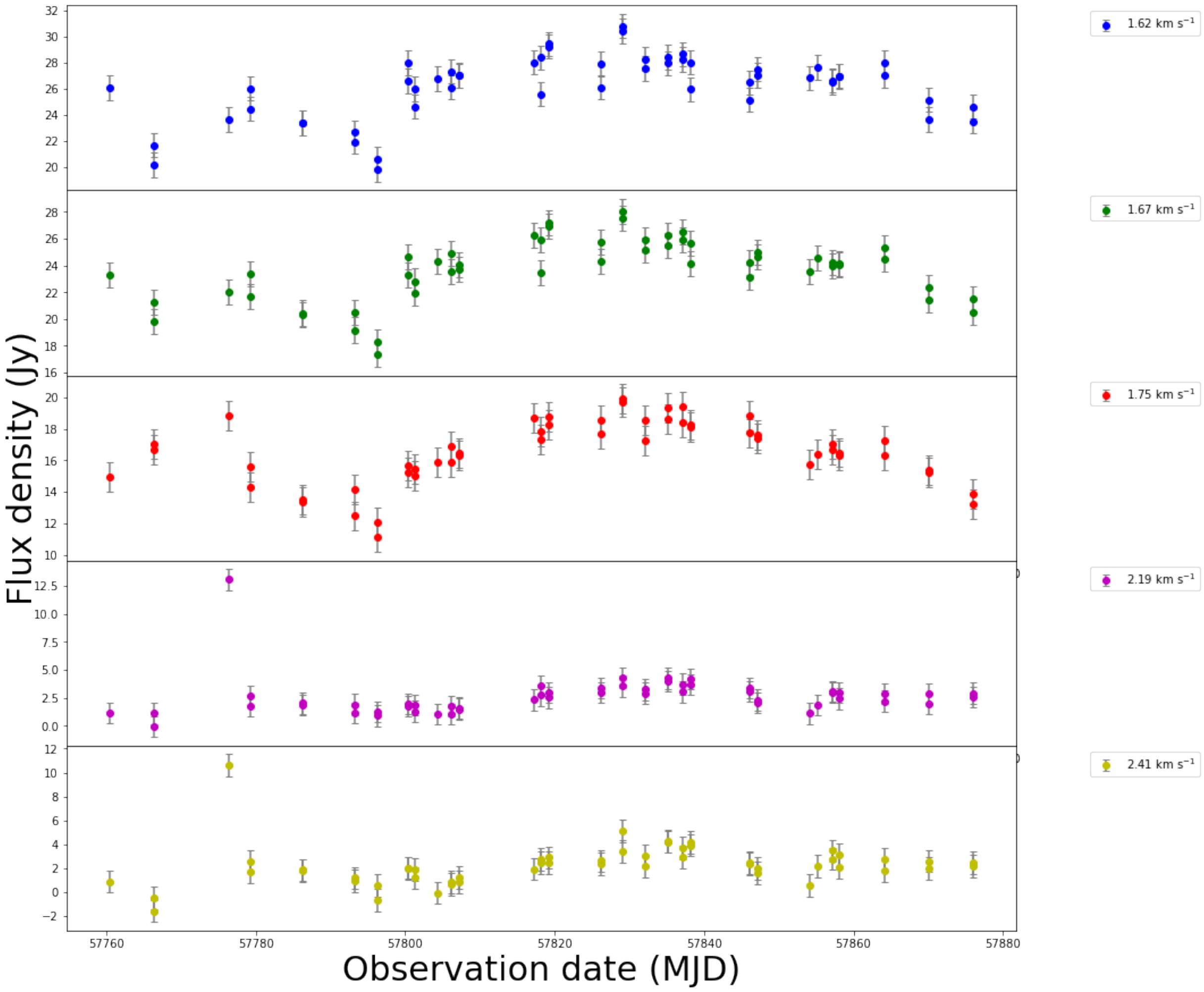

Figure 2.45: Time series for selected velocity channels of the 1667 MHz LCP component in the intensive monitoring window. The features at 1.62 km/s, 1.67 km/s and 1.75 km/s show significant variation of the peak from 10 Jy to 30 Jy whilst the features at 2.19 km/s and 2.41 km/s show no variation.

From Figure 2.43 and Figure 2.45 the time series for the 1665 MHz and 1667 MHz lines show short term variation of flux density for the LCP components. Variations within the noise levels of the RCP components of both transitions are shown in Figure 2.44 and 2.46. For both spectra of the 1665 MHz line the data between 57820 MJD and 57890 MJD have been flagged because of RFI. The methanol line is also shown in 2.47 with a flare between 57780 MJD and 57860 MJD.

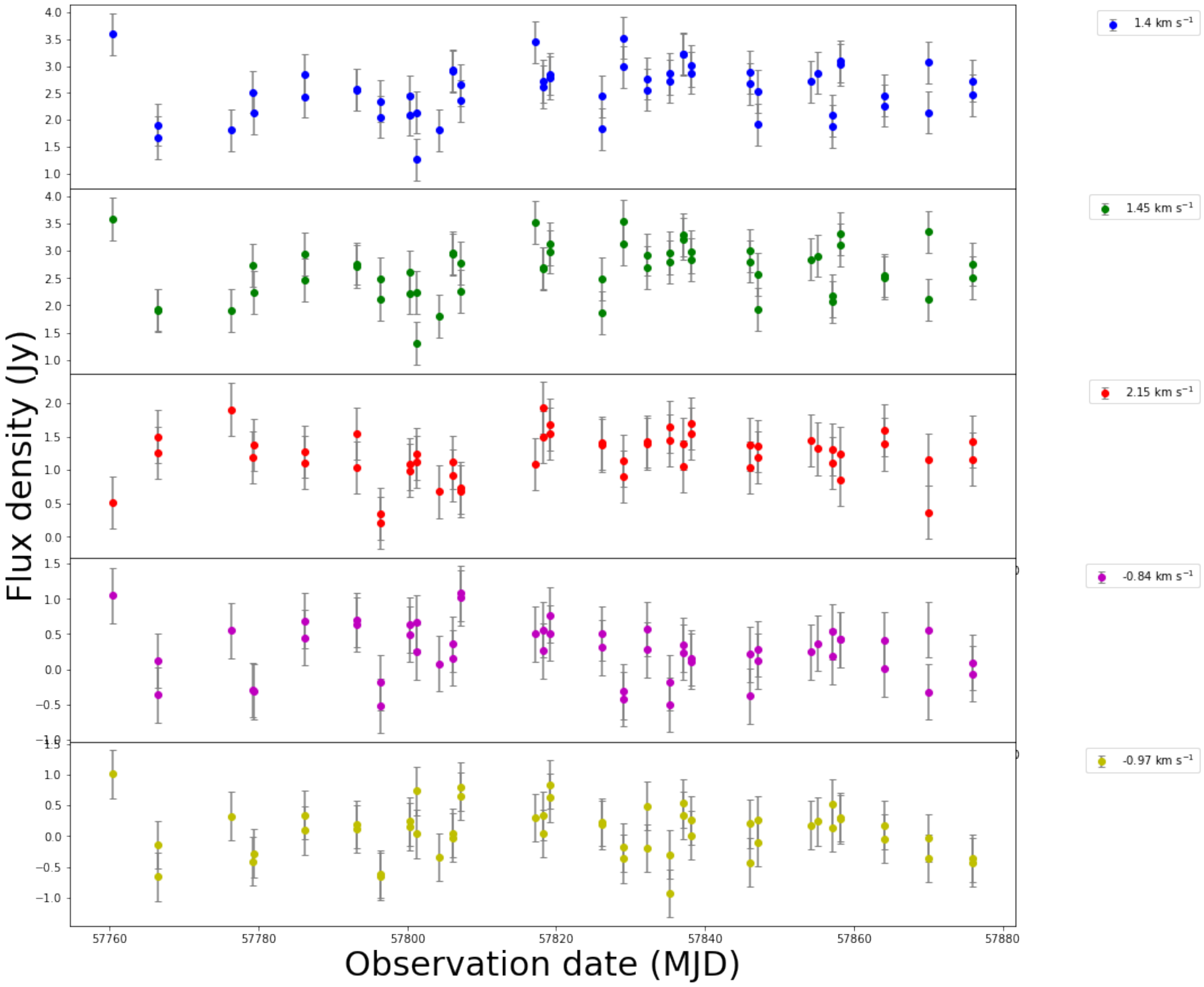

Figure 2.46: Time series for selected velocity channels of the 1667 MHz RCP component in the intensive monitoring window. The features in channels 1.4 km/s, 1.45 km/s, 2.15 km/s are only slightly variable with a slow change in amplitude whilst the features in −0.84 km/s and −0.97 km/s are weak and show no variation.

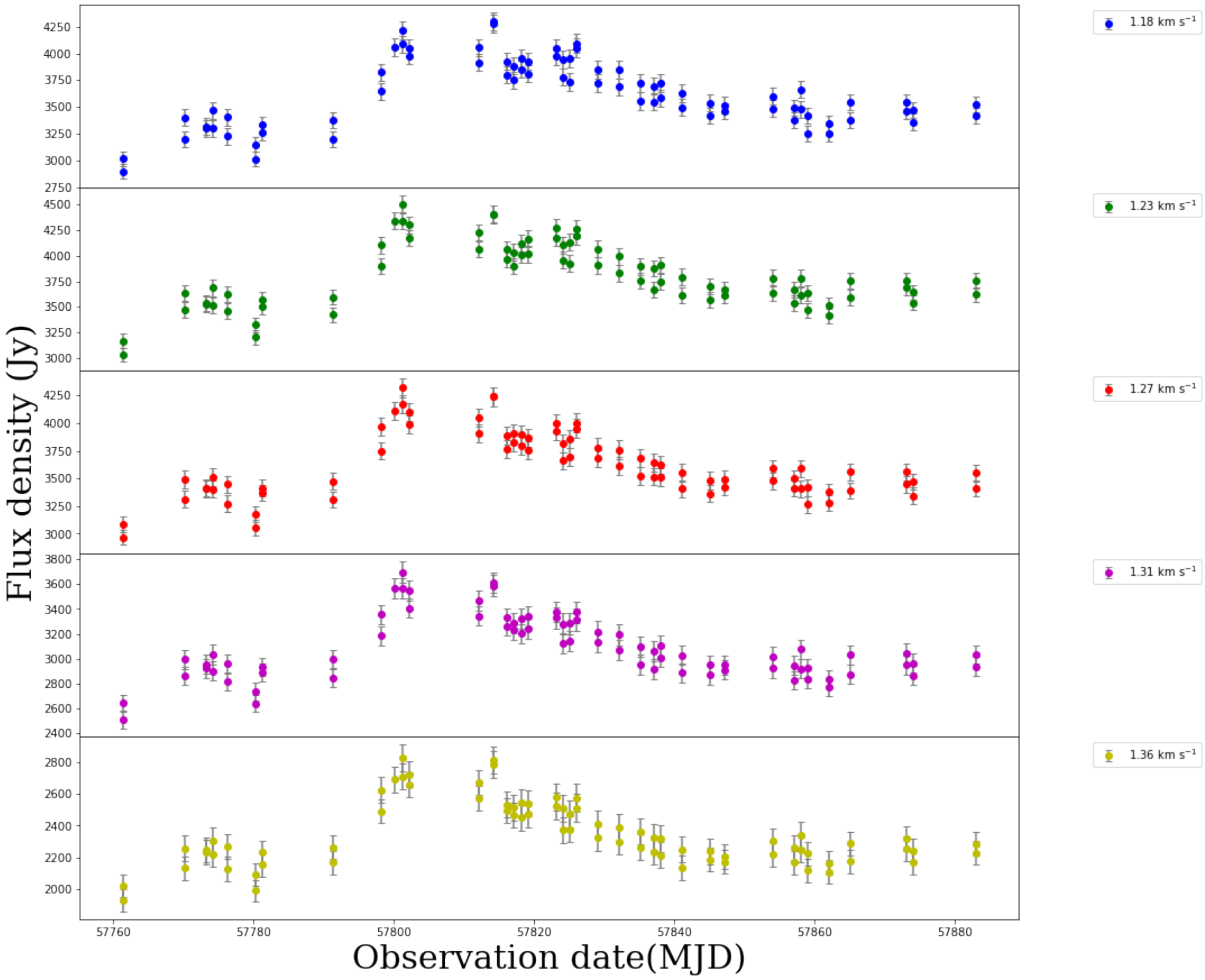

Figure 2.47: Time series for selected velocity channels of the 6668 MHz methanol maser transition in the intensive monitoring window. The features in the velocity channels 1.18 km/s, 1.23 km/s, 1.27 km/s, 1.31 km/s and 1.36 km/s show variability with a flare between 57780 MJD and 57860 MJD.

In comparison with the time series for the regular monitoring window, the intensive monitoring window shows an increase in the flux density of the LCP component for 1665 MHz whereas the flux density for the LCP component for 1667 MHz remained the same. The flux density decreased for the RCP components in both transitions of the maser species.

### 2.3.11 Regular monitoring of some selected channels in all transitions

Figure 2.48 shows the time series of the most varying features of the LCP and RCP components of the OH as well as the methanol lines. Five adjacent most varying features at the peak of each main line are averaged and plotted for each transition. This was done after inspecting the spectrum so as not to combine peaks from other spots or double peaked spectra. The plots are restricted to the period common to all species; that is, between 56700 MJD and 57200 MJD. In the plot for the regular monitoring window, the 1665 MHz LCP component shows variations with a noticeable flare from 56800 MJD to 57080 MJD but the data at peak of the flare have been flagged because of RFI. The 1665 MHz RCP component, however, shows no variation in flux density. The 1667 MHz LCP component shows significant variability with two flares, the first rising steeply from 56850 MJD and falling off gradually at 56900 MJD and the second rising at 57080 MJD and falling off at 57200 MJD. The 1667 MHz RCP component shows no variation in flux density.

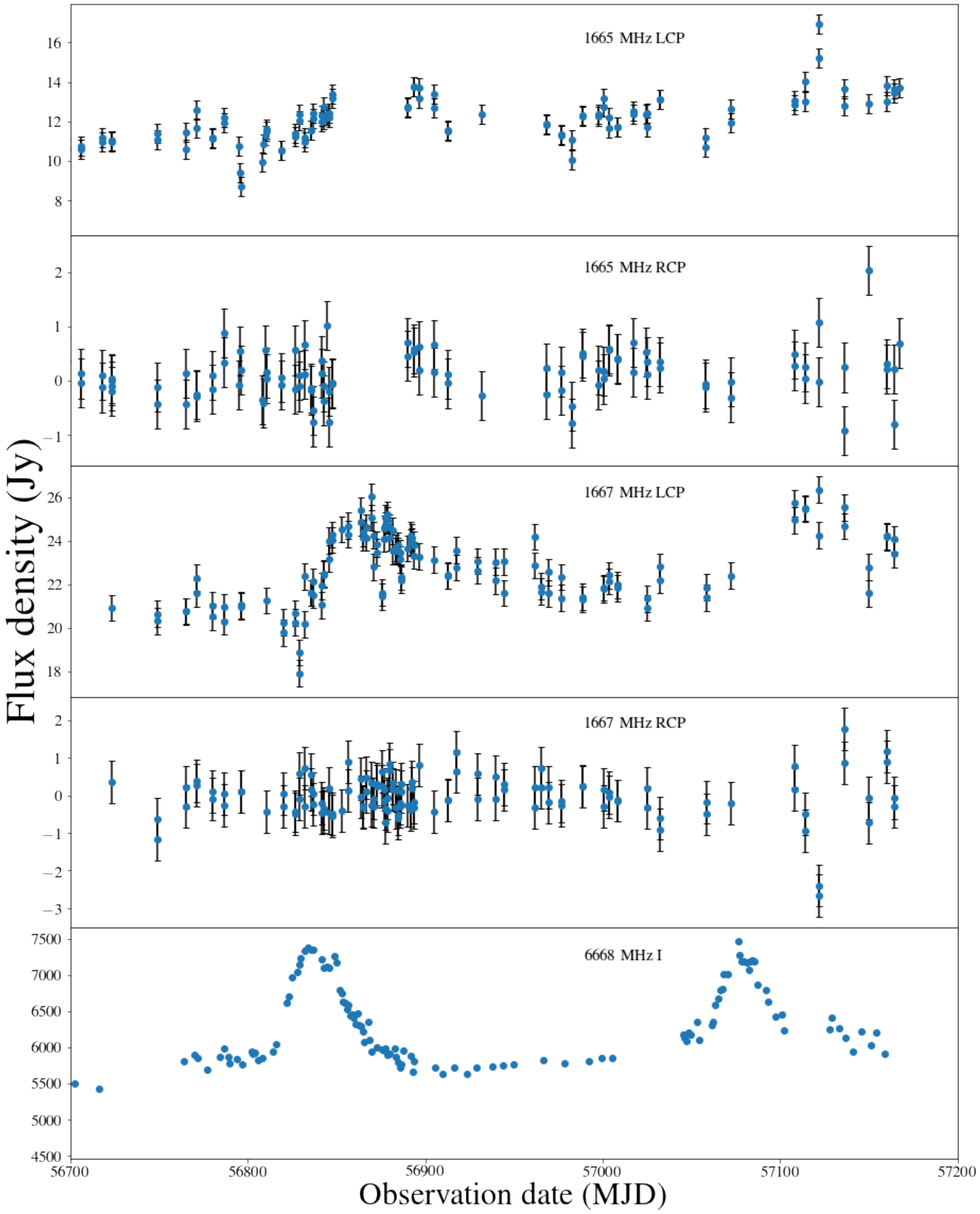

Figure 2.48: Some selected channels of the 1665 MHz and 1667 MHz hydroxyl maser lines in both polarizations together with the 6668 MHz methanol maser line during the regular monitoring window.

The 6668 MHz transition shows significant variation with two flares, one at 56850 MJD and the other at 57080 MJD separated by 246 days as calculated by Goedhart et al. (2004) and confirmed by van der Walt et al. (2009); van der Walt (2011*b*). Visual examination of the data of the flare activities in Figure 2.48 indicates that for both OH transitions the flare occurs for a duration of 120 days with the same separation as that of the methanol line. However the OH starts to rise steeply 20 days after the methanol has risen and starts to decay gradually 30 days after the methanol has decayed and settled into the quiet phase.

### 2.3.12 Intensive monitoring of some selected channels in all transitions

In the plot for the intensive monitoring window displayed in Figure 2.49 the 1665 MHz LCP component exhibits variations with a flare rising at 57790 MJD and decaying at 57880 MJD. The 1665 MHz RCP component does not show any form of variability. In the 1667 MHz LCP component, a flare rising slowly at 57790 MJD and subsequently decaying at 57880 MJD is noted. The 1667 MHz RCP component however shows no significant variability in flux density. The 6668 MHz line shows a significant variability with a steep rise at 57780 MJD followed by a slow decay which eventually plateaus at 57880 MJD with flux density 2500 Jy as before the rise.

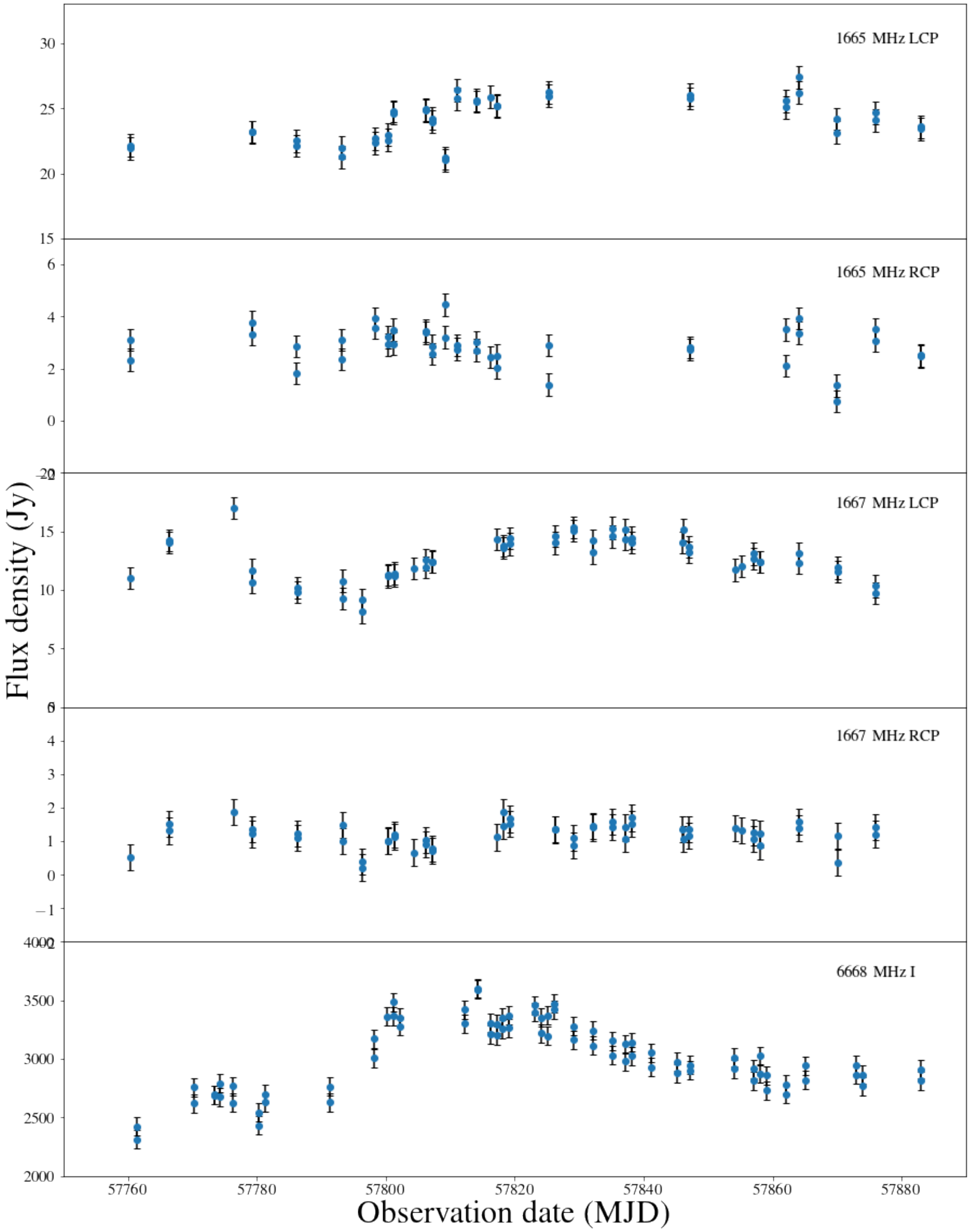

Figure 2.49: Some selected channels of the 1665 MHz and 1667 MHz hydroxyl lines in both polarizations and the 6668 MHz methanol line during the intensive monitoring window.

## 2.4 Discussion

The monitoring campaign has revealed the variation of the LCP and RCP components of the mainline OH maser transitions associated with the 6.7 GHz methanol line in G9.62 + 0.20E. A velocity range of 30 km/s was used to show all detected components in the averaged spectra of each polarization. For both maser species the main maser lines were spread from 0 km/s to 3 km/s and no velocity shifts were recorded for both the mainline and the different features in the spectrum. The results of the maser velocities presented in the foregoing sections are consistent with OH systemic velocity reported in Hofner et al. (1996). The similarity in the velocity spread of the main lines suggests that though both OH and methanol maser molecules have different systemic velocities they may emanate from the same cloud position (Bachiller and Perez- Gutierrez, 1997).

The flaring behaviour of the time series was in different forms for both methanol and OH. The LCP components of the 1665 MHz and 1667 MHz OH masers showed the same flare pattern. They both showed flares which were preceded by dips in flux densities. This pattern is consistent with those reported by Goedhart et al. (2019). The RCP component in both transitions showed sporadic variation which was only within the noise.

The similarity in the individual flare profiles of the 1665 MHz and 1667 MHz LCP components suggests that the characteristics of the mechanism underlying the flaring affects both OH masers in the same way. Both show a dip in flux density before a steep rise and gentle decay followed by a quiet phase after which they dip and slowly increase to the next flare. However in comparison with methanol whose flares are as well consistent with those reported by Goedhart et al. (2004), there is a time delay in the onset of the flare of the hydroxyl masers of about 30 days, suggesting a correlated variation between the OH and methanol masers. Following the discussion in Goedhart et al. (2019) the time lags are likely due in part to the difference in the distances between the methanol and the OH masers from the HII region associated with them. This is evidenced by the distribution of the OH and methanol masers relative to the HII region in Figure 1 of Sanna et al. (2015), from which it is clear that the OH masers are excited further from the HII region than the methanol masers. Both methanol and OH masers flare within the same time window separated by a quiescent level which remains unchanged between flares indicating that the source of the flare is intrinsic to the masers themselves.

The profile of the methanol line has a steep decay profile compared to the OH line. The slower decay of the OH masers has been discussed by Goedhart et al. (2019) within the colliding wind binary model to be due to a lower electron density for the background part of the HII region associated with it. This is consistent with the OH masers being further out in the HII region that has a decreasing radial density distribution as is needed for the radio SED as is discussed in the next chapter. Observing the separate polarizations of the 1.6 GHz OH mainline masers also confirmed the observed behaviour seen in Goedhart et al. (2019) total intensity monitoring. From the results it was found that the peak flux of the main feature in the LCP components of the OH masers and the total intensity of the methanol masers show variations. There was a correlation between the LCP's of both OH transitions and the methanol masers regarding the period of the flare. Time delays between the two species were recorded as the epochs were taken simultaneously. The OH masers arises almost a month after the methanol has risen. Also the nature of the variability profiles were different for both transitions. OH masers exhibited a steep rise and slow fall whereas the methanol exhibited a steep rise as well as fast fall. The nature of the variability has been explained within the context of the colliding wind binary model. The steep rise of the maser depicting the pulse created by the ionising radiation and the gentle decay profile being the recombination of the hydrogen plasma as it goes into its equilibrium state. With the explanation of the decay profiles for both transitions it can be assumed the source of the flaring is within the vicinity of the masers.

# CHAPTER 3

# HIGH RESOLUTION STUDIES OF THE 1.6 GHz HYDROXYL MASER SPOTS AND THE L-BAND RADIO CONTINUUM IN $G9.62+0.20E$

The HII region associated with the 1.6 GHz OH maser lines in $G9.62+0.20E$ has been observed at L-band but not at high resolution. Because of this, the variable and non-variable 1.6 GHz maser spots presented in the previous chapter have been plotted on a 43 GHz continuum to locate their positions (Sanna et al., 2015; Goedhart et al., 2019). This continuum, measured at a frequency of 43 GHz, is not the actual radio emission associated with the OH masers at 1.6 GHz. Knowledge on the position, size and flux density of the HII region will help locate the positions of the variable and non-variable masers relative to it.

High resolution observations of the variable and the non-variable OH maser spots in the 1665 MHz and 1667 MHz left and right circular polarization as well as the L-band continuum associated with them were made with e-MERLIN. This is to accurately determine the position of the maser spots relative to the L-band continuum which will aid in the explanation of the source of variability for the masers.

In this chapter a brief description of radio interferometry is given and the observation, data reduction and results for the L-band continuum and its associated 1.6 GHz OH masers in $G9.62+0.20E$ are presented. Section 3.1 gives information on the e-MERLIN interferometric array followed by Section 3.2 which gives a brief introduction to interferometry. The details of the observation of the data are given in Section 3.3. In Section 3.4 the interferometric data reduction techniques employed in the calibration process are described. Section 3.5 gives the results for the reduction and Section 3.6 discusses the results for the observation.

## 3.1 The e-MERLIN interferometric array

The observations for the 1.6 GHz OH spectral line (narrow band) and continuum (wide band) data in G9.62 + 0.20E were made with the e-MERLIN interferometric array, a United Kingdom national facility operated by the University of Manchester at Jodrell Bank Observatory (JBO) on behalf of the Particle Physics Astronomy Research Council (PPARC). The e-MERLIN array, shown in Figure 3.1, is a radio interferometer whose correlator is based at the Jodrell Bank Observatory. The array consists of two local stations (Lovell and Mark II) and five remotely linked dishes (Cambridge, Defford, Knockin, Darnhall and Pickmere) spread across the United Kingdom (Belles et al., 2015). Five of the radio antennae have an identical diameter of 25 m and the remaining two, Lovell and Cambridge, have diameters of 76 m and 32 m respectively. Shown in Figure 3.1 are the locations of the 7 antennas in an array configuration which yields 21 baselines ranging from 11 km to 217 km. Cambridge and Knockin, separated by a distance of 217 km provide the longest baseline at all bands and determine the array's maximum resolution. The shortest baseline is provided either by Mark II or Lovell (since they share the same

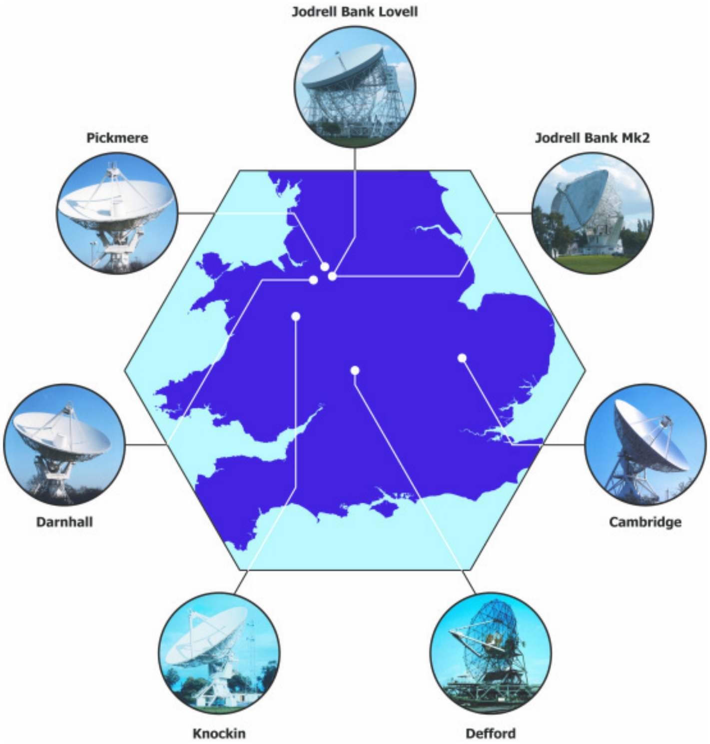

Figure 3.1: The e-MERLIN interferometric array with seven antennas distributed across the UK, with baselines spanning 11 km to 217 km. Displayed here are the seven antennas, namely; Lovell, Mark 2, Cambridge, Defford, Knockin, Darnhall and Pickmere (Belles et al., 2015).

compound at JBO) and Pickmere located about 11.2 km from JBO. The array's configuration gives it an angular resolution comparable to the Hubble Space Telescope, making it capable of carrying out centimetre-wavelength radio astronomy with micro-jansky sensitivities. Its flexible wide-band correlator enables it to observe in three modes with three observing bands, namely, L-band (1.23 GHz-1.74 GHz), C-band (4.3 GHz-7.5 GHz), and K-band (19 GHz–25 GHz). At L-band an angular resolution of 160 mas is achievable whereas at C-band an angular resolution of 50 mas can be achieved.

## 3.2 Interferometry

The interferometer makes measurements (observations) in the spatial frequency domain, sampling the $u$-$v$ coordinates in the plane perpendicular to the axis of an antenna. For a basic two-telescope interferometer with antennas separated by a distance of $b_\lambda$ as shown in Figure 3.2, the incoming waves are converted into electric signals (voltages) and sent to a correlator which multiplies and averages the signals to give the complex visibility $V$, defined by

$$V(u,v) = \int I(l,m)\, e^{-2\pi i(ul+vm)}\, dl\, dm \tag{3.1}$$

The complex visibility $V(u,v) = Ae^{i\phi}$ describes the amplitude $A$ and phase $\phi$ of the signal at a point in the $u$-$v$ plane and thus contains wavelength information in addition to atmospheric and instrumental terms. The signals add up to make an image of the sky, where $u$ and $v$ are defined as the east-west and north-south positions with respect to the $w$ axis parallel to $\mathbf{S_0}$ as shown in Figure 3.3, and $l$ and $m$ are the direction cosines of $\mathbf{S}$. The complex visibility therefore is the Fourier transform of the brightness distribution $I$ of the source from which the image of the sky is obtained, each measurement of $V(u,v)$ giving a single Fourier component of $I$ (Thompson et al., 2001). Hence, the intensity distribution can be recovered from the inverse Fourier transform of the visibilities as

$$I(l,m) = \int V(u,v)\, e^{2\pi i(ul+vm)}\, du\, dv \tag{3.2}$$

where $2\pi(ul + vm)$ is an approximate conversion required to change the observed phase $\phi =$

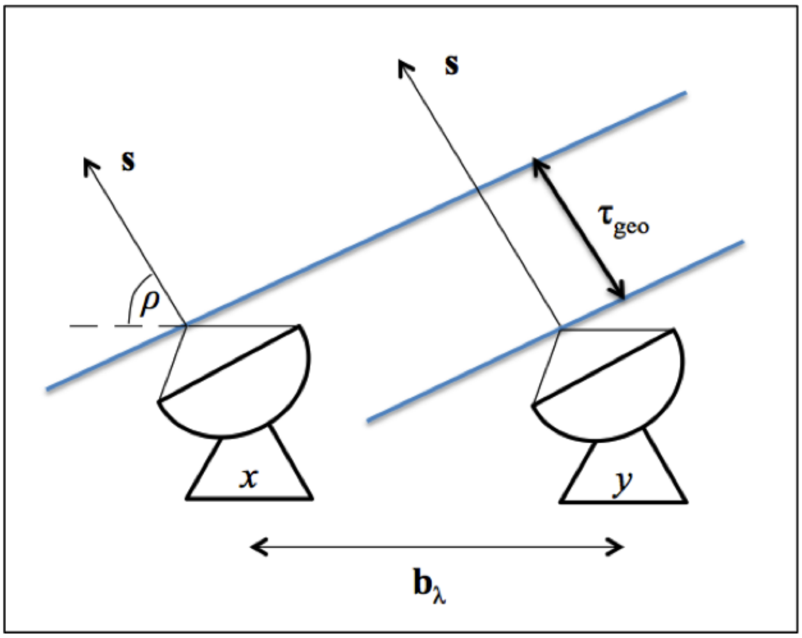

Figure 3.2: Basic telescope arrangement in an interferometer. Adopted from Burke and Graham-Smith (2002).

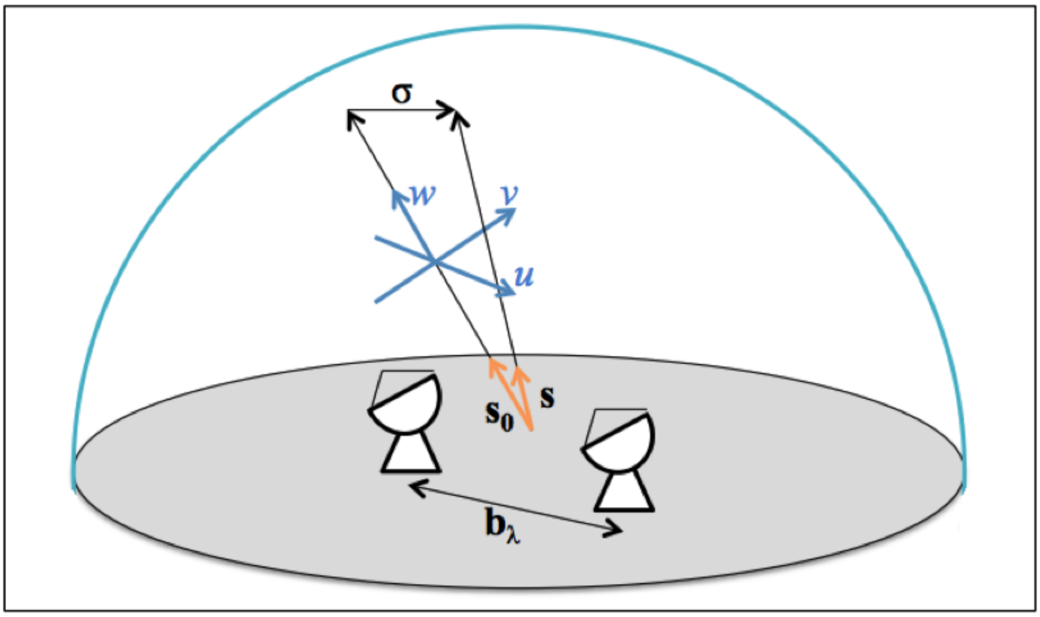

Figure 3.3: Interferometery coordinates based on Burke and Graham-Smith (2002).

$\phi(u,v)$ of $V$ to the value that would be measured with antennas in the $uv$ plane. The $(l,m)$ coordinates are the right ascension and declination, the actual celestial coordinates (position on the sky) of the brightness $I$ of the source that is used to determine the flux density.

### 3.2.1 Aperture synthesis and imaging

Aperture synthesis is employed to produce the imaging properties of an aperture by autocorrelating the radiation field at individual positions within the aperture. This technique uses a number of baselines from a configuration of telescopes to give multiple measurements of $V(u,v)$ for a given integration time. An array of $n$ telescopes generate $n(n-1)/2$ visibilities for an individual integration. Thus for e-MERLIN operating without Lovell 15 baselines are available and the same number of visibilities are generated for each integration. For $n$ telescopes the earth's rotation increases the number of projected baselines in the configuration with the effect of filling the $uv$ plane. The use of wider bandwidths also helps to fill the gaps in the $uv$ plane. The geometry of the telescopes in an interferometer in relation to the direction of the source determines the instantaneous $uv$ coverage of an interferometer. It is therefore the $uv$ coverage that determines in spatial frequency the scales of structure that can be measured by the interferometer (Marr et al., 2016).

### 3.2.2 Calibration

To determine the brightness distribution of the source function, the visibility given by the Fourier transform of the sky brightness is decomposed into components to find all the amplitudes and phases of the source. The correlator output is used for this purpose. The correlator output $V_{xy}^{\text{observed}}$ however differs from the output $V_{xy}^{\text{true}}$ from an ideal interferometer by a factor because of instrumental effects and propagation effects in the atmosphere and the ionosphere. The goal of calibration is to correct the amplitudes and phases for these atmospheric and instrumental effects. The relationship between the observed visibilities and the true visibilities on the baseline between the two telescopes $x$ and $y$ is expressed as

$$V_{xy}^{\text{observed}} = J_{xy} V_{xy}^{\text{true}} \tag{3.3}$$

where $J_{xy}$ represents all the errors affecting the the visibility measurement on the baseline $xy$. Calibration consists of deriving the set of time and frequency dependent values of $J_{xy}$ in order to determine the best approximation of $V^{\text{true}}$ from $V^{\text{observed}}$. This is done by using observations of strong calibrator sources to determine the bandpass response of the phases and amplitudes. Most of these calibrators are variable on time scales of weeks and months and their flux densities are not known accurately. However, some celestial objects are well characterised and are easily modelled and their models may be used as primary calibrators. Corrections that make an observation fit the calibrator models are determined by deriving changes in amplitude and phase with respect to frequency and time. Thus the observation of the calibrators and their models are used to derive the fluxes of the bandpass calibrator, flux density calibrator and gain calibrator.

To set the flux density correctly a calibrator (flux density calibrator) with known spectral shape and flux density is used. Gains (amplitude and phase) for the flux density calibrator and the model are used to converts the counts to flux density in janskys. The calibrated gains of the flux calibrator are compared with the gains of the other calibrators to estimate their flux densities. After the flux scaling the bandpass calibration which solves the amplitude and phase variations with respect to frequency follows. This is done by calculating the channel-to-channel variations of the observed bandpass. A smooth function which matches the model to the data is used to remove the outliers. To solve for the gain (amplitude and phase) variations with time the integration-to-integration variations are determined and a smooth function is used to remove the outliers. The solutions from the calibrations are then applied to the phase calibrator and subsequently transferred onto the target by interpolation ready for imaging (Oozer et al., 2010).

#### 3.2.2.1 Imaging

Practically an interferometer is unable to fully sample the $uv$ plane due to its nature. During the observation the source is observed for some time, and as the earth and the telescopes on it rotate with respect to the source the pattern of $uv$ coverage also rotates allowing more parts of the $uv$ plane to be sampled (Oozer et al., 2010).

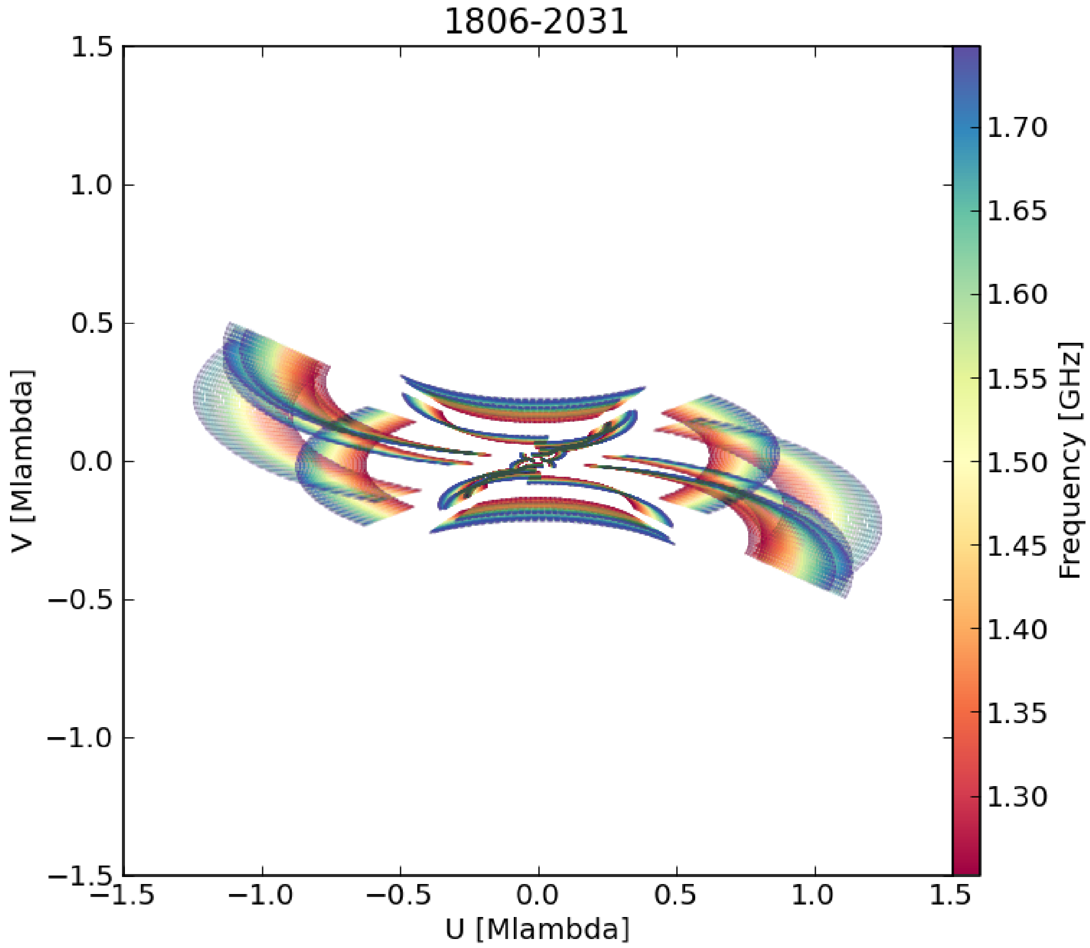

Figure 3.4: The *uv* coverage of e-MERLIN for the target during the observation.

Figure 3.4 is the *uv* coverage of e-MERLIN for the target used in this thesis. The tracks show the projected baselines in units of wavelength (M$\lambda$) in the *uv* plane. As can be seen, it is impossible to fill the *uv* plane resulting in an insufficient number of Fourier components to describe the source. To adequately map the source, a function $S(u,v)$ which samples the *uv* plane is introduced into Equation 3.2, which now becomes

$$I^D(l,m) = \int V(u,v)S(u,v)e^{(i2\pi(ul+vm))}\,du\,dv \tag{3.4}$$

where $I^D(l,m)$, the dirty image or dirty map, is related to the intensity distribution $I(l,m)$ by

$$I(l,m) = \int I^D(l,m) * B(l,m)\,du\,dv \tag{3.5}$$

Here, $*$ denotes the convolution operation and

$$B(l,m) = \int S(u,v)e^{(i2\pi(ul+vm))}\,du\,dv \tag{3.6}$$

is the dirty beam, synthesised beam or point spread function. This dirty beam and dirty image are determined from the visibility data.

To get the true sky brightness distribution the dirty beam is deconvolved from the dirty image in an iterative process using a common deconvolution algorithm in radio-astronomy called clean (Högbom, 1974). Clean considers a source to be a collection of point sources or delta functions. The clean process identifies a surface brightness (peak flux) in the dirty image, fits a dirty beam to this position and multiplies it by a gain factor. This gives a value which is a fraction of the dirty beam. The fraction of the dirty beam that has been scaled to the brightness peak is then subtracted from the collection of dirty beams from the *uv* data. Since the peak flux and the dirty beam are both considered as point sources, clean has the effect of removing all intensity components related to the peak, that is, side lobes and artefacts. A residual image is left behind whose position and peak flux are stored as clean components. This process is repeated until either the threshold noise is reached or there are no points of flux greater than the specified noise level. The clean components are convolved with the synthesised beam and added to the residual map to produce the final image. The synthesised beam is the full width at half-maximum (FWHM) of the main lobe of the dirty beam (Mcmullin, 2009).

## 3.3 Observation

The total observing time of the data (the target and the calibrators) was 21.36 hours out of which 10.32 hours was spent on source. The observation comprised datasets covering almost four consecutive days. Table 3.1 gives the breakdown of the date and time allocated for each session of observation. Each observing run consisted of about 75 scans made up of 60 minutes on the flux calibrator $1331+305$, 60 minutes on the bandpass calibrator $1407+284$, a sequence of 3 minutes on the phase calibrator $1751-1950$ and 7 minutes on the target $1806-2031$ which is repeated for the total on-source duration, and finally 60 minutes on the polarization calibrator $0319+415$. To account for any change in effect during the time of the observation the scans on the calibrators were scheduled before during and after the target scans.

Table 3.1: Data observation schedule and total on source time.

| Observation ID | Run | Date | Total time (hrs) |
|---|---|---|---|
| 0 | 20170616_L | 16 June 2017 | 2.10 |
| 1 | 20170617_L | 17 June 2017 | 1.63 |
| 2 | 20170618_L | 18 June 2017 | 4.20 |
| 3 | 20170619_L | 19 June 2017 | 2.39 |

Different correlator set-ups were employed for the continuum and spectral line data though the data were taken simultaneously. The continuum data were taken in full polarization over a frequency range of (1.25 GHz-1.76 GHz) with a total bandwidth of 512 MHz which was divided into 8 adjacent spectral windows each with 64 channels. An integration time of 1 s was used and the data were later averaged. The high spectral resolution data spread across two spectral windows were taken simultaneously with the continuum data. Two 125 kHz bands each centred on either of the two rest frequencies 1.6654018 GHz and 1.6673590 GHz were each overlaid with 512 spectral channels resulting in a high resolution channel width of 0.244 kHz. Frequency switching was used during these observations, cycling between the 1.665 GHz and 1.667 GHz line frequencies to provide data on both transitions. Table 3.2 and Table 3.3 summarise the observing parameters used for the continuum and the spectral line mode respectively.

Table 3.2: Observing parameters for the L-band continuum at a central frequency of 1.5 GHz. Antenna labels: De: Defford, Cm: Cambridge, Da: Darnhall, Kn: Knockin, Mk2: Mark 2, Pi: Pickmere.

| Parameter | Specification |
|---|---|
| Project | CY5204 |
| Band | L |
| Antennas | Mk2, Pi, Da, Kn, De, Cm |
| Number of sources | 6 |
| Integration time (s) | 1.0 |
| Frequency range (GHz) | 1.25–1.76 |
| Number of spectral windows | 8 |
| Channels per spectral window | 128 |
| Channel width (MHz) | 0.5 |
| Spectral window bandwidth (MHz) | 64 |
| Total bandwidth (MHz) | 512 |
| Polarizations | RR, RL, LR, LL |

Table 3.3: Observing parameters for the 1.6 GHz OH maser lines observation.

| Parameter | Specification |
|---|---|
| Project | CY5204 |
| Band | L |
| Integration time (s) | 1.0 |
| Central Freq 1.665 GHz | 1.6654775 GHz |
| Central Freq 1.667 GHz | 1.6674775 GHz |
| Num. spw | 2 |
| Channels/spw | 512 |
| Channel width (kHz) | 0.244 |
| Spw bandwidth (kHz) | 125 |
| Polarizations | RR, RL, LR, LL |

Table 3.4 also contains the observed calibrators and their scaled flux densities. The flux calibrator was used as a primary calibrator and the phase calibrator, bandpass calibrator and polarisation calibrator were used as secondary calibrators.

Table 3.4: Calibrators used for the 1.6 GHz OH observations and their flux densities.

| Calibrator | Flux density (Jy) |
|---|---|
| Flux density calibrator $(1331+305)$ | $13.8 \pm 0.2$ |
| Phase calibrator $(1751-1950)$ | $0.057 \pm 0.002$ |
| Band pass calibrator $(1407+284)$ | $1.013 \pm 0.003$ |
| Polarization, bandpass $(0319+415)$ | $16.41 \pm 0.06$ |

The recorded signals were correlated at the JBO correlator.

## 3.4 Data reduction

The data were reduced with the e-MERLIN CASA pipeline (version v0.10.02). Further data processing imaging and analysis were carried out using the Common Astronomy Software Applications (CASA) (version 5.4.2-1, (Mcmullin, 2009)) and IPython (version 5.1.0) packages using standard procedures. The pipeline is optimised for the calibration of both continuum and spectral line data. The pipeline was run twice on each data set for pre-processing and calibration.

### 3.4.1 Pre-processing data

During the first run the data were pre-processed by converting the visibilities in raw *uv* fits to a measurement set (MS). Here the *uv* fits were adjusted for Earth rotation, the data were sorted, and scan numbers were adjusted to increment with each source change. The continuum data was then averaged over every 8 channels and 8 seconds.

The coordinates (data position) of the phase calibrator used for the observation had an offset of half an arcsecond as compared with that from the astrogeo (catalogue) website ( VLBI Calibrator search); hence, the coordinate was corrected with the correct position information from the website ($\alpha$ (J2000)= $17^{\mathrm{h}}\ 51^{\mathrm{m}}\ 41^{\mathrm{s}}.343700$ $\delta$ (J2000)= $-19^{\circ}\ 50'\ 47''.50500$). Correction of the phase calibrator position was important because of the low elevation of the source. At low elevations such as that of the source as seen in Figure 3.5 there are phase instabilities arising in part from the longer path length through the atmosphere. The separation between the target and the phase calibrator of 3.5 degrees also introduced phase transfer errors.

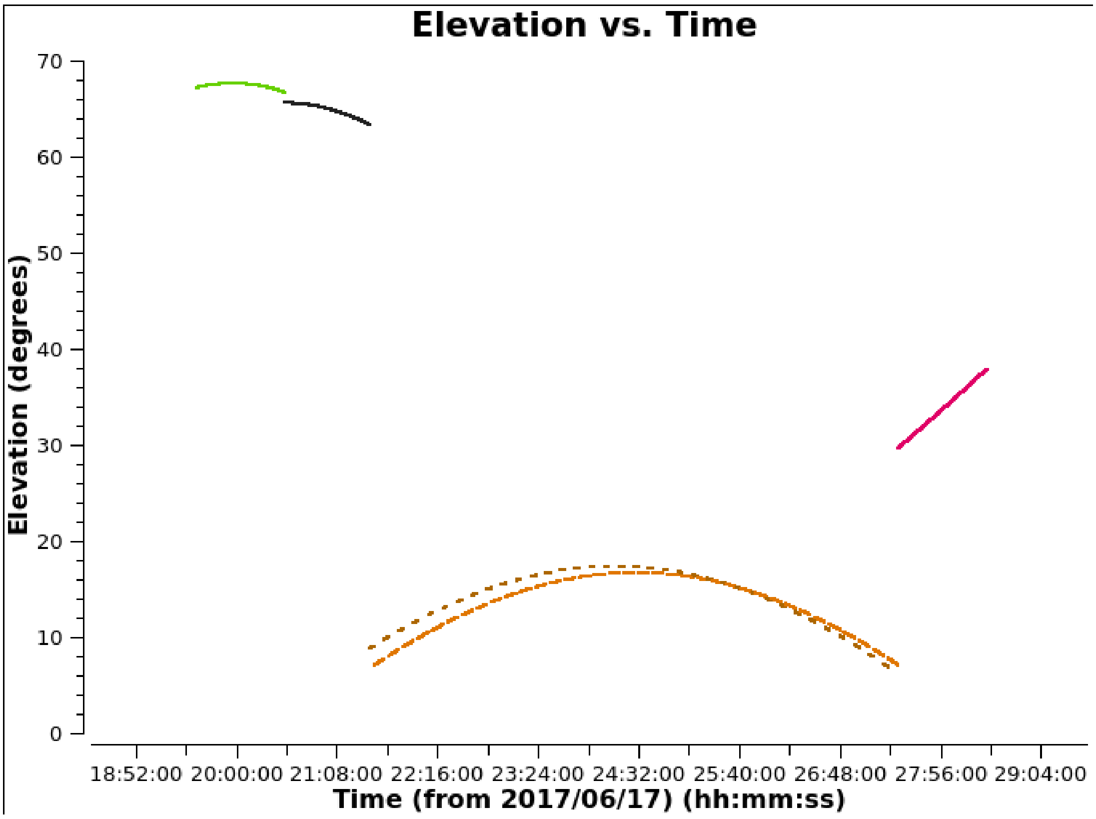

Figure 3.5: Figure showing the elevation of the individual sources in the observation. Scans of the calibrators are coded by colour. The first field, coloured green, is the flux calibrator followed by the bandpass calibrator coloured black. The phase calibrator and the target are coloured brown and orange respectively. And the last calibrator coloured pink is the polarisation calibrator. The phase calibrator and the target have low elevations because of their positions on the sky.

The three data sets were concatenated into one measurement set. A new source G9.745 + 00.106 in the field of view of the target was phase shifted to the center of the field to make it an independent source in the concatenated measurement set. This was calibrated and used as an independent source for the self calibration. The spectral line data were split from the continuum data, separating them into two measurement sets.

Bad data were excluded from the data sets using a number of processes called flagging. The automated flagging software AOflagger (Offringa et al., 2010) adapted to e-MERLIN, which uses specific strategies for known RFI at specific frequencies, was used to flag the RFI in the data. The software also used routines based on the deviation from expected spectral behaviour for more flagging. An *a priori* routine based on knowledge from the e-MERLIN setup (for example, antenna slewing time, flagged autocorrelations, the end channels ($0 \sim 3,508 \sim 511$), and any other failing antennae) was also used to flag bad data. The initial 300 seconds of the scans of the bandpass, the flux and the polarization calibrators were flagged. For the target and the phase calibrator the initial 35 seconds of each scan was flagged. From the automatic flagging and manual flagging carried out on the data a total of about 40% of the data was flagged, a fairly typical percentage for e-MERLIN L-band data. At this stage plots of the sources were generated for inspection. An example is Figure 3.4 which shows the visibility coverage of e-MERLIN for the target. This plot gives an indication of how elongated the synthesised beam looks like.

### 3.4.2 Continuum calibration

In the second run, the data were plotted and manually inspected by going through all baselines, spectral windows and channels of each calibrator and the target to see if any obviously bad data needed flagging. Flag commands for bad data were written into an external input file. This included end channels that were not flagged in the pre-processing run and bad data which the automatic flagger failed to remove. The pipeline then used the external file for additional flagging and calibrated the data. In the following sections solutions from 20170617 _L are used as illustrations for the data calibration process. The solutions for the other data are similar to 20170617_L hence the decision to use it for the illustration.

#### 3.4.2.1 Initial calibrations

Prior to calibrations, the delays of each antenna relative to the reference antenna Mk2, which has many short baselines and is likely to give good solutions for all the calibrators, were calculated. These antenna-based delays, which give values per spectral window per polarization, puts a phase limit to the frequency and channels in each spectral window. Figure 3.6 shows the delays per polarization across the bandpass for each antenna relative to the reference antenna for all the calibrators for the observation. The delays with good scatter indicate stability in time with good signal-to-noise ratio. Antenna 1 however, deviates by as much as 100 nanoseconds as can be seen in Figure 3.6. Generally a deviation by this much is still a suitable solution since the delays are stable in time.

For good time-dependent bandpass solutions the average over the small variations of phase

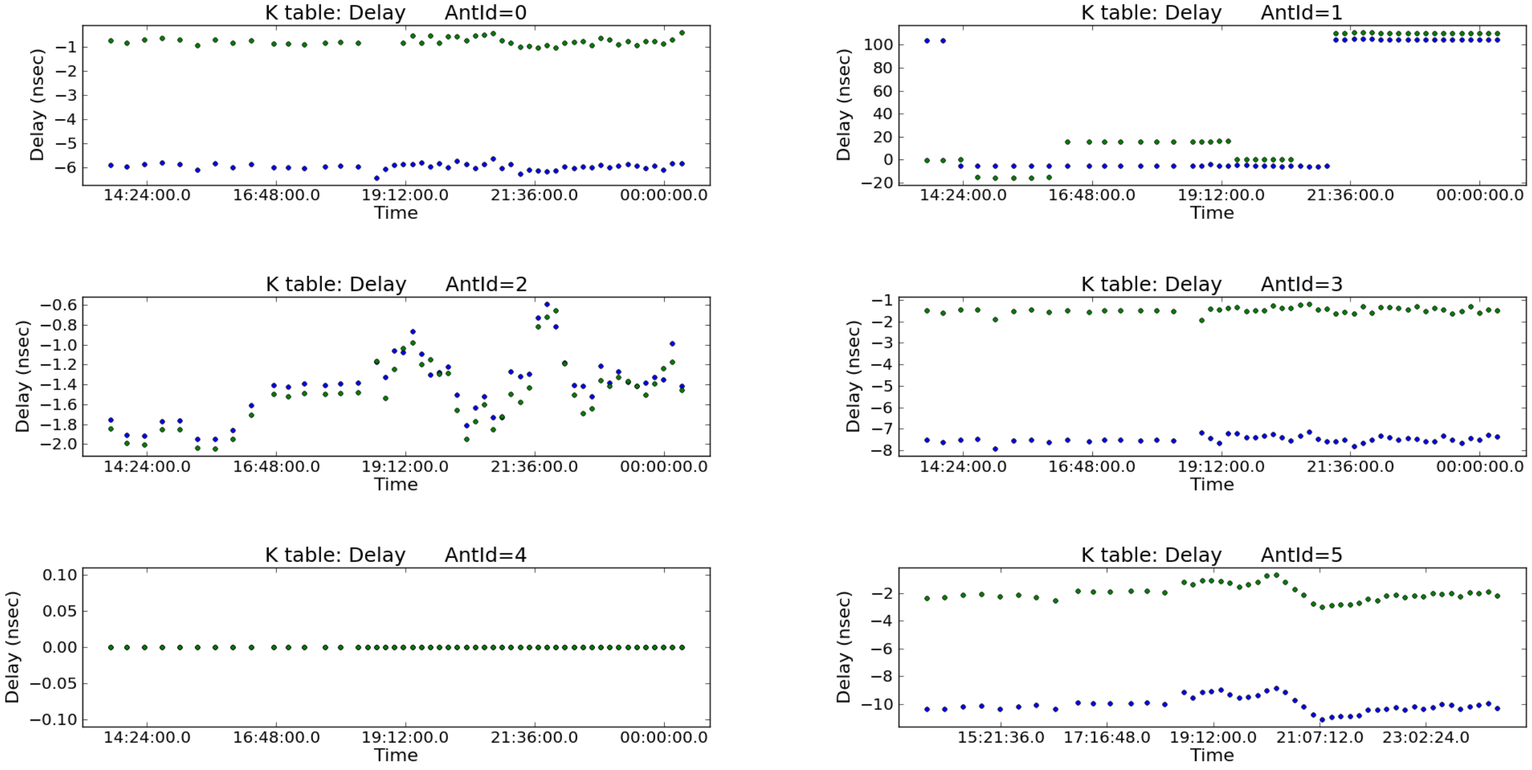

Figure 3.6: Plot of the delays for the entire duration of an observation on all the calibrators. Each antenna's delay relative to the reference antenna is plotted in a separate pane with the blue and green colour codes showing the different polarization components. Here Antid=0 represents Darnhall , Antid=1 represents Knockin, Antid=2 represents Defford, Antid=3 represents Mark2, Antid=4 represents Pickmere, and Antid=5 represents Cambridge.

with time in the bandpass with respect to the observing frequency is needed. This initial solution accounts for gain variations between different scans of the calibrators, especially if some scans were taken at different elevations. Preliminary time-dependent estimates of the phase and amplitude on all calibrators were thus calculated. These consisted of initial sets of antenna-based gains with solution intervals of 16 seconds for phase and 120 seconds for amplitude on all calibrators in order to moderate the effects of variations from integration to integration and from scan to scan. The average phase variations with time help solve the de-correlation when averaging for the final bandpass solution. The amplitude variations, however, have little effect on the bandpass solutions.

Plots of the calibration solutions showing variations in the phases and the amplitudes of the visibilities for all calibrators were generated. In Figure 3.7 the phase solutions scatter around zero by a few degrees for the phase calibrator with each scan being coloured separately by their spectral windows and a flat phase for the other calibrators (primary). Figure 3.8 shows the amplitude solutions with some discrepancies in amplitudes when the calibrators are compared to each other. The difference in amplitude shows a much weaker phase calibrator as compared to the flux calibrator. For individual calibrators both phase and amplitude plots are flat showing that averages in frequency can be made across a spectral window. Plots of this nature were generated after each process and were used to inspect the quality of the calibrations. The inspection is performed after each stage of the calibration. The calibrations were applied to the data to produce flat phases as a function of frequency. These calibration solutions were discarded after they had been applied. In the calibration plots that follow, Antid=0 represents Darnhall, Antid=1 represents Knockin, Antid=2 represents Defford, Antid=3 represents Mark2, Antid=4 represents Pickmere, and Antid=5 represents Cambridge. The calibration step was followed by flux density scaling.

#### 3.4.2.2 Flux density scaling

To effectively set the scale of flux density by which the target source is to be measured, the absolute flux density scale was found by bootstrapping the flux densities of the calibrators to the flux density of the flux calibrator 3C286 at L-band. This was done with a model derived

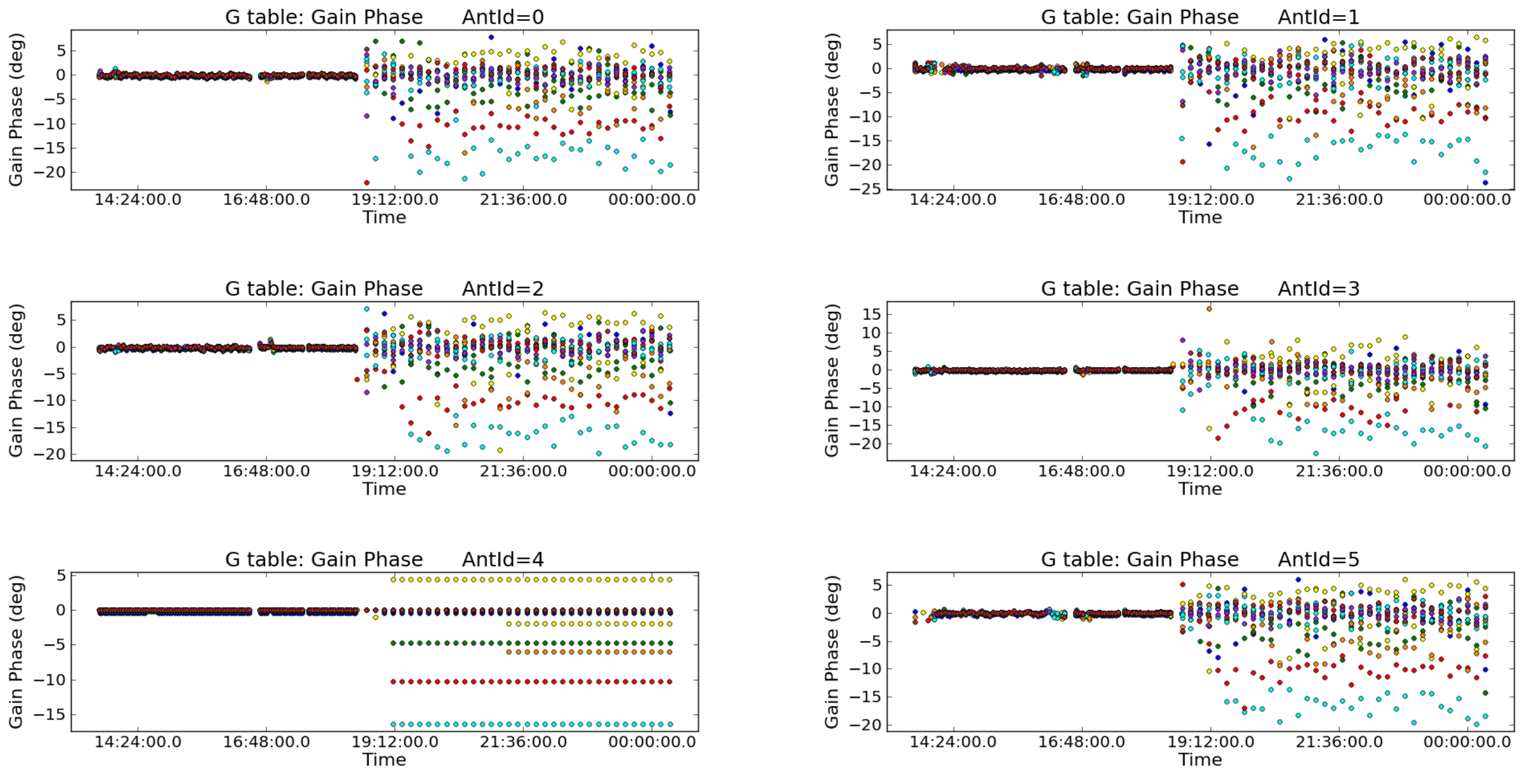

Figure 3.7: Initial gain (phase) calibration solutions for all calibrators coloured by spectral windows. Here Antid=0 represents Darnhall, Antid=1 represents Knockin, Antid=2 represents Defford, Antid=3 represents Mark2, Antid=4 represents Pickmere , and Antid=5 represents Cambridge.

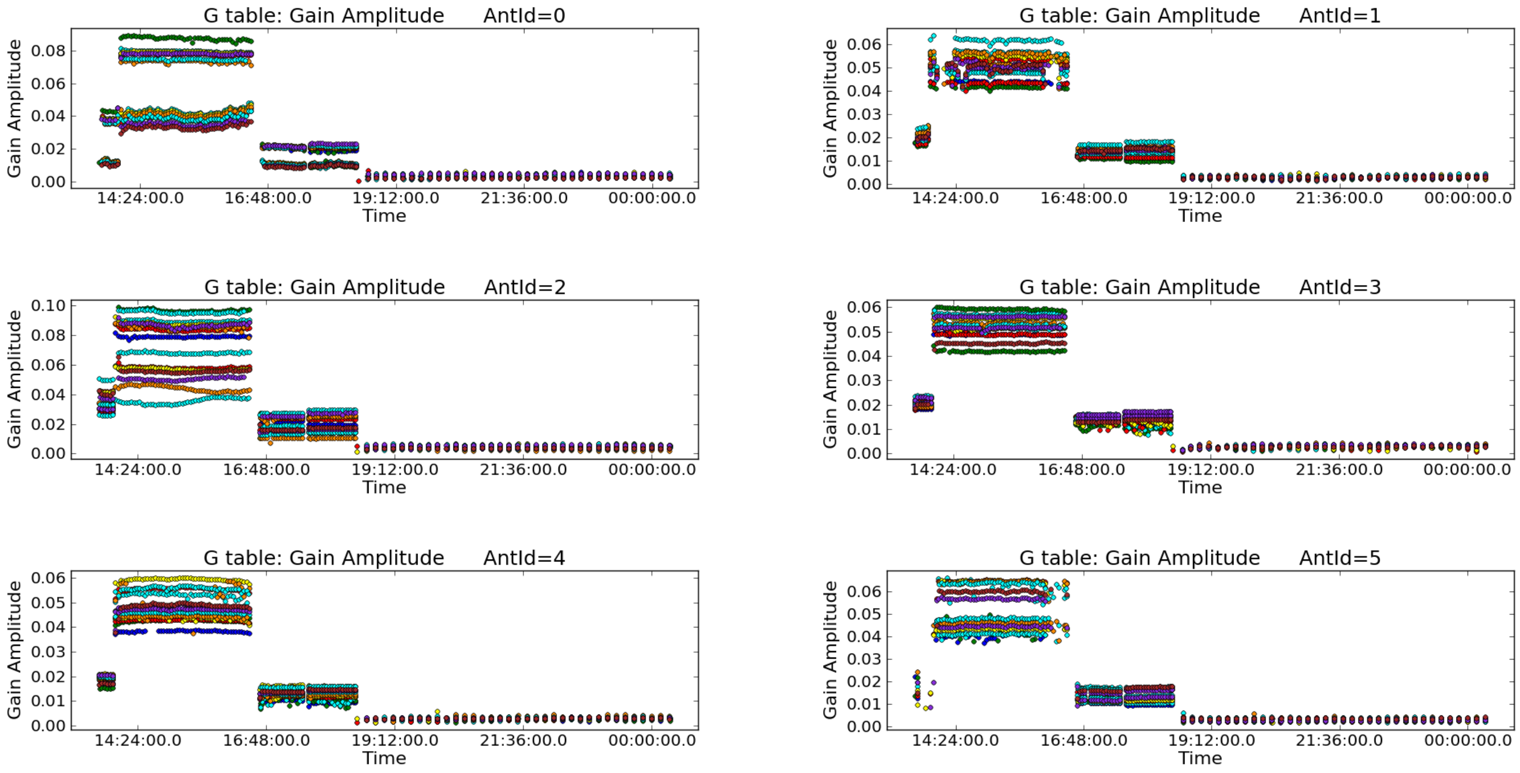

Figure 3.8: Initial amplitude calibration solution for all calibrators. In the mosaic, the first field represents the polarisation solutions, the second field represents the flux calibrator solutions, the third field represents the bandpass solutions, and the last field represents the scans of the phase calibrator solutions. Here Antid=0 represents Darnhall, Antid=1 represents Knockin, Antid=2 represents Defford, Antid=3 represents Mark2, Antid=4 represents Pickmere, and Antid=5 represents Cambridge.

from a 12 hour observation of 3C286 on 5.5 GHz and scaled to the observing frequency in the L-band, at 1.5 GHz. The flux spectral index and curvature were derived using model parameters from Perley and Butler (2013). This excluded antenna Lovell since it did not partake in the data collection.

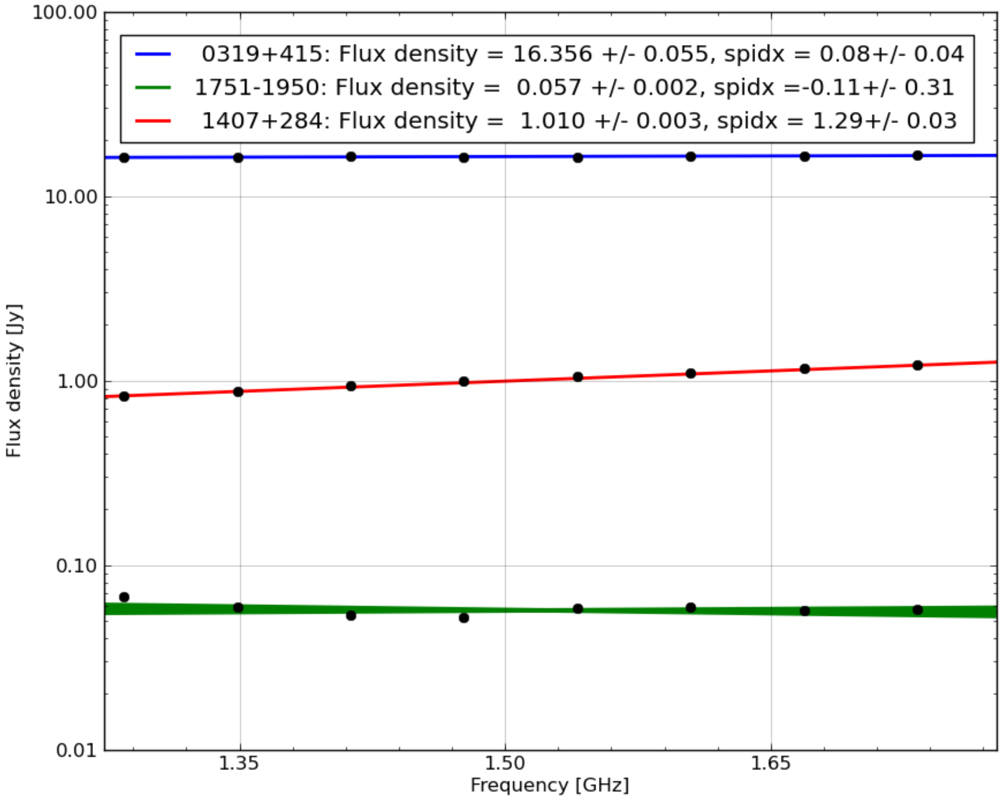

Figure 3.9: Flux density scale for the calibrators at L-band observing frequencies. The blue line shows the polarisation calibrator, the green line shows the phase calibrator and the red line shows the bandpass calibrator. The upper panel shows the flux density and the spectral index of each calibrator at the observing frequency.

The resultant values of flux density were then multiplied by the e-MERLIN factor of 0.9967 at L-band, calculated by Peck and Fenech (2013), to get a flux scale file which was used to calibrate the appropriate fluxes of the calibrators. This step compensates for the loss in flux of sources slightly resolved by e-MERLIN. Figure 3.9 is a plot showing the values of the scaled flux densities of the calibrators. Also shown in the same plot is their spectral index information.

### 3.4.2.3 Gain calibration

Gain calibration commenced after setting the correct flux densities and spectral indices. Gain calibration involved determining solutions of the amplitude gain and phase shift due to each antenna which together form the complex gain for that antenna. This was achieved in two steps because phase and amplitude vary differently with time. The phase of the complex gain varies frequently with time whereas amplitude and the bandpass response of the instrument across the frequency band vary slowly over a long time. Obtaining these solutions in two parts deals with both situations separately.

The first stage of the gain calibration is the amplitude calibration. This is derived by employing the measured antenna gain values to calculate the correction in voltage offsets in the system. A solution interval of 120 seconds with the corrected flux densities of all calibrators was used to calculate the amplitude gains against time. A plot of the amplitude calibration solutions with scaled flux densities is shown in Figure 3.10. The solutions result from comparing the different flux densities of all the calibrators except $1331+305$ with a 1 Jy model. As can be seen in Figure 3.10 the amplitudes are similar for all calibrator sources, spectral windows and polarisation components.

In the next stage, which is phase calibration, the interference fringes calculated from two antennas on each baseline are used to remove the errors in the phases introduced by the spectral windows. This aims to produce flat phases with respect to the frequency (channel) in the data by selecting a reference antenna for which the gain phase is defined to be zero. To achieve this the group delay and phase rate against time for all calibrators using a short time interval of 8 seconds were calculated and applied to the whole data. Thus, the phase variations over the time of the observation are removed.

Figure 3.11 shows the phase calibration solutions with scaled flux densities. The phase solutions for each antenna as a function of time shows a similar time-dependence as for the initial phase calibrations however the phases are not random. There are a few drifts in phase but with no phase jumps.

#### 3.4.2.4 Bandpass calibration

The last stage was the bandpass calibration which was done after the phase calibration step. This corrects for the bandpass response across the observed bandwidth to compensate for any frequency to channel differences in the system. A complex bandpass strategy which involved

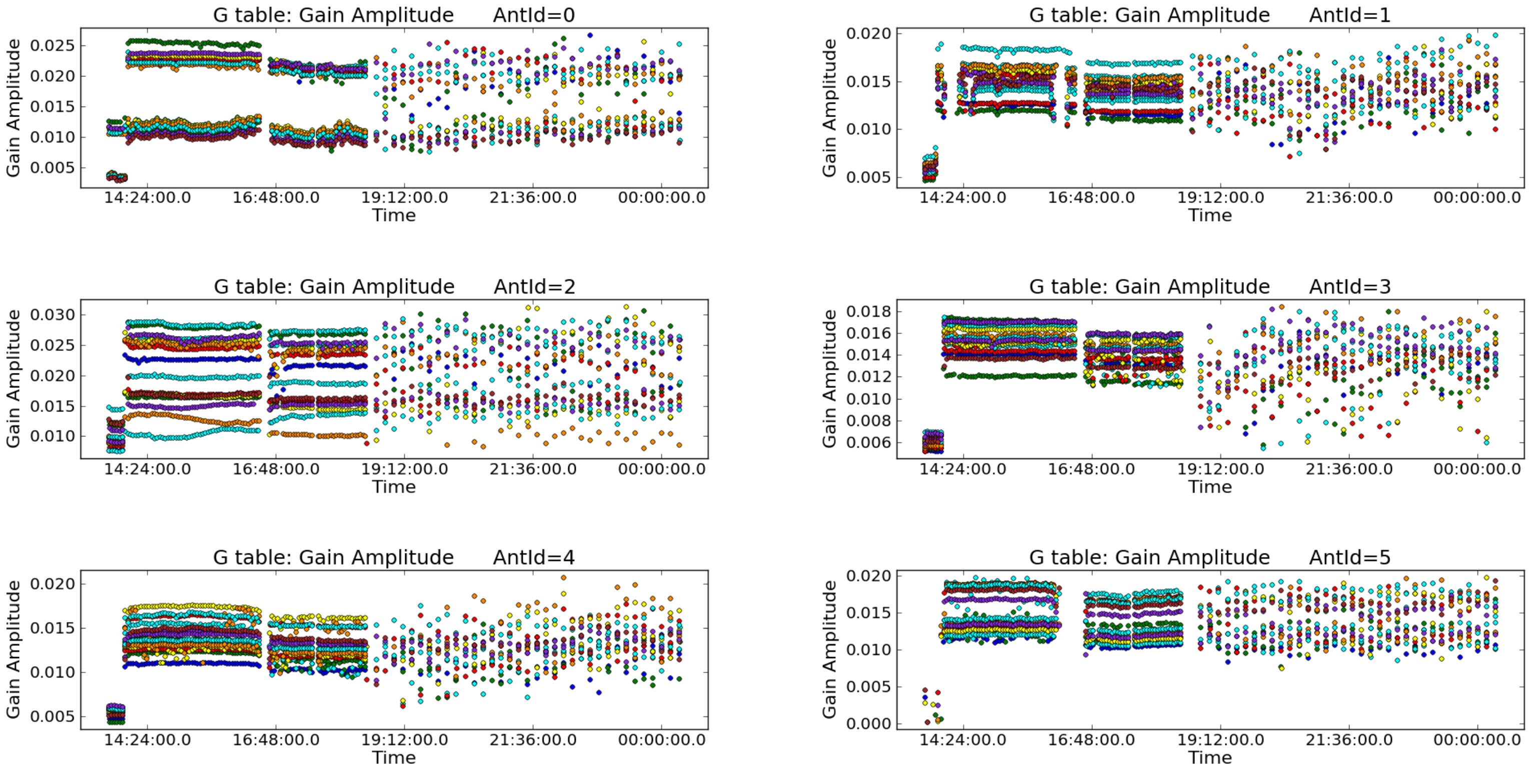

Figure 3.10: Amplitude gain solutions for all the calibrators, the scaled amplitudes for each antenna are plotted in a separate pane. Each of the spectral windows is plotted with two polarization components shown by the different colours.

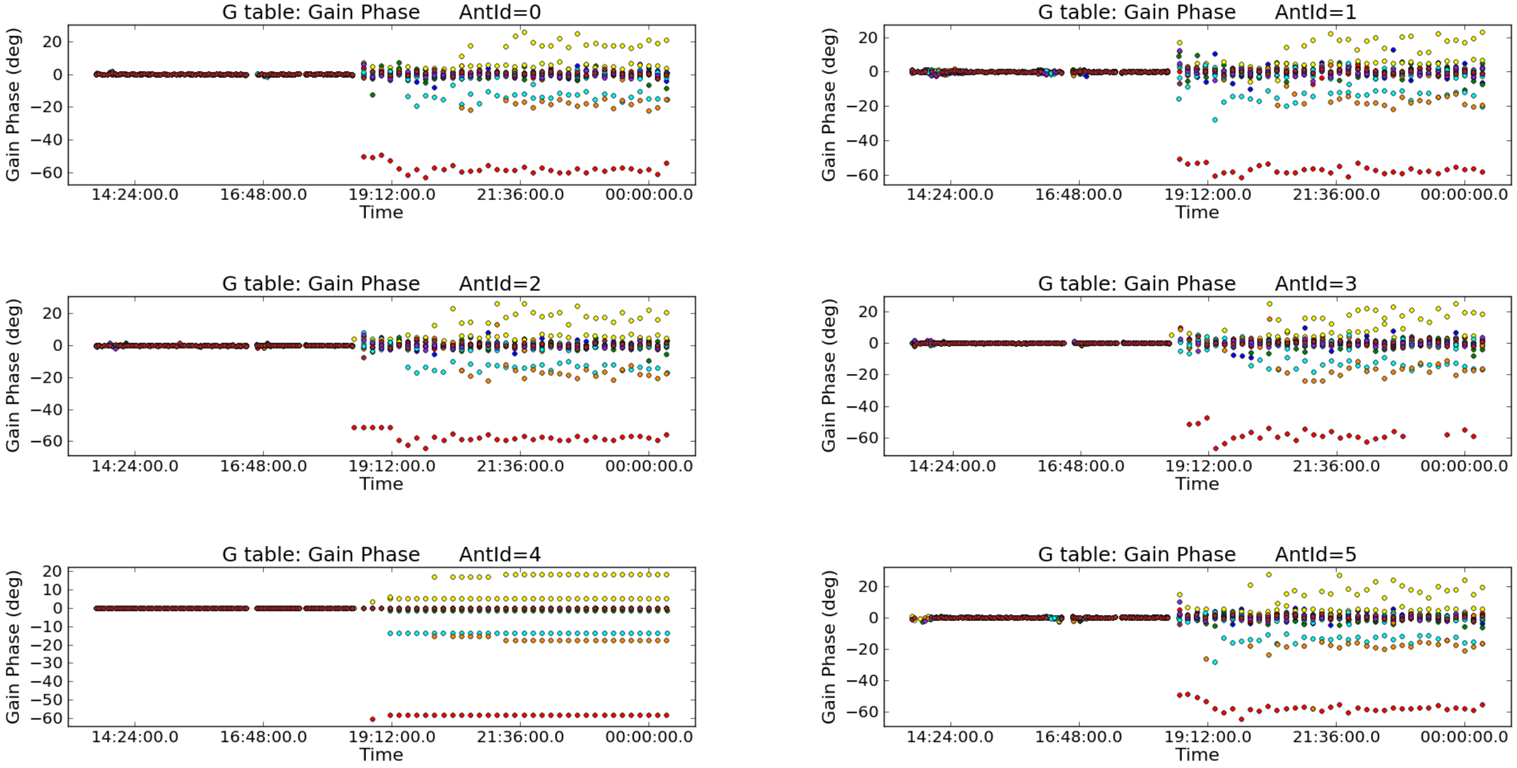

Figure 3.11: Gain phase solutions of all the calibrators. Each of the spectral windows for each calibrator is plotted with two polarization components shown by the different colours.

a phase correction and an amplitude correction was employed to calculate the solutions on the bandpass calibrator over the whole bandwidth at all times.

Figure 3.12 shows the complex phase solutions on the bandpass calibrator with flat phases across the frequency bands. Small phase variations with frequency are a reflection of the slightly different spectral windows across the bandpass.

In Figure 3.13, the complex amplitude solutions show a mean amplitude of approximately 1 Jy on all antennas across the useful parts of the band. The wiggles across the bandpass are corrected. Polarisation calibration on the calibrators were not done during this work, this was not much of a problem as OH masers are highly polarised and the percentage leakages across both polarization are negligible.

#### 3.4.2.5 Applying calibrations

At this stage the calibration solutions are applied to the target using the phase reference calibrator. Before that all the solutions of the delay calibrations, bandpass calibration and gain calibrations (amplitude and phase) calculated with the scaled flux densities were applied to all the calibrators one after the other. The measurement set has columns for the actual and corrected data and a column for the models. The strategy is to specify the appropriate solutions to be applied to the data column which will be written to the corrected data column. As the scans of the phase calibrator are interleaved with the scans of the target, solutions of the averages of the scans for the phase calibrator when linearly interpolated create a long stretch of scans incorporating the scans of the target.

Figure 3.14 and Figure 3.15 are the phase and amplitude solutions of the scan averages on the phase calibrator.

These solutions were then transferred to the target using linear interpolation. This is done because the phase calibrator is selected to be very close to the source. It is therefore assumed that they both experience similar atmospheric conditions and hence, to a good approximation, sufficiently good calibrations are transferred. Figure 3.16 shows the image of the phase calibrator which recovers a flux of 53 mJy as shown in Table 3.5.

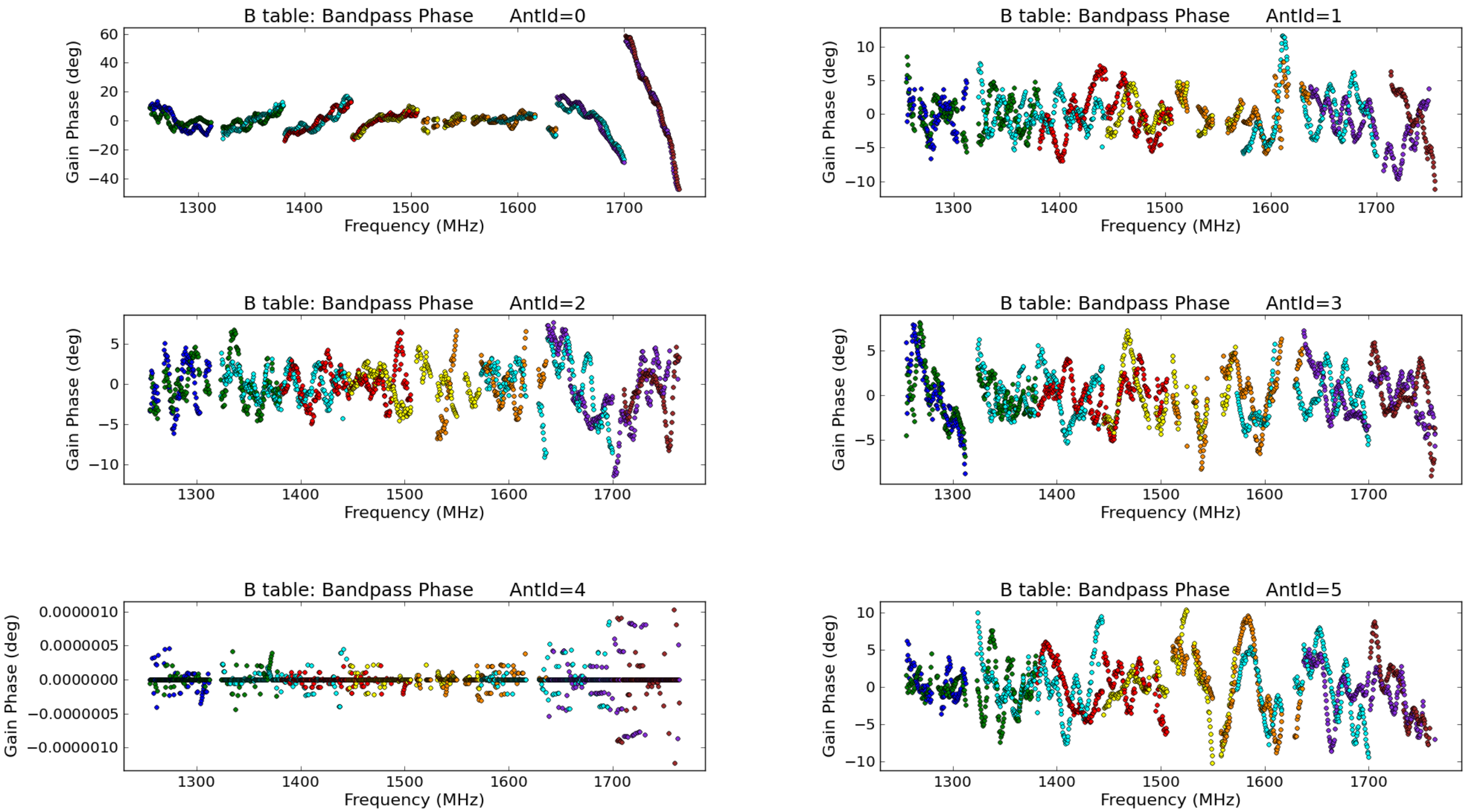

Figure 3.12: Phase solutions of the bandpass calibration on the bandpass calibrator (1407 + 284). Each of the 8 spectral windows is plotted with two polarization components shown by the different colours.

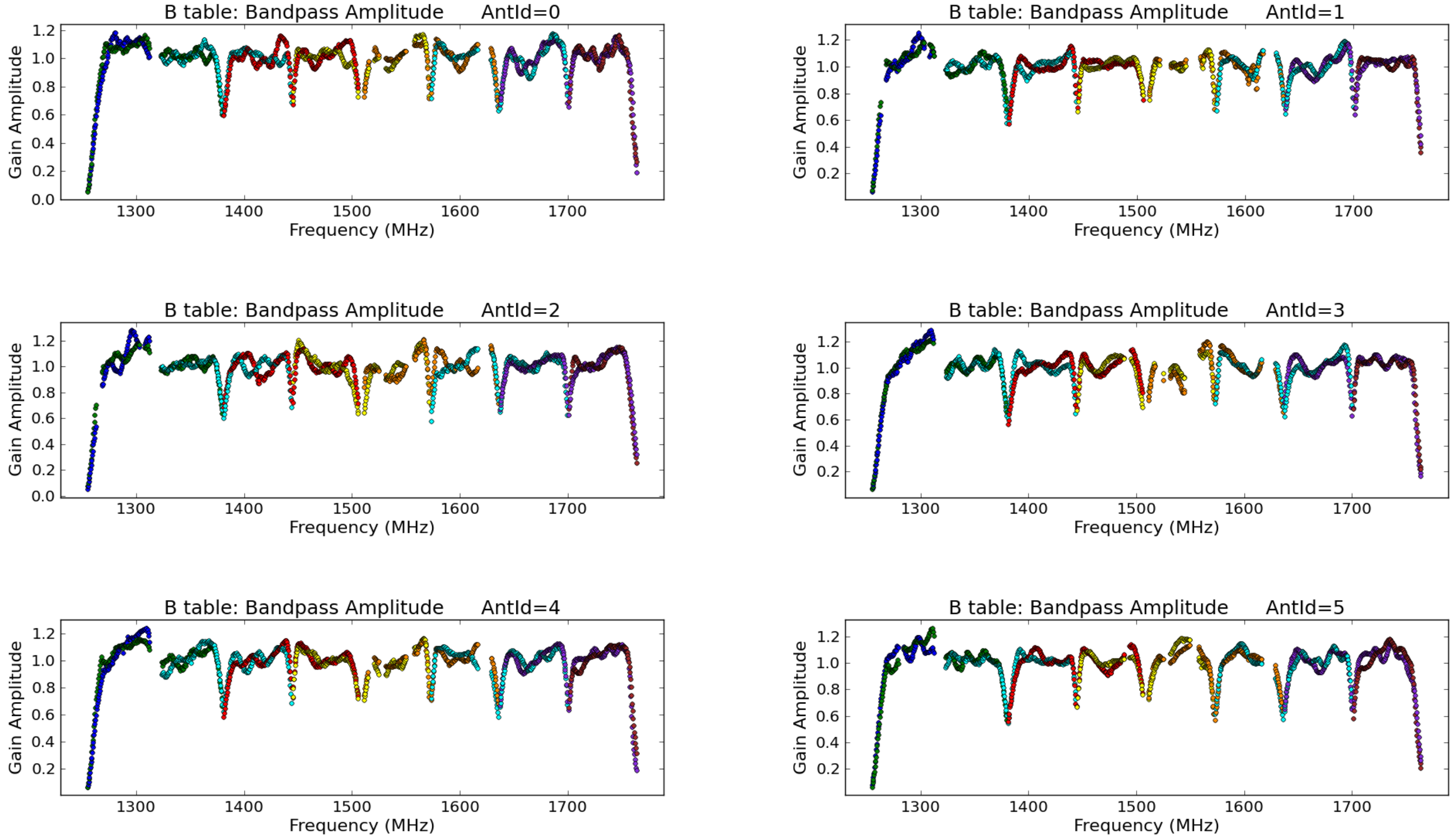

Figure 3.13: Amplitude solutions of the bandpass calibration on the bandpass calibrator (1407 + 284). Each of the 8 spectral windows is plotted with two polarization components shown by different colours. The edges of the bandpass are the fall off due to the instrumental demarcation of the frequencies by spectral windows.

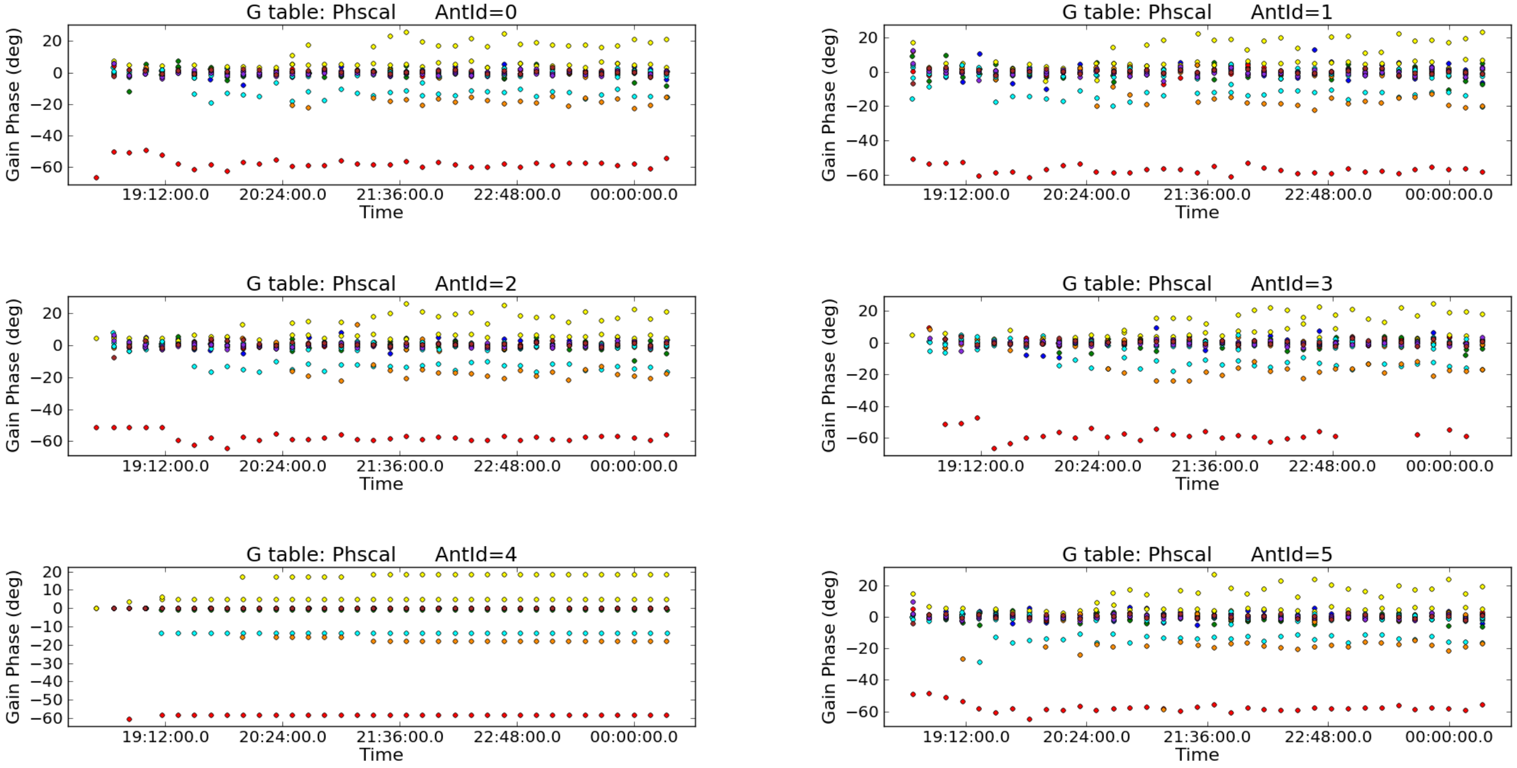

Figure 3.14: Solutions of phase scan averages on the phase calibrator transferred onto the target. Each colour represent a spectral window and a polarization component averaged over a scan.

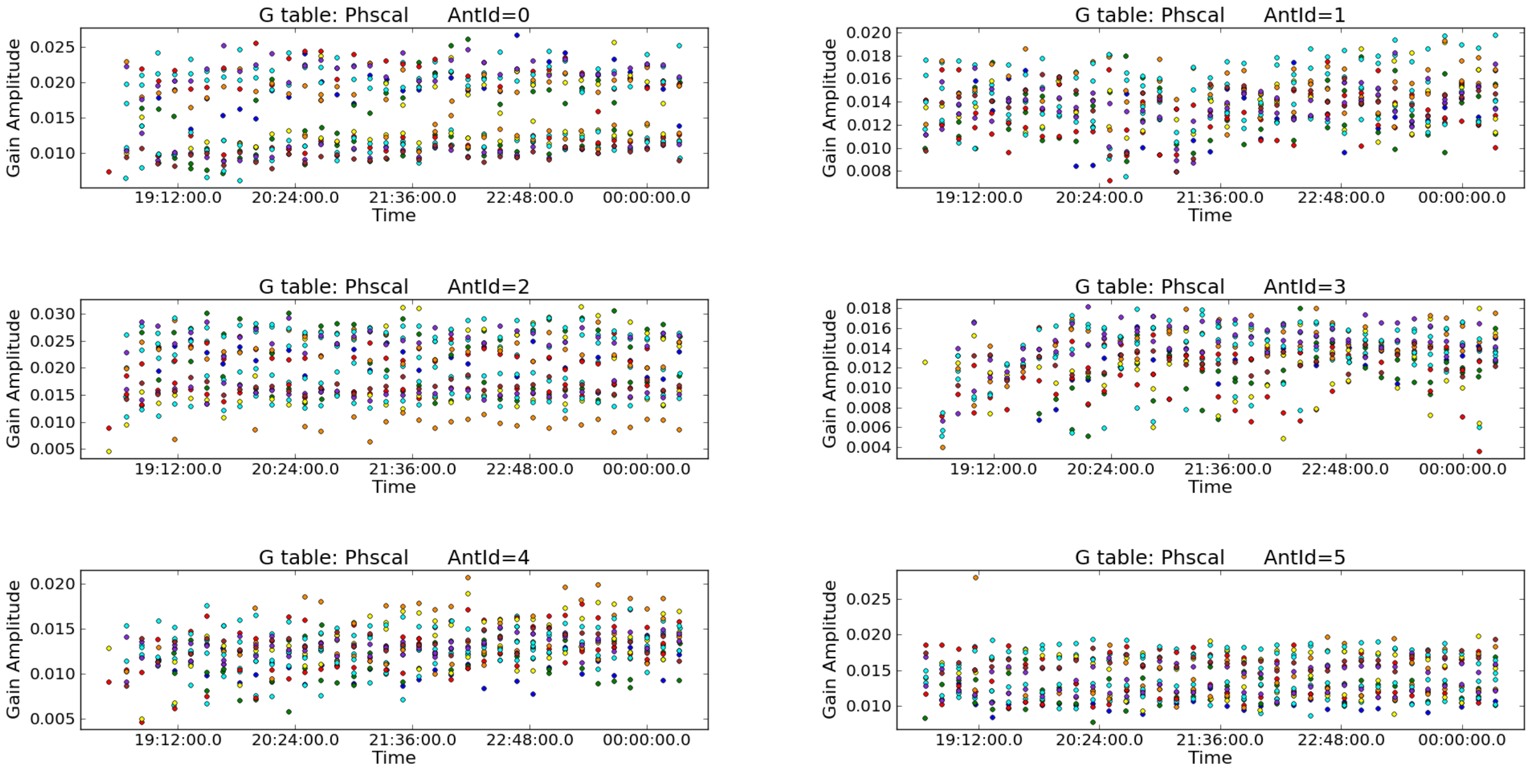

Figure 3.15: Solutions of amplitude scan averages on the phase calibrator transferred onto the target. Each colour represent a spectral window and a polarization component averaged over a scan.

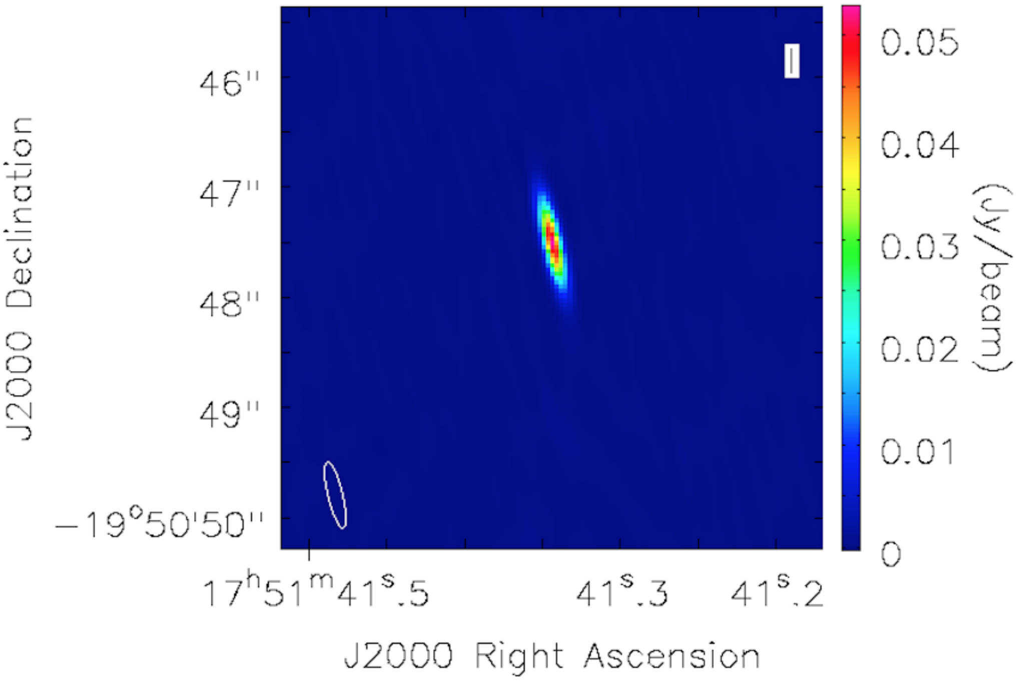

Figure 3.16: Image of the phase calibrator with a deconvolved size of $(622.61 \pm 2.31)$ mas $\times$ $(129.9 \pm 0.10)$ mas at a position angle of $(13.27 \pm 0.01)$ degrees. Shown in the lower left corner of the image is the synthesized beam.

Table 3.5: Position and flux density of phase calibrator.

| $\alpha$<br>(J2000) (h m s) | Error<br>($''$) | $\delta$<br>(J2000)($^{\circ}\,'\,''$) | Error<br>($''$) | Integrated flux density<br>(mJy) | Peak flux density<br>(mJy/beam) | Rms<br>($\mu$Jy/beam) |
|---|---|---|---|---|---|---|
| 17 : 51 : 41.3437 | 0.0002 | −19 : 50 : 47.5058 | 0.0009 | $53.08 \pm 0.09$ | $52.84 \pm 0.22$ | 58.93 |

### 3.4.3 Self calibration

Self calibration was employed to correct for the inaccuracies introduced by the transfer of solutions from the phase calibrator to the target. This procedure essentially removed the effects of the rapidly changing atmospheric conditions which had not been removed in the traditional calibration. The flux density of the maser lines at L-band in the wide band data was not bright enough to be used to self calibrate the continuum data hence the independent source G9.745 + 0.106 was used. The phase center of the independent source was shifted to the phase center of the target and was used for self calibration. Figure 3.17 is the L-band continuum image of G9.745 + 0.106 in the field which recovers an integrated flux density of 91.5 mJy as given in Table 3.6. Previous 1.4 GHz observation of the source in a VLA survey reports a recovered flux of 161 mJy (Becker et al., 1994).

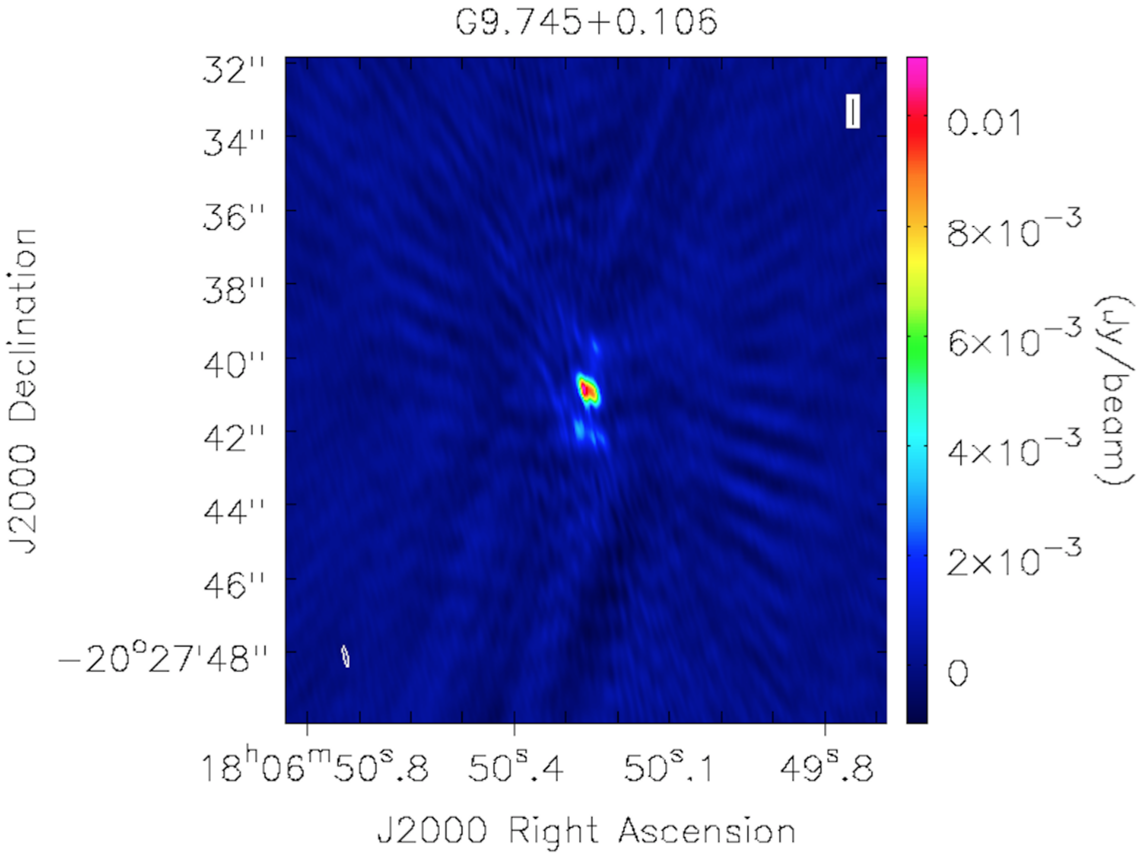

Figure 3.17: An image of G9.745 + 0.106 in the field of view which was used for the self calibration with a deconvolved size of $(456 \pm 54)$ mas × $(280 \pm 17)$ mas at a position angle of $(67 \pm 12)$ degrees. Shown in the lower left corner of the image is the synthesized beam of size 0.57 arcsecs × 0.10 arcsecs at a position angle of 11.49 degrees.

Table 3.6: Position and flux density of G9.745 + 0.106.

| $\alpha$<br>(J2000) (h m s) | Error ($''$)<br>($''$) | $\delta$<br>(J2000)($^{\circ}\,'\,''$) | Error<br>($''$) | Integrated flux density<br>(mJy) | Peak flux density<br>(mJy/beam) | Rms<br>($\mu$Jy/beam) |
|---|---|---|---|---|---|---|
| 18 : 06 : 50.2557 | 0.0082 | −20 : 27 : 41.296 | 0.012 | $91.5 \pm 3.1$ | $11.27 \pm 0.66$ | 368.7 |

The model of this image was written to the model column of the measurement set. This model image made after applying the phase calibration retains the absolute position information. Starting from the point source model an iteration of a phase self calibration on G9.745 + 0.106 with solutions as presented in Figure 3.18 was calculated and these solutions were applied to all the 8 spectral windows. An iteration of amplitude and phase self calibration was calculated using the model derived from the phase self calibration of G9.745 + 0.106. The results are presented in Figure 3.19, which shows the amplitude and phase self calibration solutions. The solutions from the self calibration were applied to all the 8 spectral windows in the continuum.

#### 3.4.3.1 Imaging of the continuum at L-band

Total intensity maps of the continuum using line-free channels were made by cleaning the 8 spectral windows. The rms noise in the image was calculated by averaging the rms from five different emission free areas of the image using boxes of the same size.

### 3.4.4 Spectral line calibration

The high spectral resolution data made up of two spectral windows in the measurement set that was split from the continuum measurement set was used for the narrow band calibration. The residual continuum in the spectral line data was subtracted from the spectral lines in the *uv* plane by specifying the spectral line channels and fitting a first order polynomial to the spectral line. The parameters used for the acquisition of the data are recorded in Table 3.3. The initial 40 seconds of each scan in the high resolution data were flagged.

#### 3.4.4.1 Gain calibration

The phase offset between the wide and narrow band channelisation was calculated on the bright calibrator 0319 + 415. This was done by importing the delay solutions in Figure 3.6 and gain phase solutions in Figure 3.11 from the wide band calibrations and calculating the gain phase solutions on the narrow band maintaining the same reference antenna. The calculation assumed that the narrow-band spectral windows do not need delay corrections as any slope is negligible over a narrow bandwidth. Usually there was no amplitude offset. The solutions of the offsets are shown in Figure 3.20.

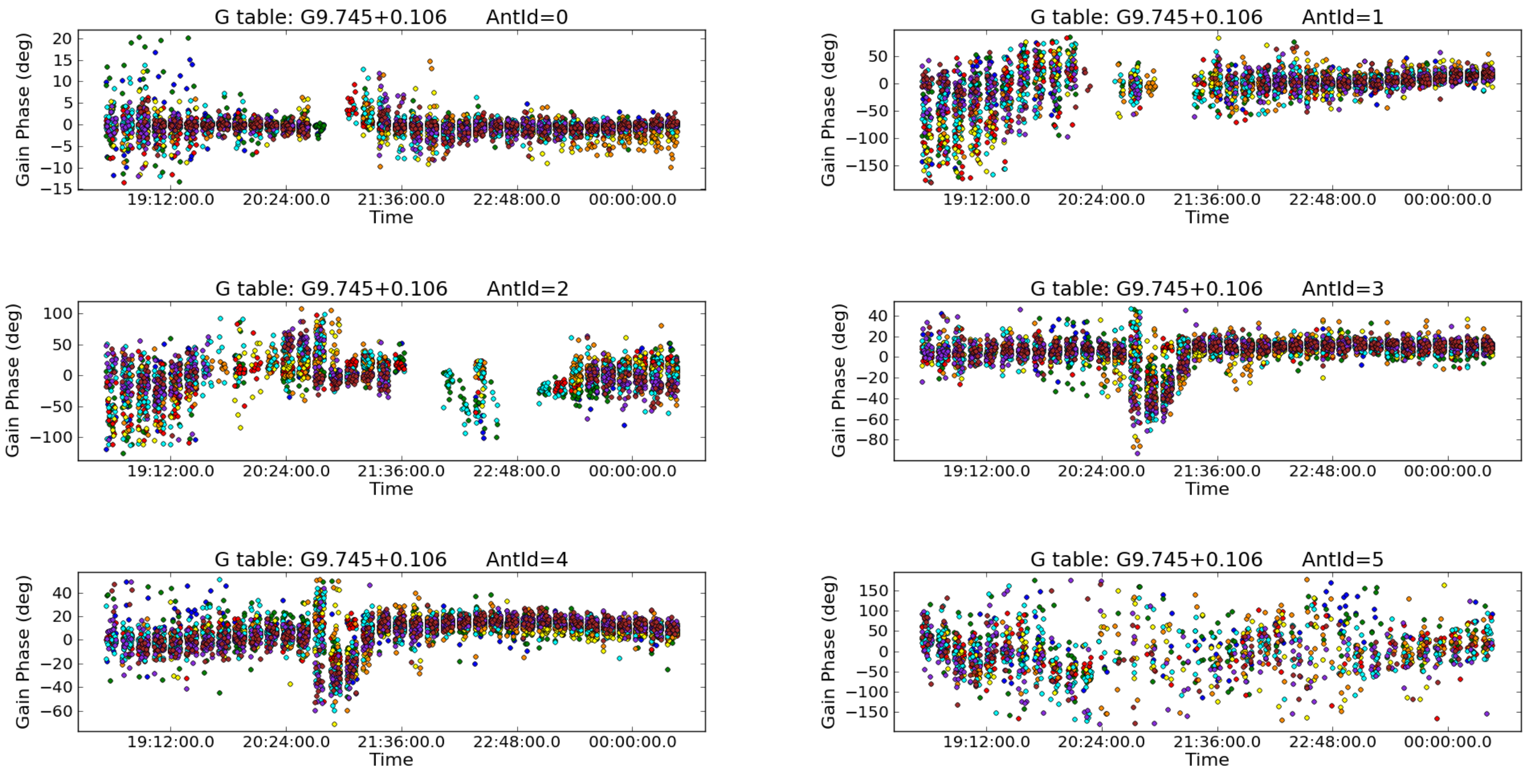

Figure 3.18: Phase only solutions on $G9.745+0.106$ applied to the continuum with a spell of bad weather recorded between $20:20$ hours and $21:30$ hours. Some solutions were lost on Cambridge.

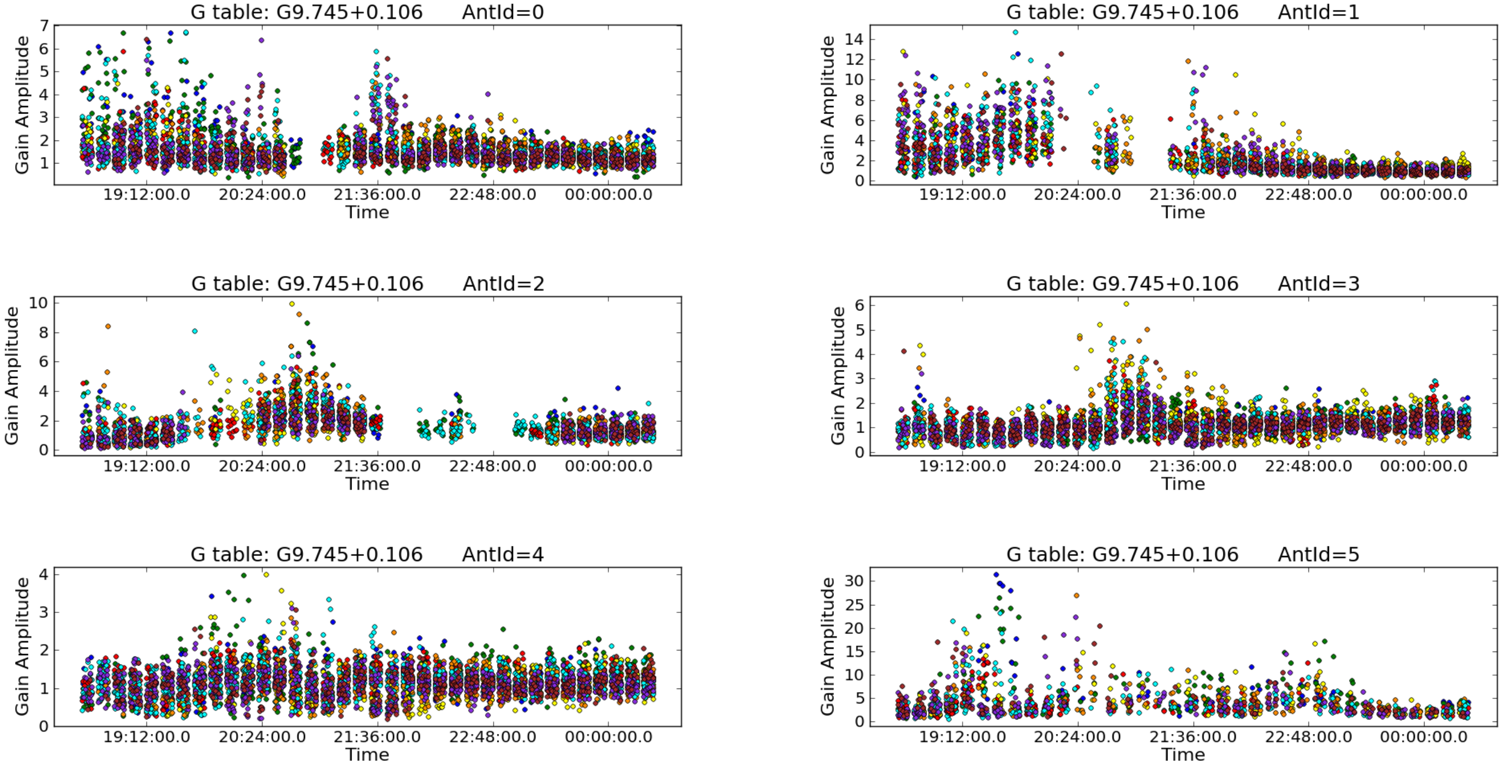

Figure 3.19: Amplitude self calibration on G9.745 + 0.106 applied to the continuum with a spell of bad weather recorded between 20 : 20 hours and 21 : 30 hours.

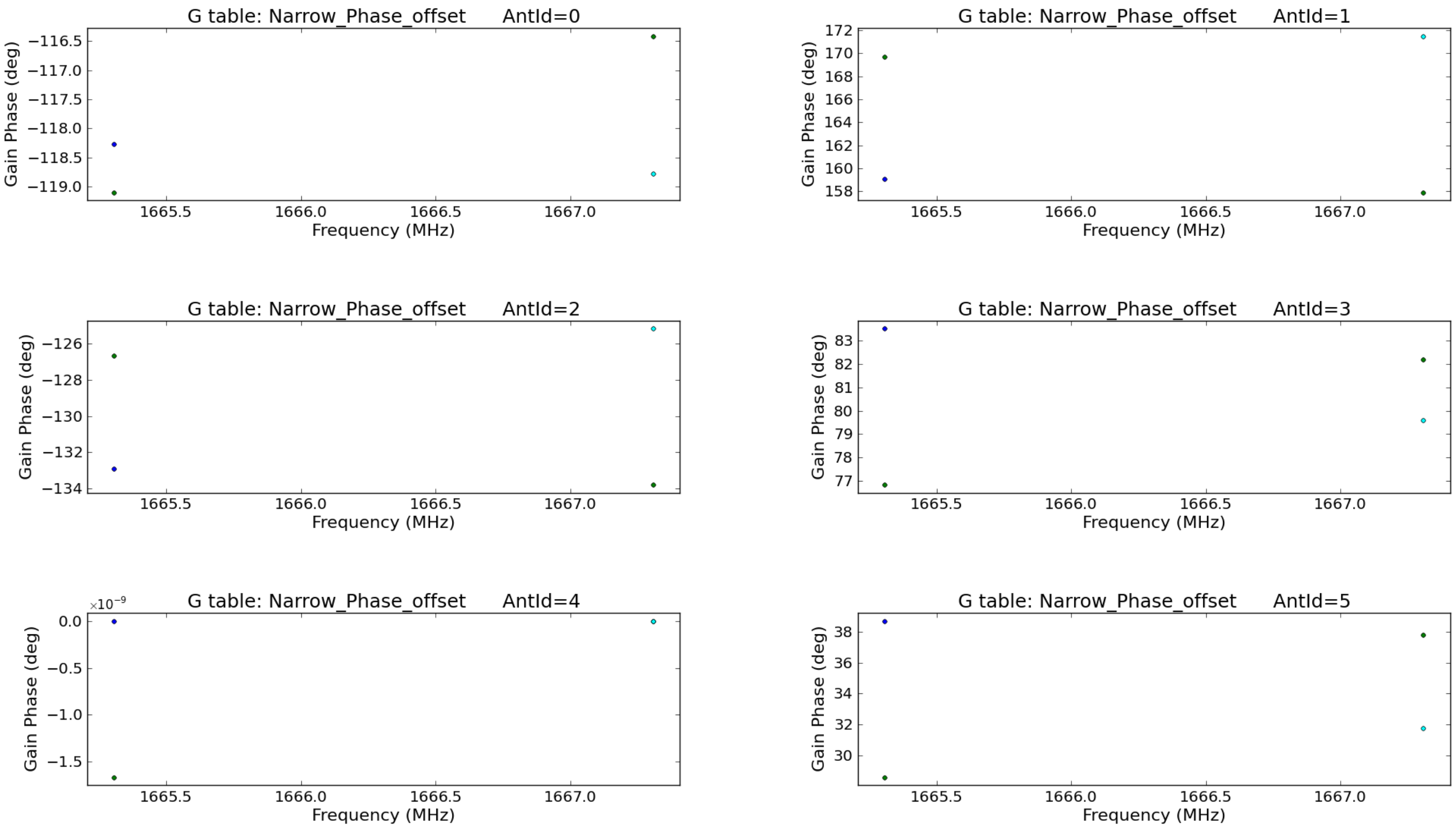

Figure 3.20: Phase offset solutions between the narrow and wide band channelisation at 1665 MHz and 1667 MHz. The two polarisation components are shown by the different colours.

#### 3.4.4.2 Bandpass calibration

The gain phase offset solutions were used to calculate the bandpass solutions on the narrow-band bandpass. The same calibrator was used to derive the bandpass solutions in Figure 3.21 and Figure 3.22 exactly as for wide band but without delay corrections. This also assumed that the phase and amplitude solutions derived from the wide band phase reference included the flux scale hence no flux scaling was done.

The corrections in Figure 3.21 and Figure 3.22 were applied to the target on the narrow band data. In this case the time-dependent offset corrections from the wide band spectral windows were applied to the two spectral windows. The target was then split from the measurement set and the measurement set was shifted to constant velocity of the hydroxyl maser lines.

#### 3.4.4.3 Imaging of the spectral line

No further calibrations were carried out on the high resolution data. Spectral window 0 and 1 were set to the rest frequencies of 1.6654018 GHz and 1.6673590 GHz respectively. The final image cubes of the left and right circular polarizations of each transition were produced by identifying the maser emissions in each velocity plane of the cube and setting a clean mask around them. The cubes were cleaned to the residual flux limit.

At this point, the data consisted of image cubes of 511 channels at $1024 \times 1024$ pixels per Stokes parameter (LCP and RCP) per frequency. The velocity planes within which the masers occurred were recorded. Components were considered as spectral features if they occurred in three or more consecutive channels and had a peak flux density at least three times higher than the rms noise in the field. The flux densities were measured by creating polygons around the emissions in the image and recording the peak and integrated flux densities. A two dimensional Gaussian component was fitted to the brightest peak in each channel map to obtain their positions and sizes. The uncertainties in the flux densities were calculated by averaging the rms noise from five different emission-free areas of the image using boxes of the same size.

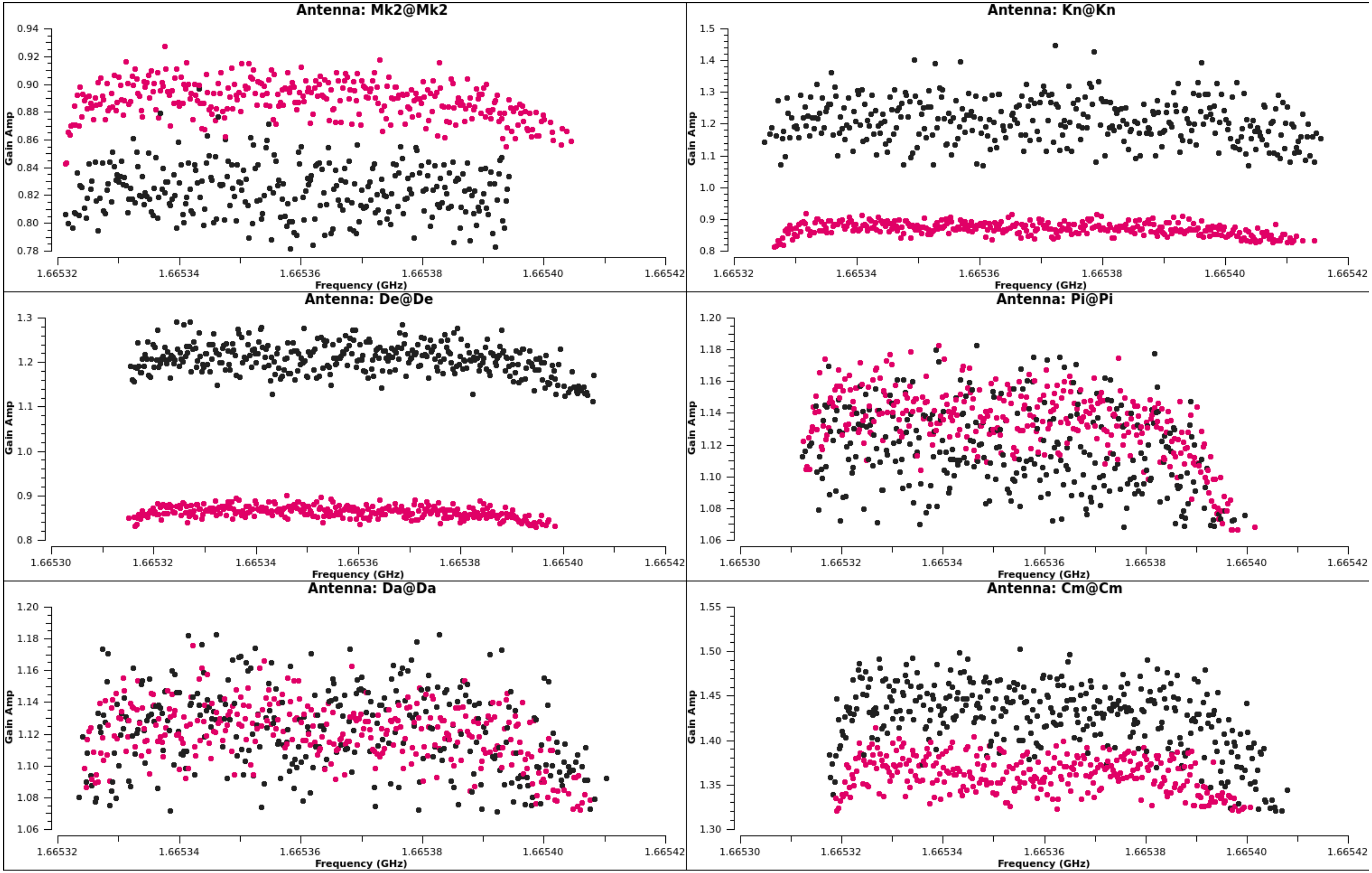

Figure 3.21: Bandpass calibration on the narrow band data for the 1665 MHz maser line. The calculated solutions are coloured by the two polarizations.

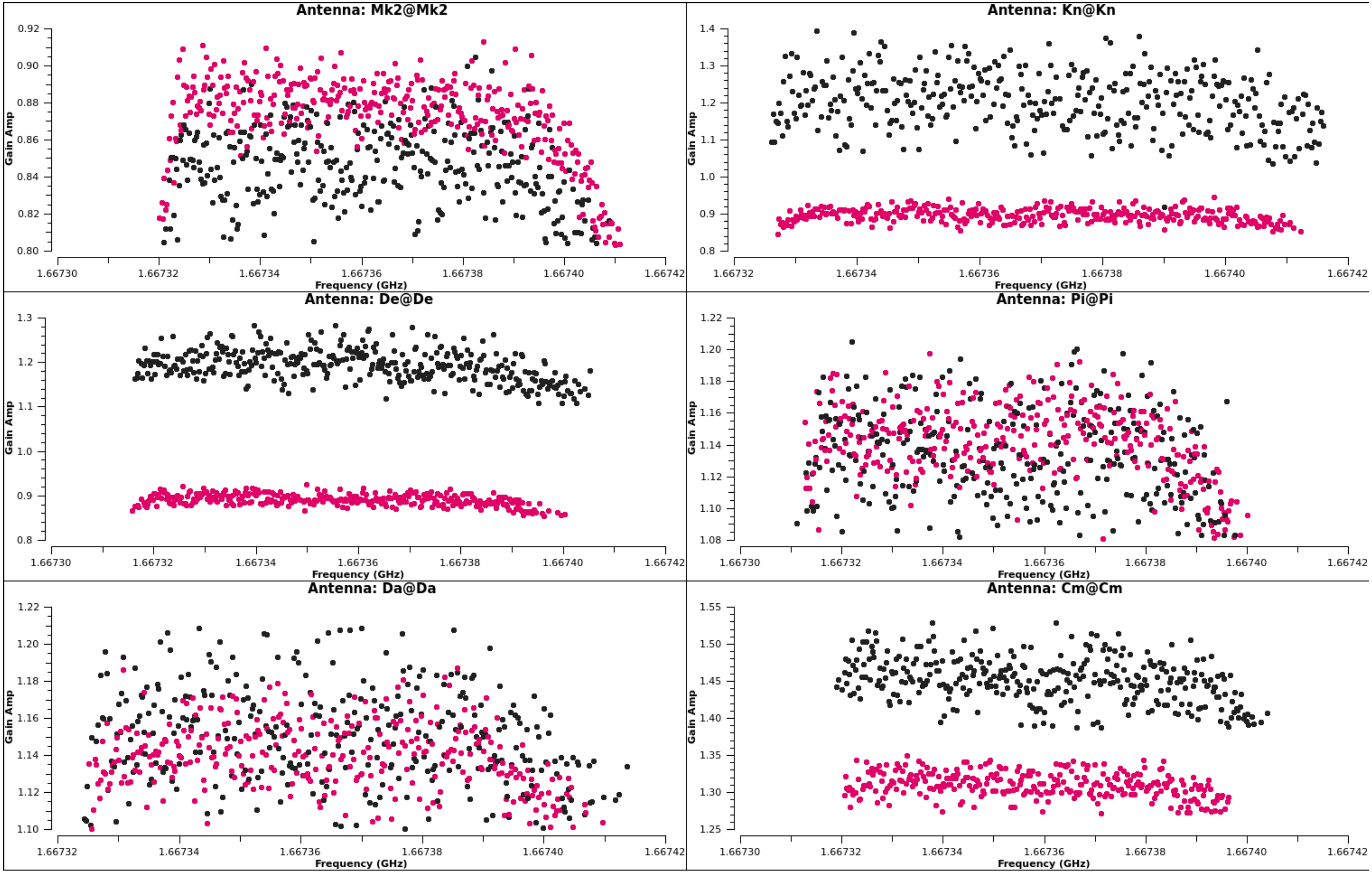

Figure 3.22: Bandpass calibration on the narrow band data for the 1667 MHz maser line. The calculated solutions are coloured by the two polarizations.

## 3.5 Results

Presented in this section are the results from the imaging of the L-band continuum and the maser emissions in the left and right circular polarizations of both the 1.665 GHz and 1.667 GHz lines.

### 3.5.1 The L-band continuum

The continuum map was generated by imaging all the channels in the spectral bandwidth containing emissions except the channels that contained the maser lines. Figure 3.23 shows the site for the G9.62 + 0.20E star forming region with the expected position of the continuum emission marked with a pink cross. At this position no radio continuum emission was recorded above the e-MERLIN sensitivity limit. Measuring the rms noise gave a value of 54 $\mu$Jy/beam which is a $1\sigma$ limit on the peak flux density. At L-band with a target well above a declination of 20 degrees, under good conditions and with vigorous RFI removal techniques a theoretical noise limit of 14 $\mu$Jy/beam is expected for a 12 hour continuum observation for e-MERLIN without Lovell. However, for this work Table 3.1 reports a total on-source time of 10 hours. When the e-MERLIN noise level is extrapolated to 10 hours a noise level of 15 $\mu$Jy/beam is expected but a noise level of 54 $\mu$Jy/beam was recorded. This value which is almost four times the expected value is likely due to the low elevation of the source as shown in Figure 3.5, bad weather conditions as seen in Figure 3.18 and Figure 3.19, and also side lobes from nearby sources G9.62 + 0.20C and G9.62 + 0.20D. The loss of the long north-south most sensitive Cambridge baseline as seen in solutions from Figure 3.18 also resulted in the increase in the noise. The upper limits on the flux density was obtained by finding the average of the absolute values of the flux from five boxes taken around the pink cross. This resulted in a value of 54 $\mu$Jy which gives a $3\sigma$ upper limit on the flux density of 162 $\mu$Jy. The resulting upper limit was significantly lower then the expected flux of 0.6 mJy which comes from extrapolating the higher frequency measurements from Franco et al. (2000) using their spectral index of 0.95.

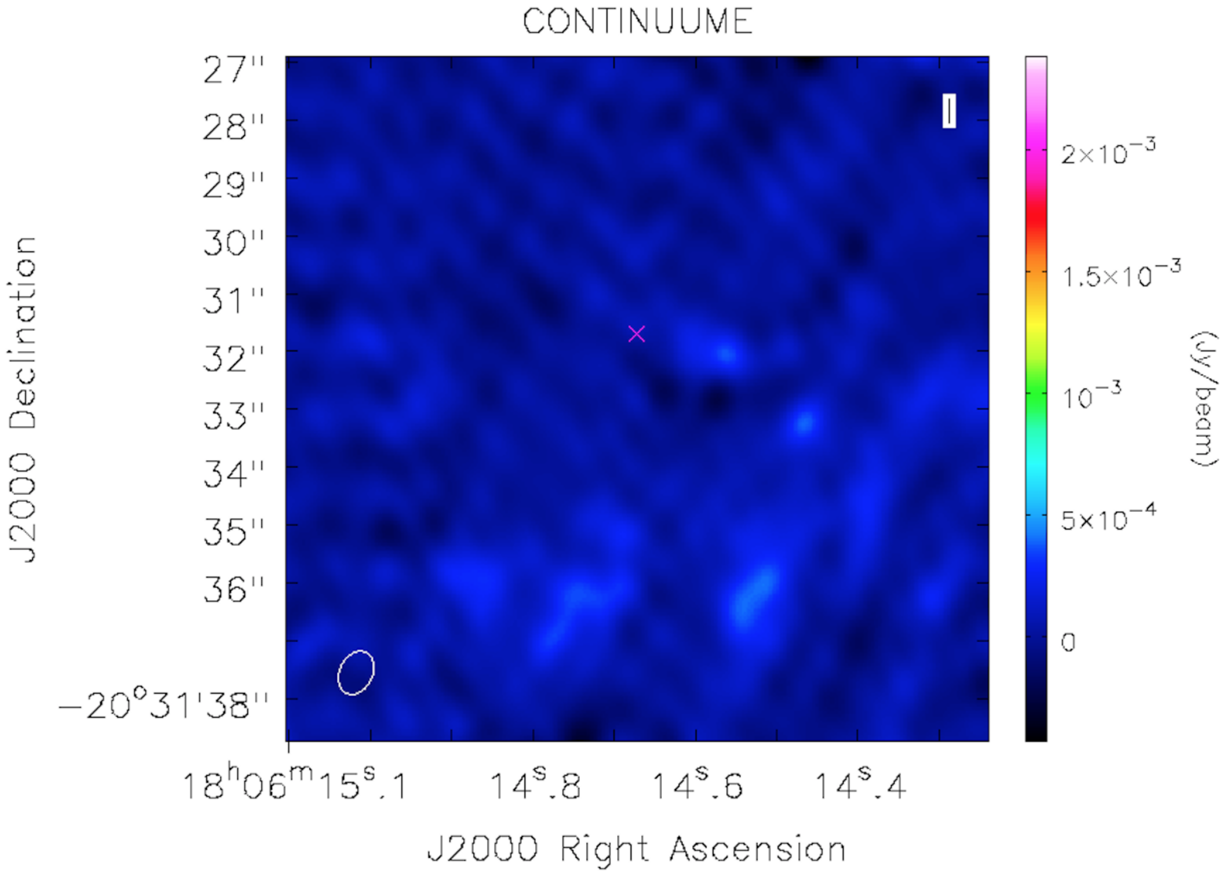

Figure 3.23: Image of the field of the L-band radio continuum of G9.62 + 0.20E. The pink cross shows the expected position of the radio continuum. Shown at the lower left corner of the image is the synthesized beam of size 0.78 arcsecs × 0.57 arcsecs at a position angle of −25.36 degrees.

The upper limit value when plotted on the spectral index plot of Figure 5 of Franco et al. (2000) yields Figure 3.24. This plot will be discussed in the discussion section of Chapter 4.

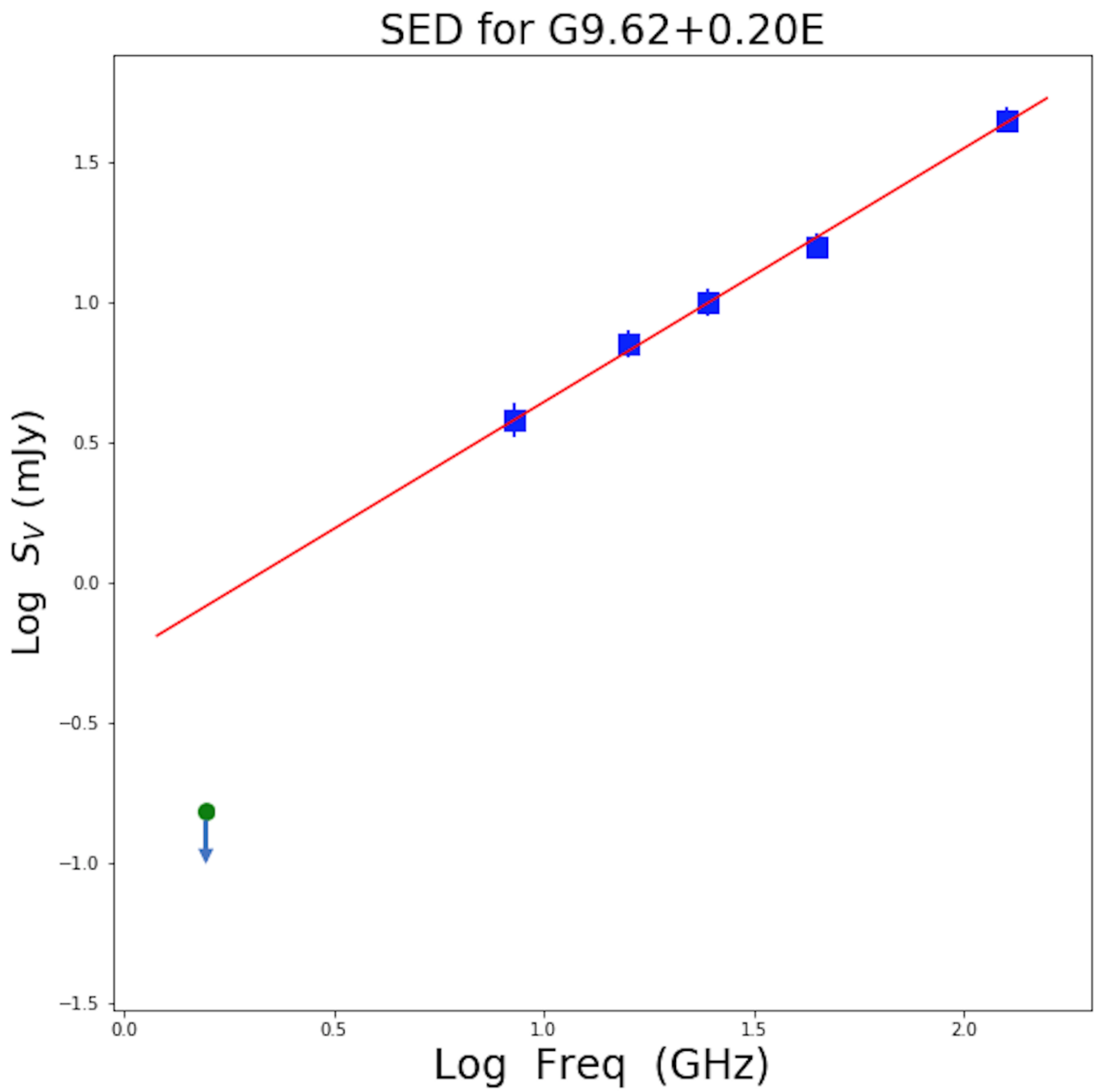

Figure 3.24: Spectral index plot of the G9.62 + 0.20E HII region. Shown in blue squares are the flux density values from different high frequencies adapted from Franco et al. (2000). The red line is the least squares fit to the higher frequency detections only. Plotted in green circle is the $3\sigma$ upper limit on the flux density for the G9.62 + 0.20E star forming region at 1.5 GHz.

In the field of view of G9.62 + 0.20E two UCHII regions were detected. The northerly source observed coincides with the position of G9.62 + 0.20C. Table 3.7 gives the position and the flux density of G9.62 + 0.20C. A previous observation by Kurtz et al. (1994) at 8.6 GHz measured a flux density of 175 mJy whereas at 4.9 GHz Garay et al. (1993) measured 50 mJy. Figure 3.25 shows the continuum emission in G9.62 + 0.20C resolved into two objects. The flux density quoted is for the two objects, the size of the structure however cannot be determined by Gaussian fit hence an estimate of 3.93 arcsec × 2.31 arcsec is made by inspection. The measured flux of 22.1 mJy compares favourably with the flux of 26 mJy at 1.4 GHz measured by Becker et al. (1994).

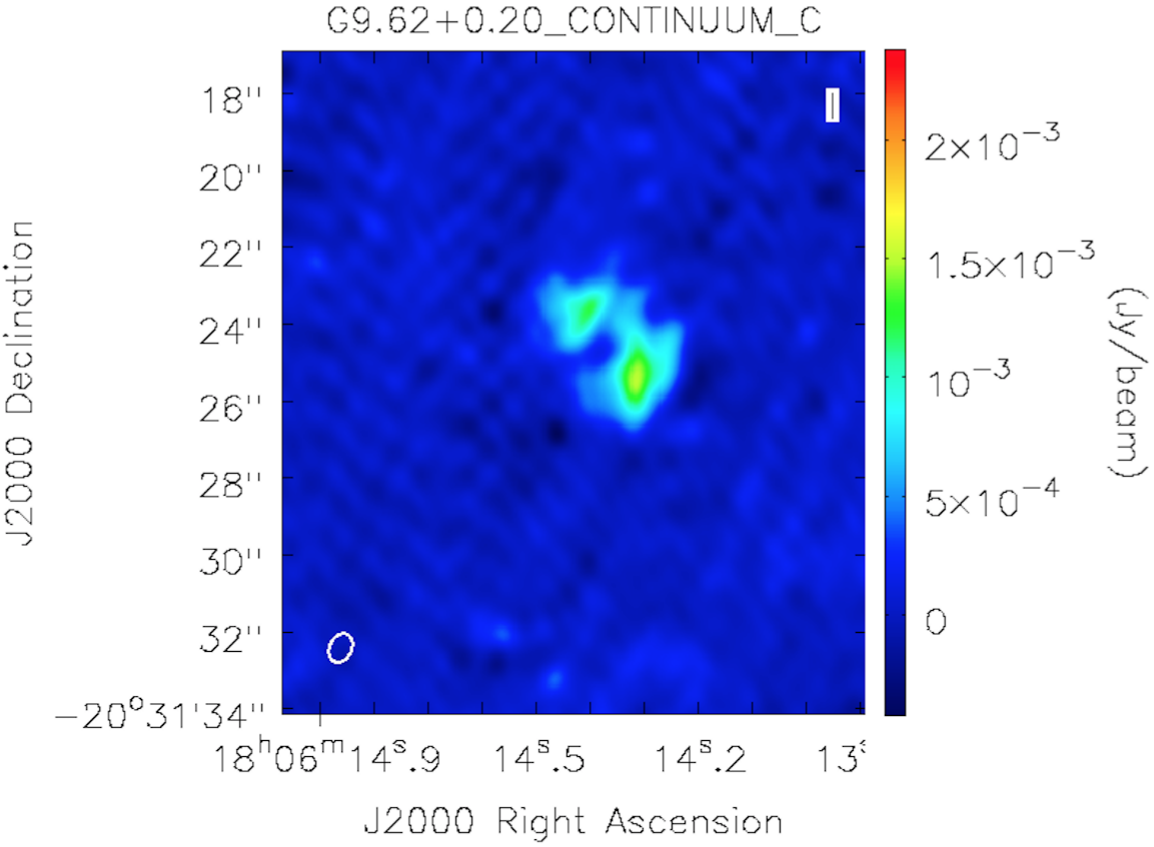

Figure 3.25: Image of the L-band radio continuum emission of G9.62 + 0.20C shown in colour scale. Shown at the lower left corner of the image is the synthesized beam of size 0.78 arcsecs × 0.57 arcsecs at a position angle of −25.36 degrees.

The more southerly detection is the UCHII region associated with G9.62 + 0.20D. The radio continuum emission from G9.62 + 0.20D is shown in Figure 3.26 and Table 3.7 presents the positions and flux density, 11.84 mJy, recorded for the source. A flux density of 70 mJy at 4.9 GHz had been reported previously by (Garay et al., 1993) whereas a flux of 65.8 mJy was measured at 8.6 GHz by Kurtz et al. (1994). At 1.4 GHz an upper limit of 17 mJy is reported by Becker et al. (1994) but inspection of the cut out images indicates a source with a flux of around 10 mJy which is consistent with the recorded flux of 11.84 mJy.

Table 3.7: Positions and flux densities of the L-band continuum associated with source C, D and E in G9.62 + 0.20. The expected position of the source E is adopted from Sanna et al. (2015). For G9.62 + 0.20E the peak flux is given by the non-detection upper limit.

| Source | $\alpha$<br>(J2000)(h m s) | Error<br>($''$) | $\delta$<br>(J2000)($^\circ\ '\ ''$) | Error<br>($''$) | Integrated flux<br>(mJy) | Peak flux<br>(mJy/beam) | Rms<br>($\mu$Jy/beam) |
|---|---|---|---|---|---|---|---|
| G9.62 + 0.20C | 18 : 06 : 14.3522 | 0.010 | −20 : 31 : 24.652 | 0.013 | $22.1 \pm 1.9$ | $1.50 \pm 0.09$ | 52 |
| G9.62 + 0.20D | 18 : 06 : 14.9514 | 0.011 | −20 : 31 : 42.620 | 0.045 | $11.84 \pm 0.46$ | $2.38 \pm 0.10$ | 52 |
| G9.62 + 0.20E | 18 : 06 : 14.6562 | – | −20 : 31 : 31.671 | – | $< 0.16$ | – | 52 |

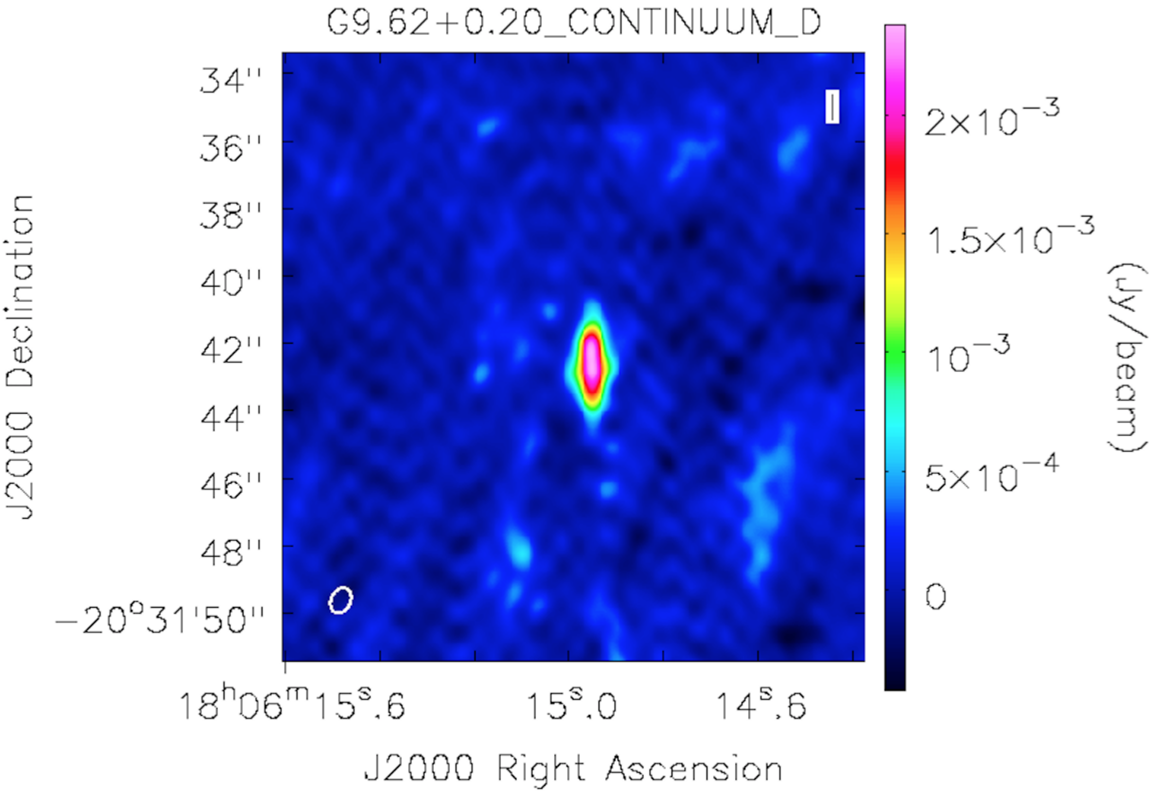

Figure 3.26: Image of the L-band radio continuum emission of G9.62 + 0.20D with a deconvolved size of $(2.090 \pm 0.106)$ arcsecs × $(0.781 \pm 0.025)$ arcsecs and a position angle of $(1.9 \pm 1.4)$ degrees shown in colour scale. At the lower left corner of the image is the synthesized beam of size 0.78 arcsecs × 0.57 arcsecs at a position angle of −25.36 degrees.

When the continuum results for G9.62 + 0.20C in Figure 3.25 and G9.62 + 0.20D in Figure 3.26 are compared to the results for G9.745 + 0.106 in Figure 3.17 and the phase calibrator in Figure 3.16 it can be seen that the beam size is larger and rounder than expected for the full array. This is due to the loss of the long north-south Cambridge baselines as seen in the solutions from Figure 3.18.

### 3.5.2 Maser spots in the LCP and RCP components at 1.665 GHz and 1.667 GHz

From the emission channels in the cubes moment maps of the maser emissions were obtained. Displayed from Figure 3.27 to Figure 3.37 are the moment maps showing the flux density and velocity distribution of some of the LCP and RCP components of both the 1665 MHz and 1667 MHz maser lines. The rms noise within the cube of both the 1665 MHz and the 1667 MHz maser spots were typically 200 mJy. Also presented in Table 3.8 are the positions and flux densities of the maser spots. Some weak spots do not show in the maps because the threshold range set to eliminate the side lobes in the image was above the flux density of these spots. The spectral features here are compared with the results from Chapter 2.

Within the cube for the 1665 MHz maser lines two spots were found for the LCP component with spots shown in Figure 3.27 and Figure 3.28. In Figure 3.29 the spectrum for the LCP component of the 1665 MHz maser shows two lines at 1.64 km/s and 1.95 km/s. In comparison these two velocity components appear blended in Figure 2.16 of Chapter 2.

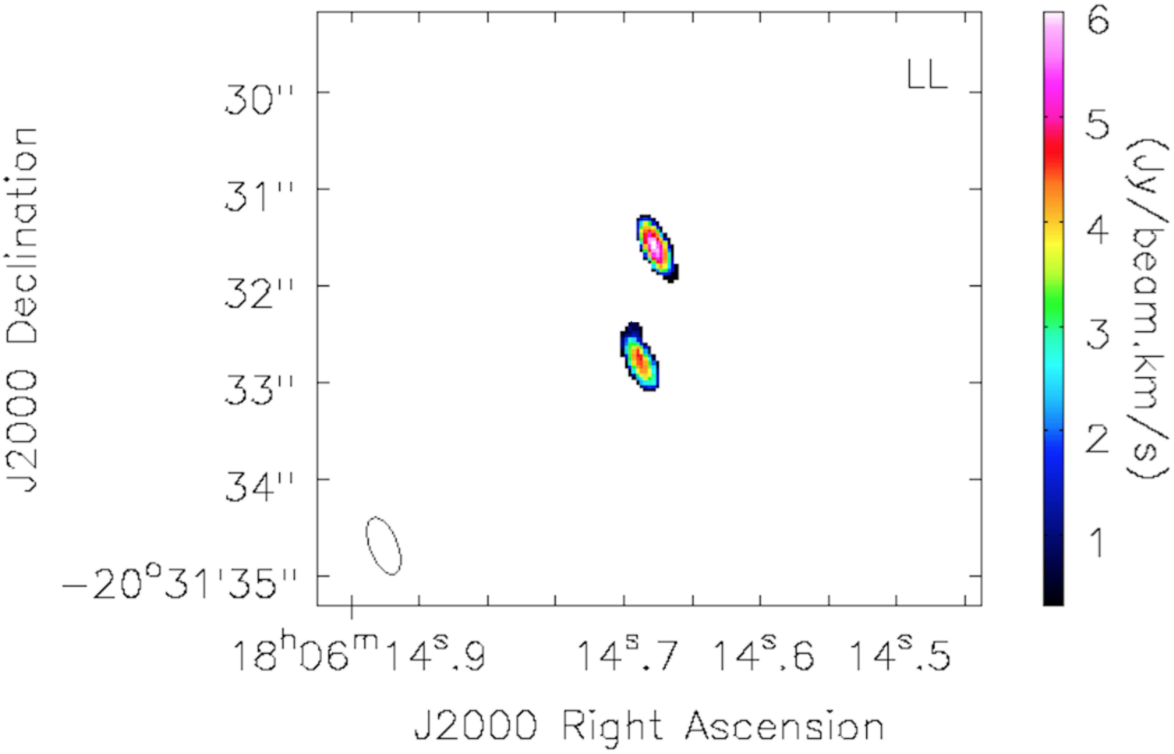

Figure 3.27: The flux density distribution for the 1.665 GHz LCP component over the intensity range 7.5 Jy/beam to 100 Jy/beam. At the lower left corner of the image is the synthesized beam.

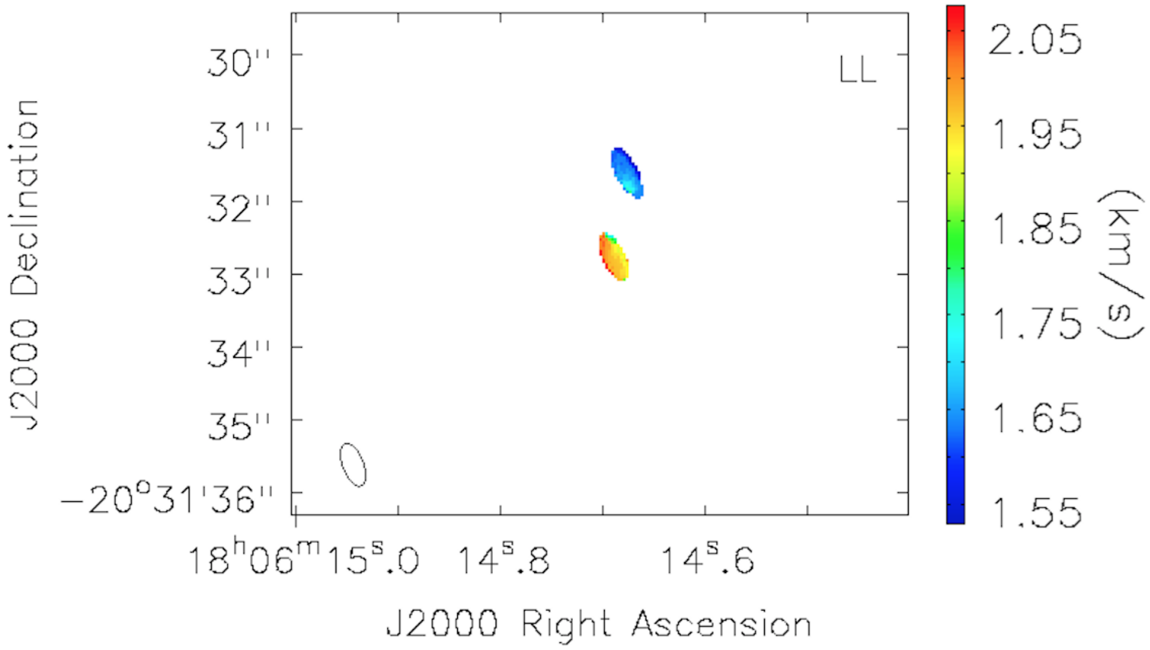

Figure 3.28: First moment map for the LCP component of the 1.665 GHz maser line shown in colour scale. The maser spots in the 1.64 km/s and 1.95 km/s velocity channels are displayed. At the lower left corner of the image is the synthesized beam.

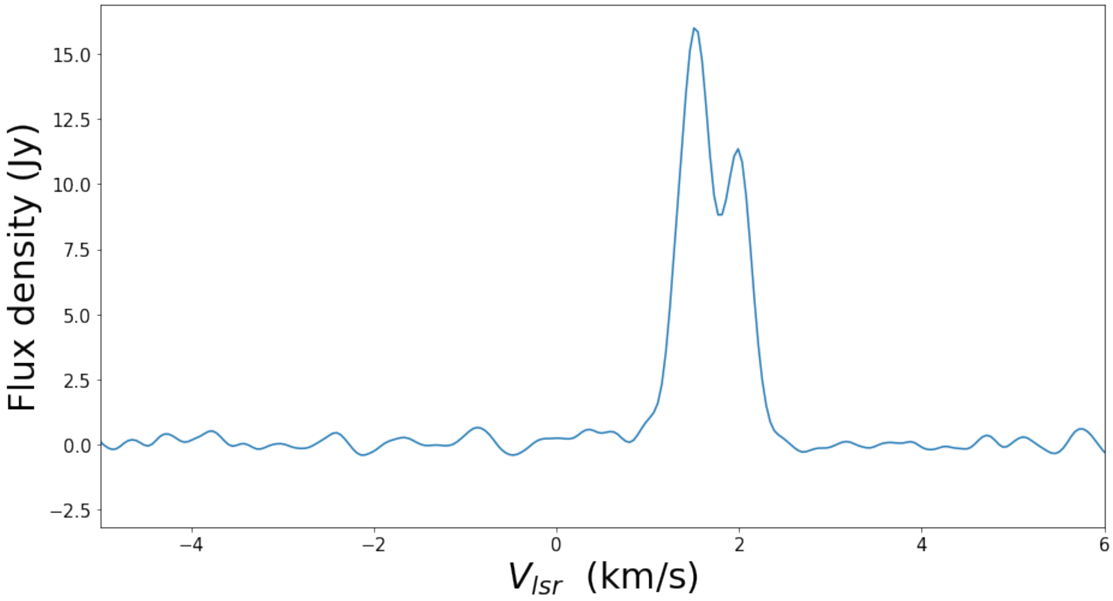

Figure 3.29: The spectrum for the LCP component of the 1665 MHz OH maser line.

The RCP component of the 1665 MHz maser line had three spots of which only the spot at velocity channel 1.38 km/s is shown in Figure 3.30 and Figure 3.31. The spectrum for the

RCP component of the 1665 MHz maser line shown in Figure 3.32 however shows all three features at velocity channels 1.38 km/s, 2.12 km/s and 5.29 km/s. The components of Figure 3.29 correspond with the spectral features in Figure 2.17 of Chapter 2.

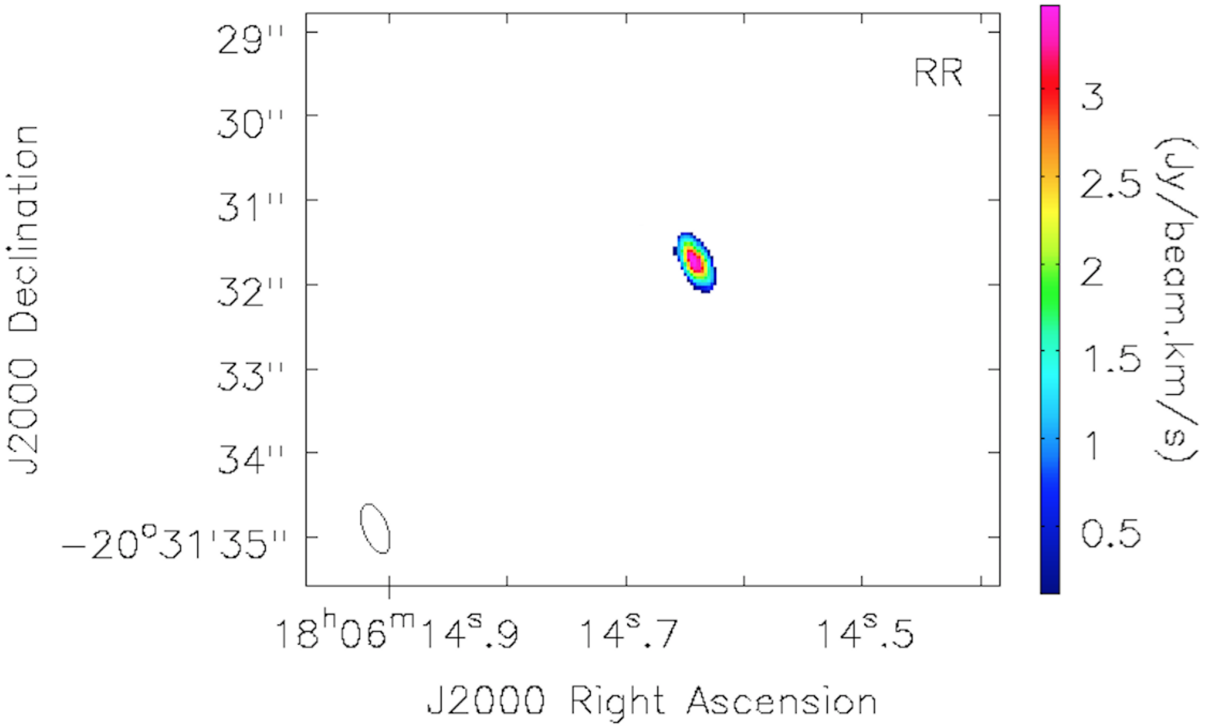

Figure 3.30: The flux density distribution for the RCP component of the 1.665 GHz maser line over the intensity range 2.5 Jy/beam to 100 Jy/beam. At the lower left corner of the image is the synthesized beam.

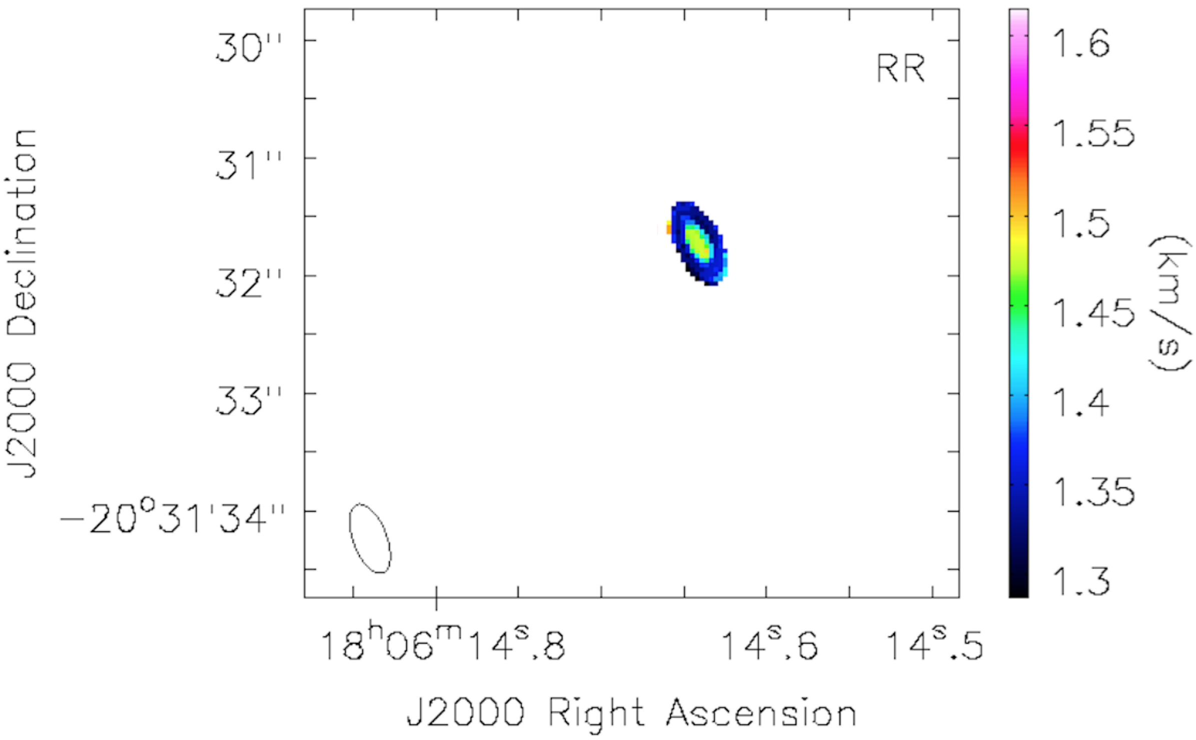

Figure 3.31: First moment map for the RCP component of the 1.665 GHz maser line shown in colour scale. The maser spots in the 1.38 km/s velocity channel is displayed. At the lower left corner of the image is the synthesized beam.

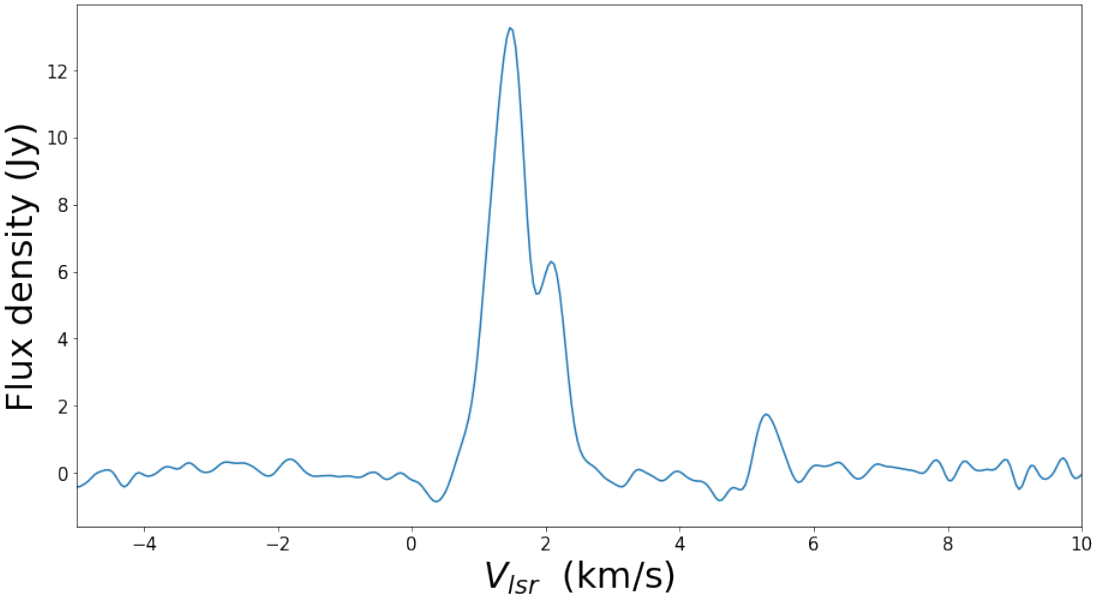

Figure 3.32: The spectrum for the RCP component of the 1665 MHz OH maser line showing the maser lines at the velocity channels 1.38 km/s, 2.12 km/s and 5.29 km/s.

Three spots were found in the cube of the LCP component of the 1.667 GHz maser line. Only one maser spot at velocity channel 1.77 km/s is presented in Figure 3.33 and Figure 3.34. In the spectrum for the LCP component of the 1.667 GHz maser line presented in Figure 3.35 all three features at velocity channels −0.95 km/s, 1.77 km/s and 2.56 km/s are shown. These features correspond with the spectral features in Figure 2.18 of Chapter 2 .

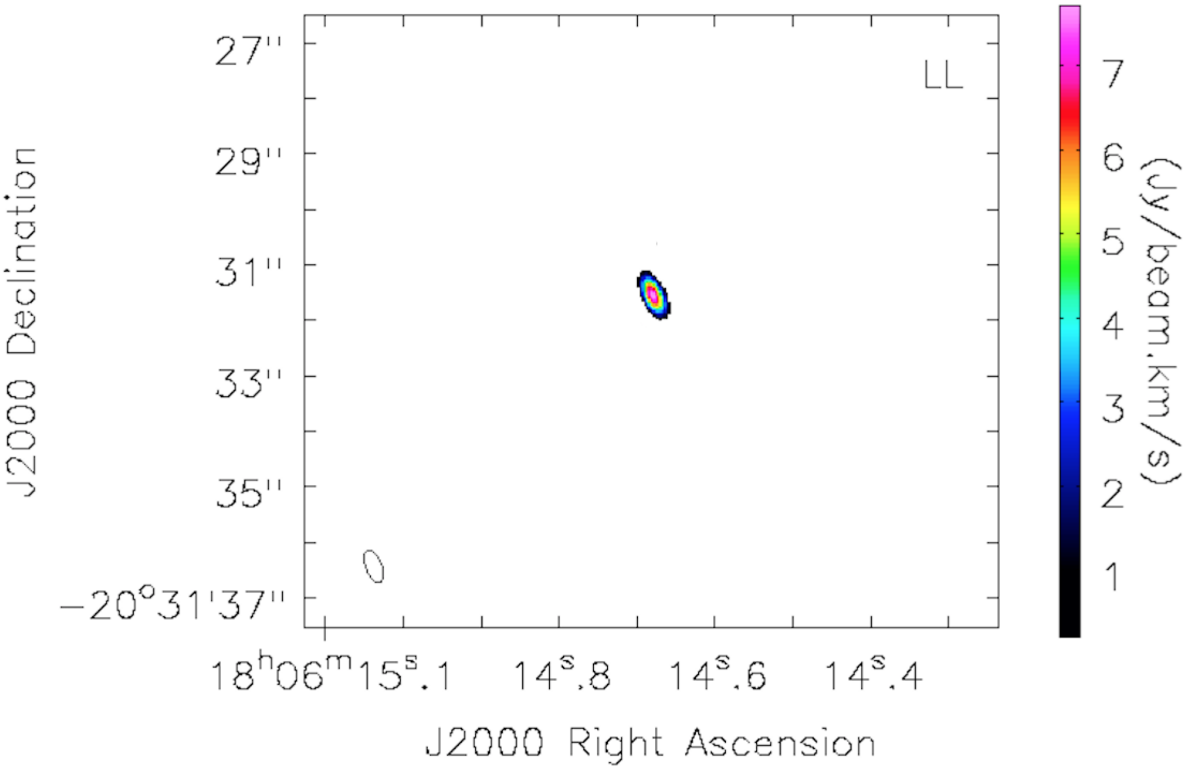

Figure 3.33: The flux density distribution for the LCP component of the 1.667 GHz maser line over the intensity range 4.5 Jy/beam to 100 Jy. At the lower left corner of the image is the synthesized beam.

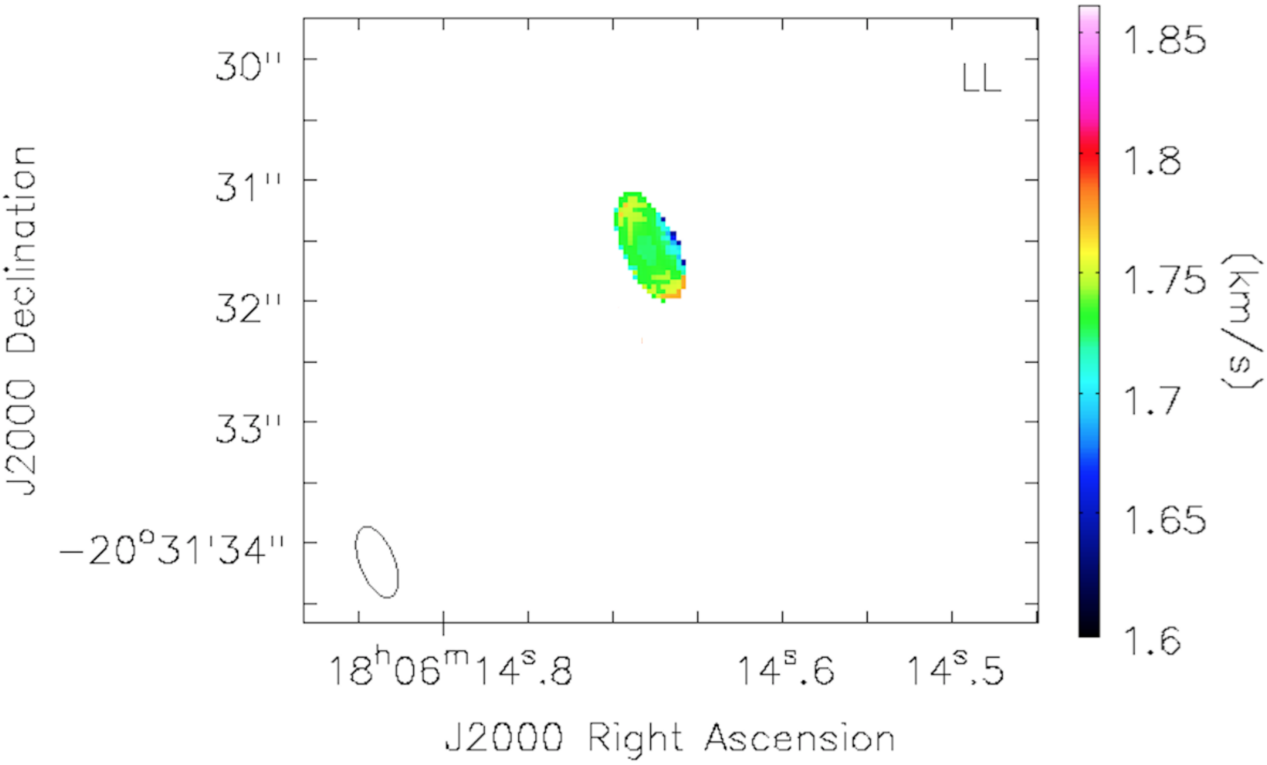

Figure 3.34: First moment map for the LCP component of the 1.667 GHz maser line shown in colour scale. The maser spot in the 1.77 km/s velocity channel is displayed. At the lower left corner of the image is the synthesized beam.

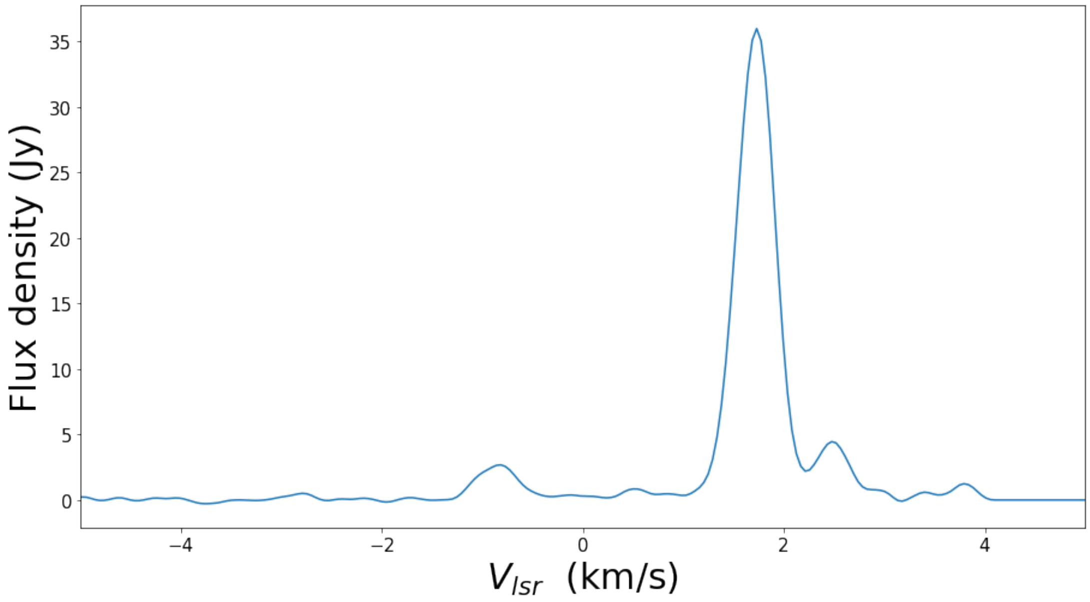

Figure 3.35: The spectrum for the LCP component of the 1667 MHz OH maser line showing the spectral features at −0.95 km/s, 1.77 km/s and 2.56 km/s.

In the cube for the RCP component of the 1.667 GHz maser line four spots were recorded.

Three maser spots in the velocity channels 0.63 km/s, 1.69 km/s and 2.21 km/s are shown in Figure 3.36 and Figure 3.37. All four features are seen in the spectrum in Figure 3.38. In comparison with Figure 2.19 of Chapter 2 all the spectral features are also seen.

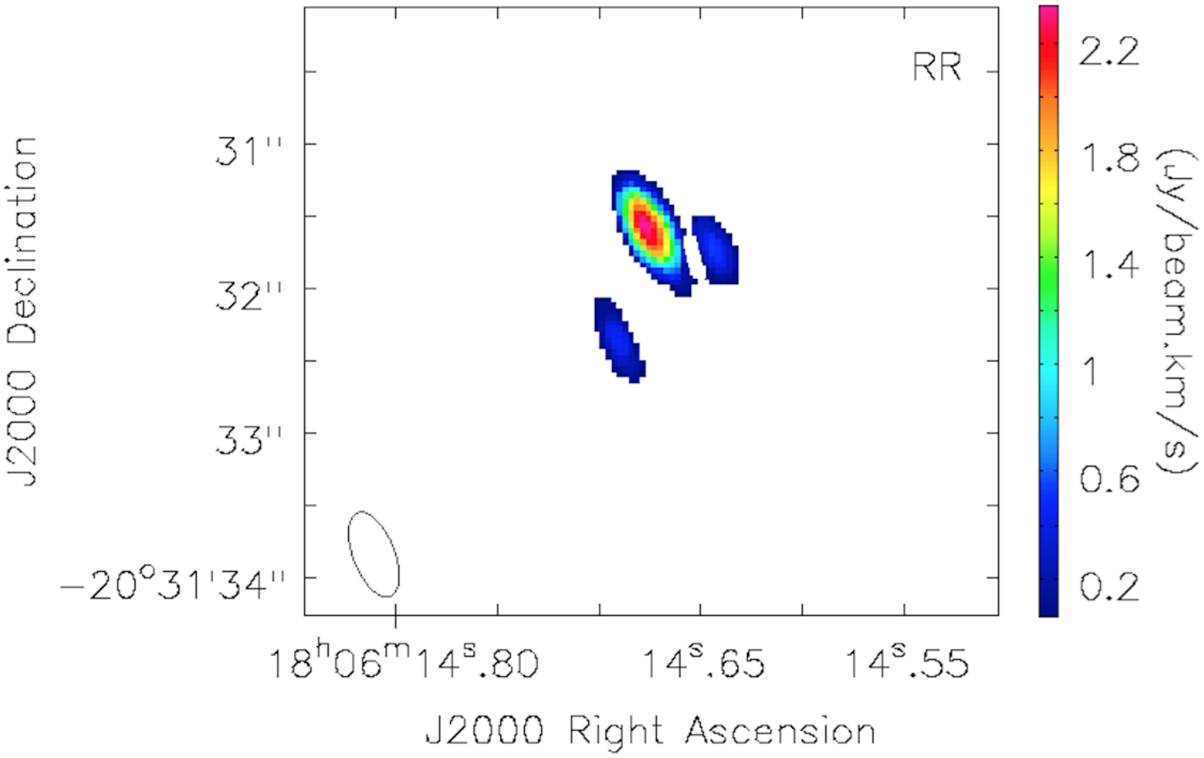

Figure 3.36: The flux density distribution for the RCP component of the 1.667 GHz maser line over the intensity range 1.3 Jy/beam to 100 Jy/beam. At the lower left corner of the image is the synthesized beam.

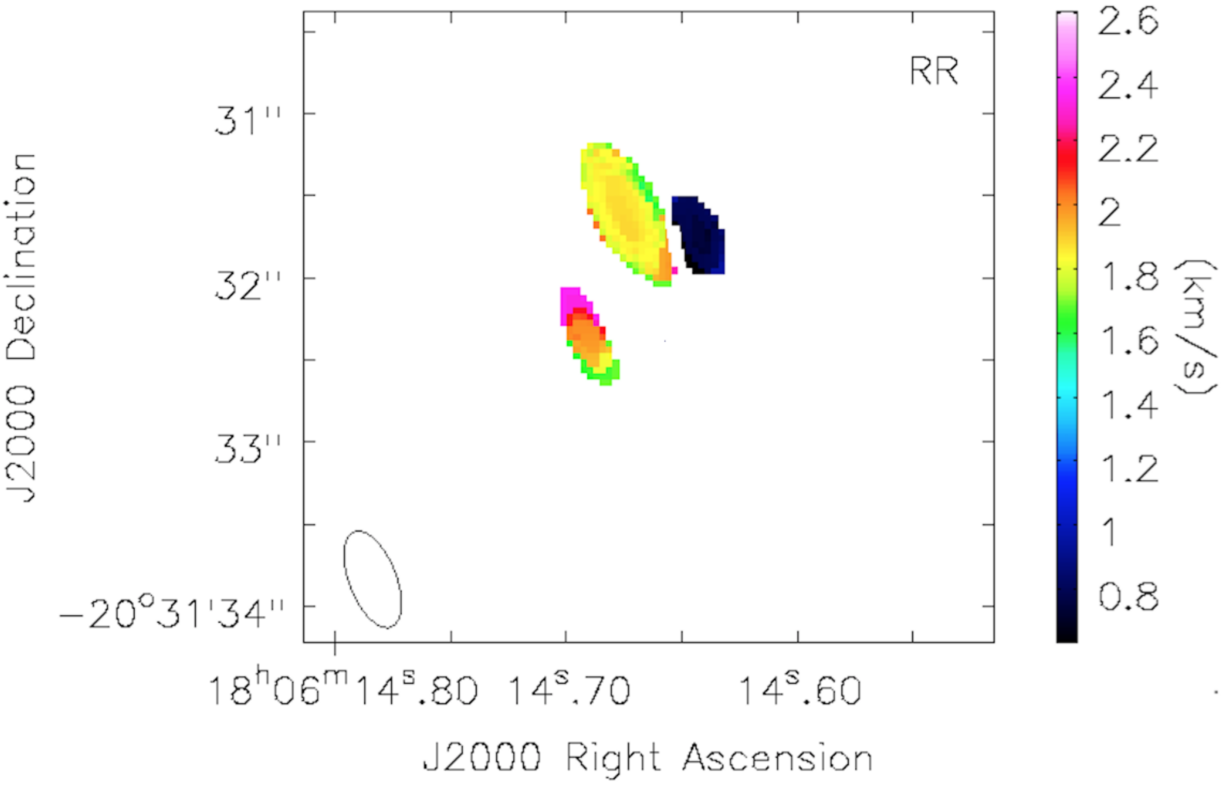

Figure 3.37: First moment map for the RCP component of the 1.667 GHz maser line shown in colour scale. The maser spots in the 0.63 km/s, 1.69 km/s and 2.21 km/s velocity channels are displayed. At the lower left corner of the image is the synthesized beam.

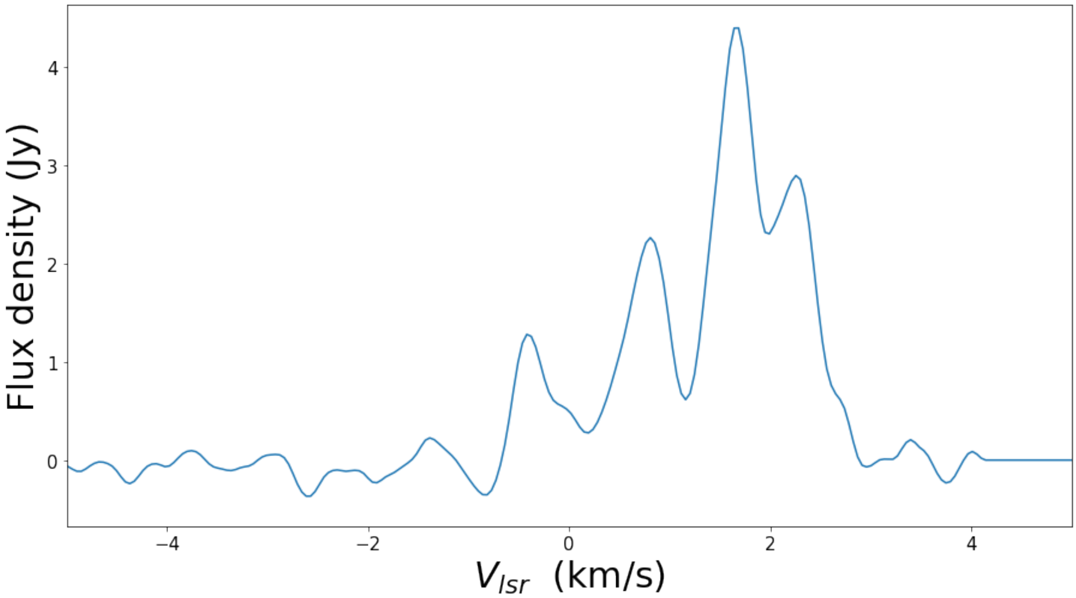

Figure 3.38: The spectrum for the RCP component of the 1667 MHz OH maser line showing the spectral features at velocity channels −0.46 km/s, 0.63 km/s, 1.69 km/s and 2.21 km/s.

More flux was measured in the LCP and RCP components of the 1665 MHz line than the 1667 MHz line. The flux measured in the LCP component of the 1665 MHz line was greater than that measured for the RCP component. The 1667 MHz line followed this same pattern but with lower flux densities in the RCP. The equatorial coordinate position measurements, flux densities and velocity channels of the LCP and RCP components of the 1665 MHz and 1667 MHz maser are presented in Table 3.8. The first column of Table 3.8 gives the identity number for the maser spots in this work. The second column gives the OH maser transitions and their polarisations. In the third column the velocity channels within which the maser spots are found are given. The fourth and the sixth columns specify the right ascension ($\alpha$) and declination ($\delta$) of the maser spots determined by Gaussian fit. The leading terms of the positions are $\alpha$ (J2000)= $18^{\mathrm{h}}\ 06^{\mathrm{m}}$ and $\delta$ (J2000)= $-20^{\circ}\ 31'$. The fifth and seventh columns give the corresponding errors for $\alpha$ and $\delta$ respectively. The eighth and ninth columns give the integrated flux density and peak flux density respectively from the present work. In the tenth column the rms noise levels in the image channels are given. The eleventh and the twelfth columns give the maser feature numbers as they appear in the numbered rows of Table 2 of Sanna et al. (2015) and Table of 3 Fish et al. (2005) respectively.

The flux densities measured in the 1.665 GHz and 1.667 GHz LCP and RCP components are higher than the total intensity results in Figure 3 and Figure 4 of Goedhart et al. (2019). Likewise, the peak flux densities listed in Table 3.8 of the present work are also higher than those seen in the high resolution measurements of Sanna et al. (2015). For the LCP component of the 1.665 GHz maser line spot ID 1 measured 16.08 Jy whereas its corresponding feature 12 in Sanna et al. (2015) measured 10.01 Jy. In the RCP component of the 1.665 GHz maser line spot ID 3 measured 6.56 Jy whereas feature 18 in Sanna et al. (2015) measured 5.00 Jy. In spot ID 4 a flux density of 3.10 Jy was measured whereas its corresponding feature in Sanna et al. (2015) measured 4.35 Jy. For the LCP component of the 1.667 GHz line, the reference and brightest maser spot in Sanna et al. (2015) referred to in the present work as spot ID 7 measured a flux of 22.97 Jy as against the 21.15 Jy reported in Sanna et al. (2015). Spot ID 6 measured 1.1 Jy against the 0.62 Jy reported in Sanna et al. (2015). The RCP component of the 1.667 GHz as well followed the same pattern. Spot ID 9 measured 0.63 Jy more flux than

Table 3.8: Absolute positions, velocities and flux densities of the polarisations of the mainline OH masers in G9.62 + 0.20E.

| Maser spot ID | Transition (GHz) | $V_{LSR}$ (km/s) | $\alpha$ (J2000)(s) | Error ($''$) | $\delta$ (J2000)($''$) | Error ($''$) | Integrated flux density (Jy) | Peak flux density (Jy/beam) | Rms (Jy/beam) | Sanna feature | Fish feature |
|---|---|---|---|---|---|---|---|---|---|---|---|
| 1 | 1.665 LCP | 1.64 | 14.6788 | 0.0034 | 31.5694 | 0.0072 | 16.12 ± 0.61 | 16.08 ± 0.32 | 0.247 | 12 | 9 |
| 2 | | 1.95 | 14.6901 | 0.0032 | 32.7603 | 0.0071 | 15.79 ± 0.31 | 14.93 ± 0.31 | 0.337 | – | 10 |
| 3 | 1.665 RCP | 1.38 | 14.6402 | 0.0093 | 31.7291 | 0.009 | 8.33 ± 0.40 | 6.56 ± 0.19 | 0.115 | 18 | 3 |
| 4 | | 2.12 | 14.6412 | 0.0085 | 31.749 | 0.013 | 3.46 ± 0.24 | 3.10 ± 0.12 | 0.109 | 19 | 1 |
| 5 | | 5.29 | 14.6812 | 0.0094 | 32.738 | 0.018 | 1.32 ± 0.07 | 1.10 ± 0.13 | 0.187 | – | 10 |
| 6 | 1.667 LCP | −0.95 | 14.6603 | 0.0068 | 31.922 | 0.012 | 1.98 ± 0.13 | 1.79 ± 0.06 | 0.153 | 3 | – |
| 7 | | 1.77 | 14.6787 | 0.0028 | 31.5581 | 0.0057 | 22.97 ± 0.68 | 22.04 ± 0.35 | 0.107 | 1 | 25 |
| 8 | | 2.56 | 14.6883 | 0.0076 | 32.786 | 0.016 | 2.57 ± 0.21 | 2.32 ± 0.10 | 0.103 | – | 26 |
| 9 | 1.667 RCP | −0.46 | 14.657 | 0.016 | 31.970 | 0.029 | 1.21 ± 0.11 | 0.89 ± 0.17 | 0.101 | 11 | – |
| 10 | | 0.63 | 14.644 | 0.012 | 31.763 | 0.030 | 2.17 ± 0.38 | 1.96 ± 0.24 | 0.157 | 8 | 21 |
| 11 | | 1.69 | 14.674 | 0.012 | 31.597 | 0.020 | 6.05 ± 0.51 | 4.74 ± 0.23 | 0.190 | 7 | 25 |
| 12 | | 2.21 | 14.6762 | 0.0071 | 31.566 | 0.015 | 3.60 ± 0.28 | 3.42 ± 0.14 | 0.139 | 9 | 24 |

its corresponding feature 11 in Sanna et al. (2015). Spot ID 11 measured more than double the flux density of its corresponding feature 7 in Sanna et al. (2015). The discrepancy seen when the peak flux densities in the present work and the work of Sanna et al. (2015) are compared arise in part from the variability of the masers and the higher resolution of the measurements reported in Sanna et al. (2015).

On the positions of the maser spots, spot ID 7 which is the brightest corresponds to feature 1 in Table 2 of Sanna et al. (2015). This position is only off by 46 mas in RA and 16 mas in Dec. The spot with ID 1 corresponds to feature 12 in Table 2 of Sanna et al. (2015) and feature 9 in Table 3 of Fish et al. (2005). Maser spot ID 2 corresponds to feature 10 in Fish et al. (2005). A cross reference of the positions of the spots with Sanna et al. (2015) and Fish et al. (2005) are presented in Table 3.8. The relative positions of the remaining spots agree with Sanna et al. (2015) within 50 mas. A comparison of the positional accuracy of 2 mas reported for the maser spots in Sanna et al. (2015) and the offset of about 50 mas in the present work suggests that the uncertainties in this work dominate.

## 3.6 Discussion

This chapter sought to find the positions of the 1.665 GHz and 1.667 GHz OH masers relative to their L-band HII region in G9.62 + 0.20E. This is the first L-band continuum study for the G9.62 + 0.20E massive star forming region placing a constraint on the upper limit of the detectable continuum flux density. The L-band continuum was not detected to a limit of 162 $\mu$Jy. The non-detection could be attributed to the continuum being too weak to detect or the continuum could be completely resolved out by the interferometer. However, at L-band the size of the source as extrapolated from Q-band and C-band (see Chapter 4) is estimated to be 180 mas which is comparable to the e-MERLIN beam size of 150 mas. The estimated size of 180 mas in comparison with the Q-band size of 81 mas (Sanna, 2019) suggests the source is getting larger at low frequencies. It is therefore likely the measured upper limit of 162 $\mu$Jy on the flux density is genuine and not an artefact, implying that the real flux density is less than the predicted flux of 0.6 mJy. This seems to suggest that the actual spectrum turns over steeply at low frequencies. This will be discussed further in Chapter 4.

Twelve maser spots were detected from the LCP and RCP components of both 1.665 GHz and 1.667 GHz in this thesis. The flux densities as determined by Gaussian fitting were typically similar to the results from Sanna et al. (2015). In comparing the absolute position of the RCP and LCP components of both transitions of the 1.6 GHz OH masers with previous results it has become apparent that both RA and Dec positions are in agreement with their corresponding peak positions in Table 2 of Sanna et al. (2015) to about 50 mas. The deviation in the absolute positions can be accounted for by some factors: the position accuracy of the phase calibrator and subsequent self calibration for the wide band data, and the declination of the source. The positional accuracy of the target is inferred from the quality of the phase of the phase calibrator. Self calibration on the extended $G9.745+0.106$ compromised the absolute position information of the data. Even though no self calibration was done on the spectral line results calibrations from the continuum which in itself had errors in addition to phase transfer from the phase calibrator were used to calculate the offsets for the the high resolution band calibrations. The transfer of the continuum information to the narrow band introduced uncertainties into the narrow band data which could have affected the positions of the maser lines. In addition if a brighter phase calibrator had been used there would have been no need for self calibration of the continuum and the relative position of the continuum and maser would be accurate even if the absolute position was compromised. For e-MERLIN greater accuracy in position and sensitivity is achieved at higher declinations. Thus for $G9.62+0.20E$ at a declination of $-20$ degrees the propagation of the radiation through the ionosphere compounded with the *uv* coverage of the observation causes the beam to be very elliptical and elongated. This means the low elevation of the source which causes the elongation of the beam in declination presents a large error.

# CHAPTER 4

# HIGH RESOLUTION STUDIES OF THE 6.7 GHz METHANOL MASER SPOTS AND THE C-BAND RADIO CONTINUUM IN $\mathbf{G9.62+0.20E}$

The periodically variable and nonvariable 6.7 GHz methanol maser spots in $G9.62+0.20E$ from Chapter 2 have been imaged simultaneously with the C-band continuum using the e-MERLIN array. Presented in this chapter are the observation, calibration and results of the observation of the 6.7 GHz masers and the C-band continuum.

Section 4.1 gives the observation details for the data acquisition. Aspects of the data reduction strategy employed for the 6.7 GHz maser lines and C-band continuum which differ from the strategy employed for the 1.6 GHz line and L band continuum are given in Section 4.2. Section 4.3 presents the results which are discussed and interpreted in Section 4.4.

## 4.1 Observation

The e-MERLIN interferometric array was employed to observe the 6.7 GHz methanol spectral line (narrow band) and the C-band continuum (wide band) in $G9.62+0.20E$. A total of 60.689 hours were spent on the observations out of which 20.18 hours were on the source (science target). Table 4.1 shows the date and time allocated for each session of the observations. During the observations 75 scans made up of 60 minutes on the flux calibrator $1331+305$, 57 minutes on the bandpass calibrator $1407+284$, a sequence of 3 minutes on the phase calibrator $1751-1950$ and 7 minutes on the target $1806-2031$, and finally 60 minutes on the polarization $0319+415$ calibrator were made

Table 4.1: Data observation schedule and total on source time.

| Observation Id | Run | Date | On source time (hrs) |
|---|---|---|---|
| 0 | 20170624 _C | 24 June 2017 | 4.20 |
| 1 | 20170711 _C | 11 July 2017 | 4.08 |
| 2 | 20170714 _C | 14 July 2017 | 4.20 |
| 3 | 20170716 _C | 16 July 2017 | 3.50 |
| 4 | 20170717 _C | 17 July 2017 | 4.20 |

All the data were taken in full polarization using a total bandwidth of 512 MHz. Four spectral windows placed across the C-band frequency range 6.3 GHz-6.812 GHz were employed for the continuum data collection. Table 4.2 is the summary of the parameters for the continuum data observation.

Table 4.2: Observing parameters for the C-band continuum at a central frequency of 6.5 GHz. Antenna labels: De: Defford, Cm: Cambridge, Da: Darnhall, Kn: Knockin, Mk2: Mark 2, Pi: Pickmere.

| Parameter | Specification |
|---|---|
| Project | CY5204 |
| Band | C |
| Antennas | Mk2, Pi, Da, Kn, De, Cm |
| Number of sources | 5 |
| Integration time (s) | 1.0 |
| Frequency range (GHz) | 6.300–6.812 |
| Number of spectral windows | 4 |
| Channels per spectral windows | 128 |
| Channel width (MHz ) | 1 |
| Spectral window bandwidth (MHz ) | 128 |
| Total bandwidth (MHz ) | 512 |
| Polarizations | RR, RL, LR, LL |

The continuum and the spectral line data were taken simultaneously. For the spectral line data acquisition an additional spectral window of spectral bandwidth 1 MHz was placed within spectral window 2 of the continuum configuration centred at the expected spectral line central frequency of 6.66866 GHz. The 1 MHz bandwidth spectral window was overlaid with 512 spectral channels. This resulted in the further channelisation of spectral window 2 of the continuum configuration into the high resolution channels. Table 4.3 gives the parameters used for the acquisition of the spectral line data

Table 4.3: Observing parameters for methanol lines at 6.7 GHz.

| Parameter | Specification |
|---|---|
| Project | CY5204 |
| Band | C |
| Number of sources | 5 |
| Integration time (s) | 1.0 |
| Central frequency (GHz) | 6.66866 |
| Number of spectral windows | 1 |
| Channels per spectral windows | 512 |
| Channel width (MHz) | 1.95 |
| Spectral window bandwidth (MHz)) | 1 |
| Polarizations | RR, RL, LR, LL |

Presented in Table 4.4 are the calibrators used for the observations and their flux densities at C-band. The flux calibrator was used as primary calibrator and the phase, bandpass and polarisation calibrators were used as secondary calibrators.

Table 4.4: Calibrators used for the observations at 6.7 GHz and their flux densities.

| Calibrator | Flux density (Jy) |
|---|---|
| Flux calibrator $(1331+305\ )$ | $6.5 \pm 0.1$ |
| Phase calibrator $(1751-1950)$ | $0.0832 \pm 0.0003$ |
| Band pass calibrator $(1408+284)$ | $1.51 \pm 0.01$ |
| Polarization, bandpass $(0319+415)$ | $35.90 \pm 0.22$ |

## 4.2 Data reduction

The data were calibrated with the e-MERLIN CASA pipeline (version v0.10.02). Further data processing, imaging, and analysis were carried out using the Common Astronomy Software Applications (CASA) (version 5.4.2-1, (Mcmullin, 2009)) and IPython (version 5.1.0) packages using standard procedures. The pipeline processed the data using two steps on each data set, that is, the pre-processing and the calibration, for both continuum and spectral line.

### 4.2.1 Preprocessing data

For each of the data sets, preprocessing of data involved converting the fits to measurement sets (MS) as discussed in the previous chapter. The position of the phase calibrator was corrected as was done for the L-band data during the conversion to measurement set. The spectral line data were split from the continuum data into a separate measurement set since they were taken simultaneously. The continuum data was then averaged after every 4 channels and 4 seconds. An *a priori* flagging routine was employed to flag the beginning and end of the channels of the data, and failing antennas. The beginning of each scan and any data that deviated from expected spectral behaviour were flagged. The calibration solutions from 20170717_C are used to illustrate the calibration processes in this chapter.

### 4.2.2 Continuum calibration

#### 4.2.2.1 Data flagging

The data were manually inspected and the locations of the bad datasets were written into an input file which was fed into the pipeline for flagging. For the observation made on day 20170711_C, antenna Knockin was flagged because of low sensitivity. The data were examined and the strongest maser line in spectral window 2 channel 112 on the target was masked to prevent the automatic flagger which acts on bandpass calibrated data from flagging it. Manual flagging of bad data which the automatic flagger failed to remove was also done.

#### 4.2.2.2 Gain and bandpass calibration

The same standard gain and bandpass calibration procedures as described in Chapter 3 for L-band were performed on the data after completing the flagging routines. However, during the flux scaling the absolute flux density scale was found by setting the flux densities of all the calibrators to that of 3C286 at C-band. This was multiplied by the e-MERLIN factor of 0.9393 to get a flux scale file which was used to calibrate the fluxes of the calibrators. The calibration solutions with the scaled flux densities were applied to all the calibrators. Scan averages of the phase and amplitude calibrations on the phase calibrator were plotted and are shown in Figure 4.1 and Figure 4.2 respectively. Figure 4.1 shows that the phase corrections were small as the delay solutions were already applied. In Figure 4.2 the local deviations from the bandpass shown in the amplitude solutions have been removed by assuming that the bandpass is flat in each spectral window. The calibrations were then transferred from the phase calibrator onto the target by linear interpolation. In the calibration plots that follows Antid=0 represents Darnhall, Antid=1 represents Knockin, Antid=2 represents Defford, Antid=3 represents Mark2, Antid=4 represents Pickmere, and Antid=5 represents Cambridge.

Figure 4.3 shows the image of the phase calibrator which recovers a flux of 74 mJy as shown in Table 4.5.

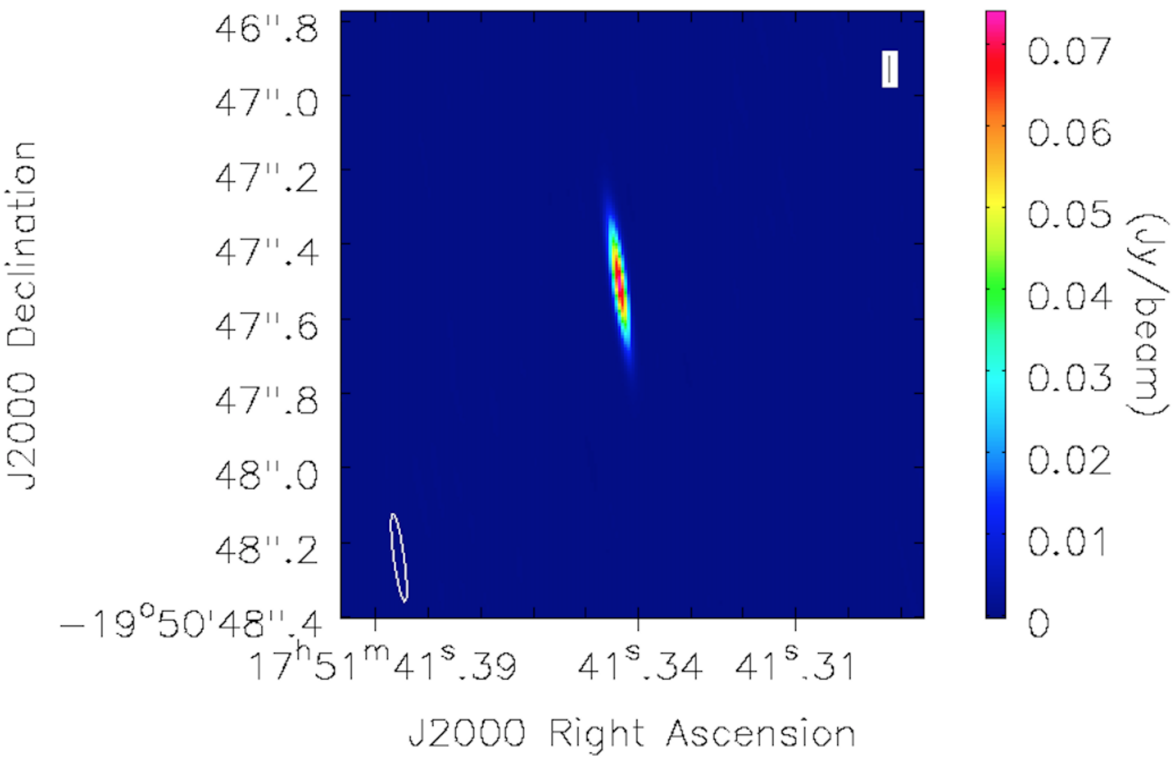

Figure 4.3: Image of the phase calibrator with a deconvolved size of $(234.59 \pm 0.30)$ mas $\times$ $(27.391 \pm 0.004)$ mas at a position angle of $(7.721 \pm 0.001)$ degrees. Shown in the lower left corner of the image is the synthesized beam.

Table 4.5: Position and flux density of Phase calibrator.

| $\alpha$ (J2000) (h m s) | Error ($''$) | $\delta$ (J2000)($^{\circ}\,'\,''$) | Error ($''$) | Integrated flux density (mJy) | Peak flux density (mJy/beam) | Rms ($\mu$Jy/beam) |
|---|---|---|---|---|---|---|
| 17 : 51 : 41.34369 | 0.00002 | −19 : 50 : 47.5058 | 0.0001 | $74.24 \pm 0.03$ | $73.94 \pm 0.11$ | 77.90 |

#### 4.2.2.3 Self calibration on the continuum

The five measurement sets were concatenated into one measurement set after the mandatory amplitude and phase calibrations. The target source was then split from the continuum data into a separate measurement set to reduce imaging time. An image of the protected spectral

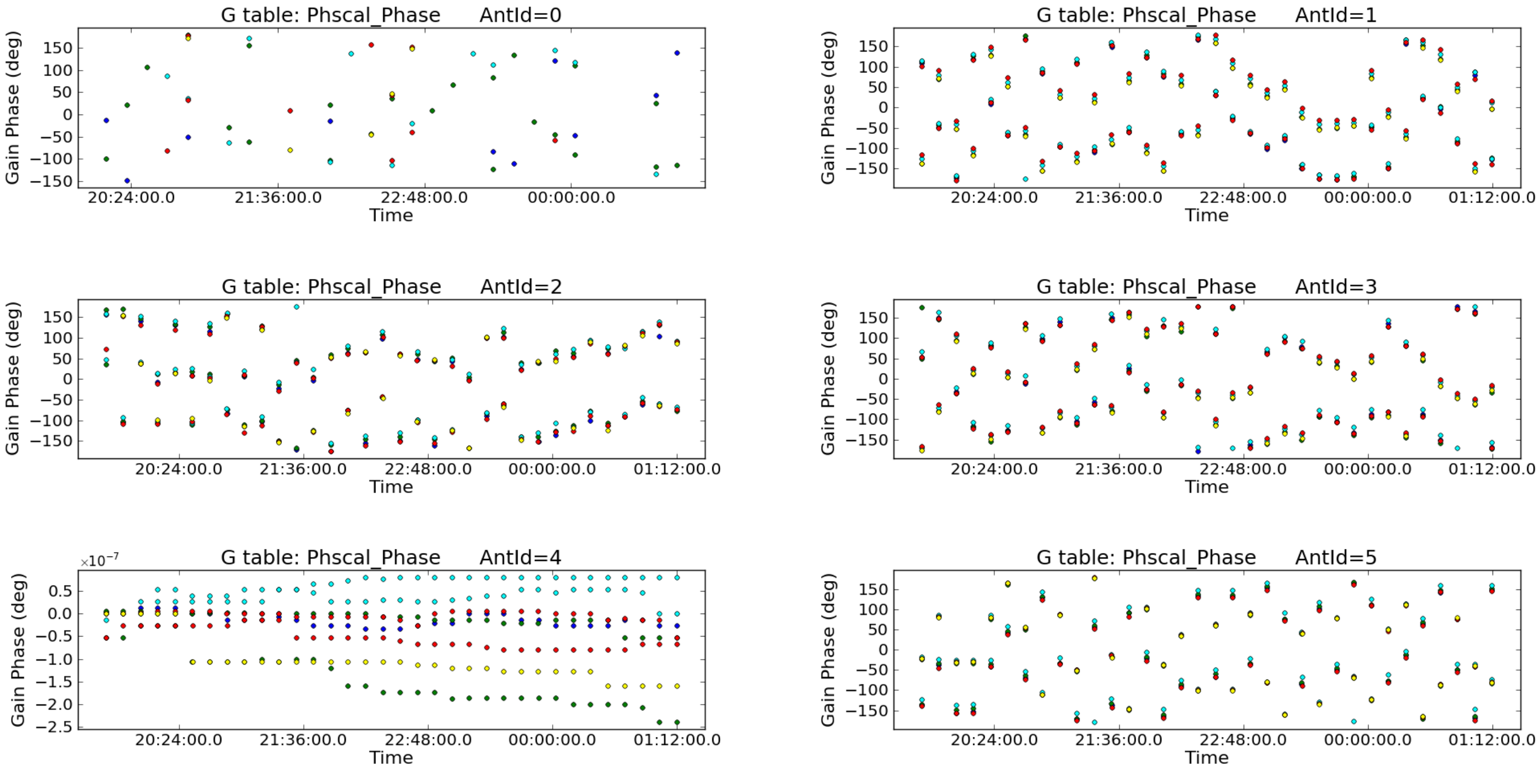

Figure 4.1: Phase calibration solutions on the phase calibrator for day 20170717. Each scan consists of the spectral windows plotted with the two polarization components shown by the different colours.

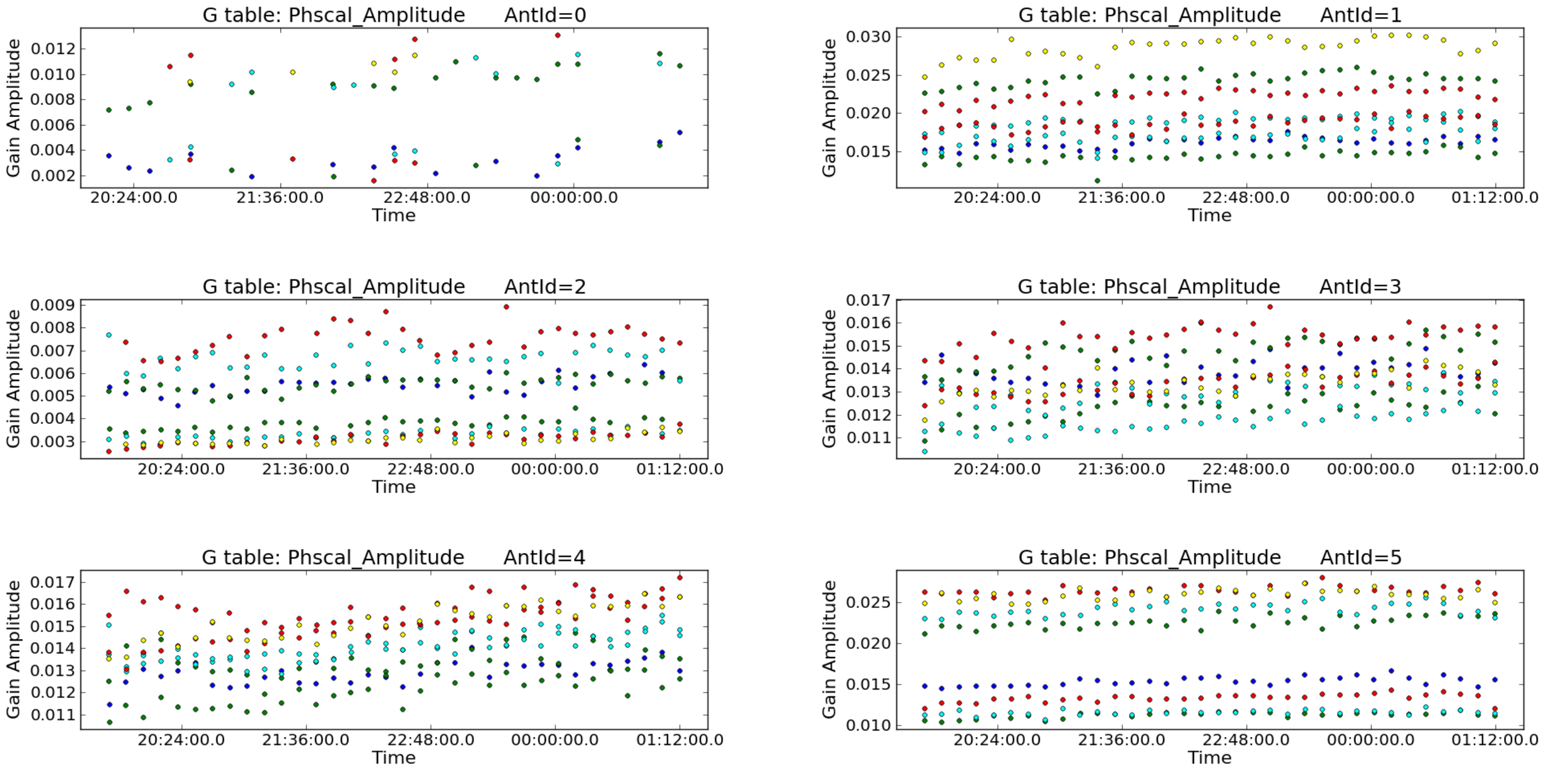

Figure 4.2: Amplitude calibration solutions on the phase calibrator for day 20170717. Each scan consists of the spectral windows plotted with two polarization components shown by the different colours.

channel 112 was made and the model of the image was Fourier transformed and saved to the model column of the measurement set. A phase self calibration of the spectral channel 112 was calculated and applied to all the four spectral windows of the continuum. An image of the phase self calibrated line was made and the model was saved. A single iteration of amplitude and phase self calibration of the spectral channel 112 was calculated and applied to the four spectral windows. The continuum map was made by making a multi frequency spectrum image of the four spectral windows excluding the maser line channel. These spectral channels also avoided the 15 adjacent channels before and after the maser channels in the bandwidth

### 4.2.3 Spectral line calibration

The high resolution (spectral line) data in the measurement set that was split from the continuum measurement set was used for the narrow band calibration. The end channels and the beginning of all scans in the data were flagged. All the data for baselines to antenna Knockin on day 20170711_C were flagged as was done for the continuum data. The continuum data was subtracted from the spectral lines in the *uv* plane by specifying the spectral line channels and fitting a first order polynomial to the spectral line.

#### 4.2.3.1 Gain calibration

For the gain solutions the phase offsets between the wide band and narrow band channelisation on the bright calibrator $0319+415$ were calculated. The gain calibration solutions from the wide band was imported from the wide band calculations, usually with no amplitude offset. This calculation assumed that the narrow band spectral windows needed no delay corrections as any slope is negligible over a narrow bandwidth.

#### 4.2.3.2 Bandpass calibration

The calculated phase offset between the wide and narrow band channelisation, and the delay solutions from the wide band were used to calculate the bandpass solutions on the narrow band bandpass exactly as was done for wide band. Presented in Figure 4.4 and Figure 4.5 are the phase and amplitude calibration respectively.

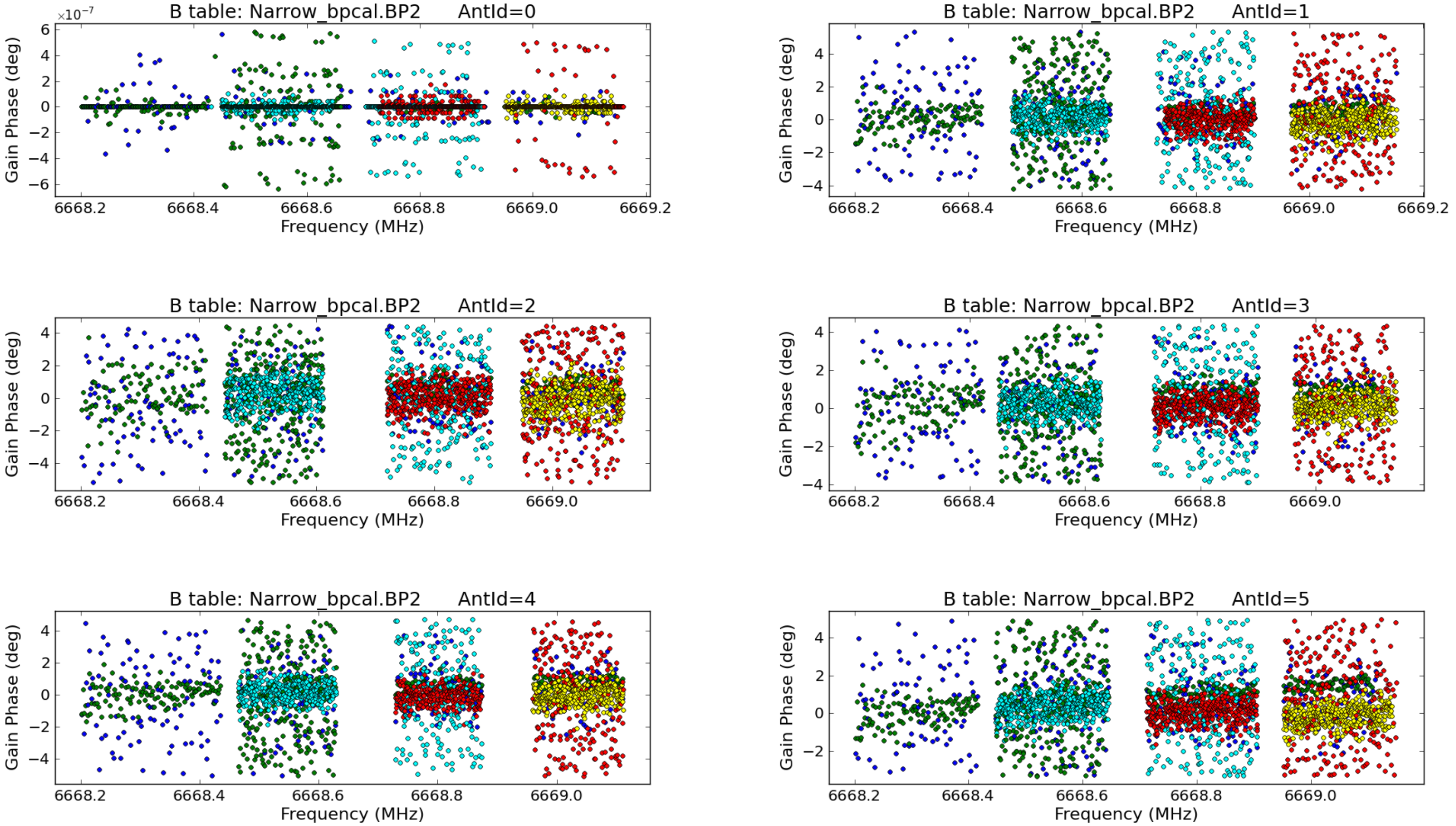

Figure 4.4: Phase component of the bandpass calibration on the narrow band data coloured by the spectral windows and the two polarization components.

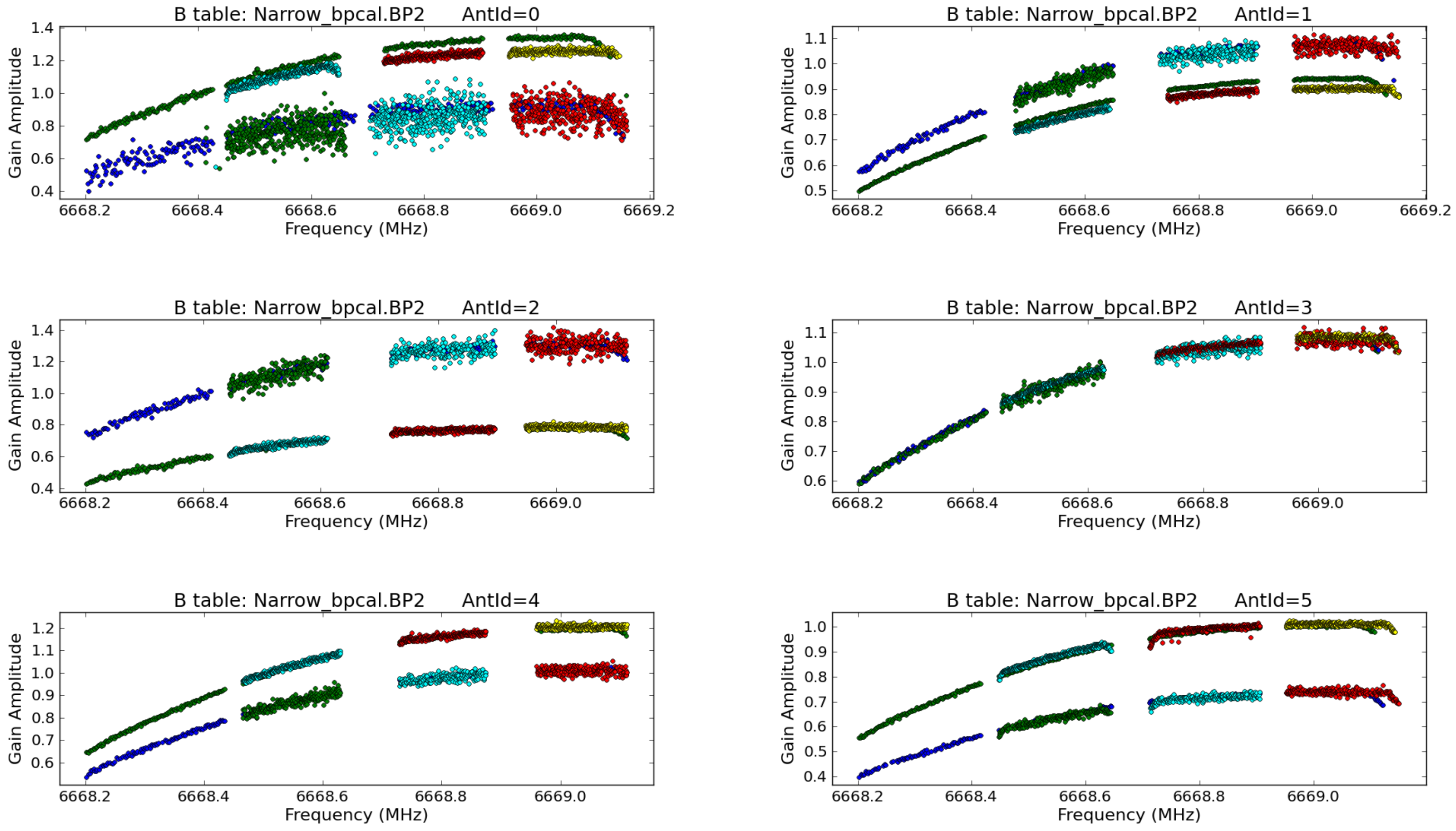

Figure 4.5: Amplitude component of the bandpass calibration on the narrow band data coloured by the spectral windows and the two polarization components.

The phase and amplitude solutions derived from the wide band phase calibrator assumed they included the flux scale. The offset calibrations were then applied to the target of the narrow band data. The target was split from the measurement set and the measurement set was shifted to the constant velocity of the methanol maser line. All corrections were then applied to the target.

#### 4.2.3.3 Self calibration on the maser line

An initial image of the maser line channel was made, Fourier transformed and saved. A phase only self calibration of the maser line was calculated and the solutions were applied to the whole high resolution data. Solutions of the phase only self calibration are presented in Figure 4.6. The model of the phase only self calibrated data was Fourier transformed and saved. An amplitude and phase only self calibration of the image was calculated and applied to the data. The amplitude solutions are shown in Figure 4.7.

A cube of all the channels was made and the channels with signals were cleaned. Images of the maser spots were saved. The flux density and rms noise were acquired as was done on the L-band data.

## 4.3 Results

Figure 4.8 shows the image of the C-band continuum. A Gaussian fit to the continuum gives the position and flux density recorded in Table 4.6. The flux density of 2.25 mJy from the free-free emission of the continuum in Figure 4.8 is consistent with the expected flux density of 2.252 mJy as extrapolated from higher frequencies using a spectral index of 095 (Franco et al., 2000) suggesting that most of the flux was recovered. The position however is offset by 320 mas in RA and 152 mas in Dec when compared with the Q-band JVLA-A position in Table 1 of (Sanna et al., 2015).

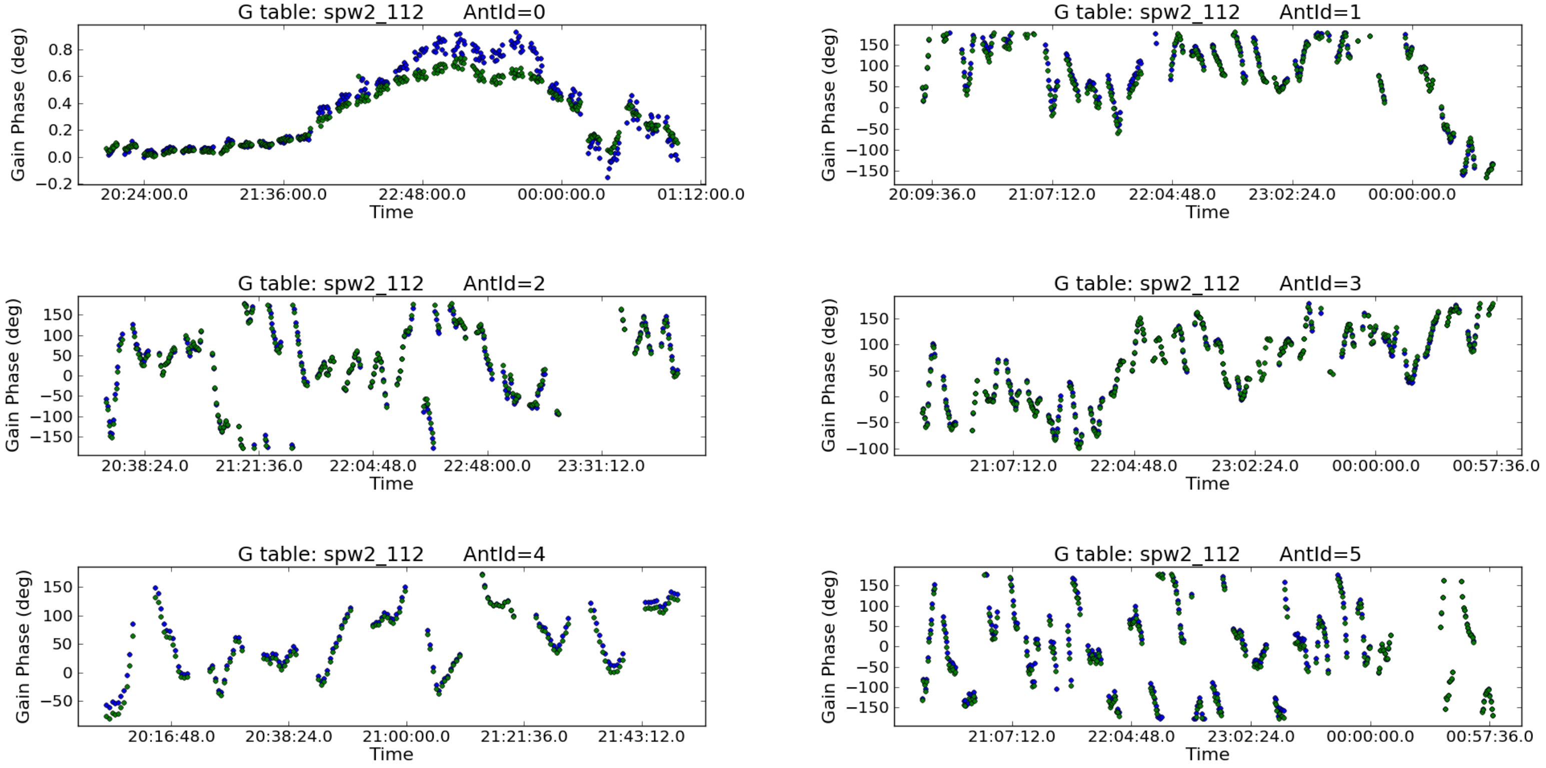

Figure 4.6: Phase self calibration solutions on the narrow band data coloured by the two polarizations.

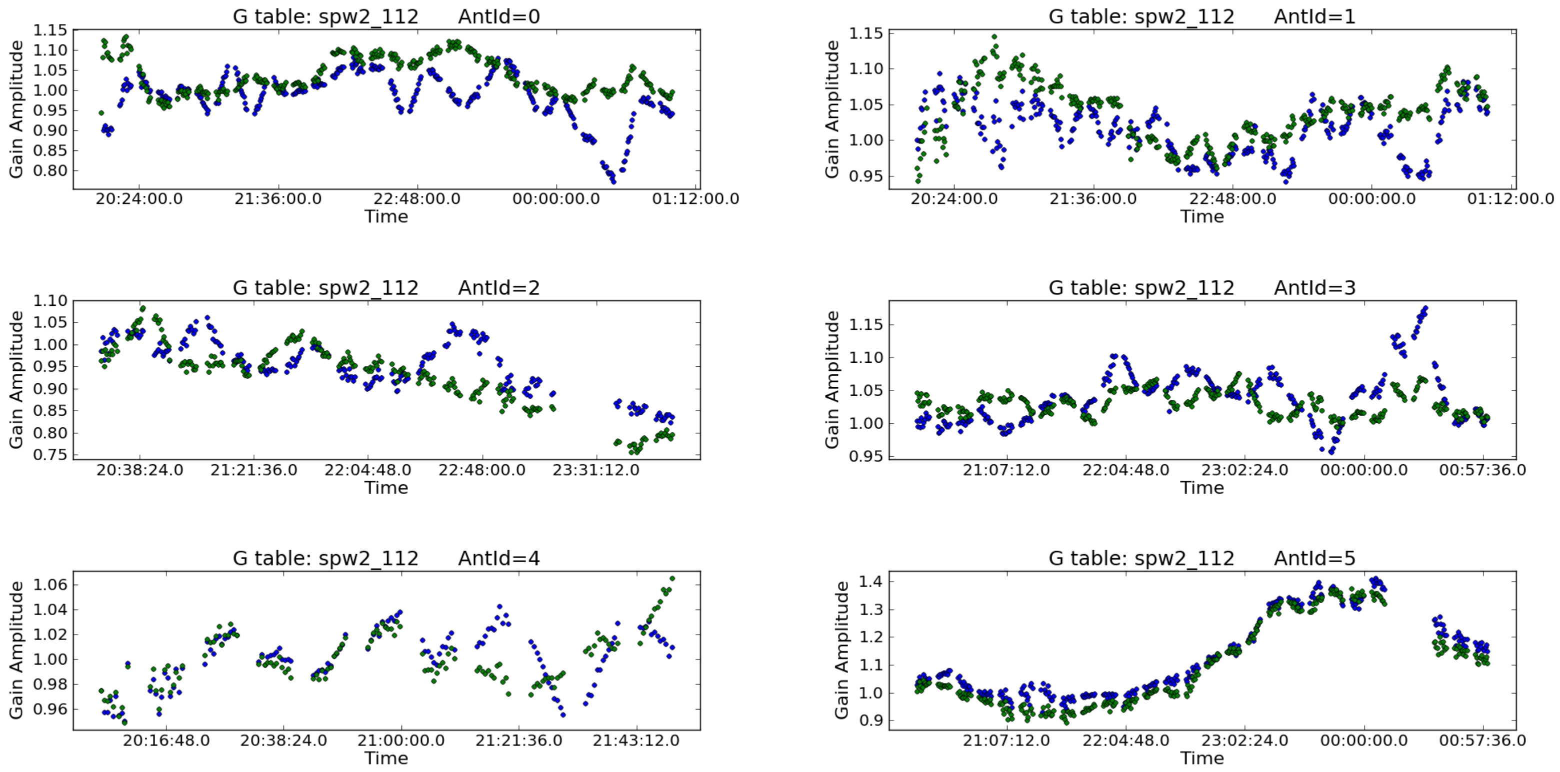

Figure 4.7: Amplitude self calibration solutions on the narrow band data coloured by the two polarizations.

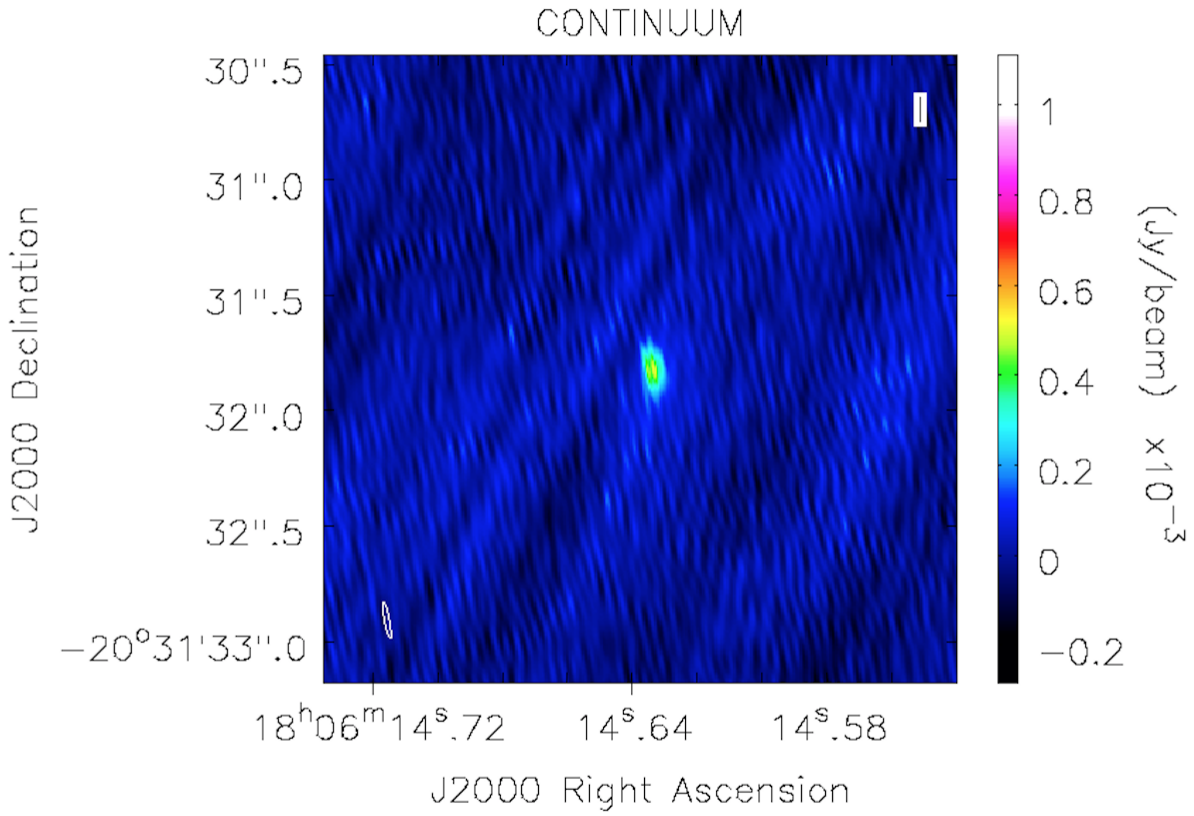

Figure 4.8: Image of the C-band radio continuum of G9.62 + 0.20E shown in colour scale. At the lower left corner of the image is the synthesized beam.

Measuring the rms noise gave a value of 50 $\mu$Jy/beam. Under good conditions a theoretical rms noise limit of 13 $\mu$Jy/beam is expected for a 12 hour continuum observation at this frequency. For a 20 hour observation a lower rms noise limit of 8 $\mu$Jy/beam is expected however a rather high rms noise has been measured. As explained in the previous chapter this is attributed to the low elevation of the source, bad weather conditions and also side lobes from nearby source G9.62 + 0.20D. Figure 5 of Franco et al. (2000) shows the spectral index plot of the flux density of the HII region associated with G9.62 + 0.20E at different wavelengths. The index was estimated to be equivalent to the slope of the line of best fit of the plot of logarithm of flux density and frequency for G9.62 + 0.20E. At these frequencies a spectral index of 0.95 ± 0.06 was calculated for this region(Franco et al., 2000). Flux densities at lower frequencies are arrived at when this plot is extrapolated. Table 4.6 presents the continuum size of G9.62 + 0.20E at Q-band and C-band.

At C-band the angular size of 130 mas converts to a physical size of 0.003 pc placing the source

Table 4.6: Position and flux density of the C-band continuum of G9.62 + 0.20E and G9.62 + 0.20D. Also given are the beam dimensions and the position angles of the maser spots.

| Source | $\alpha$ (J200)(h m s) | Error ($''$) | $\delta$ (J200)($^{\circ\prime\prime\prime}$) | Error ($''$) | Integrated flux (mJy) | Peak flux (mJy/beam) | Rms ($\mu$Jy/beam) | Deconvolved size $\Theta_{maj.}$(mas) × $\Theta_{min.}$(mas) | Position angle ($^{\circ}$) |
|---|---|---|---|---|---|---|---|---|---|
| G9.62 + 0.20E | 18 : 06 : 14.6332 | 0.0022 | −20 : 31 : 31.8232 | 0.009 | 2.25 ± 0.20 | 0.520 ± 0.001 | 50 | 165 ± 42 × 97 ± 23 | 176 ± 28 |
| G9.62 + 0.20D | 18 : 06 : 14.9103 | 0.0077 | −20 : 31 : 43.125 | 0.009 | 43.4 ± 2.0 | 1.24 ± 0.02 | 50 | 734 ± 19 × 541 ± 16 | 58.9 ± 3.9 |

in the hypercompact category in the Kurtz-Franco classification system (Kurtz and Franco, 2002). The VLA configuration A beam size is similar to the e-MERLIN C-band beam size; therefore, the measured VLA Q-band size of 81 mas for this source (Sanna et al., 2015) translates to a physical size of 0.002 pc. The results presented in the present work suggest the source is getting larger at low frequencies.

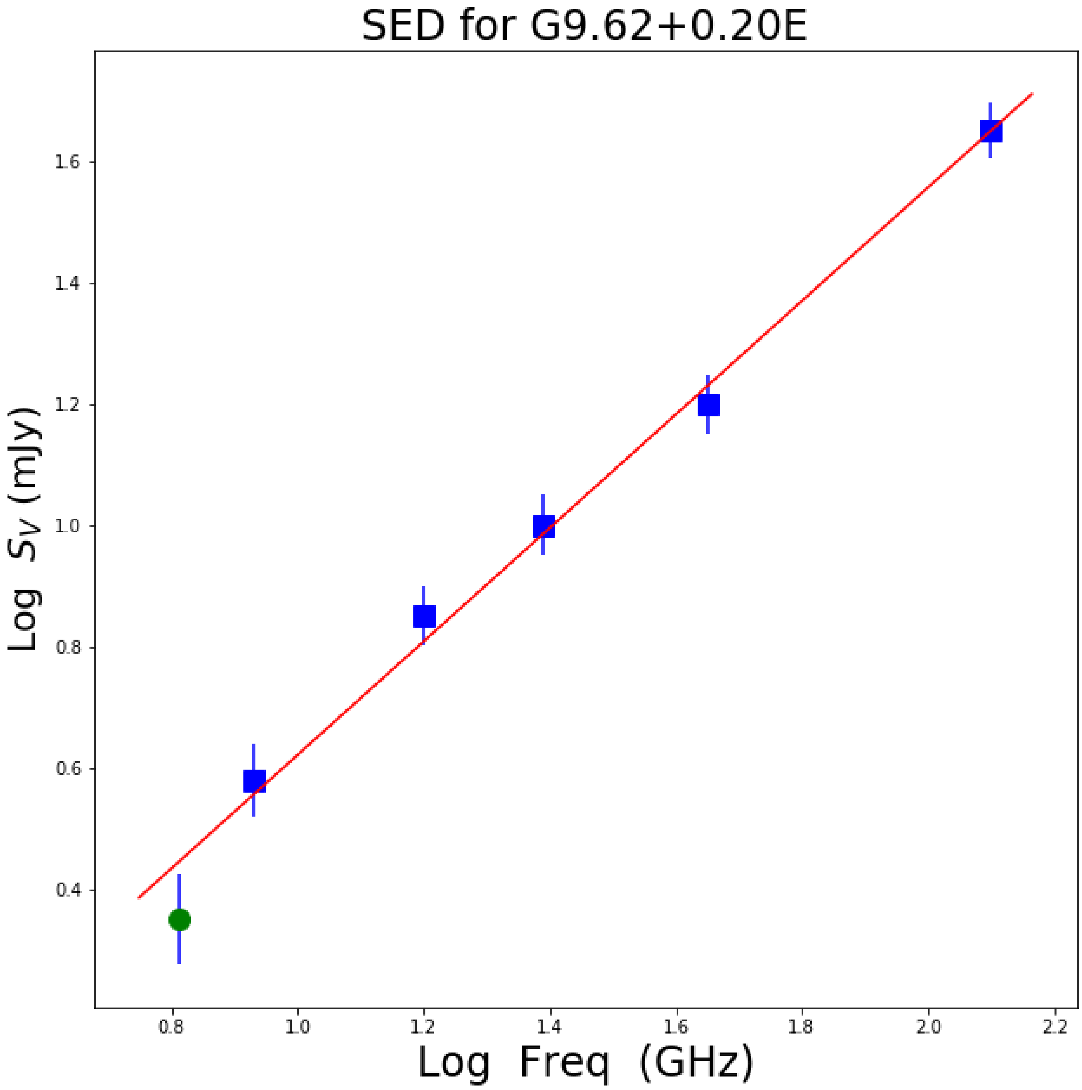

Figure 4.9: Spectral index plot of the G9.62 + 0.20E HII region. Shown in blue squares are the flux density values from different frequencies adapted from Franco et al. (2000). The flux density for the C-band continuum is shown with a green circle.

The C-band flux density of the HII region at 6.5 GHz has been added to the plot in Figure 5 of Franco et al. (2000) and presented in Figure 4.9. Inclusion of the 6.5 GHz flux density result in the spectral index calculation gives $0.94 \pm 0.05$. The upper limit on the integrated flux density from the expected position of the L-band continuum of G9.62 + 0.20E in Chapter 3 has also

Table 4.7: Physical properties of G9.62 + 0.20E. The size of the Q-band continuum comes from Sanna (2019) based on the results in (Sanna et al., 2015).

| Band | Beam size<br>(*mas*) | Position angle<br>(°) | Convolved size<br>$\Theta_{maj.}$(mas) × $\Theta_{min.}$(mas) | Position angle<br>(°) | Deconvolved size<br>$\Theta_{maj.}$(mas) × $\Theta_{min.}$(mas) | Position angle<br>(°) |
|---|---|---|---|---|---|---|
| Q | $93 \pm 50$ | $-1.5$ | $145 \pm 5 \times 77 \pm 3$ | $174 \pm 2$ | $112 \pm 7 \times 58 \pm 6$ | $172 \pm 6$ |
| C | $160 \pm 20$ | 10.55 | $229 \pm 26 \times 102 \pm 9$ | $5 \pm 2$ | $165 \pm 42 \times 97 \pm 23$ | $176 \pm 28$ |

been added to Figure 4.9 to produce Figure 4.10.

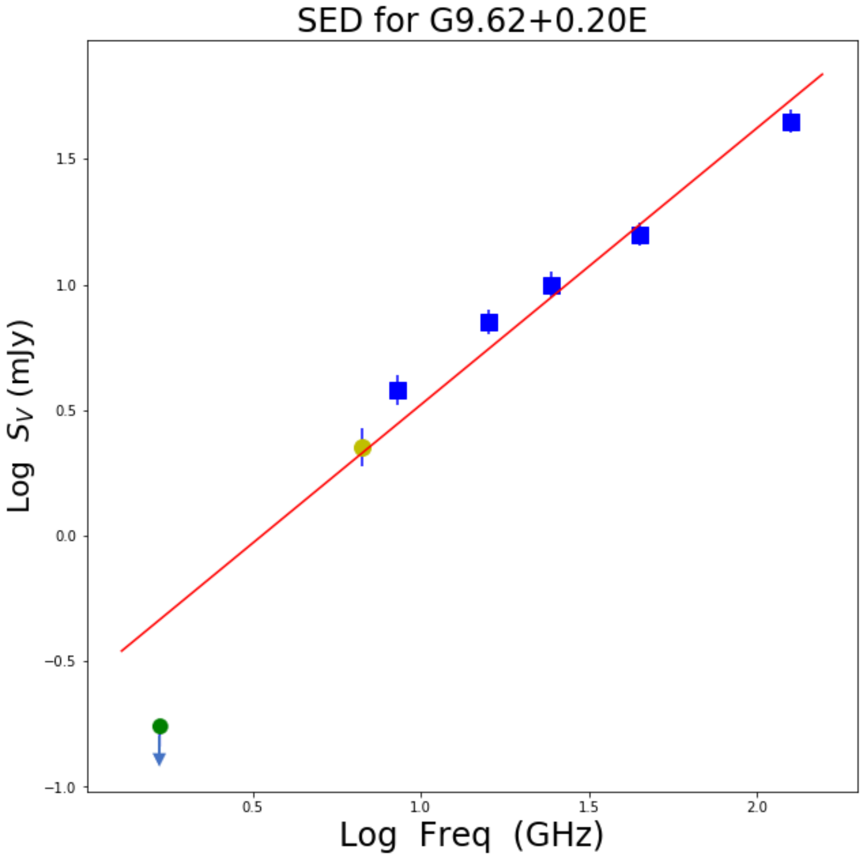

Figure 4.10: An updated spectral index plot of the flux density distribution of the G9.62 + 0.20E region at different frequencies adapted from Franco et al. (2000). The update to the plot is the flux density for the C-band continuum shown with a yellow circle and the $3\sigma$ upper limit of the peak flux density at L-band also shown with a green circle.

Figure 4.10 shows the updated spectral index plot with the addition of the upper limit of the flux density from the expected position of the continuum at L-band. The modified spectral index for G9.62 + 0.20E is 0.94 ± 0.06.

In the field of view of the C-band continuum in G9.62 + 0.20E is the source G9.62 + 0.20D shown in Figure 4.11. Here G9.62 + 0.20C is resolved out. Presented in Table Table 4.6 is the position and flux densities for source G9.62 + 0.20D.

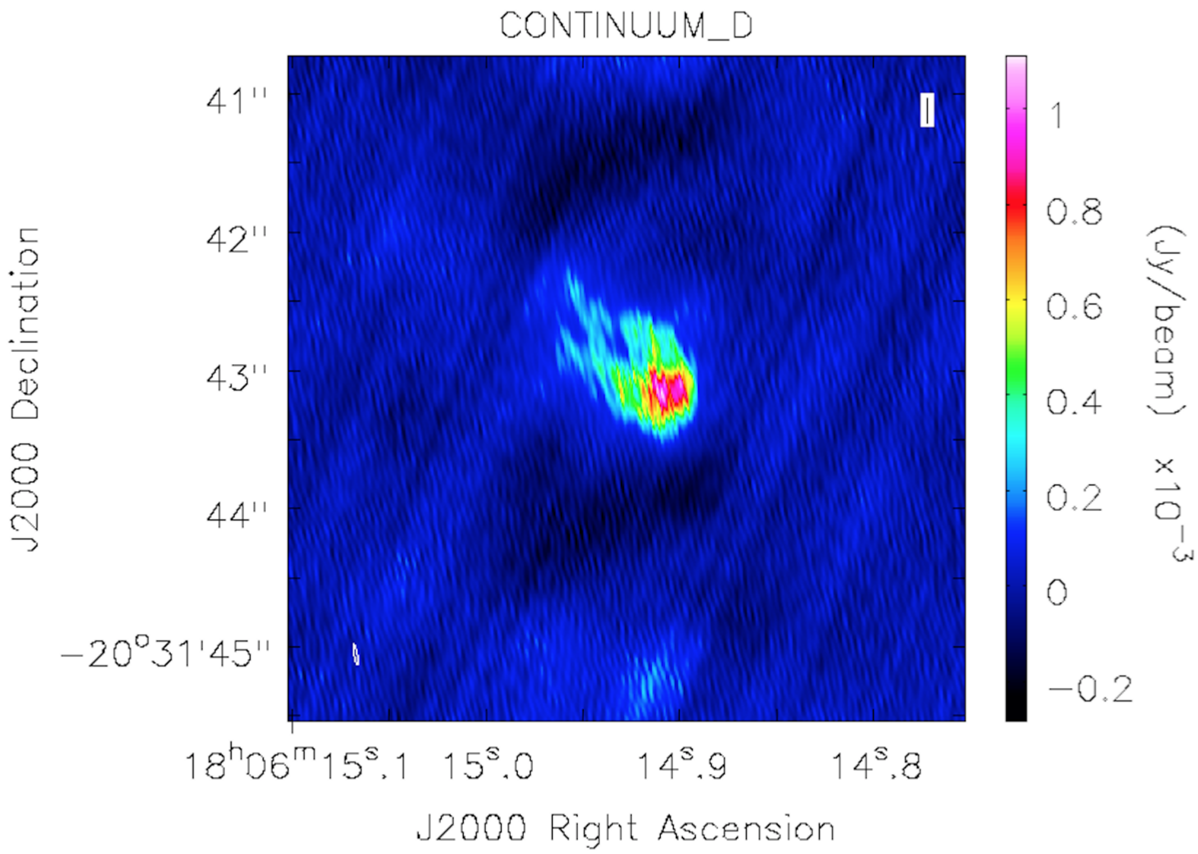

Figure 4.11: C-band radio continuum image of G9.62 + 0.20D shown in colour scale. At the lower left corner of the image is the synthesized beam.

At 6.5 GHz the HII region is cometary in shape recovering a flux of 43 mJy whereas Kurtz et al. (1994) recovers a flux of 65.8 mJy at 8.6 GHz. Becker et al. (1994) also reports a flux of 36.6 mJy at 5 GHz. Thus at 6.5 GHz a flux of 50 mJy is expected. The recorded flux in comparison with the expected flux suggests that most of the flux is recovered. The cometary morphology is also consistent with the 8.6 GHz radio continuum image in Figure 1 of Testi et al. (2000). In comparing the results of the positions in Table 4.6 with that in Table 3 of Kurtz et al. (1994) there is an offset of 615 mas in RA and 105 mas in Dec for source D. This is almost similar to the offset that source E's continuum is off by in (Sanna et al., 2015). Thus the offset for source D and source E are about 0.5 arcsecs to the west compared to the previous positions (Kurtz et al., 1994; Sanna et al., 2015).

#### 4.3.0.1 Maser spots at 6.7 GHz

Only two bright maser spots with high signal-to-noise ratios in their velocity channels were seen in the cube. Those with low signal-to-noise ratios were not seen and are not recorded here. However of the two spots identified in the cube only one spot is shown in the maps presented in Figure 4.12 and Figure 4.13. This is because the threshold range set to eliminate the side lobes in the image was above the flux density of the weaker spot. The diagonal blue feature in Figure 4.12 also seen as a red feature in Figure 4.13 is a side lobe

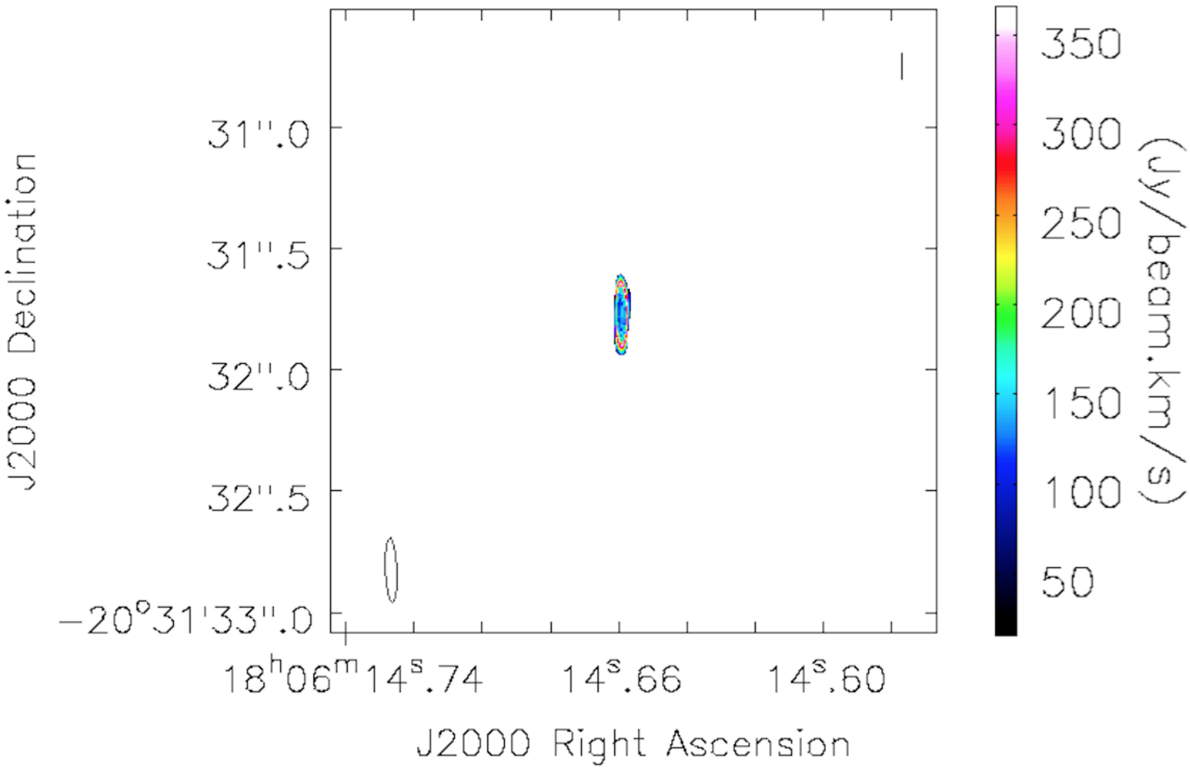

Figure 4.12: The flux density distribution for the 6.7 GHz methanol masers over the intensity range 700 Jy/beam to 1500 Jy/beam. At the lower left corner of the image is the synthesized beam.

The flux density for the bright maser spots is seen in Figure 4.12. The −0.26 km/s maser spot is not seen because of the 700 Jy/beam threshold set to exclude the sidelobes of the 1.25 km/s spot but it is seen in addition to the 1.25 km/s spot in the spectrum in Figure 4.14.

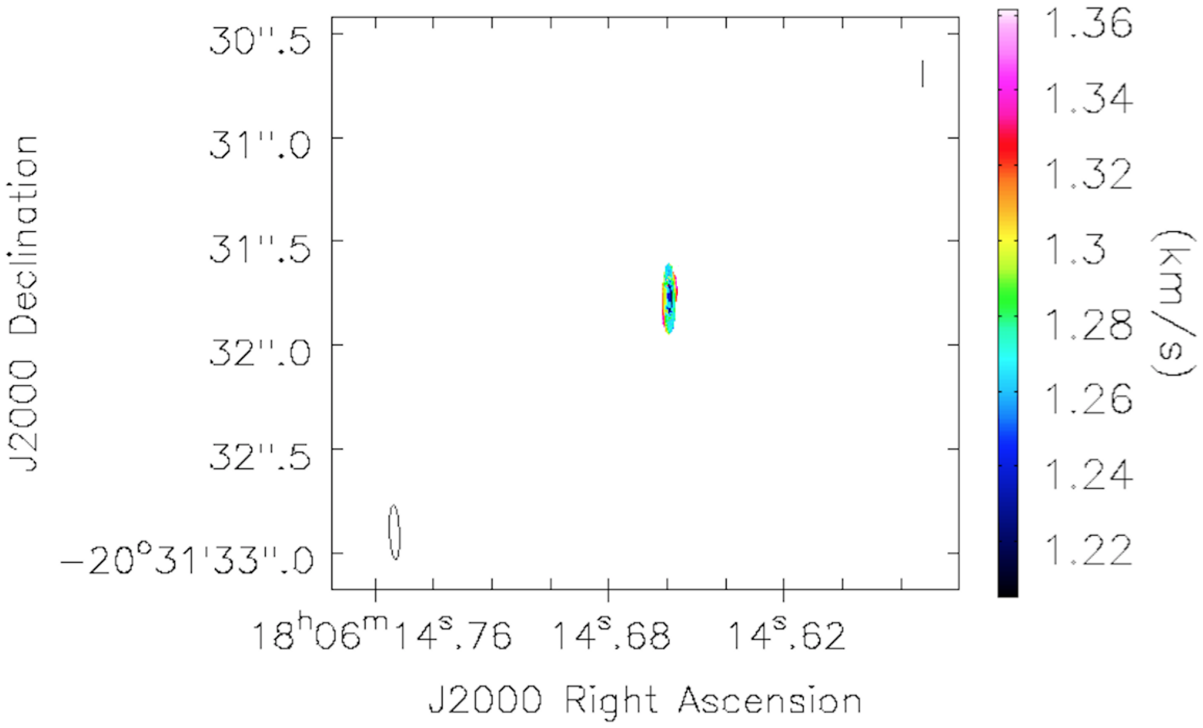

Figure 4.13: First moment map for the 6.7 GHz methanol masers shown in colour scale. The maser spot in the 1.25 km/s velocity channel is displayed. At the lower left corner of the image is the synthesized beam

Figure 4.14 presents the spectrum of the 6.7 GHz methanol maser lines showing the 1.25 km/s line and the −0.26 km/s line. The components of Figure 4.14 correspond with the spectral features in Figure 2.25 of chapter 2.

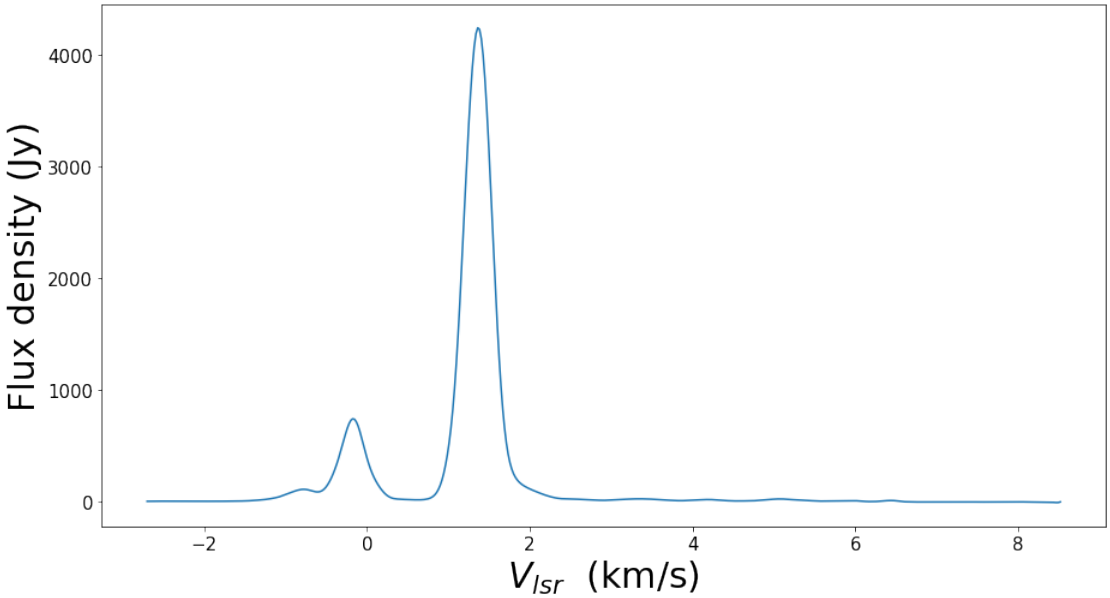

Figure 4.14: The spectrum for the methanol masers at 6.7 GHz.

A Gaussian fitted to the maser spots gave the positions and flux densities presented in Table 4.8. The first column of Table 4.8 gives the velocity channels of the maser spots. The second and fourth columns specify the right ascension ($\alpha$) and declination ($\delta$) of the maser spots determined by Gaussian fit. The leading terms of the positions are $\alpha$ (J2000)= $18^{\mathrm{h}}$ $06^{\mathrm{m}}$ and $\delta$ (J2000)= $-20^{\circ}$ $31^{\prime}$. The third and fifth columns give the error in $\alpha$ and $\delta$ respectively. The sixth and seventh columns give the integrated flux density and peak flux density respectively. The eighth column also gives the rms noise level in the image channels. The ninth and the tenth columns give the beam dimensions and the position angles of the maser spots respectively. The maser spot in the velocity channel 1.25 km/s corresponds to the LBA C-band results in velocity channel 1.05 km/s of Table 1 in Sanna et al. (2015). The position is off by 9 mas in RA and 172 mas in Dec. For the −0.26 km/s spot when compared with feature 2 of the 6.7 GHz spots in Table 2 of Sanna et al. (2015) an offset of 123 mas in RA and an offset of 67 mas in Dec are recorded. The measured integrated flux density for both maser spots are however consistent with the integrated flux in Table 1 and Table 2 of Sanna et al. (2015) for 1.25 km/s and −0.26 km/s respectively.

Table 4.8: Absolute positions, velocities and flux densities of the 6.7 GHz methanol maser spots in G9.62 + 0.20E.

| $V_{LSR}$ (km/s) | $\alpha$ (J2000)(s) | Error ($''$) | $\delta$ (J2000)($''$) | Error ($''$) | Integrated flux (Jy) | Peak flux (Jy/beam) | Rms (Jy/beam) | Deconvolved size $\Theta_{maj.}$(mas) × $\Theta_{min.}$(mas) | Position angle (°) |
|---|---|---|---|---|---|---|---|---|---|
| 1.25 | 14.6593 | 0.0004 | 31.776 | 0.013 | $3626.88 \pm 0.41$ | $3237.34 \pm 0.17$ | 43.04 | $551.8 \pm 18.3 \times 104.7 \pm 7.9$ | $182.6 \pm 1.6$ |
| −0.26 | 14.6587 | 0.024 | 31.794 | 0.090 | $653.28 \pm 0.33$ | $99.95 \pm 8.46$ | 6.48 | $611.02 \pm 27.37 \times 164.48 \pm 0.97$ | $158.45 \pm 0.73$ |

#### 4.3.0.2 Map of maser spots on the C-band continuum

The positions of the maser spots are overlayed on the continuum in Figure 4.15. Here the position of the continuum is shifted to the position reported by Sanna et al. (2015). This gives an overview of the positions of the maser spots relative to the continuum.

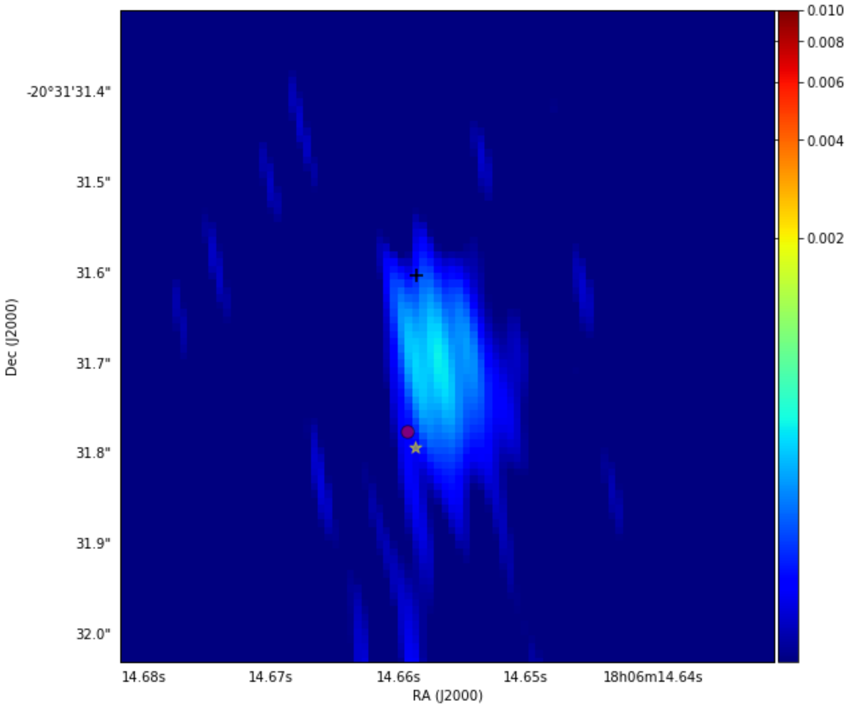

Figure 4.15: The C-band radio continuum of the G9.62 + 0.20E with the positions of the maser spots overlayed on it. The peak position of the 1.25 km/s maser spot is represented by a red circle and the −0.26 km/s maser spot is marked by a yellow star. The peak position of the 1.05 km/s maser spot in Sanna et al. (2015) is shown with a black plus sign.

The maser spots are located on the edge of the continuum. The 1.05 km/s brightest maser spot in Sanna et al. (2015) plotted on the continuum reveals that the 172 mas offset in Dec of the brightest methanol spot is quite significant

## 4.4 Discussion

The HII region associated with G9.62 + 0.20E has been detected at 6.5 GHz. This is the first C-band continuum detection of this source. The recovered flux density of 2.25 mJy is consistent with the expected results of 2.252 mJy at this frequency. The size of the HII region places it in the hypercompact HII region of the Kurtz-Franco classification system (Kurtz and Franco, 2002). The shape of the HII region as revealed by the resolved morphology of the object is elliptical which agrees with a similar elliptical shape and orientation found by Sanna et al. (2015).

The spectral index plot of the flux density in Figure 5 of Franco et al. (2000) has been updated with the addition of the C-band continuum and the upper limit of the noise level at L-band to that in Figure 4.10. The spectral index which characterises the strength of the spectra from the continuum has been modified from $0.95 \pm 0.06$ to $0.94 \pm 0.06$ for the G9.62 + 0.20E star forming region. This suggests that there is a spectral index drop between C-band and L-band confirming the turnover of the flux density at L-band. This index is consistent with thermal emission from an optically thick HII region. As discussed by Marsh (1975) the turnover of the radio spectrum at low frequencies can be explained using the truncated inverse-squared density gradient distribution model. This radio continuum behaviour has been observed in the spectra of some mass outflows (Marsh, 1975). Previously, Franco et al. (2000) invoked a steep density gradient to explain the 0.95 spectral index but from the results of the C-band and L-band continuum this model no longer explains the low frequency spectrum hence the Marsh (1975) model is adopted instead. Thus the turnover of the spectrum at L-band can be explained in terms of the truncated inverse-square density distribution model.

The turn over in the radio SED indicates that the source is going optically thick. This has been checked by examining the brightness temperature as a function of frequency assuming an electron temperature of 8000 K to estimate the optical depths. The peak flux at Q-band corresponds to a peak brightness temperature of about 80 K translating to an optical depth of 0.01. The C-band peak flux puts the brightness temperature at about 4000 K translating to an optical depth of about 0.5. These optical depth values show that at higher frequencies the source is optically thin and remains optically thin at C-band. However, when the optical depth is extrapolated to L-band it is then very optically thick.

The high resolution results of the masers from the e-MERLIN observation at a resolution of 40 mas have shown that the maser spots resolve into two spots with different velocities. However, with VLBA's high resolution, the masers resolve into 52 spots (Sanna et al., 2015). This shows that the maser observations in this work suffered from poor resolution and spatial blending of spots as compared to that reported by Sanna et al. (2015). The flux density of the two maser spots 1.25 km/s and $-0.26$ km/s found in the high resolution observations were also found to be consistent with the results in Chapter 2 for velocity channel 1.23 km/s and $-0.22$ km/s and also with Goedhart et al. (2004)'s velocity channels 1.26 km/s and $-0.14$ km/s. The nonvarying masers have not been detected. Figure 4.15 graphically shows that the variable spot is on the edge of the actual C-band continuum that supplies the seed photons as opposed to Fig 1 in Sanna et al. (2015) which was overlaid on the Q-band continuum.

# CHAPTER 5

# CONCLUSION AND FUTURE RESEARCH

In this work the left and right circular polarization components of the 1.6 GHz mainline hydroxyl masers and the 6.7 GHz methanol masers have been used to study the massive star forming region G9.62 + 0.20 E. This is the first time the LCP and RCP components of the mainline OH masers in G9.62 + 0.20 E have been monitored. Monitoring of G9.62 + 0.20 E from 2011 to 2017 has shown the continual variability of the flux density of the 6.7 GHz methanol masers and the left and right circular polarization components of the 1.6 GHz OH mainline masers. The variability profile for the separate polarizations of the 1.6 GHz OH mainline masers also confirmed the observed behaviour seen in Goedhart et al. (2019)'s total intensity monitoring. Between the OH and the methanol profiles, the OH masers exhibited a dip before a steep rise and a slow fall whereas the methanol exhibited a steep rise as well as a fast fall. Time delays between the two species were recorded.

High resolution observation of the L-band and C-band radio continuum were conducted with the e-MERLIN array. The results showed a radio continuum at C-band with a flux density of 2.25 mJy consistent with the calculated flux density of 2.252 mJy and an angular size of 130 mas. For the L-band continuum an upper limit of 162 $\mu$Jy on the flux density has been calculated by finding the average of the absolute value of the flux density from five regions at the expected position of the continuum. The continuum emission results from both the C-band and the L-band suggest that the actual spectrum turns over steeply from C-band to L-band. A truncated inverse-square density distribution model (Marsh, 1975) was more successful at explaining the results than a steep density gradient model for the 0.95 spectral index Kurtz and Franco (2002). Estimation of the optical depth from the peak brightness temperature of both L-band and C-band revealed that the continuum at C-band is optically thin whereas the continuum at L-band is optically thick. The positions of detected masers in the high resolution data at C-band have been plotted relative to the associated continuum. The results of the maser spots on the continuum observations show that the bright periodic methanol spots are on the edge of the observed C-band continuum consistent with the colliding wind binary model.

The work gives new evidence to support the correlated variability of circularly polarised components of the 1.6 GHz OH mainline masers and the 6.7 GHz methanol maser in G9.62 + 0.20E. The results of the radio SED constrain the density distribution of the actual frequencies of the seed photons of the C-band and L-band continuum. This adds on to the wealth of constraints from various observations and theoretical calculations put forward within the context of the colliding wind binary model to explain the observed periodicity for the masers in G9.62 + 0.20E. The results of these independent constraints such as the direct imaging of the HII region provides direct constraints on the density distribution which presents a good chance to test the model and predict the electron density distribution indirectly. With these results a photo-ionisation nebulae model such as CLOUDY (van den Heever et al., 2019) which uses a constant density can be modified by taking into account the density gradient of the HII region and in particular the truncated inverse-square density distribution of the L-band implied by the radio SED found in this thesis. This will take inputs such as the luminosity and density gradient of the HII region to predict the size of the radio continuum (extent of ionisation) and also test the variation of the radiation from the colliding wind binary model.

The LCP and RCP components of the 1.6 GHz OH maser saw a dip just before the flares and also recorded time delays between the onset of their flares and those of the methanol maser. The radio SED measured has also put constraints on the density distribution of the seed photons in the HII region. In the context of the colliding wind binary model the electron density at the background location of the HII region determines the decay time. Slower decays observed for the 1.6 GHz OH maser imply a low electron density and VLBI imaging (Sanna et al., 2015) showing OH masers farther away than methanol masers from the HII region which is consistent with a density gradient. The above described photo-ionisation nebulae model could be fit with the Marsh model (Marsh, 1975) used to explain the L-band spectrum behaviour to test if the variation of the radiation of the HII region is associated with the time delays and dips observed in the 1.6 GHz OH maser. But will such a model be consistent with the decay time? Would the model predict a dip in the L-band continuum seed photons in order to explain the 1.6 GHz OH variability profile? If so, is this because of the optical depth or due to the penetration of hard xrays as explained by (Goedhart et al., 2019)?

## 5.1 Improving observational constraints

The observation of the G9.62 + 0.20E region made with e-MERLIN interferometric data can be improved by adopting different strategies. For instance, the astrometry of the methanol maser spots and the C-band continuum did not work well to achieve the original aim of the thesis. This has been attributed to a number of factors. First is the selection of a weak phase calibrator which was too weak to give good solutions. A solution will be the use of a brighter source with high position accuracy or the use of two phase calibrators one with strong flux density and the other with good astrometry. Second was the adoption of self calibration which ultimately sacrifices the astrometry information. There would have been no need for a self calibration if the previous solutions were adhered to. The third factor was the loss of data at L-band due to bad data and the high noise level in the data. At L-band it is almost impossible to get rid of all the bad data. An attempt at this will leave insufficient data for calibration. With the addition of one or more 30 m antennas at Goonhilly into the existing e-MERLIN radio interferometer in future the the longer north-south baselines that will then be available will improve the resolution in the declination direction giving a rounder beam shape (Heywood et al., 2011). In this way the initial goal of the work will be achieved.

Further observations of the polarised 1.6 GHz OH and the 6.7 GHz methanol masers taken simultaneously with the continuum emission from the HII region associated with them in G9.62 + 0.20 E will be made with the VLA in the A configuration. A detection of the L-band continuum will allow a better model to be developed.

Also other future work will be based on selecting from the 6.7 GHz methanol sample provided by Goedhart et al. (2004) and from the many more recent periodic sources discovered the sources that show similar variability profile as that of G9.62 + 0.20 E and conducting monitoring observation of their 1.6 GHz OH maser polarization in search of more dips and time lags. A follow up with high angular resolution observation of the flaring and non-flaring phases of the masers and their associated continuum to ascertain if dips only occur if the continuum is optically thick. These results will then be used to test the colliding wind binary model.

# REFERENCES

Abbott, B., Abbott, R., Adhikari, R., Ajith, P., Allen, B., Allen, G., Amin, R., Anderson, S., Anderson, W. and M., A. (2009*a*), 'All sky LIGO search for periodic gravitational waves in the early fifth-science-run data', *Phys. Rev. Lett.* **102**(11), 111102.

Abbott, B., Abbott, R., Adhikari, R., Ajith, P., Allen, B., Allen, G., Amin, R., Anderson, S., Anderson, W. and M., A. (2009*b*), 'LIGO: The Laser Interferometer Gravitational-Wave Observatory', *Rep. Prog. Phys.* **72**(7), 076901.

Abbott, B., Abbott, R., Adhikari, R., Ajith, P., Allen, B., Allen, G., Amin, R., Anderson, S., Anderson, W. and M., A. (2017), 'LIGO:Observation of Gravitational Waves from a Binary Neutron Star Inspiral', *Phys. Rev. Lett.* **119**, 16–20.

Adams, F. C., Lada, C. J. and Shu, F. H. (1987), 'Spectral evolution of young stellar objects', *ApJ* **312**, 788.

Andre, P., Thompson, D. W. and Barsony, M. (1993), 'Submillimeter continuum observations of rho Ophiuchi A - The candidate protostar VLA 1623 and prestellar clumps', *ApJ* **406**, 122–141.

Andrews, J., Calzetti, D., Chandar, R., Elmegreen, B., Kennicutt, R., Kim, H., Krumholz, M., Lee, J., Mcelwee, S., O'Connell, R. and Whitmore, B. (2014), 'Big fish in small ponds: Massive stars in the low-mass clusters of M83', *ApJ* **793**, 4.

Araya, E. D., Hofner, P., Goss, W. M., Kurtz, S., Richards, A. M. S., Linz, H., Olmi, L. and Sewitlo, M. (2010), 'Quasi-periodic formaldehyde maser flares in the massive protostellar object IRAS 18566+0408', *ApJL* **717**, L133–L137.

Argon, A. L. and Reid, M. J. (2003), 'A class of interstellar oh masers associated with protostellar outflows', *ApJ* **593**, 925–930.

Artymowicz, P. and Stephen , H. L. (1996), 'Mass flow through gaps in circumbinary disks', *ApJ* **467**, L77–L80.

Arzoumanian, D., Andre, P., Didelon, P., Konyves, V., Schneider, N. and Men'shchikov, A. (2011), 'Characterizing interstellar filaments with Herschel in IC 5146', *A&AS* **529**, L6.

Bachiller, R. and Perez- Gutierrez, M. (1997), 'Shock chemistry in the young bipolar outflow L1157', *ApJ* **487**, L93–L96.

Batrla, W., Matthew, H., Menten, K. and Walmsley, C. (1987), 'Detection of strong methanol maser towards galactic HII regions', *Nature* **326**, 49.

Becker, R. H., White, L. R., Helfand, D. and Zoonematkermani, S. (1994), 'A 5 GHz VLA survey of the galactic plane', *ApJS* **91**, 347–387.

Belles, P. E., Beswick, R., Argo, M., Jackson, N., Muxlow, T. and Richards, A. (2015), *e-MERLIN CookBook*, The University of Manchester, Manchester.

Beuther, H., Churchwell, E., McKee, C. and Tan, J. (2007), The formation of massive stars, *in* B. K. K. and J. David, eds, ‘Protostars and Planets V’, Vol. V, University of Arizona Press, Tucson, Arizona, p. 165–180.

Beuther, H., Walsh, A., Johnston, K., Henning, T., Kuiper, R., Longmore, S. and Walmsley, C. (2017), ‘Fragmentation and disk formation in high-mass star formation: The ALMA view of G351.77-0.54 at 0.06” resolution’, *A&A* **603**, A10.

Beuther, H., Zhang, Q. and Hunter, T., Sridharan, T. and Bergin, E. (2007b), ‘The 105 $L_\odot$ high-mass protostellar object IRAS 23151+5912’, *A&A* **473**, 493–500.

Billington, S., Urquhart, J., Figura, C., Eden, D. and Moore, T. (2018), ‘The RMS survey: Ammonia mapping of the environment of young mas- sive stellar objects II’, *MNRAS* **483**, 3146–3167.

Bonnell, I. A. and Bate, M. R. (2006), ‘Star formation through gravitational collapse and competitive accretion’, *MNRAS* **370**, 488–494.

Bonnell, I. A., Bate, M. R. and Clarke, C. J.and Pringle, J. E. (1997), ‘Accretion and the stellar mass spectrum in small clusters’, *MNRAS* **285**, 201–208.

Bonnell, I. A., Bate, M. R. and Vine, S. G. (2003), ‘The hierarchical formation of a stellar cluster’, *MNRAS* **343**, 413–418.

Bonnell, I. A. and Davies, M. B. (1998), ‘Mass segregation in young stellar clusters’, *MNRAS* **295**, 691–698.

Bonnell, I. A., Vine, S. G. and Bate, M. R. (2004), ‘Massive star formation: nurture, not nature’, *MNRAS* **349**, 735–741.

Breen, S. L., Ellingsen, S. P., Caswell , J. L. and Lewis, B. E. (2010), ‘12.2-GHz methanol masers towards 1.2-mm dust clumps: quantifying high-mass star formation evolutionary schemes’, *MNRAS* **410**, 2219–2244.

Burke, B. F. and Graham-Smith, F. (2002), *An Introduction to Radio Astronomy*, 2nd edn, Cambridge University Press, Cambridge.

Caselli, P. and Ceccarelli, C. (2012), ‘Our astrochemical heritage’, *Astron. Astrophys. Rev.* **20**, 56.

Caswell, J. L. (1998), ‘Positions of hydroxyl masers at 1665 and 1667 MHz’, *MNRAS* **297**, 215–235.

Caswell, J. L., Green, J. A. and Phillips, C. J. (2013), ‘Parkes full polarization spectra of OH masers – I. galactic longitudes 350 through the galactic centre to 41’, *MNRAS* **431**, 1180–1219.

Caswell, J., Vaile, R. and Ellingsen, S. (1995), ‘Variability of methanol masers’, *Proc. Astron. Soc. of Aust.* **12**, 37.

Caswell, J., Vaile, R. and Forster, J. (1995), ‘Methanol and hydroxyl maser positions’, *MNRAS* **277**, 210–216.

Cesaroni, R., Galli, D., Lodato, G., Walmsley, C. and Zhang, Q. (2006), Disks around young O-B (proto)stars:observations and theory, *in* B. K. K. and J. David, eds, ‘Protostars and Planets IV’, Vol. IV, University of Arizona Press, Tucson, Arizona.

Chen, H. V., Keto, E., Zhang, Q., Sridharan, T. K., Liu, S. and Su, Y. (2016), 'A hot and massive accretion disk around high mass protostar IRAS20126+ 4104', *ApJ* **823**, 125.

Clegg, A. W. and Cordes, J. M. (1991), 'Variability of interstellar hydroxyl masers', *ApJ* **374**, 150.

Cohen, R. J. (1989), 'Compact maser sources', *Rep. Prog.Phys.* **52**, 881–943.

Commerçon, B., Hennebelle, P. and Henning, T. (2011), 'Collapse of massive magnetized dense cores using radiation magnetohydrodynamics:Early fragmentation inhibition', *ApJ* **L9**, 742.

Condon, J. J. and Ransom, S. M. (2016), *Essential Radio Astronomy*, Princeton University press, Princeton, New Jersey.

Cragg, D., Sobolev, A. M. and Godfrey, P. (2002), 'Modelling methanol and hydroxyl masers in star forming regions', *MNRAS* **331**, 521–536.

Cragg, D., Sobolev.A.M. and Godfrey, P. (2005), 'Models of class II methanol masers based on improved molecular data', *MNRAS* **360**, 533–546.

Das, A., Acharya, K., Chakrabarti, S. and Chakrabarti, S. (2008), 'Formation of water and methanol in star forming molecular clouds', *A&A* **486**, 209.

Davies, B.and Hoare, M. L. S., Hosokawa, T.and Oudmaijer, R., Urquhart, J., Mottram, J. and Stead, J. (2011), 'The Red MSX source survey: critical tests of accretion models for the formation of massive stars', *MNRAS* **416**, 972–990.

De Buizer, J. (2000), A mid infrared imaging survey of star forming regions containing methanol and water maser emissions, PhD thesis, Graduate school of the university of Florida,Florida,USA.

De Buizer, J. M. (2003), 'Testing the circumstellar disc hypothesis: a search for $H_2$ outflow signatures from massive young stellar objects with linearly distributed methanol maser', *MNRAS* **341**(1), 277–298.

De Buizer, J. M., Osorio, M. and N., C. (2005), 'Observations and modeling of the 2-25 $\mu$m emission from high mass protostellar object candidates', *ApJ* **635**, 452–465.

De Buizer, J. and Minier, V. (2005), 'Investigating the nature of the dust emission around massive protostar NGC 7538 IRS 1: Circumstellar disk and outflow?', *ApJL* **L151**, 628.

Dobbs, C. L., Bonnell, I. A. and Clark, P. C. (2005), 'Centrally condensed turbulent cores: massive stars or fragmentation?', *MNRAS* **360**, 2–8.

Dunham, M. M. and Vorobyov, E. I. (2012), 'Resolving the luminosity problem in low mass star formation', *AJ* **747**, 52.

Dzib, S., Loinard, L. and Rodriguez, L. F. (2011), 'VLBA Determination of the distance to nearby starforming regions. vi. The distance to the young stellar object HW 9 in Cepheus A', *ApJ* **733**, 71.

Eden, D. J., Liu, T., Kim, K.-T., Juvela, M., Liu, S.-Y., Tatematsu, K., Francesco, J. D., Wang, K., Wu, Y., Thompson, M. A., Fuller, G. A., Li, D. and et. al. (2019), 'SCOPE: SCUBA-2 Continuum observations of pre-protostellar evolution – survey description and compact source catalogue', *MNRAS* **485**(2), 2895–2908.

Edris, K. A., Fuller, G. A. and Cohen, R. J. (2007), 'A survey of OH masers towards high mass protostellar objects', *A&A* **465**, 865–877.

Elitzur, M. (1976), 'Inversion of the OH 1720-MHz line', *ApJ* **203**, 124–131.

Elitzur, M. (1992), *Astronomical Masers*, Dordrecht Netherlands.

Elitzur, M. (1998), 'Polarization of astronomical maser radiation IV. Circular polarization profiles', *ApJ* **504**, 390–395.

Ellingen, S. P., Breen, S., Voronkov, M., Caswell, J., Chen, X. and Titmarsh, A. (2011), An evolutionary timeline for high mass star formation, *in* 'Science with Parkes @ 50 Years Young, 31 Oct. – 4 Nov., 2011'.

Ellingsen, S. (2006), 'Methanol masers: reliable tracers of the early stages of high-mass star formation', *ApJ* **638**, 241–261.

Farmer, H. (2014), 'Disk-outflow models as applied to high mass star forming regions through methanol and water maser observations', *IJAA* **4**, 571–597.

Feigelson, E. D. and Montmerle, T. (1999), 'High-energy processes in Young Stellar Objects', *ARA&A* **37**, 363–408.

Fish, V. L. and Reid, M. J. (2006), 'Full- polarization observation of OH masers in massive star forming regions. II. Maser properties and the interpretation of polarization', *ApJS* **164**, 99–123.

Fish, V. L., Reid, M. J., Argon, A. L. and Zheng, X.-W. (2005), 'Full- polarization observation of OH masers in massive star forming region. I. Data', *ApJS* **160**, 220–271.

Forster, J. and Caswell, J. (2000), 'Radio continuum emission at OH and $H_2O$ maser sites', *ApJ* **530**, 371–386.

Franco, J., Kurtz, S., Hofner, P., Testi, L., Garcia-Segura, G. and Martos, M. (2000), 'The density structure of highly compact HII regions', *ApJ* **542**, L143–L146.

Garay, G., Rodriguez, L. F., Moran, J. M. and Churchwell, E. (1993), 'VLA observation of strong IRAS point sources associated with compact HII regions', *ApJ* **418**, 368.

Garcia-Barreto, J. A., Burke, B. F., Reid, M. J., Moran, J. M., Haschick, A. D. and Schilizzi, R. T. (1988), *ApJ* **325**, 954–966.

Genzel, R., Reid, M., Moran, J. and Downes, D. (1981), 'Proper motions and distances of $H_2O$ maser sources. I—The outflow in Orion-KL', *ApJ* **244**, 884.

Goedhart, S., Gaylard, M. J. and van der Walt, D. J. (2003), 'Periodic flares in the methanol maser source G9.62+0.20E', *MNRAS* **339**, L33–L36.

Goedhart, S., Gaylard, M. J. and van der Walt, D. J. (2004), 'Long term monitoring of 6.7 GHz methanol masers', *MNRAS* **355**, 553–584.

Goedhart, S., Maswanganye, J. P., Gaylard, M. J. and van der Walt, D. J. (2014), 'Periodicity in class II methanol masers in high-mass star-forming regions', *MNRAS* **437**, 1808–1820.

Goedhart, S., van Rooyen, R., van der Walt, D. J., Maswangangye, J., Sanna, A., Macleod, G. and van den Heever, S. (2019), 'Periodic variability of the mainline hydroxyl masers G9.62+0.20E', *MNRAS* **485**, 4676–4685.

Green, J. A., Caswell, J. L., Fuller, G. A., Avison, A., Breen, S. L., Ellingsen, S. P., Pestalozzi, M., Quinn, L., Thompson, M. A. and Voronkov, M. A. (2010), 'The 6-GHz methanol multibeam maser catalogue – II. Galactic longitudes 6 ° to 20 °', *MNRAS* **409**(3), 913–935.

Green, J. A., Caswell, J. L., Voronkov, M. and Mcclure-Griffths, N. M. (2012), 'Variability monitoring of the hydroxyl maser emission in G12.889+0.489', *MNRAS* **425**, 1504–1510.

Greene, T. (2001), 'Protostars: "Stellar embryology" takes a step forward with the first detailed look at the youngest Sun-like stars', *American Scientist* **89**, 316–325.

Guzman, A., Garay, G., Rodrıguez, L., Contreras, Y., Dougados, C. and Cabrit, S. (2016), 'A protostellar jet emanating from a hypercompact HII region', *ApJ* **826**, 208.

Hacar, A., Tafalla, M., Kauffmann, J. and Kovacs, A. (2013), 'Cores, filaments, and bundles: hierarchical core formation in the L1495/B213 Taurus region.', *A&AS* **554**, A55.

Hatchell, J., A., T. M., Millar, T. J. and Macdonald, G. (1998), 'A survey of molecular line emission towards ultracompact HII regions', *A&AS* **133**(1), 29–49.

Heywood, I., Klöeckner, H., Beswick, R. Garrington, S. T., Hatchell, J., Hoare, M. G., Jarvis, M. J., Jones, I., Muxlow, T. W. B. and S., R. (2011), 'Expanding e-MERLIN with the Goonhilly Earth Station', *arXiv:astro-ph.IM/1103.1214* .

Hill, T., Minier, V., Thompson, M. A., Walsh, A. J., Burton, M. G., Huny- Cunningham, M. and Garay, G. (2005), 'Millimetre continuum observations of southern massive star formation regions – I. SIMBA observations of cold cores', *A&A* **429**, 946–960.

Hirota, T., Bushimata, T. and Choi, Y. K. (2007), 'Distance to Orion KL measured with VERA', *PASJ* **59**, 897.

Hoare, M. G. (2002), 'Hot Star Workshop 111:The earliest phases of massive star birth', *ASP Conf. Ser.* **267**, 137.

Hoare, M. G. and Franco, J. (2007), 'Massive star formation', *arXiv:astro-ph 0711.4912v1* .

Hoare, M. G., Lumsden, S. L. and Oudmaijer, R. D. (2005), Hypercompact HII regions,IAU Symposium proceedings of the International Astronomical Union massive star birth: A crossroads of astrophysics, Vol. 227, Cambridge University Press, Cambridge.

Hoare, M. G.and Kurtz, S. E., Lizano, S., Keto, E. and Hofner, P. (2007), Ultra-compact HII regions and the early lives of massive stars, *in* B. K. K. and J. David, eds, 'Protostars and Planets V', Vol. V, University of Arizona Press, Tucson, Arizona, p. 181–196.

Hofner, P., Kurtz, S., Churchwell, E. and Walmsley, C. M.and Cesaroni, R. (1996), 'Massive star formation in the hot dense cloud of G9.62+0.19', *ApJ* **460**, 359.

Hofner, P., Wiesemeyer, H. and Henning, T. (2001), 'A high velocity molecular outflow from the G9.62+0.19 star forming region', *ApJ* **549**, 425.

Högbom, J. A. (1974), 'Aperture synthesis with a non-regular distribution of interferometer baselines', *A&AS* **15**, 417.

Hosokawa, T. and Omukai, K. (2009), 'Evolution of massive protostars with high accretion rates', *ApJ* **691**, 823–846.

Hosokawa, T., Yorke, H. W. and Omukai, K. (2010), 'Evolution of massive protostars via disk accretion', *ApJ* **721**, 478.

Hoyle, F. (1954), 'On nuclear reactions occuring in very hot stars.I. The synthesis of elements from carbon to nickel', *ApJS* **1**, 121.

Inayoshi, K., Sugiyama, K., Hosokawa, T., Motogi, K. and Tanaka, K. E. I. (2013), 'Direct diagnostics of forming massive stars: Stellar pulsation and periodic variability of maser sources', *ApJL* **769**(L20), 5.

Isella, A. (2006), Interferometric observations of pre-main sequence disks, Phd, Universit'a degli Studi di Milan, Milan, Italy.

Jackson, J. D. (1999), *Classical Electrodynamics*, 3rd edn, New York.

Johnston, K. G., Robitaille, T. P., Beuther, H., Linz, H., Boley, P.Kuiper, R., Keto, E., Hoare, M. G. and Boeke, R. v. (2015), 'A keplerian-like disk around the forming O-type star AFGL 4176', *ApJL* **813**, L19.

Keto, E. (2007), 'The formation of massive stars: Accretion, disks, and the developement of hypercompact HII regions', *ApJ* **666**, 976–981.

Kolligan, A. and Kuiper, R. (2017), 'From accretion to outflows of massive protostars.', *Mem. Soceita Astronomica Italiana* **88**, 793.

Krumholz, M. (2014), 'The big problems in star formation: The star formation rate, stellar clustering, and the initial mass function', *Phys. Rep.* **539**, 49–134.

Krumholz, M. (2015*a*), The formation of very massive stars, *in* 'Very Massive Stars in the Local Universe', Vol. 412 of *Ap&SSL*, p. 43.

Krumholz, M. (2015*b*), 'Notes on star formation', *arXiv e-prints* .

Krumholz, M. R., Cunningham, A. J., Klein, R. I. and Mckee, C. F. (2010), 'Radiation feedback, fragmentation, and the environmental dependence of the initial mass function', *ApJ* **713**, 1120–1133.

Kuiper, R., Klahr, H., Beuther, H., Henning, T. and Yorke, H. (2013), Radiation pressure in massive star formation, *in* B. K. K. and J. David, eds, 'Protostars and Planets VI', University of Arizona Press, Tucson, Arizona.

Kuiper, R., Turner, N. and Yorke, H. (2016), 'Protostellar Outflows and Radiative Feedback from Massive Stars. II. Feedback, Star-formation Efficiency, and Outflow Broadening', *ApJ* **832**, 40.

Kurtz, S. (2005), Hypercompact HII regions,massive star birth: A crossroads of astrophysics, iau symposium proceedings of the international astronomical union, Vol. 227, Cambridge University Press, Cambridge, pp. 111–119.

Kurtz, S., Cesaroni, R., Churchwell, E., Hofner, P. and Walmsley, C. M. (2000), 'Hot molecular cores and the earliest phases of high-mass star formation', *Protostars and Planets IV* pp. 299–326.

Kurtz, S., Churchwell, E. and Wood, D. O. S. (1994), 'Ultracompact HII regions: New high-resolution radio images', *ApJS* **91**, 659–712.

Kurtz, S. and Franco, J. (2002), 'Ultracompact HII regions', *Rev. Mex. AA (Serie de Conferencias)* **12**, 16–21.

Lada, C. (1985), Star formation : From OB associations to protostars, *in* 'IAU Symposium', Vol. 115, Dordrecht, D. Reidel Publishing Co, pp. 1–18.

Linz, H., Stecklum, B., Henning, T. and Hofner, P. and. Brandl, B. (2005), 'The G9.62+0.19 F hot molecular core : The infrared view on very young massive stars', *A&A* **429**(3), 903–921.

Liu, T., Lacy, J., Shing Li, P., Wang, K., Qin, S., Zhang, Q., Kim, K. andGaray, G., Wu, Y., Mardones, D., Zhu, Q. andTatematsu, K. H. T. and Ren, Z. andLu, S. a. H. a. Y. L. D. (2017), 'ALMA reveals sequential high mass star formation in the G9.62+0.19 complex', *ApJ* **849**, 25–46.

Liu, T., Wu, Y., Liu, S.-Y., Qin, S.-L., Su, Y.-N., Chen, H.-R. and Ren, Z. (2011), 'Infall and outflows motions in the high- mass star-forming complex G9.62+0.19', *ApJ* **730**(102), 17.

Loinard, L., Torres, R., Mioduszewski, A. and Rodriguez, L. (2008), 'A preliminary VLBA distance to the core of Ophiuchus, with an accuracy of 4%', *ApJ* **675**, L29–L32.

Luhman, K. L., Rieke, G. H., Lada, C. J. and Lada, E. (1998), 'Low mass star formation and the initial mass function in IC 348', *ApJ* **508**, 347–369.

Macleod, G. and Gaylard, M. (1996), 'Variable hydroxyl and methanol masers in G351.78-0.54', *MNRAS* **280**, 868–876.

Marr, J. M., Snell, R. L. and Kurtz, S. E. (2016), *Fundamentals of Radioastronomy : Observational methods*, Series in Astronomy and Astrophysics.

Marsh, K. A. (1975), 'The radio spectra of mass-outflow stars', *ApJ* **201**, 190–193.

Maud, L. T., Cesaroni, R., Kumar, M. S., Van Der Tak, F. F., Allen, V., Hoare, M. G., Klaassen, P. D., Harsono, D.and Hogerheijde, M. R., Sánchez-Monge, A., Schilke, P., Ahmadi, A., Beltrán, M. T., Beuther, H., T., C., Etoka, S., Fuller, G.and Galván-Madrid, R., Goddi, C., Henning, T. and Johnston, K. G. (2018), 'Chasing discs around O-type (proto)stars: ALMA evidence for an SiO disc and disc wind from G17.64+0.16', *A&A* **620**, A31.

McGuire, C., Fuller, G., Peretto, N., Zhang, Q., Traficante, A., Avison, A. and Jimenez-Serra, I. (2016), 'The structure and early evolution of massive star forming regions. Substructure in the infrared dark cloud SDC13', *A&A* **594**, A118.

McKee, C. F. and Tan, J. C. (2003), 'The formation of massive stars from turbulent cores', *ApJ* **585**, 850–871.

Mcmullin, J. (2009), *CASA synthesis and single dish Reduction cookbook*, beta release edition edn.

Menten, K. M. (1991), 'The discovery of a new, very strong, and widespread interstellar methanol maser line', *ApJL* **380**, L75.

Meyers, A. T. and Mckee, C. F. (2013), 'The fragmentation of magnetized, massive star-forming cores with radiative feedback', *ApJ* **766**, 97–115.

Mezger, P. and Henderson, A. (1967), 'Galactic HII regions I Observations of their continuum radiation at the frequency 5 GHz', *ApJ* **147**, 471–489.

Minier, V., Burton, M., Hill, T., Pestalozzi, M., Purcell, C. R., Garay, G. and Walsh, J. (2005), 'Star forming protoclusters associated with methanol masers', *A&A* **429**, 945.

Minier, V., Conway, J. E. and Booth, R. (2001), 'VLBI observations of 6.7 and 12.2 GHz methanol masers towards high mass star forming regions: Tracing massive protostars.', *A&A* **369**, 278–290.

Minier, V., Ellingsen, S. P., Norris, R. P. and Booth, R. S. (2003), 'The protostellar mass limit for 6.7 GHz methanol masers. I. A low-mass YSO survey', *A&A* **403**, 1095–1100.

Morton, D. C. (1967), 'The Far-ultraviolet spectra of six stars in Orion', *AJ* **147**, 1017.

Moscadelli, L. and Reid, M. J.and Menten, K. M. (2009), 'Trigonometric parallaxes of massive star-forming regions. II. Cep A and NGC 7538', *ApJ* **693**, 406.

Offringa, A., De Bruyn, A., Biehl, M., Zaroubi, S., Bernardi, G. and Pandey, V. (2010), 'Post-correlation radio frequency interference classification methods', *MNRAS* **405**, 155–167.

Oozer, N., Bietenholz, M. and Goedhart, S. (2010), *An introduction to CASA: A KAT-7 Data reduction guide*, SKA, SA.

Ott, M., Witzel, A., Quirrenbach, A., Krichbaum, T., Standke, K., Schalinski, C. and Hummel, C. (1994), 'An updated list of radio flux density calibrators', *A&A* **284**, 331–339.

Parfenov, S. Y. and Sobolev, A. M. (2014), 'On the class II methanol maser periodic variability due to the rotating spiral shocks in the gaps of discs around young binary stars', *MNRAS* **444**, 620.

Peck, L. and Fenech, D. M. (2013), 'SERPent: Automated reduction and RFI-mitigation software for e-merlin', *Astron and Comput* **2**, 54–66.

Peretto, N. and Fuller, G. A. (2009), 'The initial conditions of stellar protocluster formation. I. A catalogue of spitzer dark clouds', *A&A* **505**, 405–415.

Perley, R. A. and Butler, B. J. (2013), 'An accurate flux density from 1 to 50 GHz', *ApJS* **204**, 19–39.

Pestalozzi, R., Elitzur, M., Conway, J. E. and Booth, R. S. (2004), 'A circumstellar disk in a high mass star forming region', *ApJ* **603**, L113–L116.

Purcell, C., Balasubramanyam, R., Burton, M., Walsh, A., Minier, V., Hunt-Cunningham, M., Kedziora-Chudczer, L., Longmore, S., Hill, T., Bains, I., Barnes, P., Busfield, A., Calisse, P., Crighton, N., Curran, S., Davis, T., Dempsey, J., Derragopian, G., Fulton, B., Hidas, M., Hoare, M. and Lee, J. K. Lumsden, S. (2006), 'A $CH_3CN$ and $HCO^+$ survey towards southern methanol masers associated with star formation', *MNRS* **367**(2), 553–576.

Purser, S., Lumsden, S., Hoare, M., Urquhart, J., S., Cunningham, N., Purcell, C.R.and Brooks, K. G. G. a. A. and Voronkov, M. (2016), 'A search for ionized jets towards massive young stellar objects', *MNRAS* **460**, 1039–1053.

Reid, M. J. and Moran, J. M. (1981), 'Masers', *ARA&A* **19**, 231–276.

Sakai, T., Sakai, N., Hirota, T. and Yamamoto, S. (2010), 'A survey of molecular lines towards massive clumps in early evolutionary stages of high-mass star formation', *ApJ* **714**, 1658–1671.

Sanchez-Monge, A., Beltran, M., Cesaroni, R.and Etoka, S., Galli, D., Kumar, M.S.N.and Moscadelli, L., Stanke, T.and van der Tak, F., Vig, S., Walmsley, C., Wang, K., Zinnecker, H., Elia, D., Molinari, S. and Schisano, E. (2014), 'A necklace of dense cores in the high-mass star forming region G35.20-0.74 N: ALMA observations', *A&A* **569**, A11.

Sanna, A. (2019), 'Size of the G9.62+0.20E HII region at Q band', Private email communication.

Sanna, A., Menten, K. M., Carreasco-Gonzalez, C., Reid, M. J., Ellingsen, S. P., Brunthaler, A. and Moscadelli, L. (2015), 'The environment of the strongest galactic methanol masers', *ApJL* **804**, L2.

Sanna, A., Reid, M. J., Moscadelli, L., Dame, T. M., Menten, K. M., Brunthaler, A., Zheng, X. W. and Xu, Y. (2009), 'Trigonometric parallaxes of massive star forming regions. VII. G9.62+0.20 and the expanding 3 kpc arm', *ApJ* **706**, 464–470.

Shu, F. H., Adams, F. C. and Lizano, S. (1987), 'Star formation in molecular clouds: observation and theory', *ARA&A* **25**, 23–81.

Slysh, V. I., Kalenskii, S. V. and Val'tts, I. E. (2002), 'Methanol radio emission at millimeter wavelengths: New masers at 1.3 and 2.8 millimeters', *Astron. Rep.* **46**(1), 49–56.

Smith, R. J., Glover, S. C. O. and Klessen, R. S. (2014), 'On the nature of star-forming filaments - I. filament morphologies', *MNRAS* **445**, 2900–2917.

Sobolev, A. M., Cragg, D., Ellingsen, S., Gaylard, M., Goedhart, S., Henkel, C. and Voronkov, M. (2007), 'How do methanol masers manage to appear in the youngest star vicinities and isolated molecular clumps?', *Proc. IAU Symp.* **3**(S242), 81–88.

Sridharan, T., Williams, S. J. and Fuller, G. A. (2005), 'The direct detection of a (proto) binary/disk system in IRAS 20126+4104', *ApJL* **631**, L73.

Stahler, S. W. and Palla, F. (2004), *The formation of Massive Stars*, 1st edn, Wiley-VCH.

Strömgren, B. (1939), 'The physical state of interstellar hydrogen', *ApJ* **89**, 526–547.

Sullivan, W. T. and Kerstholts, J. (1976), 'Time variation in the 18cm OH emission profiles over the period 1965-1972', *A&A* **51**, 427–450.

Svoboda, B. E., Shirley, Y. L., Alessio, T., Cara, B., Fuller, G. A., Qizhou, Zhang and Henrik, B., Peretto, N., Brogan, C. and Hunter, T. (2019), 'ALMA Observations of fragmentation, substructure, and protostars in high-mass starless slump candidates', *ApJ* **886**(1), 36.

Swift, J. J. and Welch, J. W. (2008), 'A case study of low mass star formation', *ApJSS* **174**, 202–222.

Szymczak, M., Blaszkiewicz, L., Etoka, S. and M., L. A. (2001), 'Variations of polarisation properties of OH maser emission from three semiregular variables', *A&A* **379**(3), 884–892.

Tan, J. C., Beltran, M. T., Caselli, P., Fontani, F., Fuente, A., Krumholz, M. R., Mckee, C. F. and Solte, A. (2014), Massive star formation, *in* B. K. K. and J. David, eds, 'Protostars and Planets', Vol. VI, University of Arizona Press, Tucson, Arizona.

Tennyson, J. (2003), *Molecules in space*, Vol. 3 of *Handbook of Molecular Physics and Quantum chemistry*, John Wiley & Sons, chapter 14.

Testi, L., Felli, M. and Persi, P. andRoth, M. (1998), 'HII region and hot dust emission around young massive stars in G9.62+0.19', *ApJ* **508**, L91–L94.

Testi, L., Hofner, P., Kurtz, S. and Rupen, M. (2000), 'Detection of the thermal radio continuum emission from the G9. 62+ 0.19-F Hot Core', *A&A* **359**, l5.

Thompson, A. R., Moran, J. M. and Swenson, G. W. (2001), *Interferometry and synthesis in radio astronomy*, 2nd edn, Wiley, New York.

Tielens, A. G. G. M. (2013), 'The molecular universe', *Rev. Mod. Phys.* **85**, 1021.

Traficante, A., Fuller, G. A., Peretto, N., Pineda, J. E. and Molinari, S. (2015), 'The initial conditions of stellar protocluster formation - II. A catalogue of starless and protostellar clumps embedded in IRDCs in the galactic longitude range 15deg$\leq l \leq$55deg$'$,*MNRAS***451**, $3089 - -3106$.

Traficante, A., Fuller, G., Duarte Cabral, A., Elia, D.and Heyer, M. H., Molinari, S., Peretto, N. and Schisano, E. (2020), 'Multi-scale dynamics in star-forming regions: the interplay between gravity and turbulence', *MNRAS* **491**, 4310–4324.

Trung, D.-V. (2009), 'On the theory of astronomical maser II. Polarization of maser radiation', *MNRAS* **399**, 1495–1505.

Urquhart, J., Figura, C., Moore, T., Csengeri, T., Lumsden, S., Pillai, T., Thompson, M., Eden, D. and Morgan, L. (2015), 'The rms survey: ammonia mapping of the environment of massive young stellar objects', *MNRAS* **452**, 4029.

Urquhart, J. S., Busfield, A. L., Hoare, M. G., Lumsden, S. L., Oudmaijer, R. D., Moore, T. J. T., Gibbs, A. G., Purcell, C. R., Burton, M. G., Marrechal, W. L.and Jiang, Z. and Wang, M. (2008), 'The RMS survey: CO Observation of the candidate massive YSO in the northern galactic plane', *A&A* **487**, 253–264.

Urquhart, J. S., Thompson, M. A., Moore, T. J. T., Purcell, C. R., Hoare, M. G., Schuller, F., Wyrowski, F., Csengeri, T., Menten, K. M., Lumsden, S. L., Kurtz, S., Walmsley, C. M., Bronfam, L., Morgan, L. K., Eden, D. J. and Russeil, D. (2013), 'ATLASGAL – Properties of compact HII regions and their natal clumps', *MNRAS* **435**, 400–428.

van den Heever, S. P., van der Walt, D., Pittard, J. and Hoare, M. (2019), 'Periodic methanol masers from a colliding wind binary perspective', *MNRAS* **485**, 2759–2771.

van der Walt, D. (2011*a*), 'On the methanol masers in G9.62+0.20E and G188.95 + 0.89', *AJ* **141**, 152.

van der Walt, D. (2011*b*), 'On the periodic class II methanol masers in the high mass star forming region G9.62+0.20E', *Bulletin del a Societe Royale des Science de Liège* **80**, 260–264.

van der Walt, D., , Goedhart, S. and Gaylard, M. J. (2009), 'Periodic class II methanol masers in G9.62+0.20E', *MNRAS* **398**, 961.

van Dishoeck, E. F. and Blake, G. A. (1998), 'Chemical evolution of star forming regions', *ARA&A* **36**, 317–368.

Viti, S. and Williams, D. A. (1999), 'Time-dependent evaporation of icy mantles in hot cores', *MNRAS* **305**, 755–762.

Viti, S., Williams, D. A. and O'Neill, P. (2000), 'Hydrocarbons in diffuse and translucent clouds', *A&A* **354**, 1062–1070.

Walsh, A. J., Burton, M. G., Hyland, A. R. and Robinson, G. (1999), 'Studies of ultracompact HII regions-III. near infrared survey of selected regions', *MNRAS* **309**, 905–922.

Walsh, A. J., Burton, M., Hyland, A. R. and Robinson, G. (1998), 'Studies of ultracompact HII region II. high resolution radio continuum and methanol maser survey', *MNRAS* **301**, 640–698.

Walsh, A. J., Hyland, A. R., Robinson, G. and Burton, M. G. (1997), 'Studies of ultracompact HII regions - I. Methanol maser survey of IRAS-selected sources', *MNRAS* **291**, 261–278.

Wang, J. W., Lai, S. P., Chakali, E., Kate, P., Francesco, J. D., Doug, J., Koch, P. M., Tie, L., Motohide, T., Furuya, R. S., Takashi, O., Ward-Thompson, D., Soam, A., Kim, K., Lee, C., Lee, C., Mairs, S., Arzoumanian, D., Kim, G., Hoang, T., Hwang, J., Liu, S., Berry, D., Bastien, P., Hasegawa, T., Kwon, W., Qiu, K. and André, P. (2019), 'JCMT BISTRO Survey: Magnetic fields within the hub-filament structure in IC 5146', *ApJ* **876**, 42.

Wang, K., Zhang, Q., Testi, L., van der Tak, F., Wu, Y. and Zhang, H. (2014), 'Hierarchial fragmentation and differential star formation in the Galactic 'Snake': infrared dark cloud G11. 11-0.12', *MNRAS* **439**, 3275–3293.

Willacy, K. and Williams, D. (1993), 'Desorption processes in molecular clouds:quasi steady state chemistry', *MNRAS* **260**, 635–642.

Wilson, T. L., Rohlfs, K. and Hüttemeister, S. (2009), *Tools of radio astronomy*, 2nd edn, Springer, Berlin.

Wood, D. O. S. and Churchwell, E. (1989), 'The morphologies and physical properties of ultracompact Hii regions', *ApJS* **69**, 831–895.

Yamamoto, S. (2017), *Introduction to Astrochemistry: Chemical evolution from interstellar clouds to star formation*, 1st edn, Springer Japan.

Yorke, H. W. and Sonnhalter, C. (2002), 'On the formation of massive stars', *ApJ* **569**, 846–862.

Zhang, Q., Wang, K. and Lu, X. (2015), 'Fragmentation of molecular clumps and formation of a protocluster', *ApJ* **804**, 141.

Zinnecker, H. (1982), *Symposium on the Orion Nebula to Honour Henry Draper. NY Acad. Sci.* p. 226.

Zinnecker, H. and Yorke, H. W. (2007), 'Toward understanding massive star formation', *ARA&A* **45**, 481.